PREPARATION AND CHARACTERIZATION OF Co-Ni-Ga FERROMAGNETIC SHAPE MEMORY ALLOYS

A thesis submitted

by

Sidananda Sarma
Roll 004604

to

Indian Institute of Technology Guwahati

in

partial fulfillment of the requirement for the award of the degree of
Doctor of Philosophy in Physics

Department of Physics

Indian Institute of Technology Guwahati

Guwahati – 781039, Assam, India

August 2008

Statement

The work contained in the thesis entitled “Preparation and characterization of Co-Ni-Ga ferromagnetic shape memory alloys” has been carried out by me under the supervision of Prof. A. Srinivasan, Department of Physics Indian Institute of Technology Guwahati. This work has not been submitted elsewhere for the award of any degree.

August 29, 2008

(Sidananda Sarma)

Roll No: 004604

Department of Physics

Indian Institute of Technology Guwahati

Guwahati - 781039

Certificate

It is certified that the work contained in the thesis entitled “Preparation and characterization of Co-Ni-Ga ferromagnetic shape memory alloys” by Sidananda Sarma, a Ph. D. student of the Department of Physics, Indian Institute of Technology Guwahati for the award of degree of Doctor of Philosophy has been carried out under my supervision. This work has not been submitted elsewhere for the award of any degree.

August 29, 2008

(Dr. A. Srinivasan)
Professor
Department of Physics
Indian Institute of Technology Guwahati
Guwahati - 781039

To my Parents …

and

daughter Jumon

Acknowledgements

First of all, I would like to thank my thesis supervisor Prof. A. Srinivasan for introducing me into the world of Shape memory alloys. I am grateful to him for his endless effort, constant encouragement and keen interest in the progress of my work. He made all the arrangement for me in advance to prepare and analysis of my samples. His guidance turned me into an independent research worker.

I would like to thank my doctoral committee members, Dr. S. Ravi, Dr. P. Agarwal and Prof. P. S. Robi for their suggestions to improve my research work. I would like to express my appreciation to Prof. Robi for permitting me to work freely in the material science laboratory of Mechanical Engineering Department after office hours and on holidays.

I am thankful to Prof Alika Khare for her constant encouragement and mental support during my Ph.D. work. I'm grateful to the Department of Physics and the Institute for allowing me to carry out research as a part-time research scholar. My thanks are due to all faculty members of our Department for their help and suggestion. It is my pleasure to record my gratitude to my colleague Lokesh Chakraborty, Atul Ch. Deka, Pankaj Goswami, Madan Deka, Bimal Kr. Sarma, Basab B. Purakayastha and Jyoti P. Borah for their mental support during my research work.

My sister's friend Ms. Ranju Bhuyan used to write me letters in my college days describing how the research workers work in laboratories. I was motivated towards research with her letters in those days itself. I sincerely acknowledge her at this moment. I am grateful to Ms. A. Janaki for inspiring me to carry out the research sincerely without unnecessarily worrying for results. She used to say me that work is like an insurance policy and it never goes waste. My sincere thanks are due to Mr. Chandan Borgohain, Mr. Kula Kamal Senapati, Mr. Rituraj Saikia, late Ramananda Das and Mr. Sanjib Sarma for extending technical help at Central Instrumentation Facility and Material Science Laboratory, ME. During my work, I have benefited from the mechanical workshop in the

fabrication of the instrumental set up. I would like to thank all the members in the workshop. I express my special gratitude to my co-research workers and friends for their affection and encouragement. My special thanks go to Manos, Rajendra, Debabrata, Amal, Anto, Munima, Indrajit, Manoranjan, Amit, Panchanan, Anil Bora, Sandeep, Pramod and Ardhendu. I'm thankful to them for many useful discussions I had with them. The help extended by Manos, Rajendra, Debabrata and Mr. L.N. Sharma during printing and arrangement of my thesis is unforgettable.

I am deeply indebted to my parents, my mother-in law, sisters and brothers for their constant encouragement and moral support. My brother-in-law Mr. Dijen Goswami and sister Beuty are next to my parents. They have been taking responsibilities of my parents in many critical situations and helped me to carry out my research work freely. I'll remember this help throughout my life. My uncles, aunties and cousins have always been sources of inspiration to me. Particularly, Mr. Biren Sarma and Ms. Rina Sarma often used to phone me up and advise me not to deviate from research work until it is completed. I'm indebted to all of them.

Last but not least, I would like to offer my sincere gratitude to my wife Sumi and daughter Jumon.

Finally, I express my sincere thanks to all who helped me in whatever manner during my Ph.D. work some of whom I may have inadvertently forgotten to mention in this acknowledgement.

- Sidananda.

PRFECAE

Shape memory alloys (SMA) have been engineered for various applications and devices since the first discovery of the shape memory effect in the 1930s. The advent of Nitinol (a Ni-Ti alloy) in 1962 established SMAs as a major area of research and development. . Unlike most conventional metals that recover less than 1% of the strain before plastic deformation, SMAs undergo a diffusionless thermo-elastic martensitic phase transformation that enable them to deform *via* the movement of twins or self accommodation process rather than by conventional dislocation slip mechanism and thereby allow recovery of strain as large as 8%. Diffusionless phase transformation in an SMA can be triggered by temperature change or application of stress or magnetic field. In conventional SMA, shape change or mechanical strain is achieved by applying a mechanical stress or by temperature variation. These inherently slow processes put an upper limit on the actuation speed of the SMA. Faster change of shape / volume or mechanical strain can be achieved in some magnetic alloys by applying an alternating magnetic field. Such alloys are called ferromagnetic shape memory alloys (FSMAs). Current research activities on FSMAs are mainly aimed at understanding the properties of FSMAs and developing FSMAs with properties desirable for actuator applications.

Quite a few FSMAs had been developed and many of them have been proposed as potential candidates for sensor and actuator applications. But till now, no practical device has been reported with these FSMAs and the material is still being investigated

intensively. Practical application of prototype Ni-Mn-Ga alloy is limited because of its extreme brittleness in polycrystalline state. Co-Ni-Ga solidifies in a peritectic reaction and forms a composite structure with fcc γ-phase and bcc β matrix. Thus, controlled amount of γ-phase can be introduced in the β-matrix by proper choice of composition and suitable heat treatment conditions. The hot workability and room temperature ductility of these alloys are significantly improved by the introduction of the γ-phase, which is a great advantage for practical applications.

Understanding the evolution of various crystalline phase in FSMAs by different processing conditions and the resulting changes in properties of the alloys is crucial for evaluating these materials for actuator applications. Although the prototype FSMA, Ni-Mn-Ga has been well studied, other FSMAs such as Co-Ni-Ga, Ni-Fe-Ga etc. have not yet been investigated with so much rigour. In this thesis work, a systematic investigation of the processing conditions and physical properties of several Co-Ni-Ga alloys has been carried out.

Three series of Co-Ni-Ga alloys have been prepared by a process consisting of arc melting technique followed by the homogenization at high temperature and quenching to low temperature. Care was taken to prepare alloys with ferromagnetic martensite near room temperature. The samples were characterized by powder X-ray diffractometer, energy dispersive spectrometer attached to a scanning electron microscope, optical microscope, differential scanning calorimeter, magnetic ac susceptometer, vibration sample magnetometer, Vickers microhardness tester, Universal testing machine (UTM) and strain gauge setup couple to an electromagnet, etc.

The present thesis work has been presented in six chapters, namely, (1) introduction, (2) experimental technique and methodology, (3) investigations on

$Co_xNi_{25}Ga_{75-x}$ ($43 \leq x \leq 50$) alloys, (4) investigations on $Co_{70-x}Ni_xGa_{30}$ ($20 \leq x \leq 25$) alloys, (5) investigations on $Co_{48-x}Ni_{22}Ga_{30-y}T_{x+y}$ (T = Fe, Mn and $x + y = 1$, 3 and 6) alloys, and (6) conclusions and scope for future work.

Chapter 1 serves as a brief introduction to shape memory alloys. A brief review of earlier work done on ferromagnetic shape memory alloys and the motivation behind the thesis work are given here.

Chapter 2 discusses the experimental techniques used in the present investigations. The basic principle and the theory behind the experiments, the experimental set up and the measurement / methodology leading to the determination of the physical properties are discussed here. Instrumentation developed for the specific needs of this research work are also discussed in this chapter.

In chapter 3, the experimental studies on $Co_xNi_{25}Ga_{75-x}$ ($43 \leq x \leq 50$) alloys are presented. It starts with the determination of crystal structure of the alloys. Rietveld refinement technique was used for crystal structure refinement of single phase alloys. The variation of martensitic transformation temperatures, Curie temperatures saturation magnetization and magneto-crystalline anisotropy of the alloys with the change of composition are discussed. The salient features of the present studies on $Co_xNi_{25}Ga_{75-x}$ alloys are summarized at the end of the chapter.

Chapter 4 is devoted to the studies on $Co_{70-x}Ni_xGa_{30}$ ($20 \leq x \leq 25$) alloys. This chapter is arranged in the same sequence as chapter 3. But the influence of quenching temperature and quenching rate on the crystal structure, microstructure, martensitic transformation temperatures Curie temperature and other properties are discussed in

details. Use of modified Arrott plot for accurate measurement of Curie temperature and critical constants involved during ferromagnetic to paramagnetic phase transition of this FSMAs is discussed using $Co_{45}Ni_{25}Ga_{30}$ as a typical sample. The optimum processing conditions for the improvement of ductility of the alloys without disturbing martensitic transformation is found. Mechanical properties such as microhardness, strength, strain induced by the mechanical compressive stress and its recovery due to shape memory or pseudo-elastic effects of ductile samples are discussed.

Effort was made to enhance the magnetic properties of Co-Ni-Ga alloys by the addition of a fourth element. Small amounts of Fe or Mn were substituted for Co and Ga in $Co_{48}Ni_{22}Ga_{30}$. The resulting modifications in various properties such as crystal structure, microstructure, magnetic and mechanical properties are discussed in chapter 5. Magnetic field induced strain in some selected samples has been measured and results are discussed in this chapter.

Chapter 6 is the concluding chapter which attempts to summaries the results obtained on the present studies on Co-Ni-Ga ferromagnetic shape memory alloys. Scope for future work on these FSMAs is also briefly touched upon at the end of this chapter.

References cited in the thesis are listed at the end of the thesis.

Contents

INTRODUCTION

Materials that respond dynamically to environmental stimuli are generally called as 'intelligent' or 'smart' materials [1-3]. Most materials are responsive to some stimuli and in this (conventional or simple) sense can be termed as 'smart'. But, it is doubtful whether all these materials can respond in an adaptive way. A 'very smart' adaptive response is exhibited by a material if it can respond dynamically to a number of input stimuli and in a repeatable manner. Thus, a simple pressure transducer that produces a voltage output dependent on the input pressure could be regarded as 'smart' in a simple way. Then, a pressure transmitter incorporating a thermocouple that measures both temperature and pressure and corrects the pressure in response to the sensor's temperature coefficient is to be regarded as 'very smart'. Fig. 1.1 summarizes the responses of different transducer materials to different stimuli.

According to the general definition of a smart material [4], the material must also respond to more than one variable. If the material can be engineered to exhibit a particular response due to a sum of inputs, then it fulfills the definition of being 'very smart'. The term 'very smart' also used to refer to materials that can (1) respond reversibly to the changes in the surrounding environment, and (2) contribute an optimal or useful response by either changing its physical properties, geometry, mechanical

properties, or electromagnetic properties. The physical change is usually a significant one which can easily be observed and detected. In recent years, these 'very smart' materials are being intensely investigated because of their ability to change their physical properties usefully when they are triggered by environmental stimuli [5]. In all cases, very smart materials are expected to provide a reversible and useful response to a change in the adapted environment [6]. Shape memory materials belong to a class of 'very smart' materials, which have the ability to remember their original shape.

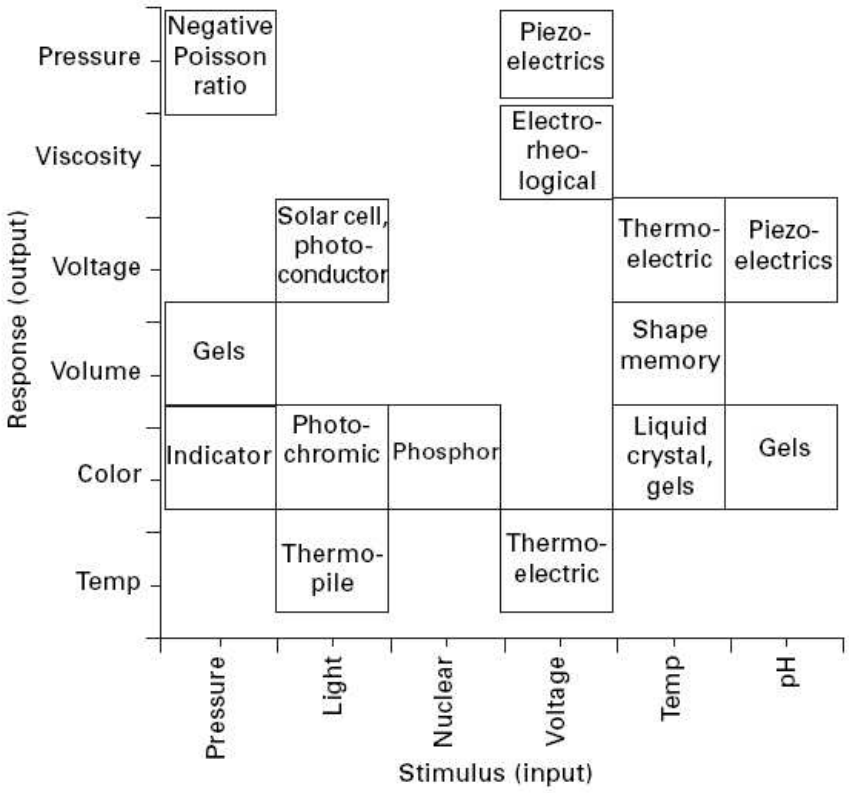

Fig. 1.1: Response of some sensor materials. These materials are often referred to as 'smart' [from reference 4].

Shape memory alloys (SMA) have been engineered for various applications and devices since the first discovery of the shape memory effect in the 1930s [7]. The advent of Nitinol (a Ni-Ti alloy) in 1962 [8] established SMAs as a major area of research and

development. Since then more than 10,000 patents have been issued for applications using SMAs. Unlike most conventional metals that recover less than 1% of the strain before plastic deformation, SMAs undergo a diffusionless thermo-elastic martensitic phase transformation that enables them to deform *via* the movement of twins or self accommodation process rather than by conventional dislocation slip mechanism and thereby allow recovery of strain as large as 8%. Diffusionless phase transformation in an SMA can be triggered by temperature change or application of stress or magnetic field. In a conventional SMA, shape change or mechanical strain is achieved by applying a mechanical stress or by temperature variation. These inherently slow processes put an upper limit on the actuation speed of the SMA. Faster change of shape / volume or mechanical strain can be achieved in some magnetic alloys by applying an alternating magnetic field. Such alloys are called ferromagnetic shape memory alloys (FSMAs) or magnetic shape memory alloys. It is generally believed that FSMAs have the potential to be the next generation 'very smart' actuator materials. The phenomenon of coupled magnetic and structural phase transitions observed in FSMAs is rare in condensed matter physics. Such systems with coupled phase transformation can exhibit many interesting properties including giant magneto-caloric effect, magneto-resistance and magneto-striction, and consequently have great technological potential. Current research activities on FSMAs are mainly aimed at understanding the properties of FSMAs and developing FSMAs with properties desirable for actuator applications. Since this thesis is concerned with the preparation and properties of Co-Ni-Ga FSMAs, a brief account of some general aspects of SMAs and FSMAs is given in the following sections.

1.1. SHAPE MEMORY ALLOYS

Shape memory alloys (SMAs) are metallic alloys that "remember" their original shapes. SMAs exhibit two unique properties, *viz*., shape memory effect and pseudo-elasticity (or super-elasticity). The remarkable properties of SMA have been known since the 1930's [9-12]. Ölander discovered the pseudo-elastic behavior of the Au-Cd alloy in 1932 and the shape memory effect was first observed in 1951 by Chang and Read in an Au-47.5 at% Cd alloy [10]. However, SMA attracted some technological interest only after the discovery of Nitinol. In 1962, Buehler and co-workers [9], of the U.S. Naval Ordnance Laboratory, discovered shape memory effect in an equiatomic Ni-Ti alloy which began to be known as NITINOL. These discoveries led to the development of a considerable number of shape memory alloys (SMAs), some of which are listed below:

Table 1.1: Different types of shape memory alloys [10].

- Ag - 44/49 at.% Cd
- Au - 46.5/50 at.% Cd
- Cu -14/14.5 wt.% Al-3/4.5 wt.% Ni
- Cu - approx. 15 at.% Sn
- Cu -38.5/41.5 wt.% Zn
- Cu - Zn-X (X = Si, Al, Sn)
- Ti-Pd in various concentrations
- Ni -Ti
- Ni-Mn-Ga
- Fe-Pd
- Fe_3 Pt
- Ni-Mn-Al
- Ni-Mn-In
- Ni-Fe-Ga
- Co-Ni-Al
- Co-Ni-Ga

The widely researched, as well as the most prominent SMA currently used in various applications is Ni-Ti. Ni-Ti alloys are generally more expensive; however they

possess superior mechanical properties when compared to copper-based SMAs. Because of their unique properties, SMAs can be utilized as 'multifunctional' materials in structural, sensing, and actuating applications.

1.1.1. The Shape Memory Effect

When temperature of an SMA is lowered below its transformation temperature, it has very low yield strength and can be deformed quite easily into new shape which it can retain. However, when the material is heated above a specific (characteristic) temperature, it undergoes a change in crystal structure which causes it to return to its original shape. If the SMA encounters any resistance during the transformation, it can generate extremely large forces to counter it [10]. The high temperature phase is called austenite phase and low temperature phase is called martensite phase. To give the so-called 'original' shape to an SMA which it can remember, the alloy is stressed or heat treated for a long time in the parent (austenite) phase. When the SMA in the parent phase is cooled down to some critical temperature called M_s (martensitic start temperature), its structure changes into martensitic (low temperature and low symmetry) phase. In this stage, multiple formations of martensites with the same structure in different orientations are possible. These are called 'variants' of martensite. These structural domains have well defined boundaries and they are called 'twin variants'. The line joining the two variants is known as the 'twin boundary'. Due to easy movement of twin boundaries, the sample can be deformed easily in the martensitic phase. Thus, a sample with a parent shape could be deformed in the martensite phase by the application of stress. The SMA retains the deformed shape after removal of the stress. The schematic diagram of temperature

induced martensitic transformations and shape memory effect is shown in Fig. 1.1.1a and Fig. 1.1.1b.

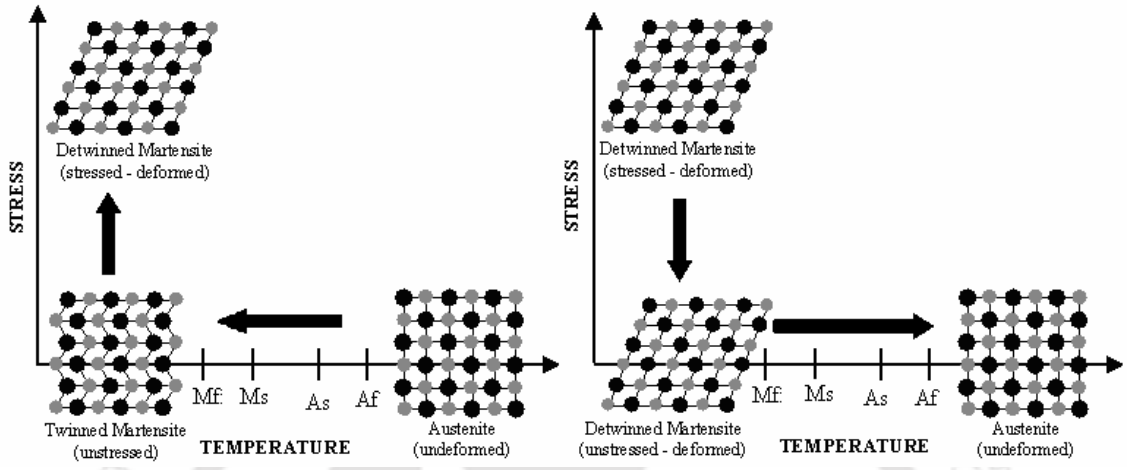

Fig. 1.1.1a: Temperature and stress induced phase transformations.

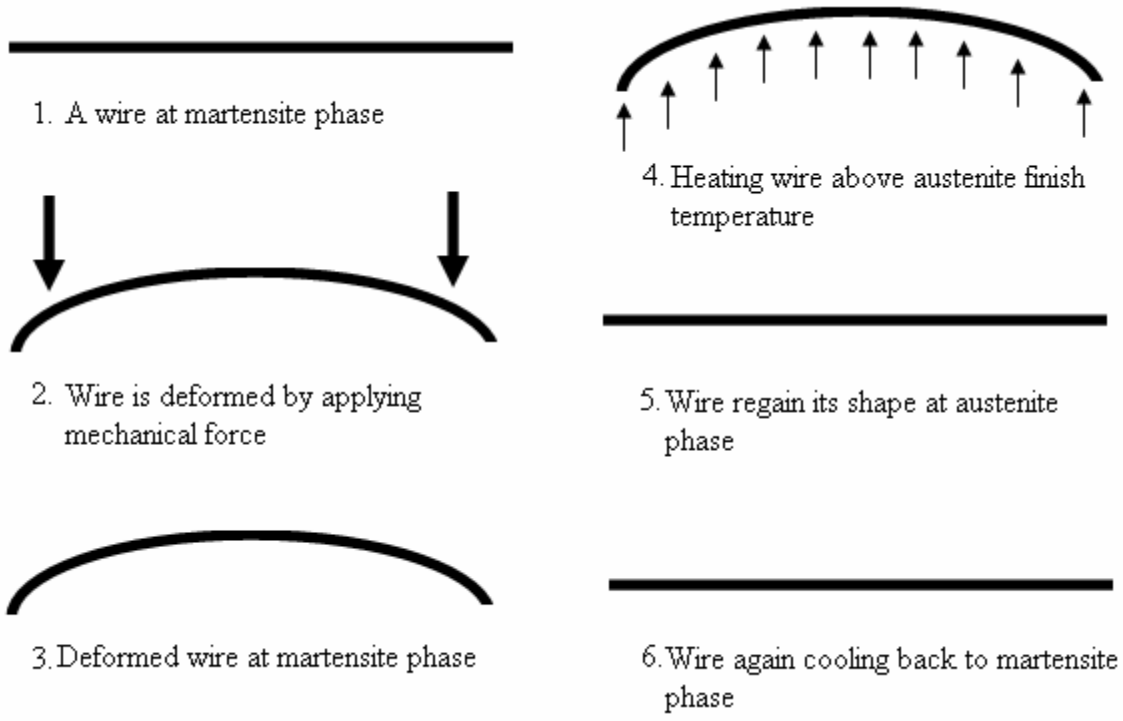

Fig. 1.1.1b: Shape Memory Effect in a straight wire.

However, when the sample is heated back to the austensite phase, the sample will recover to its original shape, *i.e*., it will 'remember' the shape it had before being cooled to the martensite phase. Hence, the sample can be claimed to possess a memory of its parent shape and has the ability to revert back to the parent shape if it is heated back to the austenite phase. The temperature at which the SMA changes its crystallographic structure which is called the martensitic transformation temperature, is characteristic of the alloy, and can be tuned by varying the elemental ratios in the alloy.

A typical differential scanning calorimeter (DSC) curve showing the transformation temperatures obtained under constant heating and cooling rates is shown in Fig. 1.1.2.

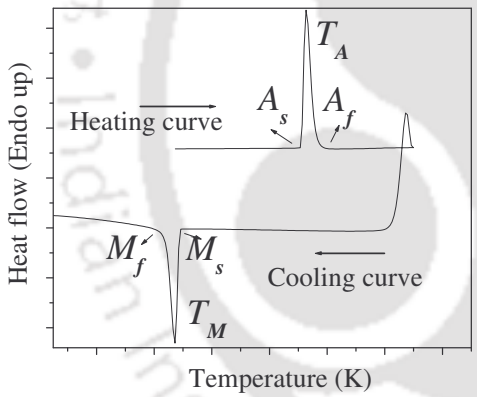

M_s: Martensite start temperature upon cooling
M_f: Martensite finish temperature upon cooling
T_A: Martensite peak temperature upon cooling
A_s: Reverse transformation start temperature upon heating
A_f: Reverse transformation finish temperature upon heating
T_M: Reverse transformation peak temperature upon heating

Fig. 1.1.2: DSC curve showing the martensite and austenite transformations.

1.1.2. Martensitic transformations

Martensite is a crystal structure that is formed by displacive transformation, as opposed to the common diffusive transformations, which is much slower. The martensitic phase transformation is diffusionless, cooperative and shear-like motion of atoms from a high

symmetry phase to a lower symmetry phase, as shown schematically in Fig 1.1.1a. For a reversible martensitic transformation to occur, the following conditions must be satisfied:

1) the driving force for the transformation should be very small,
2) the interface between the martensite and the austenite phases has to be very mobile upon heating and cooling, and
3) the transformation should be crystallographically reversible, *i.e*., the martensite should revert back to the austenite in its original orientation rather than re-nucleating into austenite in different orientations.

Martensitic transformations that satisfy these conditions are also known as thermo-elastic martensitic transformations. The following are the salient properties of this transformation.

1) Martensitic transformations are usually first order solid state structural phase transitions which are diffusionless and dislplacive.
2) Their kinetics and morphology are dictated by the strain energy arising from shear displacement.
3) The atoms move in an organized manner relative to their neighbours and therefore they are known as 'military' transformations in contrast to diffusional 'civilian' transformations. and
4) The displacement can be described as a homogeneous lattice deformation.

1.1.3. One-way and two-way shape memory effects

SMAs are known to display two different types of shape memory effects, *viz*., the one-way and the two-way shape memory effects. A schematic view of the two effects is given

in the Fig. 1.1.3. When a SMA is in its martensitic state, it can be bent or stretched into a variety of new shapes (Fig.1.1.3b) and will retain that shape until it is heated above the transition temperature. Upon heating, the shape changes back to its original shape (Fig.1.1.3c), regardless of its shape in the martensitic state. When the SMA is cooled again, it will remain in the hot shape (Fig.1.1.3c), until deformed again. Such an SMA is said to have 'one-way' shape memory. With the one-way effect, cooling from high temperatures does not cause a macroscopic shape change. A deformation is necessary to create the low-temperature shape.

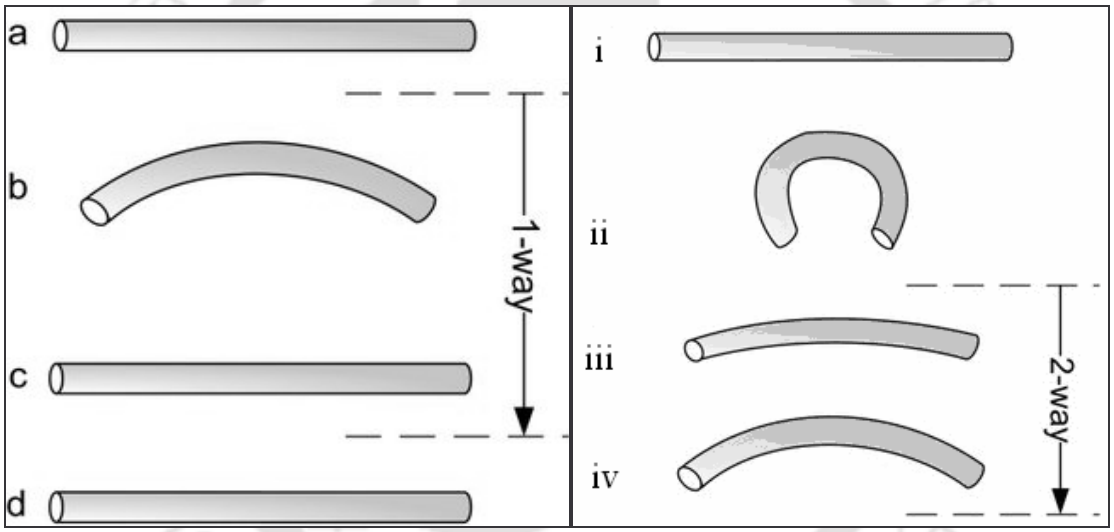

Fig. 1.1.3: One-way and two-way shape memory effects.

A material that shows a shape memory effect during both heating and cooling is called two-way shape memory. In the two-way shape memory effect, the material remembers two different shapes: one at low temperatures (*cf.* Fig. 1.1.3ii), and the other at the high temperature (*cf.* Fig. 1.1.3iv). This effect can also be obtained without the application of an external force (intrinsic two-way effect). The reason the material

behaves so differently in these situations lies in its 'training'. Training implies that an SMA can 'learn' to behave in a certain way. Under normal circumstances, a shape memory alloy 'remembers' its high-temperature shape. But upon heating to recover the high-temperature shape, it immediately 'forgets' the low-temperature shape. However, it can be 'trained' to leave some reminders of the deformed low-temperature condition in the high-temperature phase. There are several ways of doing this. If an SMA is heated up to very high temperatures (after it has been trained), then it may lose the two-way memory effect. Hence this process is said to induce 'amnesia'.

1.1.4. Pseudo-elastic effect

SMAs show almost rubber-like flexibility. This is called 'pseudo-elasticity' or 'super elasticity'. Due to this property, phase change of SMAs from austenite to martensite can be achieved by applying pure mechanical load (without varying temperature). Stress-Strain diagram corresponding to pseudo-elastic effect in an SMA is shown in Fig.1.1.4a.

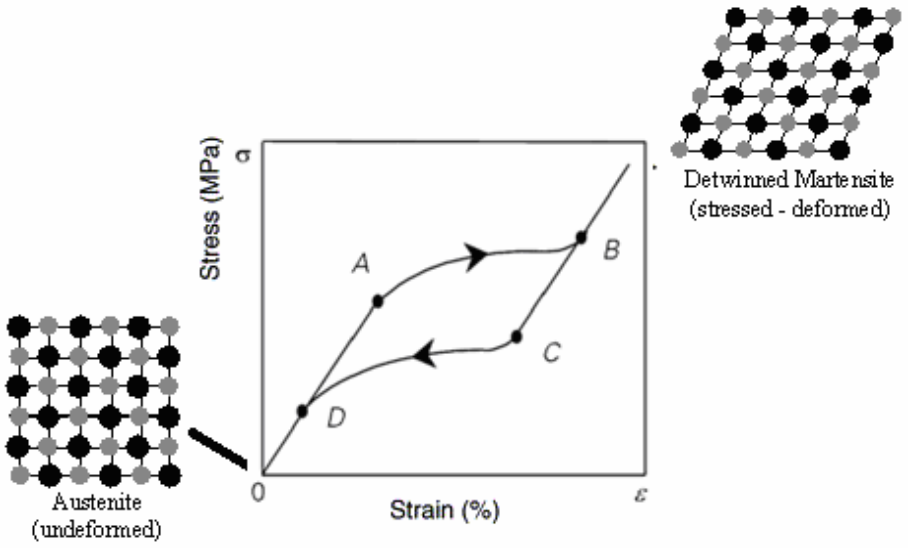

Fig. 1.1.4a: Stress-Strain diagram of the pseudo-elastic effect in an SMA.

Pseudo-elasticity occurs in SMAs when the alloy is completely composed of austenite phase (for $T > A_f$). Unlike the shape memory effect, pseudo-elasticity occurs without a change in temperature. The load on the shape memory alloy is increased until the austenite transforms into martensite, simply due to the loading (Fig.1.1.4b). The loading is absorbed by the softer martensite. But as soon as the loading is decreased, the martensite begins to transform back to austenite since the temperature of the alloy is still above A_f, and it has to regain its original shape.

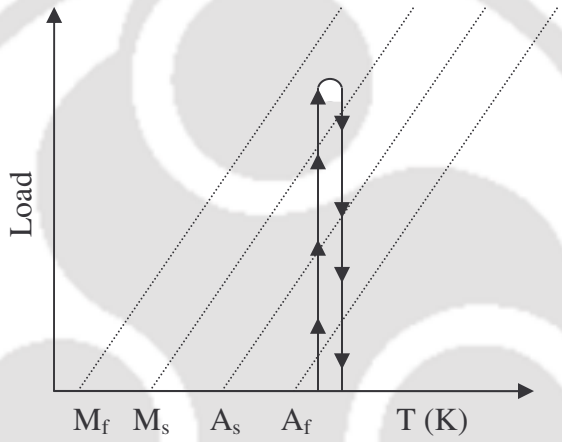

Fig. 1.1.4b: Stress induced martensitic transformations.

1.1.5. Applications of shape memory alloys

Shape memory alloys are used in a variety of applications [10-12] such as military, medical, safety, and robotics. The United States military has been using Nitinol couplers in F-14 fighter planes since the late 1960s. Many of the current applications of Nitinol have been in the field of medicine. Tweezers to remove foreign objects through small incisions were invented by NASA, U.S.A. Anchors with Nitinol hooks to attach tendons

to bone were used for Orel Hershiser's shoulder surgery. Orthodontic wires made out of Nitinol reduce the need to retighten and adjust the wire. Nitinol eyeglass frames can be bent totally out of shape and return to their parent shape upon warming. Nitinol localizers used to locate and mark breast tumors utilize the metal's shape memory property. Another successful medical application is Nitinol's use as a guide for catheters through blood vessels. Anti-scalding devices and fire-sprinklers utilizing SMAs are already in the market. Nitinol is being used in robotic actuators and micromanipulators to simulate human muscle motion. The main advantage of Nitinol is the smooth, controlled force it exerts upon activation. Other miscellaneous applications of shape memory alloys include use in household appliances, clothing and structures.

Future applications envisioned include components of engines in cars and airplanes and electrical generators utilizing the mechanical energy resulting from the shape transformations. Some of the main advantages of shape memory alloys include bio-compatibility of some SMAs and good mechanical properties (high strength, corrosion resistant). However, there are still some difficulties with SMAs that must be overcome before they can live up to their full potential. These alloys are still relatively expensive to manufacture and machine as compared to other materials such as steel and aluminium. Most SMA's have poor fatigue properties which mean that under the same loading conditions (i.e. twisting, bending, compressing), a steel component may survive for more than one hundred times more cycles than an SMA element. Moreover, the response time of SMAs is slow as it is driven by temperature/mechanical stress. These inherently slow processes put an upper limit on the actuation speed of the SMA. Faster change of shape / volume or mechanical strain can be achieved in some magnetic alloys by applying an

alternating magnetic field. Such alloys are called ferromagnetic shape memory alloys (FSMAs).

1.2. FERROMAGNETIC SHAPE MEMORY ALLOY (FSMA)

Ferromagnetic shape memory alloys are very smart materials which can undergo large reversible deformations in an applied magnetic field. As such, they can function both as sensors and actuators. Compared to the ordinary (temperature driven) shape memory alloys, the magnetic field control offers faster response, since the heating and especially cooling process is slower than alternating a magnetic field. Also, the maximum deformation obtained in FSMAs is larger than that obtained in ordinary magnetostrictive materials. When an FSMA is cooled down, it undergoes a structural (so called martensitic) transformation from a cubic to a tetragonal (or modulated) structure. There are two or more equivalent directions for the tetragonal distortions, which results in a twinned microstructure. There are regions called twin variants which have the same structure but with tetragonal distortion occurring in different directions. The twin variants are separated by well defined boundaries. The ordinary shape memory effect is based on the relatively easy movement of the twin boundaries (resulting in large shape changes) and the recovery of the original structure when heated above the structural transition temperature.

In the magnetic shape memory alloys, there are also internal magnetic moments. In the absence of an external field, the magnetic moments are aligned with the easy directions of the magnetization which differ in the different twins [Fig. 1.2a (i)]. When external magnetic field is applied, the magnetic moments try to align with the field. There

are two possibilities, *viz*., the magnetic moments can just rotate within the twins, as it happens in the ferromagnetic shape memory effect [Fig.1.2a (ii)] the twins themselves can move so that the directions of the easy magnetizations align with the field (Fig.1.2a iii). The magnetic field induced redistribution of the twin variants gives the large shape changes observed in the FSMAs.

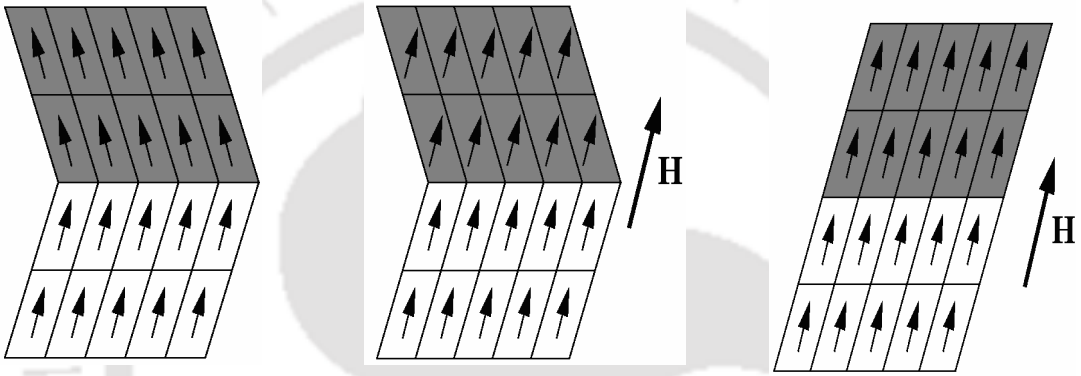

(i) Magnetic moments without external field.

(ii) Rotation of magnetic moments within the twins.

(iii) Redistribution of the twin variants

Fig. 1.2a: Rotation of magnetic moment on application of magnetic field.

The energy required to rotate the magnetization away from the easy directions is called the magnetic anisotropy energy (MAE). For better understanding, a brief discussion on MAE is included here. When the magnetic properties of a crystal are dependent on the direction in which they are measured, the crystal is said to have magneto-crystalline anisotropy. Magnetization has a certain preferable direction with respect to the crystal lattice, the so-called easy axis (the direction along which magnetization tends to align when an external magnetic field is applied). If the energy

required for rotating the magnetization out of the easy direction (i.e. MAE) is higher than the energy required to move a twin, then it is energetically more favorable to move the twin boundaries instead of rotating the magnetization. As a result, twin boundaries can move through the material to increase the volume fraction of the favorably oriented martensite variants and decrease the volume fraction of the unfavorably oriented variants, which lowers the total energy of the system. An interesting and advantageous result of this variant rearrangement is that a macroscopic strain can be induced in a FSMA by applying a magnetic field. If the applied magnetic field is reversed, the twin boundaries can move back to their original positions, recovering the magnetic field induced strain. This magnetic field induced shape memory effect is illustrated in Fig. 1.2a. In short, to be a useful FSMA, the alloy must have ferromagnetic martensite phase and a high uniaxial magneto-crystalline anisotropy.

The ferromagnetic shape memory effect is in a way analogous to super elasticity observed in traditional SMAs. The super-elastic effect occurs when a SMA in its austenitic state is stressed, resulting in the formation of a metastable martensite phase. The martensite forms because the applied stress lowers its total energy, which stabilizes the martensite even though the temperature is above the unstressed martensite-austenite transformation temperature. Analogous to stress-induced martensite, an applied magnetic field can also induce the formation of martensite. If a FSMA is in the austenitic state and an applied magnetic field lowers the total energy of the martensite, a metastable martensite can form. These materials are of particular interest as the magnetic response tends to be faster and more efficient than the temperature-induced response.

Ni-Mn-Ga [13] is the first ternary prototype FSMA developed. Subsequently, Fe-Pd [14], Fe_3Pt [15], Ni-Mn-Al [16], Co-Ni-Al [17-19], Co-Ni-Ga [19,20], Fe-Ni-Ga [21,22] FSMAs have also been developed. Among the FSMAs reported so far, Ni-Mn-Ga alloys are the most widely investigated due to their giant MFIS and excellent thermal stability. In 1996, Ullakko *et al.* [23] reported a large magnetic field induced strain of ~6% in Ni_2MnGa single crystal, which triggered a lot of interest in stoichiometric and off-stoichiometric Heusler alloys. Heusler alloys are ternary intermetallic compounds with a common composition form of X_2YZ. At high temperatures, the stable phase corresponds to a disordered body centered cubic (*bcc*) type structure, referred to as the *A2* phase, characterized by an arbitrary occupation of every site in the crystal lattice [24]. The *A2* phase undergoes a two-stage disorder–order transition on cooling to an ordered *B2* phase. In this phase, *X* atoms order themselves while *Y* and *Z* atoms occupy their sites in the crystal lattice randomly. On further cooling, the structure transforms to the ordered $L2_1$ phase, which is commonly known as the Heusler structure (Fig. 1.2b).

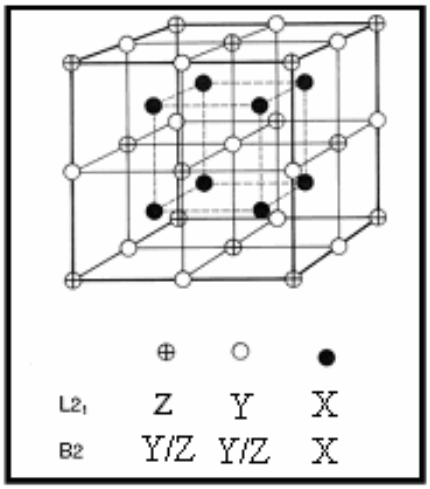

Fig. 1.2b: Atomic arrangement of Heusler alloy X_2YZ [25] for $L2_1$ and *B2* order.

Heusler alloys such as Ni_2MnGa, which are intrinsically inter-metallic compounds, suffer from a number of drawbacks as applicable to engineering materials, the most significant among them being the low toughness of the matrix. In this regard, efforts have been made to explore other systems, particularly, solid solution based alloy systems such as Co–Ni–Al [17, 18, 19] and Co-Ni-Ga [19,20].

1.2.1. Preparation

FSMAs are generally prepared by induction melting [16, 17], arc melting [19, 16, 22] or melt-spinning [26]. Single crystals of FSMAs have also been prepared from the polycrystalline material. Chernenko *et al*. [27, 28] prepared Ni-Mn-Ga alloys by repeated induction melting under argon atmosphere and casting into a cooper mold. Casting into copper mold was employed to get a regular shaped sample. Rod type sample obtained from cylindrical copper mold exhibited relatively small grain size as compared to the button ingot [29]. Wang *et al*. [30] prepared Ni-Mn-Ga alloys by arc melting constituent metals under argon atmosphere followed by the homogenization of the ingots by annealing at 827 °C for nine days in sealed quartz ampoules. Repeated melting causes weight loss of the cast sample which will change the composition of the sample from the desired value. Homogenization below melting point for long time periods yields a homogenous sample. Sometimes, annealing at high temperature is employed to get the desired single phase (*B2* or $L2_1$) sample [16]. Quenching from high temperature into ice water / liquid nitrogen is employed to avoid intermediate phase formation which may have adverse effect on shape memory properties.

The Gibbs free energy change (ΔG) of a system upon martensitic transformation (MT) may be written as a summation of change of chemical energy term (ΔG_c), surface energy term between austenite and martensite (ΔG_s) and elastic energy term around martensite (ΔG_e). In most MTs, the last two non-chemical parts ($\Delta G_{nc} = \Delta G_s + \Delta G_e$) are equally as large as the chemical energy term. Because of this, super-cooling is necessary for the nucleation of martensite [10]. So, shape memory effect will not be observed in the case of some alloys unless they are quenched into ice water or liquid nitrogen.

Often samples need to be processed in a specific way depending on experimental requirements. Brown *et al.* [31,32] prepared Ni-Mn-Ga, Co-Ni-Ga and Co-Ni-Al samples for X-ray and neutron diffraction by crushing the as cast alloys with steel pestle and mortar to a particle size of < 250 μm. The powder samples were sealed under reduced argon atmosphere in quartz ampoules and annealed at 800 °C for 40 hrs and after which they were quenched in ice water. For resistivity or thermoelectric power measurements, flat thin regular shaped samples were obtained by cutting the homogenized sample using low speed diamond cutter [33]. Oikawa *et al*. [17] prepared 2 mm thick ribbon by hot rolling the as-cast sample at 1300 °C. Further cold rolling was carried out to obtain samples of about 150 μm thick to investigate the thermally induced shape change of the Co-Ni-Al alloys. Similar methods have been adopted to obtain Fe-Ni-Ga FSMAs [34]. Martensitic transformations (MT) have been observed in Ni-Mn-Ga [35] and Ni-Fe-Ga [36, 37] in as-cast samples without the need for further processing. However, in the case of Co-Ni-Ga(Al) alloy samples, MT are observed only after rapid cooling or quenching the as-cast ingots homogenized at high temperatures.

Co-Ni-Ga solidifies in a peritectic reaction and forms a composite structure with *fcc* γ-phase and *bcc* β matrix. Thus, controlled amounts of γ-phase can be introduced in the β-matrix by suitable heat treatment procedure. The hot workability and room temperature ductility of these alloys are significantly improved by the introduction of the γ-phase, which is a great advantage for practical applications [19, 38]. So, Co-Ni-Ga(Al) alloys are prepared by arc (or induction melting) constituent metals, followed by homogenization near 1150 °C for 6 – 72 hrs [19, 39, 40] and quenching in ice water / oil bath / liquid nitrogen. Controlled amounts of γ-phase precipitates is introduced [40] by annealing the alloy samples below 1120 °C for 1 - 6 hrs time and then quenching the same in ice water. Single crystals of FSMAs are usually grown by Bridgmann or floating zone method. Müllner *et al*. [41] used single crystal of $Ni_{2.04}Mn_{1.12}Ga_{0.84}$ grown by Bridgman method to investigate the large cyclic deformation of Ni-Mn-Ga FSMAs induced by magnetic field. Chernenko *et al*. [42] also employed Bridgman method to grow $Co_{49}Ni_{22}Ga_{29}$ single crystal. Sakamoto *et al.* [43] used floating zone method to grow single-crystal rods of $Fe_{68.8}Pd_{31.2}$ and Fe_3Pt.

1.2.2. Crystal Structure of phases

The Heusler Ni_2MnGa and its non-stoichiometric compounds undergo a thermoelastic martensitic transformation from the $L2_1$-ordered cubic phase to monoclinic or tetragonal structure with 5*M* modulation or orthorhombic structure with 7*M* modulation [13]. Matrynov [44] described the stress induced martensite structure of $Ni_{2.04}Mn_{0.96}Ga$ as five layered periodic (5*M*- Monoclinic with a = 5.9 Å, b = 5.89 Å and c = 5.59 Å). Wedel *et al.* [45] determined the space group and the atomic coordinates of the stoichiometric and

non-stoichiometric low temperature Ni–Mn–Ga alloys with the help of Transmission electron microscope (TEM) and X-ray diffraction (XRD) data. The results reported by them are summarized in Table 1.2.2a along with the unit cell diagram.

Table 1.2.2a: Atomic parameters for the $Ni_{2.16}Mn_{0.84}Ga$ phase with tetragonal structure, $I4/mmm$ space group a = 3.88 Å; c = 6.48 Å; number of atom per unit cell, Z = 2; unit cell volume = 96.47 Å^3 [45].

Atom	Wyckoff position	*x*	*y*	*z*
Ga	2*a*	0	0	0
Mn[a]	2*b*	0	0	0.5
Ni1[a]	2*b*	0	0	0.5
Ni2[b]	4*d*	0	0.25	0.5

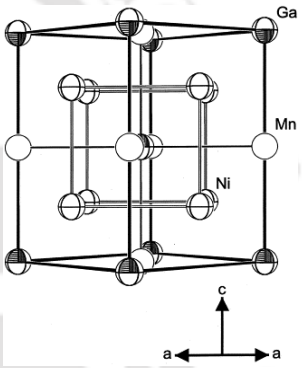

The crystal data and atomic parameters for Ni_2MnGa suggested by Webster [13] are presented in Table 1.2.2b. The crystal structure of the different martensitic phases observed in a wide variety of Ni–Mn–Ga alloy compositions have been studied in detail by Pons *et al.* [46]. A correlation of teragonality with martensite transformation start temperature M_s and *e/a* ratio was observed in the alloys undergoing MT. From Rietveld analysis of the neutron and X-ray powder diffraction data, Brown *et al.* [31] have shown that Ni_2MnGa in the martensitic phase has a 7*M* orthorhombic structure with *Pnnm* space group. Temperature-dependent powder X-ray diffraction studies were carried out by

Table1.2.2b: Crystallographic data of Ni_2MnGa. (1) high temperature cubic, (2) low temperature tetragonal, and (3) low temperature orthorhombic structures [13].

Parameter	(1)	(2)	(3)
Crystal system	Cubic	Tetragonal	Orthorhombic
Space group (atom/unit cell	$Fm\bar{3}m$ ($Z = 4$)	I_4/mmm ($Z = 2$)	$Fmmm$ ($Z = 4$)
Lattice constants (Å)	$a = 5.825$	$a = 4.18$ $c = 5.56$	$a, b = 5.92$ $c = 5.56$
Unit cell volume ($Å^3$)	192.34	97.46	194.93
Wyckoff position (x,y,z) Ni Mn Ga	 8*c*: 0.25,0.25,0.25 4*b*: 0.5, 0.5, 0.5 4*a*: 0, 0, 0	 4*d*: 0, 0.5, 0.25 2*b*: 0, 0, 0.5 2*a*: 0, 0, 0	 8*f*: 0.25,0.25,0.25 4*b*: 0. 0 0.5 4*a*: 0, 0, 0

Ranjan *et al*. [47] on $Ni_2Mn_{1.05}Ga_{0.95}$. With detailed LeBail and Rietveld analyses of powder XRD data, they concluded that the martensite phase belongs to the *Pnnm* space group with 7*M* modulation. However, the tetragonal phase did not exhibit any modulation. $Ni_{2+x}Mn_{1-x}Ga$ ($0.19 \leq x \leq$_0.35) alloys have been reported to be of non-modulated tetragonal structure at room temperature [30]. The lattice constants a and c were reported to linearly decrease and increase, respectively, as x was increased. A cubic austenite phase with $L2_1$ atomic ordering was observed at room temperature for compositions with $x \leq 0.07$. A composite austenite and martensite phase was observed for compositions in the range $0.1 \leq x \leq 0.15$. $Fm\bar{3}m$ space group was assigned to the cubic and *I4/mmm* space group was assigned for *bct* structures. It was found that modulation is

absent as Ni-Mn-Ga compositions with $c/a \geq 1$. A 7*M* modulated monoclinic phase was observed when the $x = 0.2$ alloy was annealed [25]. All the atoms have been reported to be present at fixed high-symmetry special positions. The Wyckoff positions of various atoms in the tetragonal structure are given in the Table 1.2.2b.

Unlike Ni-Mn-Ga alloy, systematic investigations have not been performed on the structure of other FSMAs. It has been reported [48, 49] that Ni_2FeGa alloy has $L2_1$ atomic ordering in its austenite phase and orthorhombic (*14M*) structure at low temperature (<142 K). Sutou *et al.* [50] concluded from stress-strain data that the $Ni_{54}Ga_{27}Fe_{19}$ alloy undergo stress induced martensitic transformation in the following sequence: $L2_1 \rightarrow 10M$, $10M \rightarrow 14M$ and finally, $14M \rightarrow L1_0$.

The crystal structures of the martensite and parent phases of Co-Ni-Al alloys have been identified as $L1_0$ and *B2*, respectively [18, 51 52] Brown *et al.* [32] determined the crystal structure and lattice constant of $Co_{38}Ni_{33}Al_{29}$ alloy from neutron powder diffraction measurements. According to them, the parent phase is the cubic *B2* structure with space group $Pm\bar{3}m$ and $a_{B2} = 2.8571$ Å at 177 °C, and the martensite phase is $L1_0$ with *P4/mmm* space group and $a_{bct} = 2.7139$ Å and $c_{bct} = 3.1311$ Å at −263 °C. Tanaka *et al*. [38] performed XRD measurements on $Co_{30}Ni_{39}Al_{31}$ alloy powder in the temperature range of −198 to 23 °C. The *a* and *c*-axis of martensite phase was found to decrease and increase, respectively, with decreasing temperature. No extra peak characteristic of modulated structure appeared in the Co–Ni–Al XRD data. The high temperature β phase in $Co_{39}Ni_{33}Al_{28}$ alloy could be retained at room temperature by rapid cooling *via* melt-spinning. The over-saturated β phase in the as-spun state exhibited a reversible

martensitic transformation to an $L1_0$ structure. A precipitate phase was formed from the over-saturated β phase upon heating to 673 K [26].

XRD studies have been performed by some researchers [26, 39, 40, 53, 54] to identify the structural phases in Co-Ni-Ga alloys. Though the martensite structure of Co-Ni-Ga alloys was reported [39-40] to be tetragonal, it became evident that the lattice parameters, Miller indices of the peaks and the angular position of peaks in the reported XRD patterns did not fit in the indexing scheme of tetragonal crystal system. The crystal structure of the austenite phase in $Co_{50}Ni_{20}Ga_{30}$ ribbons was reported [26, 54] as *B2*. However, no space group was assigned for the crystal structure. Brown *et al.* [32] analyzed the neutron diffraction data of $Co_{45}Ni_{23}Ga_{32}$ alloy and reported that its martensite phase has a bct unit cell with *I4/mmm* space group and the austenite phase belonged to the *A2*-type with $Im\bar{3}m$ space group. Oikawa *et al.* [19] preferred to designate the austenite and martensite phases of $Co_{45}Ni_{25}Ga_{30}$ alloy as *B2* and $L1_0$ (face centred tetragonal), respectively. Chernenko *et al.* proposed [55] that the martensite phase structure of $Co_{49}Ni_{21}Ga_{30}$ could be either non-modulated bct with lattice parameters $a = b = 2.7$ Å and $c = 3.2$ Å or $L1_0$ with $a = b = 3.8$ Å and $c = 3.2$Å after analyzing electron diffraction data. Selected area electron diffraction patterns revealed that the atomic order in the martensite phase was derived from *B2*-type rather than $L2_1$ type austenite phase [55]. From the above discussion, it is obvious that confusion prevails about the structure of the martensite phase of Co-Ni-Ga alloys. The inherent difficulty in obtaining fine powders suitable for diffraction experiments in this ductile system without inducing additional strain in the alloy poses considerable challenge in performing XRD measurements.

1.2.3. Effect of composition on the properties

The number of martensite phases, their structures and the sequence of their occurrence in FSMAs depend on the stoichiometry of the alloys. Chernenko *et al.* [28] investigated the variation of M_s, thermal hysteresis, Curie temperature (T_C) and transformation heat with composition in Ni-Mn-Ga alloys. Their results can be summarized as follows: (i) At a constant value of Mn content, Ga addition lowers M_s. (ii) Mn addition (instead of Ga) at constant Ni concentration causes M_s to increase. (iii) Substitution of Ni atoms by Mn at constant Ga content results in alloys with lower M_s and higher T_C. Based on these observations, Ni-Mn-Ga alloys have been classified into the following three groups. Group-I: alloys near stoichiometric composition (Ni_2MnGa), whose T_C ~ 370 K; premartensitic transition (T_{PM}) ~ 250K and martesitic transition (T_M) ~ 210K (*i.e.* $T_M < T_{PM} < T_C$). Group-II: off-stoichiometric alloys with T_M ~ 250 K and $T_M < T_C$. These alloys usually exhibit stress and thermally induced intermartensitc transition [56, 57]. Giant magnetic field induced strain is a common feature observed in these alloys. Group-III: alloys with $T_M > T_C$.

The magnetic properties and structural phase transformations of Heusler alloys $Ni_{2+x}Mn_{1-x}Ga$ and $Ni_{2-x}Mn_{1+x/2}Ga_{1+x/2}$ were investigated by Wang *et al*. [30]. It was found that the martensitic transformation temperature increases and the Curie temperature decreases with decreasing Mn concentration in the $Ni_{2+x}Mn_{1-x}Ga$ system, but the magnetic properties decrease faster than the $Ni_{2-x}Mn_{1+x/2}Ga_{1+x/2}$ system. This suggests that the influence of the conduction electron concentration and the distance between Mn atoms on the Curie temperature is stronger than the magnetic dilution effect. The

martensitic transformation temperature shows a peak value at x = 0.06 in the $Ni_{2-x}Mn_{1+x/2}Ga_{1+x/2}$ system. Similar behavior was observed by Matsumoto *et al.* [58] in $Ni_{2+x}Mn_{1-x}Ga$ alloys. They have also investigated the substitutional effect on martensitic transformation and Curie temperature of $Ni_{2+x}Mn_{1-x}Ga$ (x = 0 - 0.19) alloy system. In stoichiometric composition (x = 0), crystal transformation temperatures are around 200 K and Curie temperature is around 400 K. The transformation temperatures increased and Curie temperature decreased with an increase in Ni content. The magnetic transition and the crystal transformation occur simultaneously at the same temperature for the alloys with Ni composition $x \geq 0.18$, giving rise to a coupled magnetostructural transition. It has been found that for $x \geq 0.24$, $T_M > T_C$. In these alloys, a paramagnetic phase appears between paramagnetic cubic and the ferromagnetic tetragonal phase, and the martensitic transition occurs in the paramagnetic state [59]. Single phase martensite with tetragonal structure was observed in $Ni_{50+x}Mn_{25}Ga_{25-x}$ (x = 2 - 11) alloys for $x < 7$ [57]. When x changes from 2 to 7, a systematic change of the tetragonal structure has been observed which leads to the conclusion that unit cell volume reduces with the reduction in Ga content (or with the addition of Ni). The lattice parameters do not change for x = 7 to 11. It was inferred from the above results that 57% of Ni is the soluble limit of Ni atom in tetragonal structured martensite. A linear increase of martensitic transformation temperature with the decrease of Ga content was observed for alloys with $x \leq 7$. The variation of martensitic transformation temperatures with Ga content was correlated with electron concentration (*e/a*). Wuttig *et al*. [20] reported that the martensite start temperatures vary in the range 20 °C < T < 60 °C in $Co_2Ni_{1-x}Ga_{1+x}$, (x = 0.06, 0.09, 0.12, 0.15) alloys in their as-solidified state. Quenched $Co_2Ni_{1-x}Ga_{1+x}$, ($1 > x > 0.3$) alloys are

ferromagnetic when $x < 0.5$ and their saturation magnetization depends on the composition as well as the annealing treatment [20].

Wuttig *et al*. [60] predicted that the transformation temperatures should be higher for SMAs with higher electron/atom (*e/a*) ratio, which was also experimentally confirmed in the prototype Ni-Mn-Ga alloys [61]. The electron concentration (*e/a*) was calculated by assuming the following configurations of the valence electrons and their number per atom (in brackets): For Mn: core + $3d^5 4s^2$ (7); for Fe: core + $3d^5 4s^3$ (8); for Co: core + $3d^3 4s^1$ (9); for Ni: core + $3d^8 4s^2$ (10); for Ga /Al: core + $4s^2 4p^1$ (3); *etc*. These configurations are commonly used in band calculations of the electronic structure of Heusler alloys [62]. Krenke *et al*. [63] studied the linear variation of M_s with *e/a* for Ni–Mn–X Heusler systems, where X is a group III–group V element. It was observed that the linear dependence is not universal for all systems and that the slope of the linear behavior is different for the different X species. It increased either as X changes from Al to In (isoelectronic) or from In to Sb (increase in number of *p* electrons). The features in the M_s *versus e/a* plot and the relative stability of the various crystallographic phases of Ni–Mn based Heusler alloys have been analysed and reported.

The compositional dependence of martensitic transformation and Curie temperatures were systematically investigated for various FSMAs by Oikawa *et al*. [19] All FSMAs exhibit similar compositional dependence behavior. The compositional dependent phase diagram of Ni-Fe-Ga, Ni-Mn-Ga, Co-Ni-Ga and Co-Ni-Al alloys studied by them are shown in Fig. 1.2.3 (a-d).

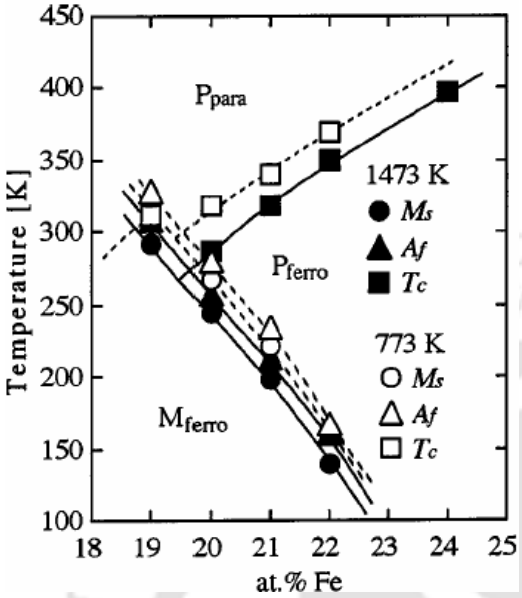

Fig.1.2.3a: T_C, M_s and A_f variation in Ni-Fe-27at%Ga annealed at 773 k and 1473 K [22].

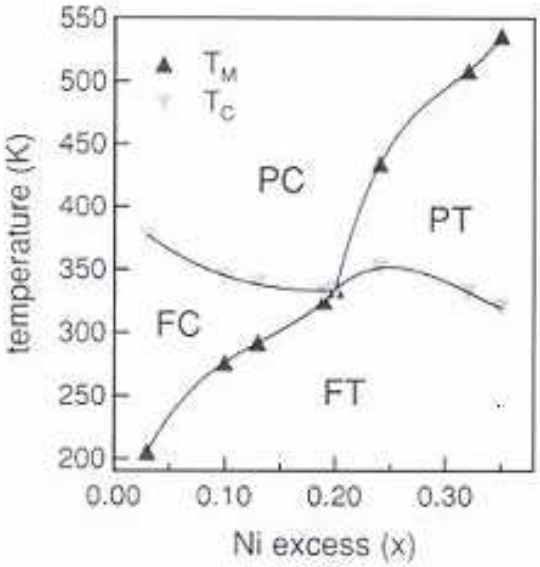

Fig.1.2.3b: T_C, M_s and A_f variation in Ni-Mn-Ga [59].

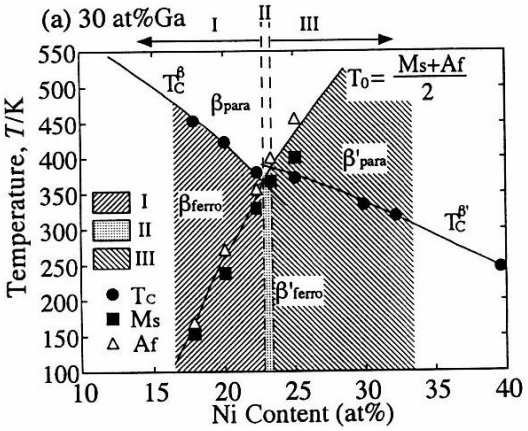

Fig.1.2.3c: T_C, M_s and A_f variation in Co-Ni-30at%Ga [19].

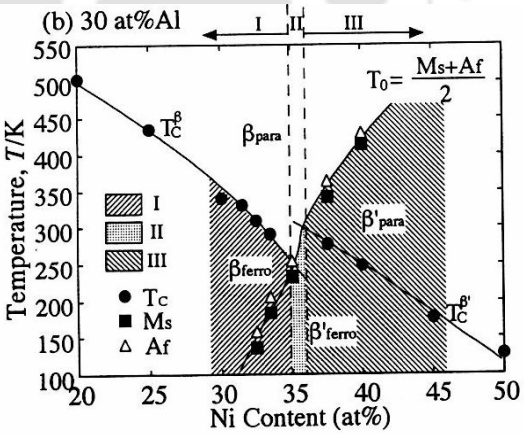

Fig.1.2.3d: T_C, M_s, A_f variation in Co-Ni-30at%Al [19].

Change of entropy at the martensitic transformation in $Ni_{2+x}Mn_{1-x}Ga$ was investigated by Khovalio *et al.* [64]. The entropy change was reported to increase with an increase in Ni content.

1.2.4. Effect of heat treatment

When dealing with high temperature shape memory alloys, thermal stabilization of martensite has to be considered. This phenomenon, consisting of the transient shift of the reverse transformation temperatures after direct quenching to martensite or after ageing in martensitic state, has been studied in depth for Cu–Zn–Al alloys [65]. Several other SMAs have been found to show some degree of martensite stabilization, including Au–Cd [66] and Cu–Al–Ni [67]. The mechanisms used to explain this phenomenon have been extensively discussed and include short-range atomic reordering and defect pinning of the martensite interfaces [67-68]. Although the relative importance of the role played by the different mechanisms in martensite stabilization is very much dependent on the alloy system and thermo-mechanical treatments, it has been clearly established that the stabilization brought about by martensite ageing is a diffusive phenomenon, hence thermally activated process. Therefore, stabilization can be promoted by ageing in martensite phase in high temperature shape memory alloys. Segui *et al.* [69] reported that in Ni-Mn-Ga, the martensite stabilization increases with ageing time and temperature. Santamarta *et al*. [34] observed the aging effect of polycrystalline $Ni_{53.5+x}Fe_{19.5-x}Ga_{27.0}$ alloys, with $x = 0$, 0.5, 1.5 by ageing at 520 K, 670 K and 770 K. All the alloys showed good long-term thermal stability after treatment at 520 K, but, ageing at 670 K and 770 K caused degradation of the martensitic transformation after ~10^5 s.

TEM studies revealed the appearance of small and mostly elongated precipitates after long ageing periods at 670 K and 770 K.

1.2.5. Magnetic properties

The magnetic properties relevant to FSMAs include variation of magnetization with applied field (*M-H* plot) at different constant temperatures, variation of magnetization with temperature (*M-T* plot) at low field, and variation of low field ac susceptibility with temperature (χ-*T*). It was experimentally observed that the martensitic transformation in the FSMAs is accompanied by (i) abrupt decrease of magnetization measured at non-saturated fields [70], (ii) nearly 40 times drop of the initial magnetic susceptibility [36], (iii) appearance of a maximum temperature dependence of the transversal magnetosriction, and (iv) an order of magnitude increase of magnetosriction. A phenomenological model relating the magnetization process in the twinned martensitic state of Fe and Ni based alloys to the strain-induced magnetic anisotropy has been analyzed by Cherenko *et al.* [70]. The lowering of point symmetry group during the austenite-martensite transformation results in a considerable enhancement of magnetocrystalline anisotropy of the martensite phase. Due to the magnetoelastic interaction, the elastic energy stored by the martensite gives rise to the magnetic anisotropy, which can dominate the magnetization process [71].

The effective magnetic anisotropy constant K_{eff} of the powders has been calculated from the initial magnetization curves using the law of approach to saturation [72]. The *M-H* data is fitted to the relation, $M = M_{sat}\left(1-\frac{a}{\sqrt{H}}-\frac{b}{H^2}-\right)$ and from it K_{eff}

could be estimated using the relation $K_{eff} = \sqrt{\frac{15b}{4}} \times M_{sat}$ .Here M_{sat} is called as saturation magnetization.

For ferromagnetic materials, at finite temperatures, M_{sat} will also depend on how well the dipole moments are aligned, as thermal vibration of the atoms causes misalignment of the moments and hereby reduction in M_{sat}. At Curie temperature (T_C), magnetization or ac susceptibility falls sharply with the increase/decrease of temperature during heating/cooling. Thus, T_C can be roughly estimated from the M-T or χ-T data. The modified Arrott plot obtained from the M-H plots yields more accurate T_C values. The M-T and χ-T behaviour close to the accurately determined T_C can be used to estimate the critical constants and nature of the ferromagnetic to paramagnetic transition. [73].

The variation of T_C with composition has been explained in terms of the magnetic valence number [38]. It was found that there is a strong correlation between saturation magnetization M_{sat} or T_C and the average magnetic valence number Z_m. The value of T_C increases with the increase of Z_m, as predicted in generalized Slater-Pauling model [74]. Magnetic valence like ordinary chemical valence is an integer for each column of the periodic table. The magnetization M (in the unit of μ_B) is given by as, $M = (N^{\uparrow} - N^{\downarrow} = 2N^{\uparrow} - Z)$; where Z is the chemical valence (atomic number – number of core electrons or $Z = N^{\uparrow} + N^{\downarrow}$). Thus, Z_m for 3d transition metal can be expressed as, $Z_m = 2N_d^{\uparrow} - Z$; where $N_d^{\uparrow}$ is the number of up spin electrons in the 3d shell. Using the above relation magnetic valence numbers for Mn, Fe, Co, Ni, ….., Zn, Ga, etc, are obtained as 3, 2, 1, 0, , -2, -3 respectively. The average magnetic valence number for an alloy of composition $A_xB_yC_z$ is calculated as

$$Z_m \text{ (average)} = \{x * (Z_m \text{ of } A) + y* (Z_m \text{ of } B) + z* (Z_m \text{ of } C)\}/100 \quad \text{--- (1.2.5)}$$

It should be noted that if the magnetic phase transition occurs in the martensite phase, the T_C values are systematically higher than the T_C in austenite phase [17, 19, 22]

1.2.6. Transport properties

Knowledge of thermal and electrical properties of FSMAs is very important because they can help us in understanding the mechanisms involved in the phase transformation process, including its electronic structures and scattering processes. The thermal stability is directly related to the thermal properties. Electron transport can be evaluated from the thermoelectric power (also known as Seebeck coefficient denoted by *S*) and electrical resistance (*R*) measurements. The temperature variation of electrical resistivity and thermoelectric power (TEP) of magnetic Heusler alloy $Ni_{2.19}Mn_{0.81}Ga$ has been investigated by Priolkar *et al.* [35]. Temperature dependence of the TEP of this alloy has been explained in terms of the crystal field splitting. The occurrence of the magnetic and martensitic transitions at almost the same temperature in $Ni_{2.19}Mn_{0.81}Ga$ has been explained from TEP data as a consequence of changes in the density of states at the Fermi level. Li *et al.* [75] measured the electrical and thermal properties of Ni–Mn–Ga FSMAs. They noticed a jump in electrical resistance and a maximum in *S* at the structural phase transformation were observed. Similar behavior of abnormal change of resitivity during the structural phase transition was also reported by other research groups [36]. The resistance jump near the transformation temperature is due to the scattering mechanism which is a result of formation of interfaces and twin boundaries during the structural transformation [75].

Magneto-resistance (MR) in the martensite phase shows different behavior as compared to the austenite phase due to the twinning and high magneto-crystalline anisotropy. A negative magneto-resistance of 5% has been reported in bulk $Ni_{2+x}Mn_{1-x}Ga$ alloys by C. Biswas *et al*. [76]. The variation of MR for different phases (austenite, martensite, intermartensite) in an alloy and as a function of alloy composition has been explained by spin disorder scattering and magnetic anisotropy.

1.2.7. Mechanical properties

Tensile and compression testing: Mechanical properties of FSMA can be determined from stress-strain (*S*-*S*) data obtained by compressing regular shaped sample or applying uniform tension to the both ends of the sample. Fig.1.2.7 shows *S*-*S* curve of a typical SMA. One can clearly see in the permanent strain after unloading (shown as curve OC in Fig.1.2.7), the recovery strain (shown as curve CD in Fig.1.2.7; shape memory strain, as indicated by the arrow) and the residual strain (irreversible strain, curve OD in Fig.1.2.7). The shape memory effect measurement using compression test involves the following steps: At the outset, the length of the samples is measured before loading (l_0), after unloading (l_1) and after heating it to a temperature higher than A_s (l_2). Residual strain after unloading (ε_r), strain recovered due to SME (ε_{SME}) and permanent strain (ε_{per}) are then obtained as: $\varepsilon_r = (l_0-l_1)/l_0 \times 100\%$, $\varepsilon_{SME} = (l_1-l_2)/l_1 \times 100\%$ and $\varepsilon_{per} = (l_0-l_2)/l_0 \times 100\%$ respectively. Recovery rate (R) is calculated as $R = \varepsilon_{SME} / (\varepsilon_{SME} + \varepsilon_{per}) \times 100\%$ [57].

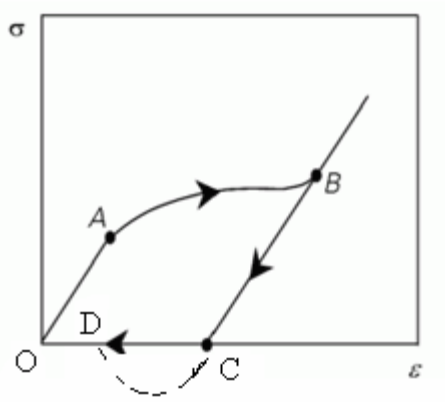

Fig.1.2.7: Stress-strain curve of a typical SMA.

It has been reported that the mechanical and shape memory characteristics of the polycrystalline $Ni_{54}Mn_{25}Ga_{21}$ high temperature shape memory alloys can be improved by grain refinement. It is known that the polycrystalline Ni-Mn-Ga alloys are extremely brittle. Li *et al*. [29] investigated the stress–strain behavior of polycrystalline NiMnGa alloys with high transformation temperature in compression mode and demonstrated the effectiveness of grain refinements. Better mechanical properties obtained for $Ni_{54}Mn_{25}Ga_{21}$ rod sample was explained in terms of its small grain size and finer martensitic twins. Super-elasticity (SE) in tensile loading of the Co–Ni–Al polycrystalline $\beta + \gamma$ alloys has been investigated by Tanaka *et al.* [38]. It was found that the SE properties in the $\beta + \gamma$ two-phase alloys strongly depend on the volume fraction of γ-phase present. In particular, the temperature dependence of the critical transition stress increased with increase in the volume fraction of γ-phase. Furthermore, the SE properties were enhanced by controlling the β-grain size. Consequently, the maximum recovery SE strain of about 6.3% was achieved in a sheet specimen with the large β. A pronounced super elasticity of ~6% was reported in single crystalline NiMnGa alloys [28].

Microhardness: Dimensional analysis and the finite element approach were employed to study the spherical indentation hardness of SMAs [77]. The reverse transformation stress does not affect the hardness of a super-elastic SMA. The scaling relationship between the hardness and other material parameters has been established through dimensional analysis. The influences of all the parameters on the spherical indentation hardness have been examined using the numerical analysis. The major conclusions are (1) hardness increases with the forward transformation stress, (2) higher Young's modulus of the martensite will lead to a larger hardness, (3) hardness decreases with an increase in the maximum transformation strain magnitude, and (4) indentation hardness increases with the maximum indentation depth. Therefore, the measured indentation hardness cannot be treated as a material property of SMAs. Contrary to the above conclusion it is found that Vickers microhardness (VHN) does not depend on the applied load or indentation depth. Thus, Vickers microhardness measurement can be used to obtain information about the ductility from the indentation fracture toughness data.

Magnetic field induced strain (MFIS): The main goal of research on FSMA is to find a magnetic alloy composition exhibiting martensitic phase transformation that would allow control of large displacements by application of a magnetic field at constant temperature. A martensitic phase generally accommodates the strain associated with the transformation by the formation of twin variants that pack together in compatible orientations to minimize strain energy. Alignment of these twin variants by the motion of twin boundaries can result in large macroscopic strains. Magnetic field control of the twin variant orientation requires that the magnetization energy $K_u = M_{sat}H_a/2$ (where M_{sat} is the saturation magnetization, H_a is the applied magnetic field) [23], be sufficient to induce

motion of the twin boundaries. This energy K_u is called magnetic anisotropy energy density. The mechanical energy required to move the twin boundaries can be obtained from stress-strain analysis using the relation $E_v = \sigma.\varepsilon/2$, σ is the critical stress required for the movement of twins and ε is the corresponding strain [23]. Here, E_v is the energy density essential for total alignment of all twin variants. σ represents the stress applied to the system and ε represents the corresponding strain. By equating K_u and E_v we can get the value of M_{sat} required to get appreciable strain induced by a given magnetic field. This input could be used to tailor sample compositions optimized for actuator applications.

Ni-Mn-Ga FSMAs exhibiting up to ~10% magnetic field induced strain [78] has led to the possibility of developing magnetic actuators with extremely fast response time. Murray *et al*. reported magnetic field induced strain of 6% [79] in single crystalline Ni-Mn-Ga martesite at room temperature. Jeong *et al*. [80] observed maximum MFIS of 0.01% at temperature ~ 37˚C under 10000 G applied magnetic field in the martensite phase of Ni-19.5at.% Mn-27at.% Ga polycrystalline alloy. Kakeshita *et al*. [81] reported MFIS in Fe–31.2 at. % Pd alloy at 77 K, Fe_3Pt at 4.2 K and Ni_2MnGa at 77 K. Magnetic field was applied along [0 0 1] direction and strain was measured along the same direction. It should be also noted that strain recovery of 0.6% observed in Fe_3Pt was not seen in Fe–31.2 at.% Pd and Ni_2MnGa. Similar results have been observed at other temperatures as well, with the highest value being ~1% at 20 K.

1.2.8. Effect of additive element

The addition of a fourth element can be an effective way to change the characteristics of the magnetic and structural transformations of Heusler (X_2YZ) and offstoichiometric Heusler alloys. The brittleness of Ni-Mn-Ga alloys is the biggest obstacle for practical applications. It is well known that proper addition of rare-earth elements can improve the mechanical properties of various alloys and intermetallic compounds. The martensitic transformation temperatures of Ni–Mn–Ga alloys are very sensitive to the presence of rare-earth elements. As reported, the substitution Tb for Ga in $Ni_{50}Mn_{29}Ga_{21}$ alloy enhanced the M_s, whereas the M_s of $Ni_{48}Mn_{33}Ga_{19}$ alloy decreased with the addition Sm [82-83]. Heavy rare-earth Gd is ferromagnetic and has the highest Curie temperature among the rare-earth elements. Addition of Gd affects the martensitic transformation temperatures, mechanical properties and magnetic properties of Ni–Mn–Ga alloys [84-85]. On adding Gd to $Ni_{50}Mn_{29}Ga_{21-x}Gd_x$, the martensitic transformation temperatures, bending strength and ductility increase remarkably. Refinement of the grains and strength of the grain boundaries resulting from the addition of Gd result in the improvement of the mechanical properties. Martensite structure changes from 5M in alloys with 0.1 at% Gd to 7M for alloys with 0.5 to 2 at.% Gd. Wu *et al*. have reported the magnetic properties and shape memory effect of Fe-doped $Ni_{52}Mn_{24}Ga_{24}$ [86]. On partly replacing Mn with Fe in $Ni_{52}Mn_{24}Ga_{24}$ with the $L2_1$ crystal structure, the material ($Ni_{52}Mn_{16}Fe_8Ga_{24}$) exhibits a large moment of $3.91\mu_B$ per *f.u.* (formula unit) and a high T_C of 381 K. Kikuchi *et al.* [87] studied the magnetic properties of the $Ni_2Mn_{1-x}Fe_xGa$ ($0 \leq x \leq 0.7$) alloys in order to investigate the electronic properties of FSMAs Ni_2MnGa and Fe–Ni–Ga. The martensitic and reverse martensitic transformation temperatures have been reported to

decrease with increasing x, whereas T_C increased with the increase of x. It is reported that μ^{total} is almost independent of x for $Ni_2Mn_{1-x}Fe_xGa$ ($0 \leq x \leq 0.7$). Assuming that the moments of Ni and Mn in $Ni_2Mn_{1-x}Fe_xGa$ ($0 \leq x \leq 0.7$) are $0.36\mu_B$ [31] and $3.08\mu_B$ [32], respectively, the moment of Fe is estimated to be about $3.0\mu_B$. This value is much larger than the moment of pure α-Fe ($2.217\ \mu_B$). The moment of Fe in $Ni_2Mn_{6/7}Fe_{1/7}Ga$ ($x \cong 0.14$) was reported to be $2.68\ \mu_B$ [87]. The large moments on Fe are brought through hybridization with the surrounding Ni atoms. Thus, the moment of Fe is enhanced when Fe is surrounded by transition elements with more *d*-electrons.

The effect of addition of many different elements has been studied in the Ni–Mn–Ga alloy. However, much less information exists on this topic in the new FSMA families. Effect of Co, In, Ag and Mn addition in Ni–Fe–Ga has been investigated [88-95]. Indium causes a strong decrease of the MT temperatures [91], while Co increases these temperatures [88]. Co substituting Ni causes a drop in T_M and an increase in T_C. The opposite behaviour occurs when Co substitutes Fe (in this case, the change of T_C is however very small) [89-90]. Finally, when Co substitutes Ga, the MT temperatures increase, while substitution of 1 at% Ni by Ag practically does not affect the transformation temperatures [92]. Besides the change of the transformation temperatures, some other effects have also been reported, such as an improvement of MFIS in alloys containing Co, increase in Curie temperature [93-94] and a large negative magneto-resistance effect in a $Ni_{50}Fe_{17}Ga_{25}Mn_8$ alloy [95]. Recently, very large MFIS (8.5% under a field of ~0.6 T) assisted by an external stress of 8 MPa applied to the sample has been reported in $Ni_{49}Fe_{18}Ga_{27}Co_6$ [96]. Picornell *et al.* [97] reported that the MT temperatures decrease and T_C increases slightly when 3 at.% Mn substitutes for Fe. Substitution of Fe

by Co causes an increase in MT temperatures, the effect being opposite when Co replaces Ni. In both cases, T_C increases, the effect being stronger in the alloy in which Ni is replaced by Co. The $L2_1 \rightarrow B2$ order–disorder transition temperatures are hardly affected by addition of Co, whereas Mn addition induces an increase of ~50 K with respect to the ternary alloy. Addition of Co or Mn to Ni–Fe–Ga alloys (substituting Ni or Fe) modifies the MT temperatures according to the changes produced in *e/a* ratio. However, the shift of MT temperatures is notably higher in the alloy in which Fe is substituted by Co, having the same change (in absolute values) of *e/a* than the others. These results suggest that, besides the density of conduction electrons, the change in the size of the atoms (and the corresponding unit-cell volume) also at play role in controlling the transformation temperatures. Although both elements additions increase T_C, the effect being stronger when Co is added, especially when it replaces Ni. The martensitic phases formed are also modified. Addition of Co (replacing either Fe or Ni) seems to increase the stability of the seven-layered martensite. Moreover, when Co substitutes Fe, the *2M* structure is also formed. Substitution of Fe atoms by Mn promotes the predominance of the six-layered phase and formation of the unusual four-layered structure.

Liu *et al.* [98] investigated the microstructure, super-elasticity and fracture behavior of $Co_{50}Ni_{22-x}Ga_{28}Fe_x$ ($x = 0,\ 1,\ 2,\ 5$) alloys. It was shown that the MT temperatures decrease as Ni is gradually substituted by Fe. The volume fraction of the second phase is also reduced with increasing Fe content, which impairs the mechanical properties. Two-phase Co–Ni–Ga–Fe alloys have been reported to exhibit complete super-elastic behaviour in a wide temperature interval between room temperature and 200 °C. Moreover, the stress hysteresis in two-phase alloy was found to be more sensitive

to temperature than the single-phase alloy. Zheng *et al* investigated [88] the effects of Co on the martensitic transformation and magnetic properties of Ni–Fe–Ga magnetic shape memory alloys. An unusual phenomenon of one martensitic transformation and two intermartensitic transformations was observed in the DSC curve of $Ni_{55.3}Fe_{17.6}Ga_{27.1}$ alloy. Addition of 3 at.% Co in $Ni_{55.3}Fe_{17.6}Ga_{27.1}$ alloy increases the M_s from 313 K to 405 K, improves the saturation magnetization from 21.64 to 97.67 emu/g and enhances the magnetocrystalline anisotropy constant from 1.253×10^6 to 4.035×10^6 erg/cm^3.

1.3. SOME FEATURES OF THIS WORK

As of now many FSMAs had been developed and many have been proposed as potential candidates for sensor and actuator applications. But till now, no practical device has been reported with these FSMAs. Practical application of Ni-Mn-Ga alloy is limited because of its extreme brittleness in polycrystalline state. The compositions of Co-Ni-Ga(Al) FSMAs are located near the two-phase (β + γ) region [19], which facilitates the introduction of appropriate amounts of the cubic γ-phase in the β-matrix by proper choice of alloy composition. Also Co-Ni-Ga solidifies in a peritectic reaction and forms a composite structure with fcc γ-phase and bcc β matrix. Thus, controlled amount of γ-phase can be introduced in the β-matrix by suitable heat treatment conditions. The hot workability and room temperature ductility of these alloys are significantly improved by the introduction of the γ-phase, which is a great advantage for practical applications [19].

Oikawa *et al.* [19] observed phase equilibrium between β and γ phases in these systems and the variation of martensitic phase transformation temperatures (M_s and A_s) and Curie temperature (T_C) of $Co_{70-x}Ni_xGa_{30}$ alloys in the β + γ region. It was observed

that the T_C increases while M_S and A_f decrease with increasing Co content. T_C and M_s plotted as a function of composition intersect near x = 23 in this series of alloys. Magnetization increases abruptly at the reverse martensite transformation temperature (A_s) and decreases sharply at T_C during heating. Similarly, magnetization increased sharply at T_C and decreased abruptly at the martensite transformation temperature (M_s) during cooling. Since T_C and M_s are very close in $Co_{47}Ni_{23}Ga_{30}$ alloy, the magnetic transition in this alloy composition could not be properly characterized by them. Properties of FSMAs have been found to be sensitive to alloy composition, homogenization (or annealing) temperature, cooling rate during preparation and post-preparation heat-treatment. Apart from tailoring the transformation temperatures, these heat-treatment procedures adopted during preparation and post-preparation stages help in understanding the stability and structural evolution in these alloys.

Understanding the structure of the crystalline phases present, the $M \leftrightarrow A$ structural transformations, magnetic properties and mechanical properties in the Co-Ni-Ga FSMA are crucial for evaluating these materials for actuator applications. Hence, an investigation on Co-Ni-Ga FSMAs was taken up in this thesis work.

Composition of alloys has been selected so as to obtain room temperature or high temperature ferromagnetic martensite samples on the basis of the *e/a* ratio. Wuttig *et al*. [60] have claimed that alloys exhibit martensitic transformations for *e/a* > 7.33. Two series of Co-Ni-Ga alloy compositions have been selected for the present investigations (Fig.1.3). In the first series ($Co_xNi_{25}Ga_{75-x}$), Co is replaced by Ga, and for each 0.5 at.% increment of x, *e/a* decreases by 0.03. It is expected that martensitic transformations will decrease when Co content in decreased at the cost of Ga. The magnetic valence number

Z_m will also decrease with the decrease of Co content. Consequently, T_C is expected to decrease. In the second series ($Co_{70-x}Ni_xGa_{30}$), Ni is replaced by Co and for each (x is changed by 1.0 at.%) decrement of x , e/a will decrease by 0.01. Thus, the transformation temperatures are expected to be lowered with the decrease of Ni. But as Z_m increases when Co content [74] is increased at the cost of Ni, T_C is expected to increase.

The variation of A_s, M_s and T_C with compositions in Co-Ni-Al(or Ga) was reported by Oikawa *et al.* [19] served as the basis for the of selection of Co-Ni-Ga compositions for the present investigation. The criteria to obtain a complete β - microstructure which transforms to martensite are (1) the β-phase must be stable across as a wide temperature range as possible (The less wide is this temperature range, the faster the cooling rate required to retain the β-phase without diffussional composition), (2) the transformation temperature must fall within a range that satisfies the requirement for shape memory application. With this choice of composition three groups of alloys has been prepared namely, Group I: $M_s < A_s < T_C$, Group II: $M_s < T_C < A_s$ and Group III: $T_C < M_s < A_s$.

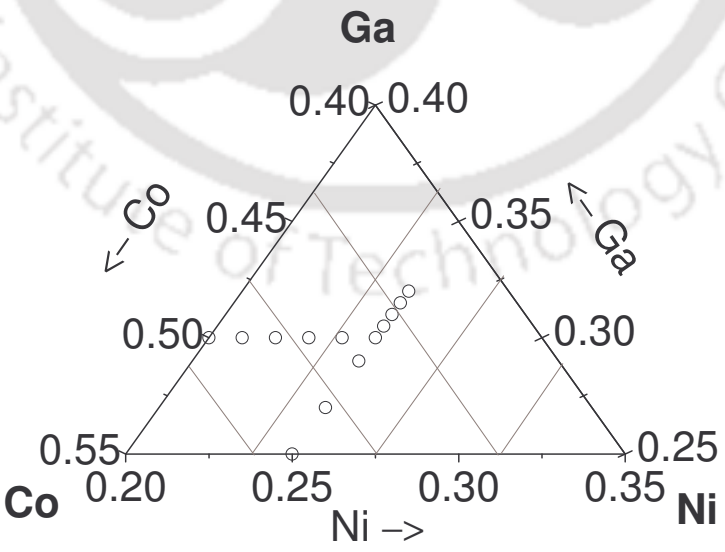

Fig. 1.3: Co-Ni-Ga compositions chosen for study in the present work.

It has been found that Co-Ni-Ga alloys have better ductility than Ni-Mn-Ga. However, saturation magnetizations (Msat) of Co-Ni-Ga are much lower than that of Ni-Mn-Ga alloys. An effort has been made to improve the M_{sat} of Co-Ni-Ga alloys without compromising the ductility by the additions of small amount of Mn or Fe to a chosen Co-Ni-Ga alloy composition with reasonably high M_s, T_C and M_{sat}.

EXPERIMENTAL TECHNIQUES AND PROCEDURES

The experimental techniques used and procedures adopted in the course of this experimental thesis work are described below:

2.1. SAMPLE PREPARATION

In the present work, the alloy ingots were prepared by arc melting the constituent elements. A commercial arc melting furnace (Vacuum Techniques, India) was used for preparing the alloy ingots. A schematic diagram of an arc melting furnace is given in Fig. 2.1.1 (A 200 A dc power supply used as electrical source is not shown here).

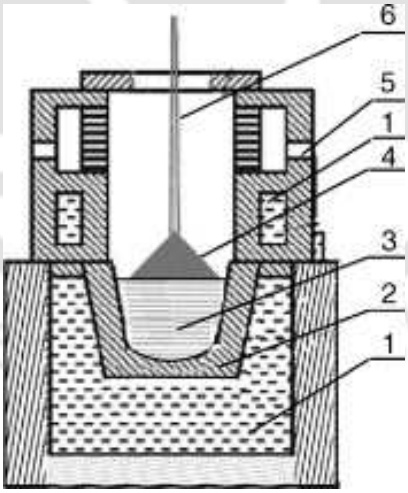

Fig. 2.1.1: Schematic diagram of water-cooled copper-hearth electric arc melting furnace used: Labels denote, (1) circulating water to cool the hearth, (2) copper hearth; (3)

compacted metal blend, (4) electric arc struck between the electrodes (5) gas inlet valve (6) water cooled flexible electrode with tungsten tip (anode).

Elemental powders of cobalt, nickel, gallium, manganese and iron, as per the requirement of the target composition, were weighed in a calibrated electronic balance of 0.01 mg resolution and blended thoroughly in an agate pestle and mortar. The blended alloy mixture was cold compacted in a stainless steel die under a pressure of 40 MPa. The compacted pellet weighing about 5 g was placed the water-cooled copper hearth of the arc furnace and the chamber was pumped down to ~ 10^{-5} Torr. The chamber was purged with argon gas to remove traces of oxidizing atmospheric gases and finally filled with argon gas pressure of 750 Torr. DC arc was then struck and the pellet was melted carefully so as to ensure that no material is lost from the pellet. The cast ingot was then flipped around and re-melted three or four times to ensure complete melting of the constituent elements.

The ingot obtained after melting was molded (re-melted) in a dismountable copper cylinder kept on the water cooled hearth in order to obtain a 10 mm diameter cylindrical sample. As-cast ingots with weight loss > 3% were rejected. The alloy ingots were processed under different conditions as required for various investigations. The different processing procedures are briefly described below.

The as-cast alloys were brittle and also needed to be homogenized further in order to obtain samples with consistent and reproducible properties. The metallic ingots cannot be heat treated in air since they might oxidize. So, the as-cast ingots were taken separately in fused silica ampoules, which were pumped down to 10^{-5} Torr using an oil

diffusion pump (Vacuum Techniques, India) and then flame-sealed. The vacuum-sealed ampoules containing the alloy ingots were placed inside a raising hearth furnace (70T-4, Okay, India), homogenized at 1150 °C for 24 hours and allowed to slowly cool inside the furnace. The slowly cooled samples did not show any signature of martensitic transformations in differential scanning calorimeter studies. So, the cylindrical ingots were cut into small discs (1mm or 8 mm thickness, as required) using a diamond saw (Isomet 2000, Buehler) and cleaned with acetone in an ultrasonic bath. The dried discs were again flame-sealed in fused silica ampoules at a pressure of 10^{-5} Torr, annealed separately at 1230 °C, 1150 °C, 1000 °C and 900 °C for six hours and quenched. Air, ice water and liquid nitrogen were used as quenching media for different investigations. The small discs ensured effective quenching of the homogenized alloy. Thick discs (8mm thickness) were annealed at 1000 °C and quenched in ice water for mechanical testing (Stress-strain studies). For the investigation of microstructure and microhardness, flat samples were mounted in resin using a thermostatic press (Simplet 2, Buehler) and polished using a polishing machine (Ecomet 6, Buehler). A mixture of 40 ml HNO_3 and 60 ml distilled water was used as etchant in order to, microscopically examine the twinned structure and secondary phase present in the samples. Liquid nitrogen quenched samples showed cracks and were very brittle. This provided a means to obtain coarse powder of the alloys for performing XRD measurements. It has to be pointed out that due to the high ductility of the Co-Ni-Ga alloys, fine powders ideally suited for good XRD measurements could not be obtained. The powdered alloys were taken in sealed fused silica ampoules, heat treated again at 1230 °C for 4 hours and quenched in ice water, so as to remove any strain induced while grinding the discs.

2.2. SCANNING ELECTRON MICROSCOPE

The scanning electron microscope (SEM) images the sample surface by scanning it with a high-energy beam of electrons in a raster scan pattern. The electrons interact with the atoms that make up the sample producing signals that contain information about the sample's surface topography, composition and other properties such as electrical conductivity. The types of signals produced by an SEM include secondary electrons, back scattered electrons, characteristic x-rays and light (cathodo-luminescence). These signals come from the beam of electrons striking the surface of the specimen and interacting with the sample at or near its surface. In its primary detection mode, *viz*., secondary electron imaging, the SEM can produce very high resolution images of a sample surface, revealing details about 1 to 5 nm in size. Due to the way these images are created, SEM micrographs have a very large depth of focus (commonly from about 25 times to 250,000 times) yielding a characteristic three-dimensional appearance useful for understanding the surface structure of a sample. Back-scattered electrons (BSE) that come from the sample may also be used to form an image.

In a typical SEM (schematically shown as in Fig.2.2.1), electrons are thermionically emitted from a tungsten filament cathode are accelerated towards an anode. The electron beam, with a typical energy of a few hundred eV to 40 keV, is focused into a very fine focal spot of 0.4 nm to 5 nm by one or two condenser lenses. The beam passes through pairs of scanning coils or pairs of deflector plates in the electron column, which deflect the beam horizontally and vertically so that it scans in a raster

fashion over a rectangular area of the sample surface. When the primary electron beam interacts with the sample, the electrons lose energy by repeated scattering and absorption. The size of the interaction volume depends on the electron's landing energy, the atomic number of the specimen and the specimen's density. The energy exchange between the electron beam and the sample results in the reflection of high-energy electrons by elastic scattering, emission of secondary electrons by inelastic scattering and the emission of electromagnetic radiation which can be detected to produce an image. The image may be captured by photography from a high resolution cathode ray tube, but in modern machines is digitally captured and displayed on a computer monitor.

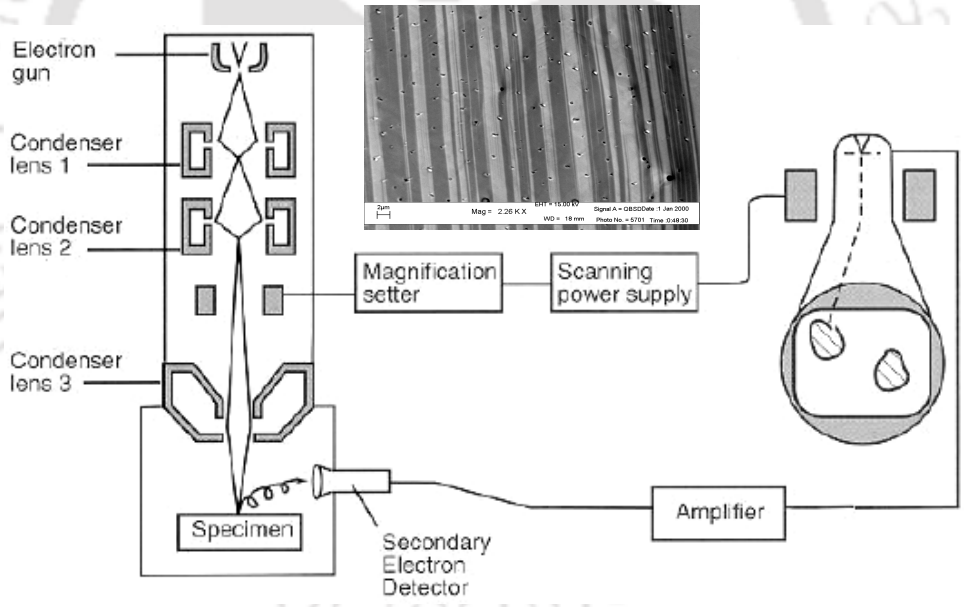

Fig. 2.2.1: A schematic diagram of a SEM.

In an SEM, as in scanning probe microscopy, magnification results from the ratio of the dimensions of the raster on the specimen and the raster on the display device. Assuming that the display screen has a fixed size, higher magnification results from reducing the size of the raster on the specimen, and vice versa. Magnification is therefore controlled by the current supplied to the *x*, *y*.

BSE images are often used in analytical SEM along with the spectra produced from the characteristic X-rays as clues to the elemental composition of the sample. The analytical technique used for the elemental analysis or chemical characterization of a sample is called energy dispersive X-ray spectroscopy (EDS, EDX or EDXRF). Its characterization capabilities are due in large part to the fundamental principle that each element has a unique atomic structure allowing X-rays that are characteristic of an element's atomic structure to be identified uniquely from each other. To stimulate the emission of characteristic X-rays from a specimen, a high energy beam of electrons is focused into the sample being studied. The incident beam may excite an electron in an inner shell, ejecting it from the shell while creating an electron-hole where the electron was. An electron from an outer, higher-energy shell then fills the hole, and the difference in energy between the higher-energy shell and the lower energy shell is released in the form of an X-ray. The X-ray released by the electron is then detected and analyzed by the energy dispersive spectrometer. There are four primary components of the EDS setup: the beam source; the X-ray detector; the pulse processor; and the analyzer. The schematic diagram of the EDS is shown as in Fig.2.2.2. A typical EDS graph is also shown in Fig.2.2.3.

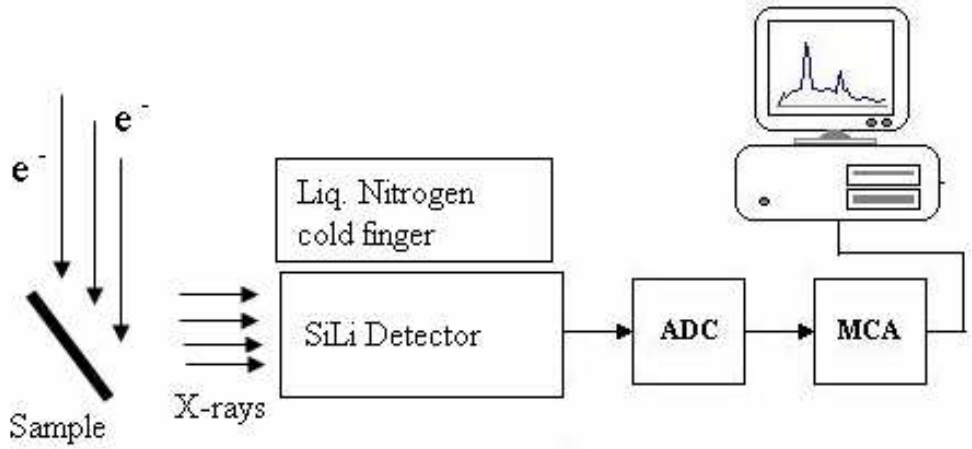

Fig. 2.2.2: A schematic diagram of the EDS attachment in a SEM

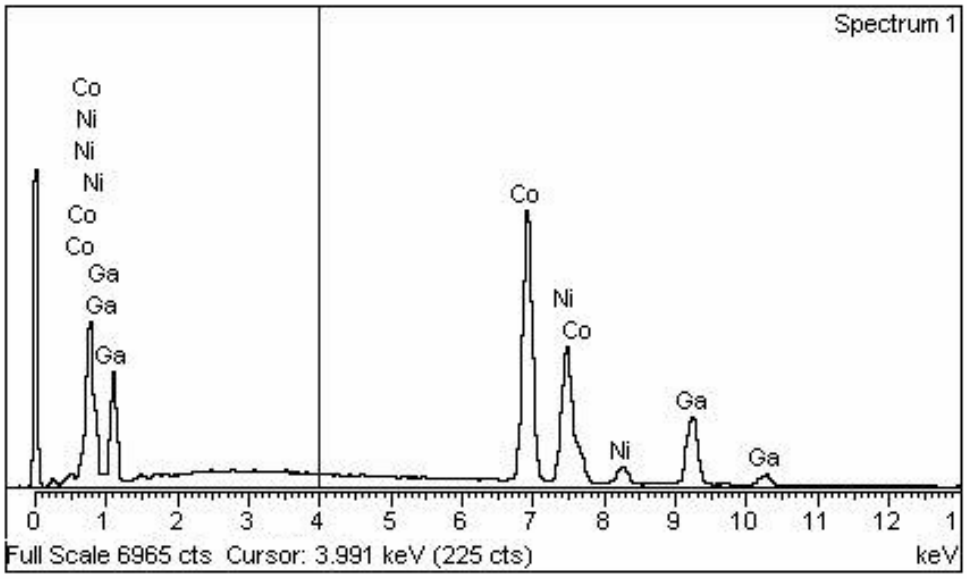

Fig. 2.2.3: A typical EDS graph of Co-Ni-Ga alloy

Emitted X-rays are allowed to fall on a radiation sensitive silicon semiconductor detector with a high impedance zone. Both, the detector and the field-effect transistor of the first stage of preamplifier are cooled to get an optimum of energy-resolution. Inside the detector, each absorbed X-ray quantum is converted into pairs of charge- carriers

(electrons and holes). With a charge-sensitive preamplifier (PA) the charge quantity is finally converted into a voltage-pulse. The pulses are digitized by the analog to digital converter (ADC) and a multi-channel analyzer (MCA), stores the digitized pulses as pulse height spectrum. Then, a pulse amplitude spectrum is developed, in which the stochastically measured discrete X-ray quanta are sorted according to the energy and are collected for different energy types. The X-ray spectrum of the EDS is thereby a histogram (energy distribution of all collected X-ray quanta).

Compositional analysis has been carried out on the prepared alloy samples using a commercial SEM (LEO 1430VP) equipped with an EDS attachment (Model 7353, Oxford Instruments) at Central Instrumental Facility (CIF), IIT Guwahati. Both spot and line analysis were performed on the samples using software provided with the instrument. The SEM-EDS was operated with an acceleration potential of 15 kV to 20 kV, and each spectrum was collected for about 100 s duration. The SEM photograph was taken for selected samples in order to study the martensite structure. A typical SEM micrograph is shown as an in-set in Fig. 2.2.1.

2.3. X-RAY POWDER DIFFRACTOMETER

A commercial X-ray powder diffraction system (Seifert XRD 3003 T/T) was used for the phase identification, quantitative measurement of secondary phase present in two-phase alloys and crystal structure determination of the FSMAs. Cu K_α radiation (1.541 Å) with a nickel filter was used. The X-ray tube was operated with an acceleration voltage of 40 kV and tube current of 30 mA. The theta-theta (θ-θ) goniometer was used in the reflection (Bragg-Brentano) geometry [99] as depicted in Fig. 2.3.1.

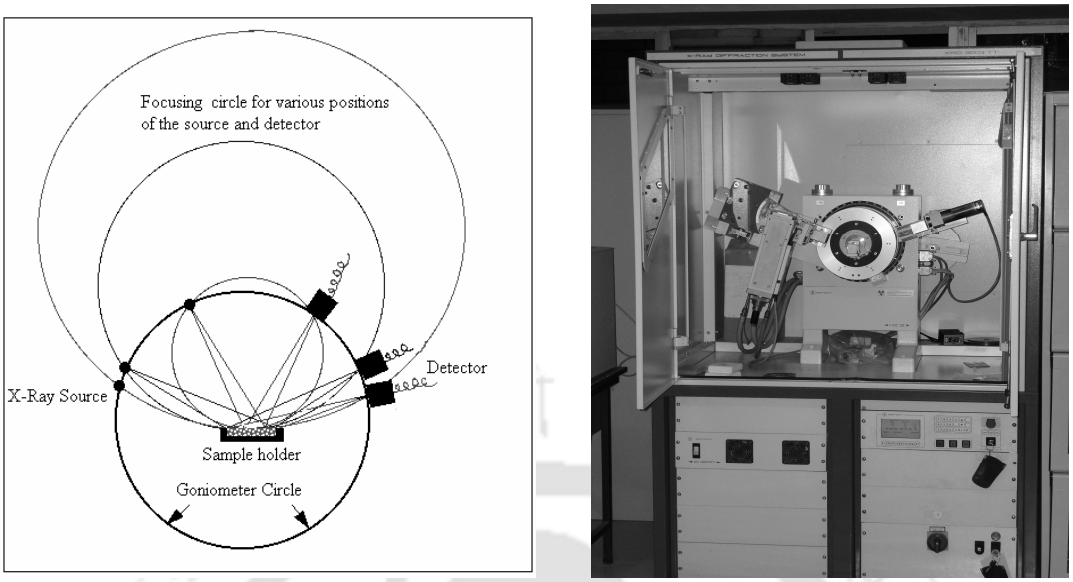

Fig. 2.3.1: A typical X-ray Diffractometer with Bragg- Brentano geometry

A polymetamethylacrylate (PMMA) plate with a square depression of dimensions 25 mm × 25 mm × 0.5 mm coated with a thin layer of high vacuum grease was used as sample holder for X-ray diffraction (XRD) measurements. A thick layer of coarsely powdered alloy sample (processed as mentioned earlier) was evenly spread over a square depression and mounted on the goniometer for recording the XRD patterns. The XRD data provides the variation of intensity / counts per second (cps), recorded by the scintillation detector as a function of 2θ, where θ is the glancing angle. A standard polycrystalline silicon (Si) sample, provided with the instrument was used for the calibration of the instrument. A typical (observed) XRD pattern of standard polycrystalline Si sample is shown in Fig. 2.3.2.

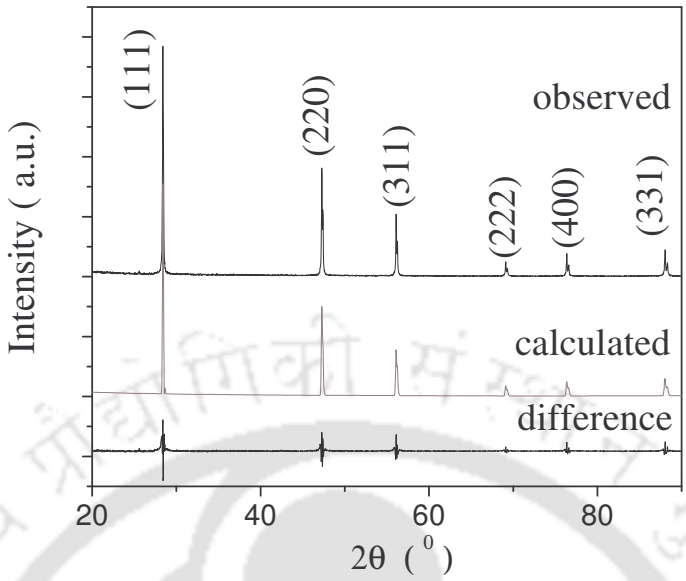

Fig. 2.3.2: XRD pattern of Si sample (observed). Calculated and difference data correspond to least squares fitting performed on the observed data.

Rietveld refinement technique has been employed to refine the crystal structures. The public-domain software, Fullprof, was used for Rietveld analysis [100-102] of X-ray powder diffraction data. There are two version of source code available. The first corresponds to a program written in FORTRAN 77 and can be used in multiple platforms. The second version developed from the previous one, is coded in FORTRAN 95. The two input files for this program are the '*.pcr' and '*. dat' files. The *.pcr file contains the title, type of analysis (X-ray, neutron or profile fitting), profile function used for fitting, number of phase present, wave length of the beam used for the collection of data along with the step size and 2θ range, number of iteration cycles, number of refined parameter and other crystallographic data. The *.dat file contains the intensity (cps) data. Some optional input files can also be used such as '*.bac' for specifying the

background at each step of the scattering variable, '*.irf' for incorporating the instrumental resolution function, *etc*. The two main output files are '*. out' and '*.sum' that contain all control variables and refined parameters. Another important output file is '*.prf' which contains observed and calculated profiles that are automatically used by another graphical interface program called *WinPLOTR*. A graph is obtained with calculated pattern from the input file (*.pcr) and observed pattern from (*.dat) and their differences. The control of the refined parameter is achieved by using a flag in the form of a code word. The sequences for refinement involves setting / optimising the following: (1) scale factor, (2). zero point of detector, first two background parameters and lattice constant(s), (3) overall Debye-Waller factor, (4) peak shape and asymmetry parameters, (5) atom occupancies, (6) individual isotropic thermal parameters, and (7) additional background parameters.

The quality of refinements are known based on the values of reliability factors such as R_p, R_{wp}, R_{exp}, R_{Bragg} , χ^2 and R_F and they are defined as follows:

Profile factor, $$R_P = 100 \frac{\sum_{i=1,n} \left| y_i - y_{c,i} \right|}{\Sigma_{i1,n} y_i} \qquad (2.3.1)$$

Here 'y_i' is the observed point (experimental), '$y_{c,i}$' is the calculated point and n represents the number of data points.

Weighted profile factor, $$R_{wp} = 100 \left(\frac{\sum_{i=1,n} \omega_i \left| y_i - y_{c,i} \right|^2}{\Sigma_{i1,n} \omega_i y_i^2} \right)^{1/2} \qquad (2.3.2)$$

Here $\omega_i = \frac{1}{\sigma_i^2}$; σ_i^2 is the variance of the observation y_i.

Expected weight factor, $$R_{\exp} = 100\left(\frac{n-p}{\Sigma_{i\,1,n}\omega_i y_i^2}\right)^{1/2} \quad (2.3.3)$$

Here (n - p) is the number of degrees of freedom. . 'p' is the number of refine parameters.

Reduced chi-square, $$\chi^2 = \left(\frac{R_{wp}}{R_{\exp}}\right)^2 \quad (2.3.4)$$

Bragg factor $$R_{\exp} = 100\left(\frac{\Sigma_h \left|I_{obs,h} - I_{cal,h}\right|}{\Sigma_h I_{obs,h}}\right)^{1/2} \quad (2.3.5)$$

Here 'h' levels the Bragg's reflections. The $I_{obs,h}$ is the observed integrated intensities and $I_{cal,\,h}$ is the calculated intensities.

The crystallographic R_F factor, $$R_F = 100\left(\frac{\Sigma_h \left|F_{obs,h} - F_{cal,h}\right|}{\Sigma_h F_{obs,h}}\right) \quad (2.3.6)$$

Here $F_{obs,h}$ and $F_{cal,h}$ are the observed and calculated structural factors respectively.

The χ^2, R_B and R_F values has been observed by fitting XRD data for Si std sample as 1.86, 10.2 and 6.2 respectively. A quantitative estimate of the percentage of secondary phase present with the primary phase (in case of alloys exhibiting two-phase structure) has been obtained from the *.out file.

2.4. DIFFERENTIAL SCANNING CALORIMETER (DSC)

DSC is a thermo-analytic technique [103] in which the difference in the amount of heat required to increase the temperature of a sample and a reference material is measured as a function of temperature. The DSC curves are recorded either under a constant heating (or cooling) rate or under isothermal conditions (time scan at a constant temperature).

A typical DSC consists of two isolated sealed pans, one containing the sample and the other a reference material (generally, Al_2O_3 or just the empty Al pan) (Fig. 2.4.1). The two pans are heated or cooled uniformly while the heat flow difference between the two is monitored. The basic principle underlying this technique is the following, when the sample undergoes a physical transformation such as phase transition, more or less heat will need to flow to it in comparison with the reference in order to maintain both at the same temperature. More or less heat flowing to the same would depend on the process being endothermic or exothermic. In the power compensation type DSC, heat is supplied to either of the pans so that both are maintained at the same temperature. The heat flow (dH/dt) is then estimated from this data. In a DSC based on the heat-flux technique, the temperature difference (ΔT) between the two isolated pans is measured from which the heat flow is estimated.

A commercial DSC (PerkinElmer, DSC7) based on the power compensation technique was used in the current investigations. Weighed quantities of Co-Ni-Ga sample pieces were crimped in Al sample pan and the thermal transformations occurring in the temperature range of 25 ^{o}C to 250 ^{o}C was studied during the heating and cooling cycles under a constant heating/cooling rate.

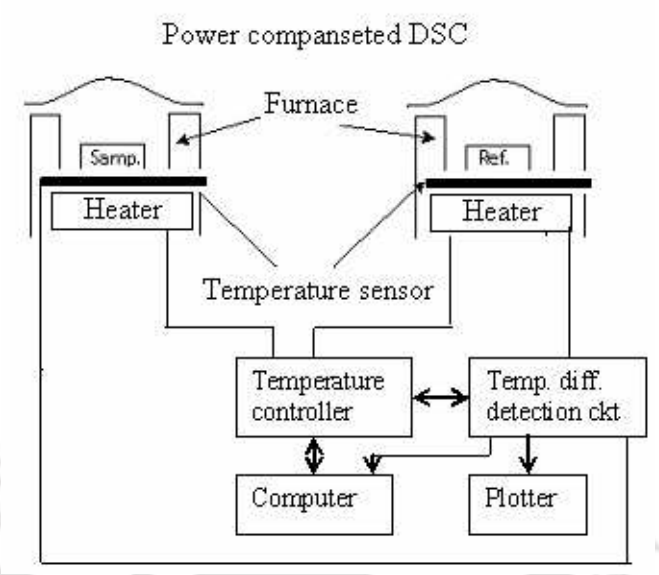

Fig. 2.4.1: A schematic diagram of a DSC

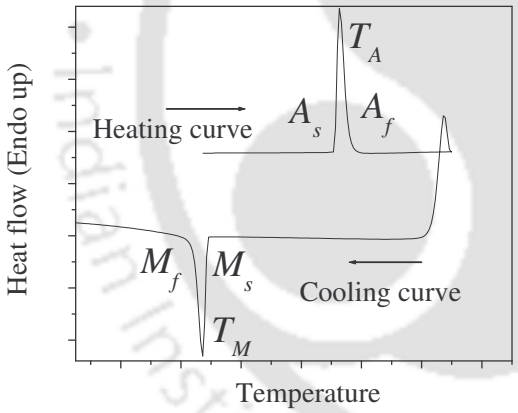

Fig. 2.4.2: Typical DSC curve obtained for an FSMA sample in the current studies.

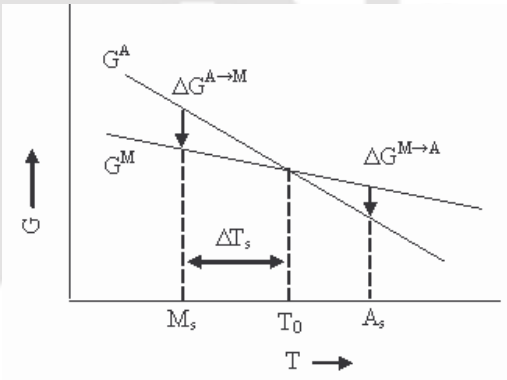

Fig. 2.4.3: Schematic representation of free energy curves of martensite and austenite phases [10]

The runs were programmed and the DSC curves (*dH/dt* versus *T* data) were recorded and analyzed using the Pyris™ software. Temperature and enthalpy calibrations

were performed using standard samples (In and Zn). High purity nitrogen gas was purged continuously throughout the runs.A typical DSC thermogram for of a shape memory alloy is shown as in Fig. 2.4.2. The endothermic peak during heating and exothermic peak during cooling represents the reverse martensitic phase transformation and forward martensitic phase transformation, respectively. The point at which the endothermic peak starts during heating is called austenite start (A_s) temperature and the point at which endothermic peak finishes is called austenite finish (A_f) temperature. Similarly the starting and finishing points of the exothermic peak during cooling are called martensite start (M_s) and martensite finish (M_f) temperature, respectively.

The free energy of the martensite phase is more than that of the austenite phase (Fig. 2.4.3). Thus, during the solid state phase transformation from martensite to austenite, energy is absorbed by the system (endothermic reaction). Similarly, during the transformation from austenite to martensite, energy is released from the system (exothermic reaction). The Gibbs free energy change of a system at $M \leftrightarrow A$ transformation may be written as,

$$\Delta G = \Delta G_c + \Delta G_s + \Delta G_e = \Delta G_c + \Delta G_{nc} \qquad (2.4.1)$$

where ΔG_c is a chemical energy term originating in the structural change from parent to martensite and ΔG_{nc} is the non chemical energy term contains a surface energy term (ΔG_s between austenite and martensite) and elastic energy term (ΔG_e around the martensite) [10]. In most martensitic transformations, ΔG_{nc} is equally large as ΔG_c. In the absence of elastic strain energy, the forward and reverse transformation temperatures (i.e. M_s and A_s) coincides with the thermodynamic equilibrium ($\Delta G = 0$) temperature T_0. This non-chemical energy term changes the driving forces and hence T_0 [104]. A further super-

cooling of ΔT_s from T_0 is necessary for inducing the martensitic transformation and superheating is necessary for the reverse martensitic transformation. The fact M_s is not the same as M_f can also be explained in a similar way. Elastic energy around the martensite resists the growth of the martensite unless a further driving force such as cooling is performed on the system.

2.5. AC SUSCEPTOMETER

AC susceptibility (ACS) technique was used to determine the ferromagnetic to paramagnetic transition (Curie) temperature in the Co-Ni-Ga samples [105]. However, ACS can also be used to determine the martensitic and reverse martensitic transformation temperatures. ACS is a useful technique in condensed matter physics since the typical magnetic fields used are very low and the relative ease with which the frequency and amplitude of the magnetic fields could be varied in the instrument. A high temperature low-field AC suseptometer with a temperature range of 25 °C to 300 °C, was designed and built in our laboratory [106]. The instrument is based on a three-coil mutual inductance bridge. The mutual inductance bridge consists of a primary coil and two Secondary coils as schematically shown in Fig. 2.5.1. The primary coil consisting of 930 turns was wound with 22 SWG copper (Cu) enameled wire on a nylon cylinder of inner diameter 15.6 cm, outer diameter 19.8 cm, and length 70 mm. The secondary coils containing ~1600 turns over a length of 13 mm, were wound with 42 SWG enameled Cu wire. A Cu plate of dimension $2\times5\times120$ mm^3 fitted with a resistive heater was used as the sample holder. The temperature of the sample was measured with a calibrated copper – constantan thermocouple. A Low pressure environment was maintained around

the sample holder with the aid of the fused silica sheath connected to a rotary pump. The primary coil was energized using an ac (sinusoidal) voltage fed from a lock-in amplifier. When a signal, $E = E_0 \sin(i\varpi t)$ is applied to the primary coil, a magnetic field of $B = B_0 \sin(i\varpi t)$ is generated along the axis of the solenoid (primary coil). When there is no sample present at the centre of the secondary coil, the induced voltage in both the secondary coils would be nearly equal and the difference output at the Lock-in Amplifier will be zero.

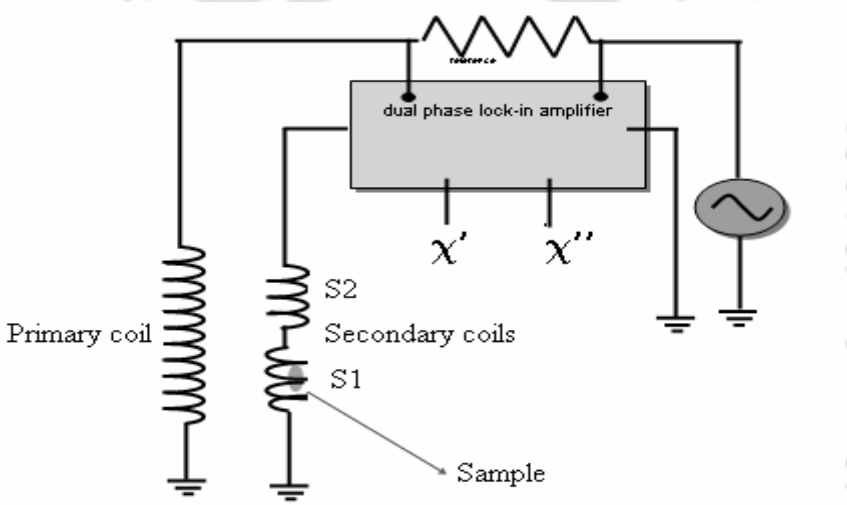

Fig. 2.5.1: Schematic diagram of the indigenously developed ACS. χ' and χ'' are in-phase and out-of-phase components of the magnetic susceptibility.

When a magnetic sample is inserted in the centre of one the secondary coils, the voltage induced in secondary coil *S1*(e_1) and *S2* (e_2) are $e_1 = NV\omega\mu_o H(1+\chi)$ and $e_2 = NV\omega\mu_o H$, where N is the number of turns / unit length in secondary coils, V is the volume of the sample, H is the applied magnetic field in the primary coil, and $\omega = 2\pi f$, where f is the frequency of the ac excitation voltage. Then, the differential output e_{rms} is $(NV\omega\mu_o$

$H\chi)/\alpha$, where the calibration constant $\alpha = [(10^8/8\pi^2 NL) - (L^2 + d^2)^{1/2}]$, where L is the length and d is the diameter of secondary coil. In the present case, $\alpha = 1.59$. Therefore, $\chi = [\alpha\, e_{rms} / V f H]$, where f is the frequency of the applied field. A small amount of sample (~20mg) is taken in the copper sample holder and the position of the rod is carefully adjusted such a way that the test sample stays at the centre of the secondary coil *S1*. A rotary pump was used to maintain an environment of low pressure (~10^{-1} Torr) around the sample. The sample is then heated to the paramagnetic phase. The phase angle of the locking amplifier is then adjusted to get almost zero value of χ''. χ'' is maximum during the ferro- to para magnetic transition and it is negligibly small at its paramagnetic phase. The sample is then cooled to room temperature. χ' and χ'' data are then recorded by heating the sample in a controlled way (@5 °C/ min) inside the coil *S1*. Temperature was measured using a calibrated Copper-Constantan (E-type, non magnetic) thermocouple connected to a 6½ digital multimeter (DMM, Hewlett-Packard 34401A). χ' and χ'' are measured using a Lock-in amplifier (Stanford Research Systems Model: SR830 DSP). Both the instruments were interfaced to a personal computer using Lab-View™ program to facilitate automatic data acquisition.

A typical graph of ac susceptibility data of a Co-Ni-Ga sample recorded as a function of temperature (heating cycle) is shown in Fig. 2.5.2. It was experimentally observed that the martensitic transformation in the FSMAs is accompanied by a sudden drop of the initial magnetic susceptibility [87]. Lowering of point symmetry group during the austenite-martensite transformation results a considerable enhancement of magneto-crystalline anisotropy of the martensite phase. Due to this difference in magneto-crystalline anisotropy, a sudden rise in ac susceptibility was observed during the reverse

martensitic transformations (or sudden fall during $A \rightarrow M$ transformation). At the ferromagnetic to paramagnetic transition, a sharp decrease in ac susceptibility is observed. The Curie temperature (T_C) is determined from the local minimum point of the derivative curve of ACS data taken near the magnetic transition region.

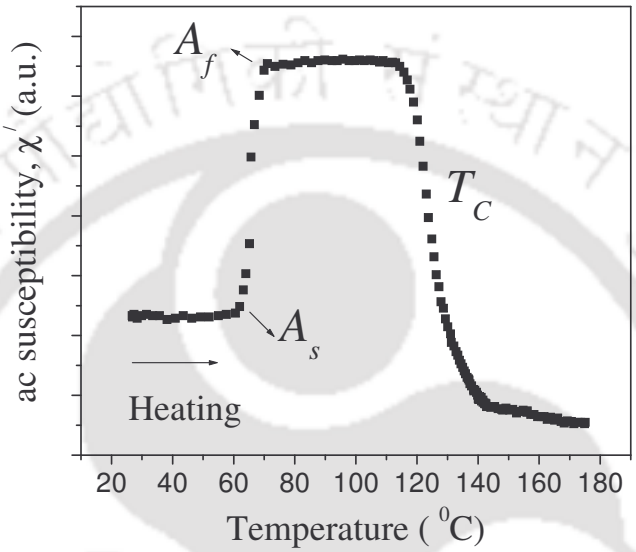

Fig. 2.5.2: Typical ac susceptibility data of an FSMA.

2.6. VIBRATION SAMPLE MAGNETOMETER

Magnetization as a function of applied field and temperature was measured for all the FSMA samples using a commercial Vibrating Sample Magnetometer (VSM, LakeShore model 7410). A block diagram of the VSM is shown in Fig. 2.6.1. The VSM operates on the principle of Faraday's law of induction, which tells us that a changing magnetic field will produce an electric field [107]. This electric field can be measured, which in turn can provide us information about the magnetic moment of the sample as magnetic field and temperature are varied. The VSM consists of nine major parts, *viz.*, 1) water cooled

electromagnet and power supply, 2) vibration exciter and sample holder (with angular position indicator), 3) sensing coils, 4) Hall probe, 5) amplifier, 6) control chassis, 7) lock-in amplifier, 8) Gauss meter, and 9) computer interface.

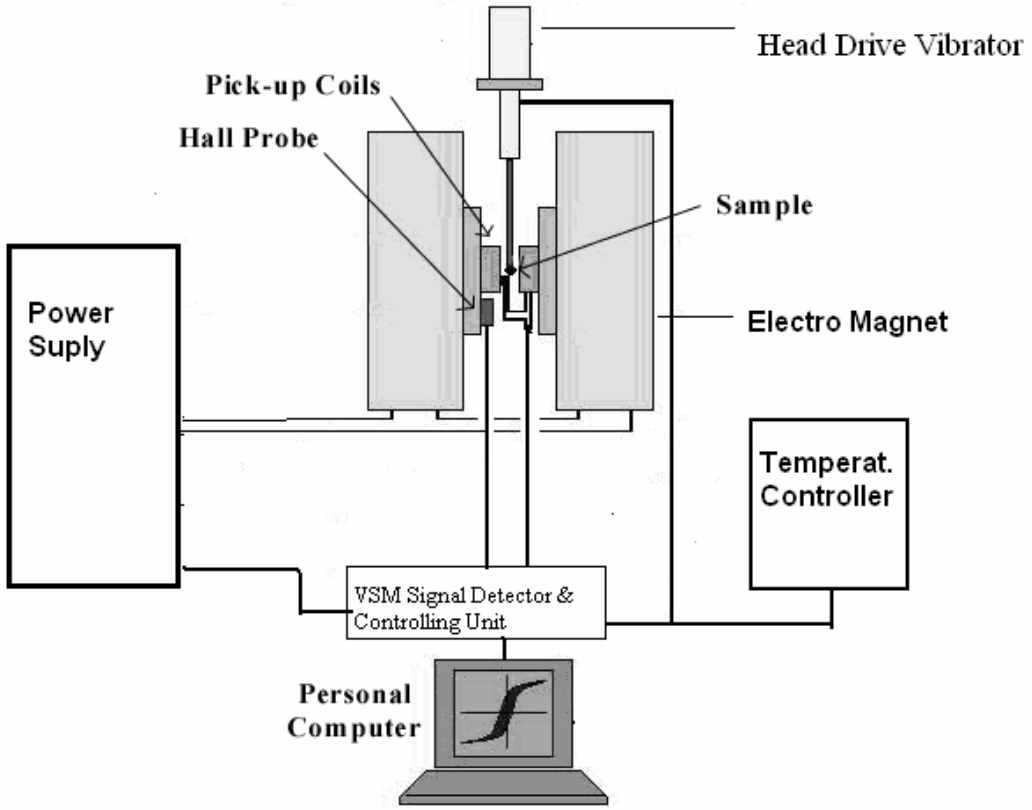

Fig. 2.6.1: A schematic diagram of a VSM.

The sample is fixed to the lower end of the quartz sample holder. The measurement sequence is then programmed using the software provided with the instrument. The vibration exciter is then started and the signal received from the probe and the pick up coils is converted into the magnetic moment value of the sample. Magnetic field up to 20,000 Oe can be applied to the sample. Normally, magnetic field is

automatically increased in steps at a constant temperature (*M-H* measurement) by setting the program. From this measurement, the value of magnetization at different applied magnetic fields is obtained in emu/g. These data provide M_{sat} value of the sample. Magnetization as a function of temperature at a constant applied field (*M-T* measurement) is recorded to obtain information of martensitic transformation temperatures and Curie temperature.

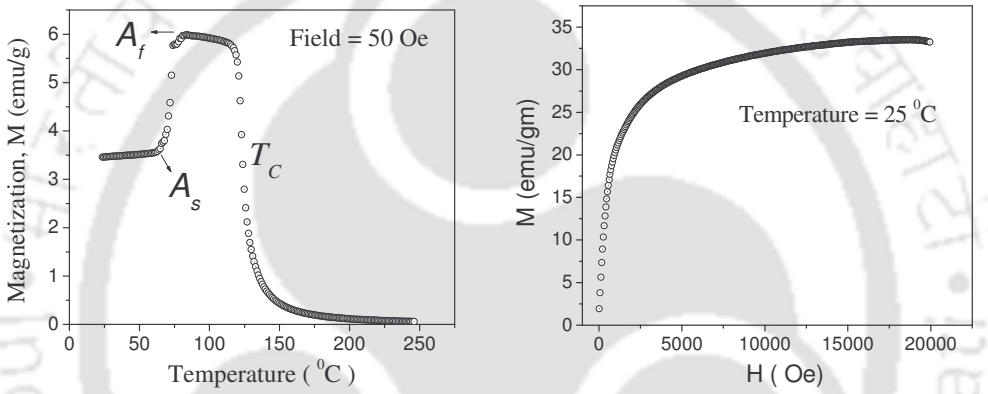

Fig. 2.6.2: Typical magnetization vs temperature (*M-T*) data at constant applied field (50 Oe) and magnetization vs applied field (*M-H*) data at constant temperature (25 °C) for a FSMA.

The martensitic transformation in the FSMAs is accompanied by an abrupt change in magnetization measured at unsaturated fields. This is due to the change of magnetocryctalline anisotropy of the material during structural phase transitions. A sharp decrease in magnetization has been observed at ferro- to paramagnetic phase transition and T_C was determined from the minimum point of its first derivative data.

The effective magnetic anisotropy constant K_{eff} of the alloys can be calculated from the magnetization curves using the law of approach to saturation [72]. Generally, the magnetization (M) as a function of applied field can be expressed as

$$M = M_{sat}\left(1 - \frac{a_{1/2}}{\sqrt{H}} - \frac{a}{H} - \frac{b}{H^2} - \cdots\right) + \chi_{hf} H + D\sqrt{H} \qquad (2.6.1)$$

where H is applied field in kOe, M_{sat} is a saturation magnetization in A/m, χ_{hf} is high field susceptibility and $a_{1/2}$, a, b, c are constant coefficients. The 'a' coefficients depend upon the amount of various structural defects and intrinsic fluctuations. According to Fähnle et.al [108], the second term $\frac{a_{1/2}}{\sqrt{H}}$ can arise from point-like defects, from intrinsic magneto-static fluctuations and from randomly distributed magnetic anisotropy (magneto-crystalline fluctuations). b is related to the magneto-crystalline anisotropy. The constant "D" arises from the partial suppression of thermal excited spin waves in magnetic field. The paramagnetic term $\chi_{hf}H$ causes an increase in spontaneous magnetization at high external magnetic fields. The straightforward method for obtaining the coefficients would be by fitting the experimental curve with this full expression. But because of the large amount of coefficients involved, the fitting procedure gives ambiguous results. To overcome this, an alternate expression [109] involving fewer coefficients given below is chosen as the fitting equation.

$$M = M_{sat}\left(1 - \frac{b}{H^2}\right) \qquad (2.6.2)$$

When applied field is increased to large values, domain wall movements become relatively unimportant and magnetization of the sample is primarily controlled by domain rotation. With the assumption that particles are oriented at random and strain distribution

is homogeneous, the above equation is the best fit equation at high fields [110]. Deciding on the appropriate low field limit is a hurdle in this procedure. Graham *et. al.* [111] discussed this problem and for the as cast metallic glass the lower field limit was set at 10 kOe.

When paramagnetic contribution is comparable with the ferromagnetic contribution, the data obtained form *M-H* measurement can not fit with the above equation. So, data are first fit to the equation,

$$M = M_{sat}(1-\frac{a}{H}) + \chi_{hf} H \qquad (2.6.3)$$

and the paramagnetic contribution χ_{hf} obtained from the above fit is subtracted from the magnetization data ($M_{sat} \rightarrow M$ - $\chi_{hf}H$) and the subtracted M_{sat} *vs* H data are again fitted with equation (2.6.2) to obtain the optimal b value. Once b value is estimated, magneto crystalline anisotropy constant, K_{eff} can be calculated using the relation,

$$K_{eff} = \sqrt{\frac{4b}{15}}\,\mu_0 M_{sat} \text{ [109]} \qquad (2.6.4)$$

In our VSM measurement M_{sat} is measured in emu/g ≅ A-m^2/kg and b is estimated from the non-linear fit has the unit (Oe)^2. Thus, by multiplying M_{sat} with its corresponding density (kg/m^3), it is converted to A/m. b is also converted to (A/m)^2 from Oe^2 (*1 Oe = 10^3/4π A/m*). Finally K_{eff} is obtained in J/m^3.

The nature of ferromagnetic transition was investigated by determining the critical constants involved in the magnetic phase transition. In order to get an accurate T_C value, *M-H* measurements was carried out at different temperature very close to T_C (0.5% above and below T_C). Arrott Noakes [112] plots were obtained to deduce the accurate value of T_C and critical constants were estimated using Kovel -Fisher method [113]. The nature of

the ferromagnetic to paramagnetic phase transition in the critical region may be characterized by a group of physical relations, *viz.*, [114-115]

$$M_{H\to 0} = A(-t)^{\beta} \text{ for } T < T_C \quad (2.6.5)$$
$$M = BH^{1/\delta} \text{ for } T = T_C \quad (2.6.6)$$

$$(M/H)_{H\to 0} = C(-t)^{-\gamma} \text{ for } T < T_C \quad (2.6.6)$$
$$= C\acute{t} \quad \text{for } T > T_C$$

with M as magnetization in the applied magnetic field, H. The parameters β, δ and γ are the critical exponents and A, B and C are the proportionality constants. The parameter t is the reduced temperature, $(T-T_C)/T_C$. The scaling law relation

$$\alpha = 2 - \beta(\delta+1) \quad (2.6.7)$$

enables us to evaluate the value of α, the specific heat exponent. In order to determine the critical constant, arbitrary β and γ value are selected and $M^{1/\beta}$ vs. $(H/M)^{1/\gamma}$ are plotted. The zero field $M_{sat}(0)$ at different temperature is determined from the intersection of the linearly extrapolated curve with $M^{1/\beta}$- axis. A similar process also performed for $\chi_0^{-1}(T)$ with the $(H/M)^{1/\gamma}$-axis. A graph is obtained $M_{satt}(T)$ vs.T and $\chi_0^{-1}(T)$ vs.T. New values of the critical exponents β and γ are obtained and they are re-introduced in the scaling of modified Arrott plot. All these processes are repeated until the iteration converges and lead to the optimum fitting values [116-117].

2.7. OPTICAL MICROSCOPE

Microstructural observation of polished samples was carried out using an upright reflected beam optical microscope (Carl Zeiss, Axiotech). The image of the specimen

was captured by a charged coupled device (CCD) camera fitted to the instrument. The image from the CCD camera is transferred to a computer memory and processed by KS-300 image analysis software.

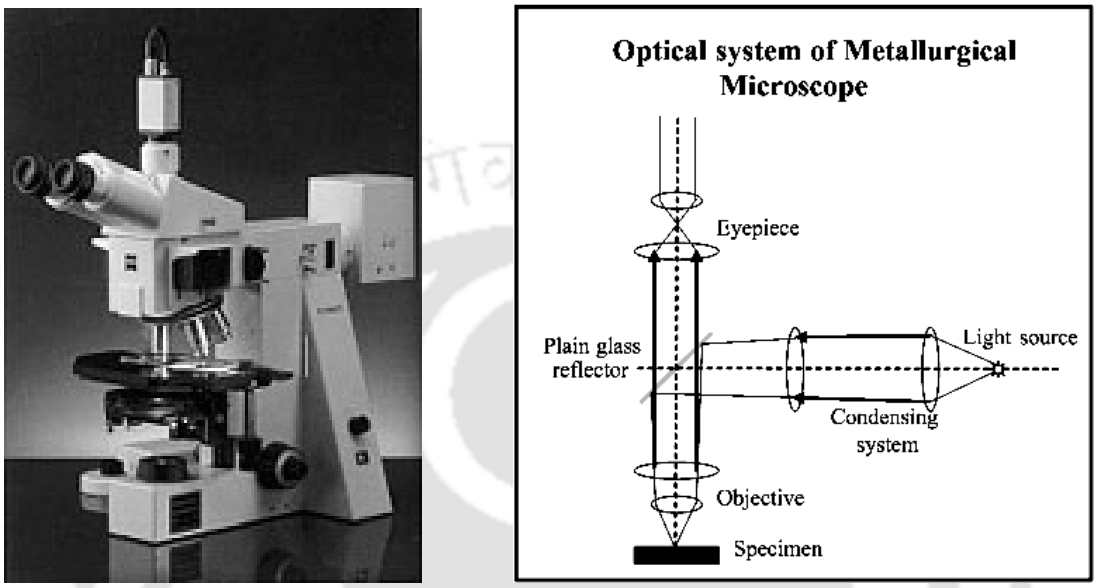

Fig. 2.7.1: Optical microscope with CCD camera.

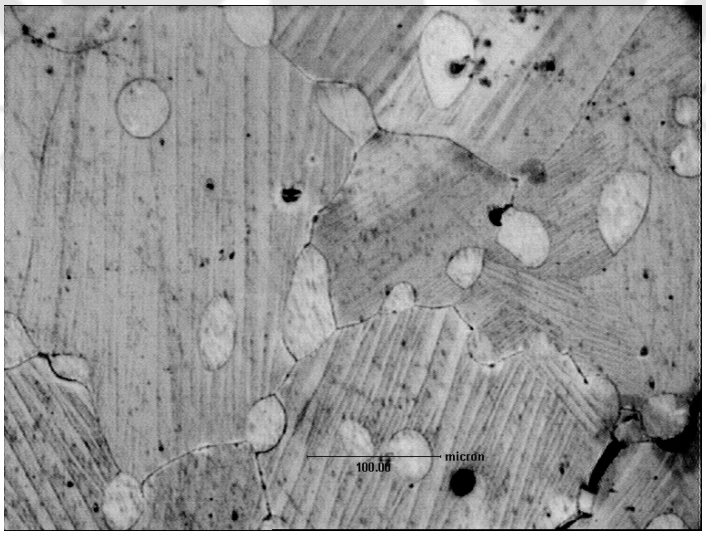

Fig. 2.7.2: A typical optical micrograph of CoNiGaFe alloy

A photograph and ray diagram of the microscope is shown as in Fig.2.7.1. The optically flat polished were carefully etched in dilute HNO_3 prior to observation. The graphical data recorded by the CCD camera was digitally stored in the computer (not shown in the figure). A typical optical micrograph of a FSMA specimen is shown in Fig. 2.7.2. The characteristic martensite twins along with secondary γ-phase precipitates are visible in the optical micrograph. The dark spots are porosities present in the cost sample

2.8. UNIVERSAL TESTING MECHINE

Stress-Strain analysis of the samples was performed using a universal testing machine (UTM, Instron 8801 Servohydraulic). A block diagram of a servohydraulic single-axis UTM is given in Fig. 2.8 [117]. The main controlling modes of the system are strain (up to 10 %), load (up to 100 kN) and position (up to 75 mm) with a loading and unloading frequency range from 0 to 200 Hz. The instrumental is equipped with a hydraulically actuated self-aligning gripping mechanism. The major parts of the instrument are 1) a load-cell based servo hydraulic system, 2) motor driven sample holder assembly for loading, 3) control system which controls the operation of the load-cells and collects data from the load-cells and extensometer, and 4) computer interface.

Since the FSMA samples could not be prepared in size and shape required for tensile testing, only compression test was performed on flat-ended cylindrical samples of diameter 7-10 mm and length of 11 – 7 mm. The samples were kept between the upper and lower grips of the machine and load was applied with proper monitoring. The data on the strain (in strain %) for a particular load (in MPa) was recorded in the computer using in-built software. From these data, stress-strain graph for the different samples were

plotted. For the sample with Mn, load up to 1200 MPa was applied, as where for the other samples, loads up to 500 MPa were sufficient to induce failure. From the graphs, strain ε (in %) corresponding to the critical stress σ (in MPa required to move the twins were found. From these calculations, the mechanical energy density $E_v = \sigma\varepsilon/2$ required for total alignment of the twin variants in the FSMA sample was determined. The compressive strength of the materials was assessed at the failure point of S-S graph.

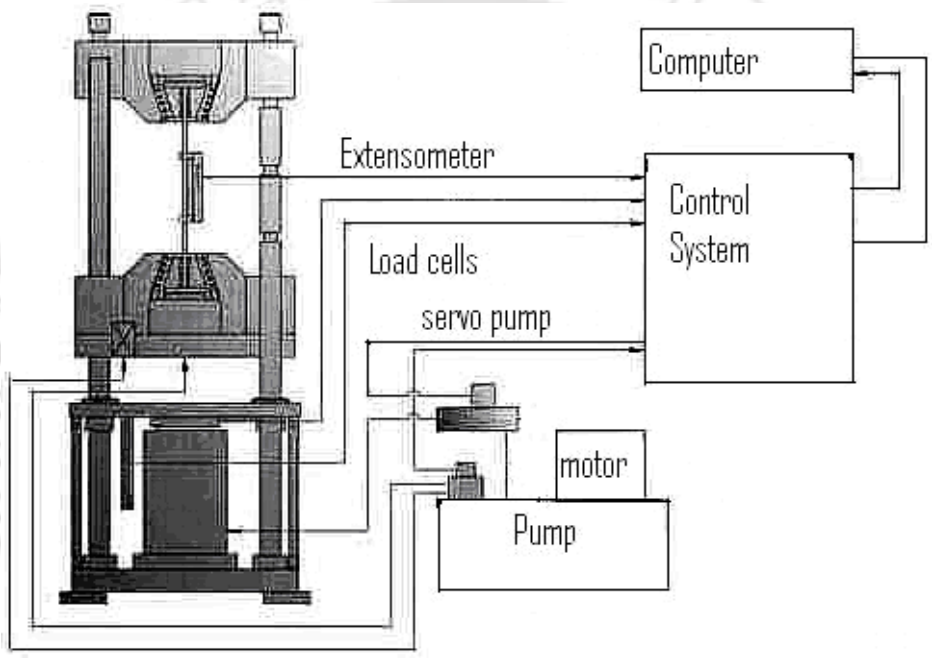

Fig. 2.8.1: A block diagram of a Universal Testing Machine.

Typical graphs of stress-strain behavior of shape memory alloys are shown as in Fig. 2.8.2. In Fig. 2.8.2a, stress was applied till failure occurred (load is released automatically after failure). The maximum stress accumulated taken by the sample without cracking is called the compressive strength of the material. In Fig. 2.8.2b,

residual strain in the sample after unloading is shown. On heating the sample above A_f, some part of the strain gets relaxed.

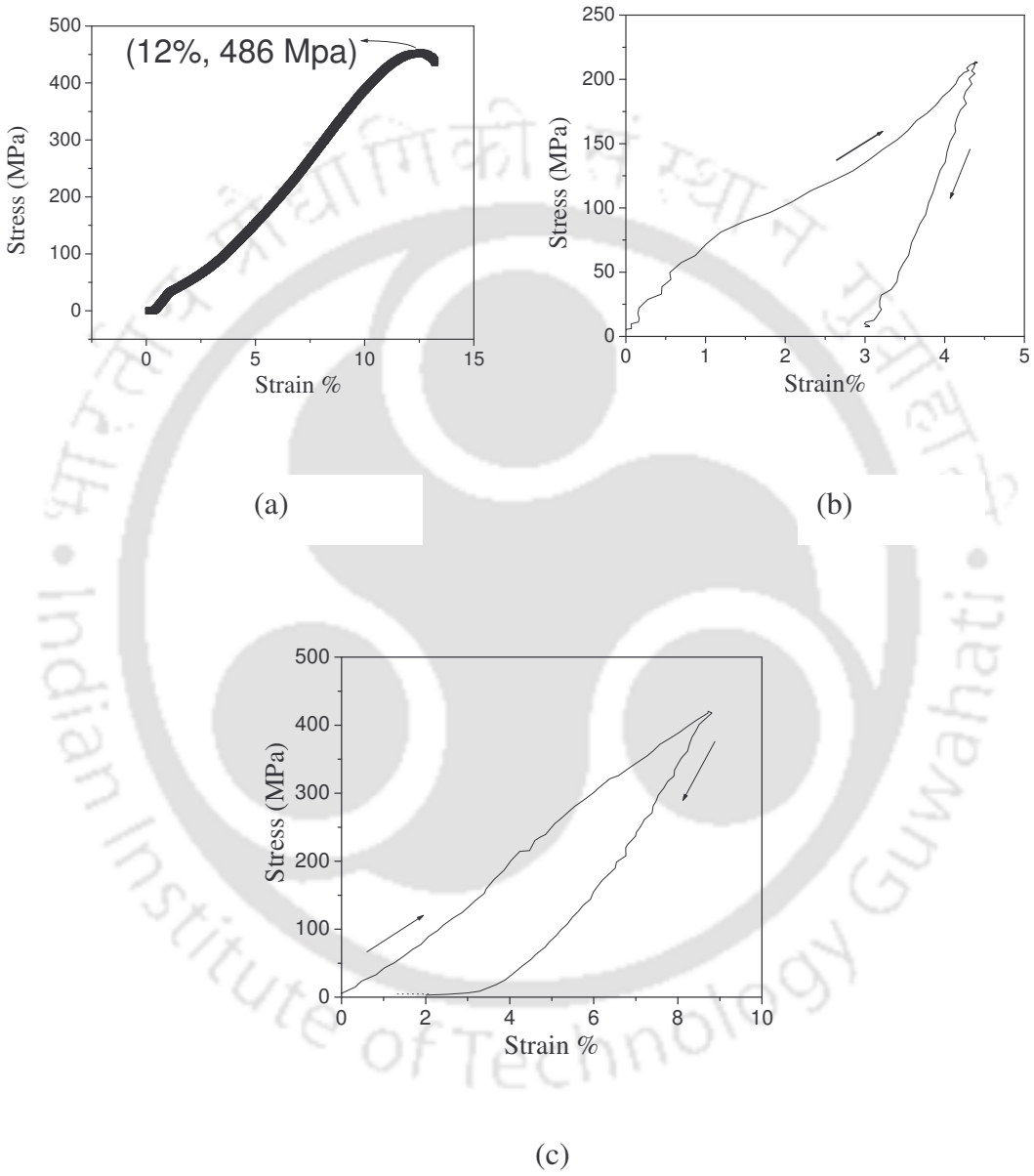

Fig. 2.8.2: Stress strain behavior of shape memory alloys.

This strain relaxation is due to the shape memory effect (SME). SME measurement using compression test involves the following steps: 1) At the outset, the length of the samples is measured before loading (l_0), after unloading (l_1) and after heating it beyond A_f (l_2). 2) Residual strain after unloading (ε_r), strain recovered due to SME (ε_{SME}) and permanent strain (ε_{per}) are then obtained using the raltions $\varepsilon_r = (l_0-l_1)/l_0 \times 100\%$, $\varepsilon_{SME} = (l_1-l_2)/l_1 \times 100\%$ and $\varepsilon_{per} = (l_0-l_2)/l_0 \times 100\%$, respectively. 3) Recovery rate (R) is calculated as $R = \varepsilon_{SME} / (\varepsilon_{SME} + \varepsilon_{per}) \times 100\%$ [57]. If 100% recovery of the strain is obtained after unloading as depicted in Fig. 2.7.2c, the sample is said to have exhibited 'super-elastic effect'.

2.9. MICROHARDNESS MEASUREMENT

Microhardness (or simply the hardness measured over a micrometer scale) is a characteristic property of solids. The hardness is a measure of the resistance of a material to being penetrated and eroded by another material's sharp projections [119].

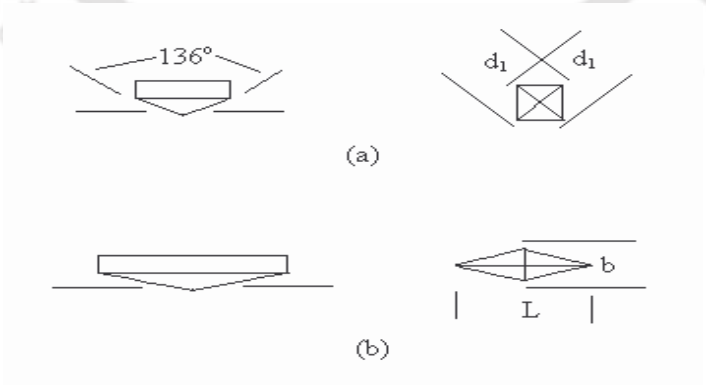

Fig. 2.9.1: Geometry of micro indenters of the (a) Vickers (b) Knoop type.

The measurement procedure involves the use of a diamond micro indenter either in the shape of a square pyramid (Vickers indenter) or an elongated pyramid (knoop indenter). Figure 2.9.1 explains the process of a small diamond indenter being pushed into the material under a known load. The size of the indentation is generally of the order of a few microns under 5 to 1000 g loads and hence the term 'microhardness'. For the Vickers indenter, the Vickers hardness number,

$$\mathrm{VHN} = \frac{\text{force}}{\text{area}} = \frac{2\mathrm{F}\sin\left(\frac{\theta}{2}\right)}{\mathrm{d}^2} \qquad (2.9.1)$$

where F is the force in kg, θ is the inclined angle of Vickers pyramid tip and d is the average diagonal of the impression in mm. Since $\theta = 136^0$ for the Vickers pyramid, VHN (expressed usually in units of kg/mm^2) may be written as

$$VHN = \frac{1.8544\,F}{d^2} \qquad (2.9.2)$$

In this work, microhardness of the alloys was evaluated from the average VHN. Generally, a total indentation time of 15-25 seconds was used for the measurement, which is sufficient for the load to gradually descend onto the surface and reach an equilibrium penetration depth. Careful preparation of the sample surface is necessary prior to indentation. For this, the samples are mounted on a thermosetting resin and polished to a mirror finish. The polished samples were then indented using a Vickers diamond pyramidal indenter and the length of the diagonals of the indents was measured

using a graduated microscope. A typical indent made on a polished Co-Ni-Ga sample is shown in Fig. 2.9.2. The indent corresponds to a load of 100 gm and loading time of 15 s. The microhardness (VHN) values reported in this thesis are the average values of at least 10 independent indents made on each sample composition under identical loading conditions. All measurements were made at room temperature.

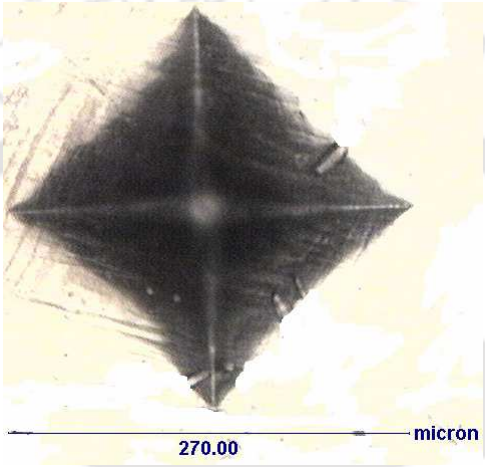

Fig. 2.9.2: Typical indent made on Co-Ni-Ga alloys using a Vickers pyramidal indenter.

2.10 STRAIN GAUGE SET-UP

A strain gauge based instrument (Hottinger Baldwin Messtechnik, Spider 8) was used to measure the magnetic field induced strain (MFIS) in the FSMA samples. The unit consists of a bonded resistance strain gauge connected to the Spider 8 unit and the data (resistance change) measured by the unit is sent to a computer through a universal serial bus. Strain gauges with gauge resistance of 120 Ω (±0.35%) and gauge factor G of 1.9 (±1.5%) were used in quarter Wheatstone bridge configuration to measure the strain produced in the samples under the application of magnetic field. Fig. 2.10.1 shows a typical bonded resistance strain gauge used as the MFIS sensor. An in-built Wheatstone

bridge circuit with the strain gauge in one of its arms forms the 'sensing part' of the instrument. If a strain gauge of resistance R_g (Fig. 2.10.2) is connected in one arm of the Wheatstone bridge, then the strain produced in the sample can be measured from the change in resistance (ΔR_g) of the strain gauge under the bridge balance condition, using the formula [120]

$$\text{Strain} = (\Delta R_g / R_g)/G \qquad (2.10)$$

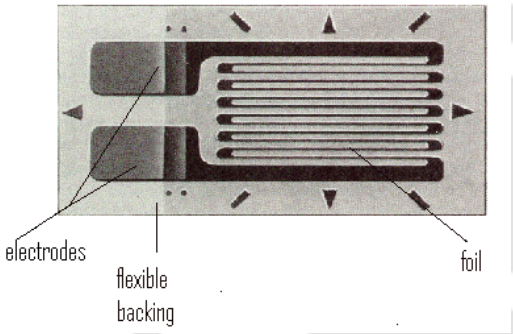

Fig. 2.10.1: A Strain Gauge. The resistive element (dark lines) is embedded on the the backing (gray) material.

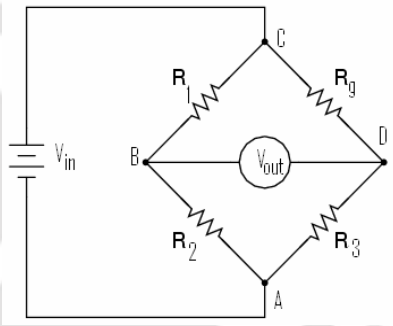

Fig. 2.10.2: Wheatstone bridge with measuring strain gauge (R_g).

Thick disk shaped samples were used for the strain measurement. The surface of the sample was cleaned in an ultrasonic bath containing acetone. The strain gauge was fixed on the sample surface with a strong adhesive (Araldite). The sample was placed in a Teflon capsule, which acted as the sample holder, and introduced between the pole pieces of an electromagnet. The software used for acquiring data requires the data acquisition channel no, the gauge constant, the bridge configuration and zero field data as inputs. The magnetic field was then turned on by energizing the electromagnetic with a variable DC power supply. The electromagnet coil current is increased in small steps and the

corresponding magnetic field at the sample is measured with a Hall probe placed close to the sample. At each field step, data was acquired for a fixed sampling time. After completing one cycle, the data was taken again by reversing the direction of the field and the data of the two runs are averaged. Fig. 2.10.3 shows a block diagram of strain gauge data acquisition procedure.

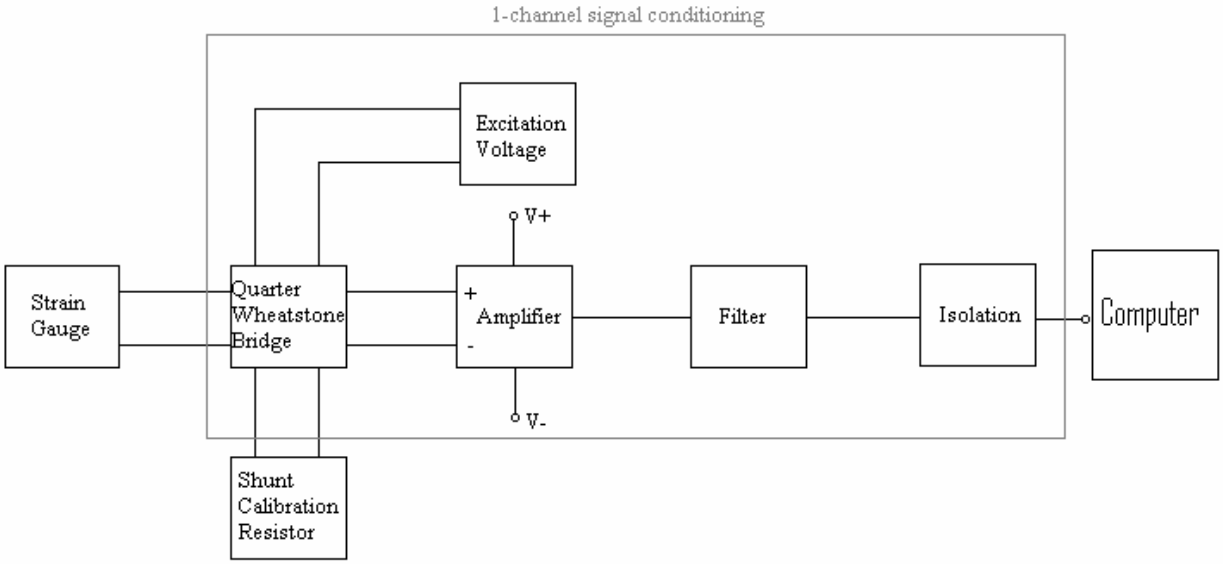

Fig. 2.10.3: Block diagram of strain gauge data acquisition system

The Spider 8 data is a processed strain gauge data. In order to obtain meaningful MFIS values from this data, the instrument has to be calibrated. Calibration of the Spider 8 strain gauge was done by simultaneous strain measurements on a standard nylon plate using the Spider 8 and the UTM extensometer (Instron 8801). Fig. 2.8.1 shows block diagram of a UTM. The details of this instrument are given in the section 2.8 of this chapter. Strain gauge was pasted on the nylon plate clamped to the UTM. The extension of the plate was measured by the extensometer in tensile mode and monitored by a computer. During the extension, Spider 8 data was also acquired simultaneously, and the

strain measured in steps of 0.005 mm, 0.01 mm and 0.1 mm extension. By comparing the Spider 8 data with the corresponding UTM extensometer data, a calibration graph was made Fig. 2.10.4. From this graph, the true MFIS (in %) could be obtained from the corresponding Spider 8 data.

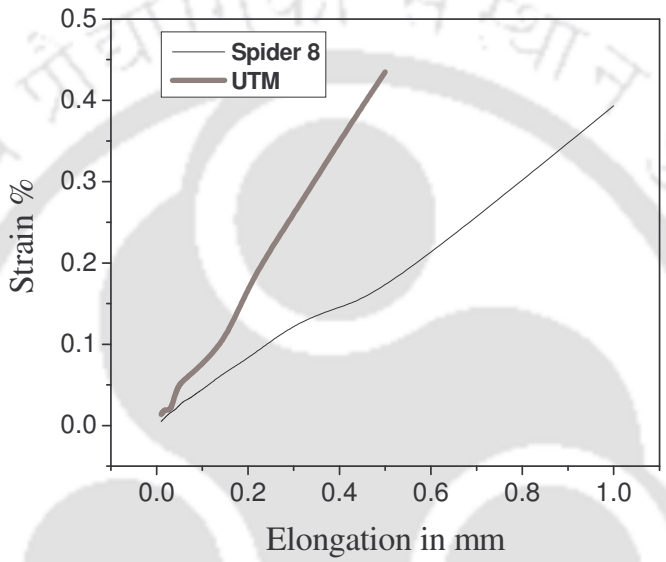

Fig. 2.10.4: Calibration of spider 8 with load strain gauge system using UTM.

2.11. DENSITY MEASUREMENT

Density is measured by weighing a suitably selected piece of alloy sample in air and delivering this weight by the buoyancy, when the sample is suspended in water. According to Archimedes principle, the buoyancy equals the weight of the displaced fluid, which, for water, equals the volume. If W_a is the weight of the specimen in air and W_b in water, then the buoyancy is (W_a-W_b) and density (assuming density of water is 1

gm/c.c),

$$\rho = \frac{W_a}{W_a - W_b} \qquad (2.11.1)$$

If W_1 is the weight of the density bottle filled with analytical grade xylene and W_2 is the weight of the density bottle with xylene and sample outside the density bottle, then the weight of the sample is (W_2-W_1). If W_3 is the weight of the density bottle with the sample immersed in xylene, then the sample weight loss in the immersion medium is (W_2-W_3). Then the specimen volume is,

$$V = \frac{W_2 - W_3}{\rho_m} \qquad (2.11.2)$$

where ρ_m is the density of xylene and the density of the specimen is,

$$\rho = \frac{W_2 - W_1}{W_2 - W_3} \times \rho_m \qquad (2.11.3)$$

Several pieces of the sample were taken in a 10 ml specific gravity bottle and the weighing was carried out in an electronic balance with 0.01 mg resolution. Each measurement was repeated at least three times and the average value was taken. Measurements were carried out in a room with temperature maintained at 24 ± 1 ˚C.

INVESTIGATIONS ON $Co_xNi_{25}Ga_{75-x}$ ($43 \leq x \leq 50$) ALLOYS

In this chapter, investigations performed on a series of Co-Ni-Ga alloys with compositions $Co_xNi_{25}Ga_{75-x}$ ($43 \leq x \leq 50$) are presented. The alloy ingots of each composition were prepared by arc melting method as per procedures explained in chapter 2. All the alloys discussed here are ingots annealed at 1150 °C and quenched in ice water. The composition of the alloys was determined by SEM-EDS. The results are listed in Table 3. It is clear from the table that the processed alloys exhibited compositions that are very close to the starting composition. The processed alloys were highly homogenous and yielded consistent results in various experiments. These consistent results were also used to optimize the annealing time so as to obtained alloys with the required homogeneity.

Table 3: Compositions of alloys obtained by SEM-EDS

Starting composition			Composition of the quenched alloys		
Co at%	Ni at%	Ga at%	Co at%	Ni at%	Ga at%
43	25	32	43.25	24.87	32.48
43.5	25	31.5	43.42	24.73	31.85
44	25	31	44.18	25.03	30.85
44.5	25	30.5	44.67	24.89	30.44
45	25	30	45.03	25.13	29.84
46	25	29	46.32	24.98	28.70
47	25	28	46.78	25.12	28.10
48	25	27	48.33	24.67	27.00
49	25	26	48.95	25.16	25.89
50	25	25	50.17	24.96	24.87

3.1. CRYSTAL STRUCTURE AND MICROSTRUCTURE

X-ray diffraction (XRD) pattern of the alloys of $Co_xNi_{25}Ga_{75-x}$ ($43 \leq x \leq 50$) alloys were recorded as per procedure outlined in the previous chapters. The XRD data are shown as in Fig.3.1.1a and c. Fig. 3.1.1b and d depict the microstructure of the various alloy compositions. Alloys with Co at % from 43 to 45 exhibited a single phase structure. The inset in Fig. 3.1.1a shows the expanded view of the XRD peaks between 2θ values of 42˚ and 48˚, which confirms the single phase nature of the alloys. Microstructure of the alloys observed under an optical microscope also exhibited the similar observation. The twinned microstructure observed in the optical micrographs of these alloys is the typical signature of the martensite phase (Fig.3.1.1b)

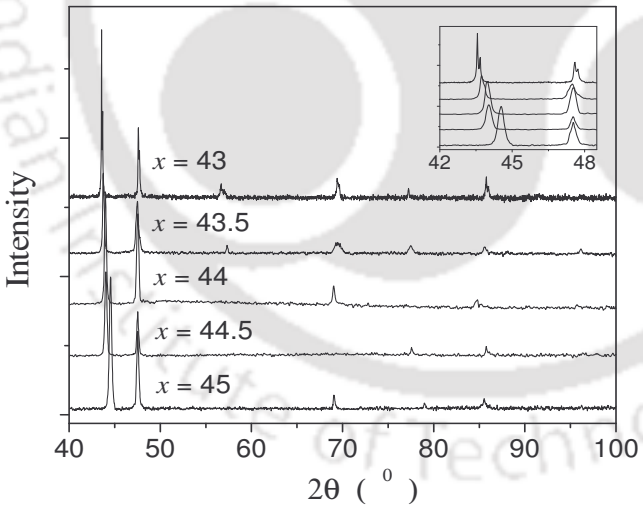

Fig. 3.1.1a: XRD pattern for $Co_xNi_{25}Ga_{75-x}$ ($43 \leq x \leq 45$) alloys

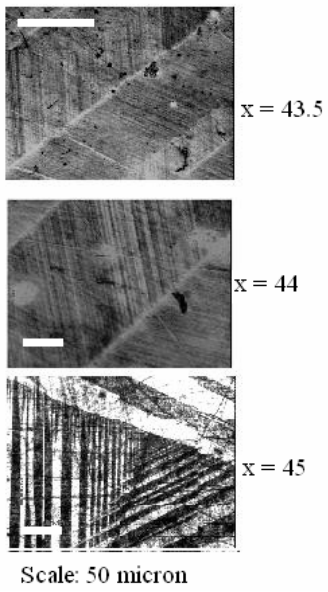

Fig. 3.1.1b: Twin microstructure of the alloys

When the amount of Co was increased above 45 at% in the $Co_xNi_{25}Ga_{75-x}$ alloys, a new phase starts appearing and at 50 at % Co, the new phase dominates over the primary phase. This can be observed from the clearly distinct XRD patterns obtained for the alloys with $x \geq 45$ shown in Fig. 3.1.1c. The optical micrographs of $x = 47$ and 50 alloys (Fig. 3.1.1d) show the dominance of this secondary phase over the primary phase. The black spots in the optical micrographs are porosities, which are common in cast alloys. Since single phase structure has been observed for the alloys with $43 \leq x \leq 45$, no further analysis has been carried out for the alloys with $46 \leq x \leq 50$.

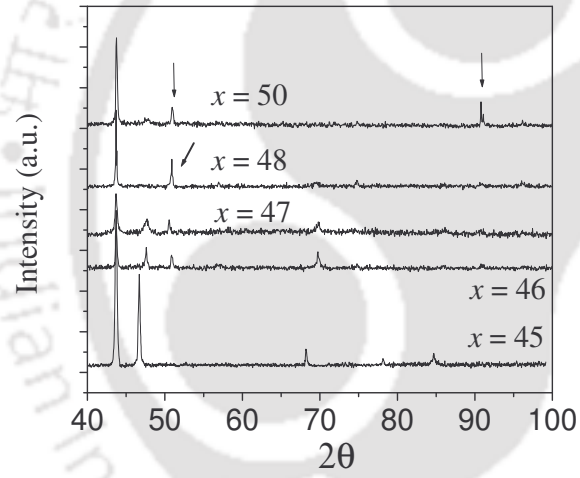

Fig. 3.1.1c: XRD pattern for $Co_xNi_{25}Ga_{75-x}$ ($46 \leq x \leq 50$) alloys

Fig. 3.1.1d: Presence of secondary phase in optical micrograph

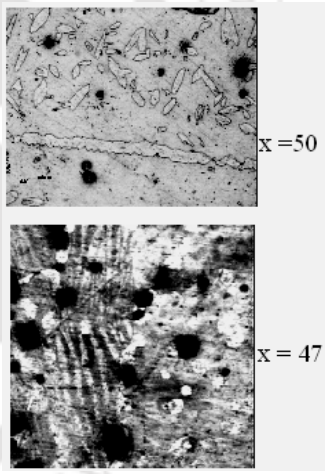

To determine the crystal structure of the single phase alloys (i.e. for alloys with Co at% $43 \leq x \leq 45$), a Rietveld refinement technique (FullProf software package) was employed (Ref. *Sec.2.3, page 52-54).* The models used in the literature for least squares fitting to the experimental diffraction data were all tested. Rietveld analysis showed that the

XRD data could be fitted well to two different models with space group I4/mmm (bct) and P4/mmm (fct), respectively. The lattice parameters and atomic positions in the unit cell for both the models are listed in Table 3.1. Typical least squares fit of both the models to the data corresponding to alloy with $x = 45$ are shown in Fig.3.1.2a and Fig.3.1.2b, respectively.

For the space group P4/mmm, the Wyckoff positions are Ga at 1a(0, 0, 0), Ni at 1c(0.5, 0.5, 0) and Co at 2e(0, 0.5, 0.5) (Fig. 3.1.2b). All the major (intense) peaks in the XRD pattern of the alloys could be fitted well with this model ($L1_0$ type structure). However, some weak peaks appeared in the calculated XRD patterns which were not observed in the experimental XRD patterns. Since these alloys were inherently very ductile, very finely powdered samples could not be prepared for XRD observation. Due to the coarseness of the samples used for XRD measurements and the upper limit of 40kV/30mA X-ray generator rating, highly noisy background was observed in the recorded XRD patterns. With these limitations, the presence of the weak peaks could not be ascertained in the observed XRD pattern. However, the lattice parameters reported by Chernenko *et a.l* from TEM observations [55] are in reasonable agreement with our results.

Table 3.1: Crystallographic data of the alloys obtained from Rietveld analysis

Space Gp.	*P4/mmm*					*I4/mmm*				
Wyckoff Position	Ga: 1a (0, 0, 0) Ni: 1c (0.5, 0.5, 0) Co: 2e (0, 0.5, 0.5)					Ga: 2a (0, 0, 0) Ni: 2a (0, 0, 0) Co: 2a (0, 0, 0)				
Co at % in alloy (x)	a (Å)	c (Å)	c/a	V (Å)^3	χ^2	a (Å)	c (Å)	c/a	V (Å)^3	χ^2
43.0	3.831	3.254	0.849	47.758	3.8	2.698	3.254	1.206	23.687	5.4
43.5	3.843	3.222	0.838	47.585	3.2	2.713	3.218	1.186	23.685	5.6
44.0	3.865	3.205	0.829	47.877	3.5	2.718	3.205	1.179	23.677	4.8
44.5	3.875	3.163	0.816	47.494	4.2	2.721	3.192	1.173	23.633	5.2
45.0	3.887	3.136	0.807	47.381	3.0	2.743	3.139	1.144	23.618	4.0

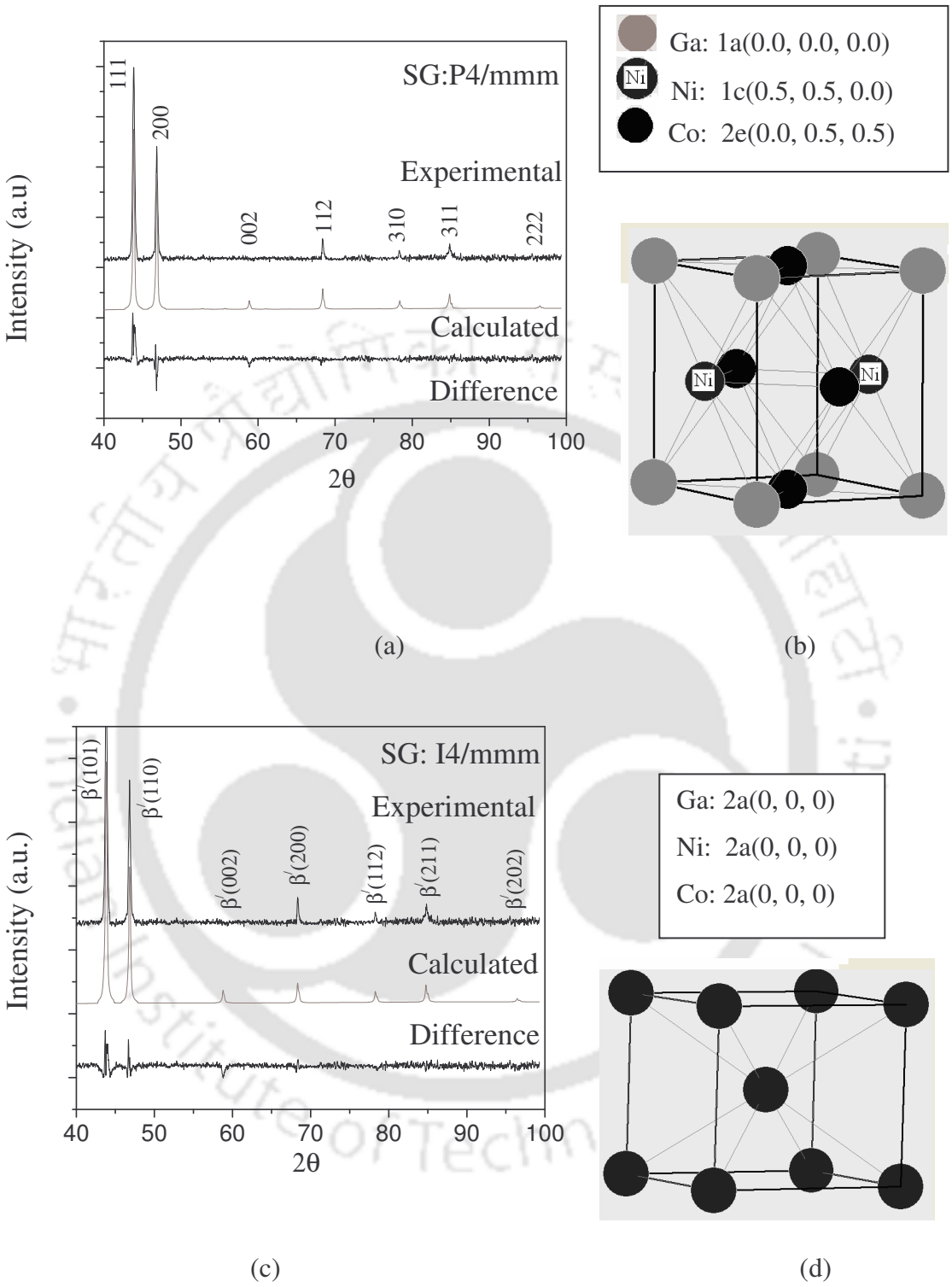

Fig. 3.1.2: Rietveld fit to the XRD data for $Co_{45}Ni_{25}Ga_{30}$ alloy considering SG (a) *P4/mmm* and (c) *I4/mmm*. (b) and (c) show the arrangement of atoms in $L1_0$ and bct unit cell respectively.

Pons *et al.* [46] pointed out that both bct and $L1_0$ unit cells can be obtained by appropriate choice of crystallographic axes. The lattice parameters of $L1_0$ and bct unit cells are related to each other by expressions, $a_{L1_0} = \sqrt{2}a_{bct}$ and $c_{L1_0} = c_{bct}$ [46]. Thus another model with *I4/mmm* space group was also considered. It was observed that if the Wyckoff position 2a (0,0,0) is assumed to be occupied by Co, Ni and Ga in an arbitrary manner (Fig.3.1.2d), the calculated pattern matched very well with the experimental XRD pattern. The lattice parameters reported by Brown *et al*. from their neutron diffraction studies [32] are in reasonable agreement with our results obtained using Rietveld analysis using this model. To solve the low temperature structure of Ni-Mn-Ga alloy, Wedel et al [45] used *I4/mmm* space group but with the Wyckoff position assigned as Ga at 2a(0,0,0), Mn at 2b(0, 0 , 0.5) and Ni at 4d(0. 0.5, 0.25). Attempts were made to fit the data using this model. Most of the peaks could be fitted well by considering the lattice parameter to be $a = b = 3.88$ Å and $c = 6.28$ Å. However, no Bragg peaks were observed below $2\theta = 40°$ in the experimental data, while two major peaks appeared at $2\theta = 28°$ and 32.5° in the generated pattern. Thus Wyckoff position mentioned above (i.e.2a, 2b and 4d) could not be assigned in case of Co-Ni-Ga system. Conversion to $L1_0$ unit cell using the relations given by Pons et.al [46] yielded lattice parameters $a = b = 5.49$ Å and $c = 6.28$ Å. This lattice parameters did not match with the results obtained by Brown et.al [32] or Chernenko et.al. [55]. Hence this model was not considered as appropriate for the fitting procedure. So, it is assumed that all Co, Ni and Ga atoms arbitrarily occupied the 2a(0,0,0,) position in the case of the bct unit cell. Khovailo et.al [24] has reported that at cooling from liquid phase Ni-Mn-Ga alloy solidify in disordered *A2* phase characterized by an arbitrary occupation of every site in the

crystal lattice. Thus an arbitrary occupation of crystal site may be possible for Co-Ni-Ga alloys quenching from 1150 °C.

3.2. THERMAL PROPERTIES

DSC curves corresponding to various compositions of $Co_xNi_{25}Ga_{75-x}$ alloys are shown in Fig.3.2.1. Each DSC run consisting of a heating and cooling cycle shows an endothermic and an exothermic peak corresponding to and A→M transformations, respectively. The M↔A transformation temperatures varied as a function of alloy composition (*cf* Table 3.2).

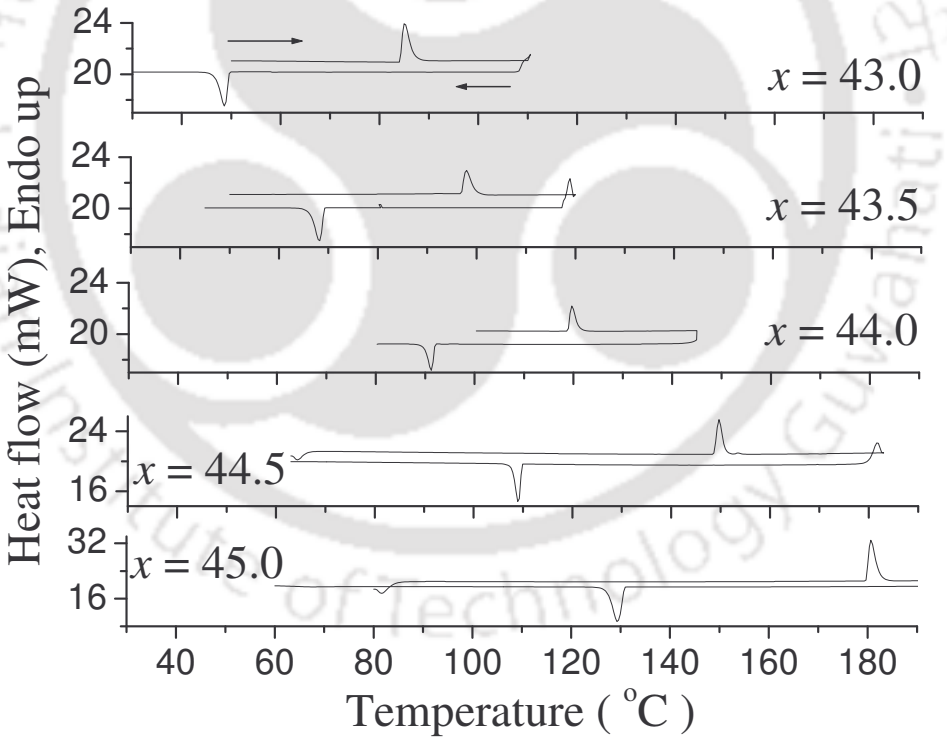

Fig. 3.2.1: DSC curves of $Co_xNi_{25}Ga_{75-x}$ ($43 \leq x \leq 45$) alloys

Table 3.2: DSC data (M_s, M_f, A_s, A_f, T_0 etc.) of $Co_xNi_{25}Ga_{75-x}$ ($43 \leq x \leq 45$) alloys

Co at % (x) ⟶	43.0	43.5	44.0	44.5	45.0
e/a	7.33	7.36	7.39	7.42	7.45
A_s [°C]	84	97	119	149	179
A_f [°C]	89	101	123	153	184
M_s [°C]	49	69	92	110	131
M_f [°C]	45	64	88	106	125
$T_0 = (A_f + M_s)/2$ [°C]	69	85	107.5	131.5	157.5
ΔH (J/g)	1.59	2.13	2.90	4.73	6.93
ΔS (mJ/g °C)	23	25	27	36	44
Hysteresis (A_f - M_s)	40	32	31	43	53

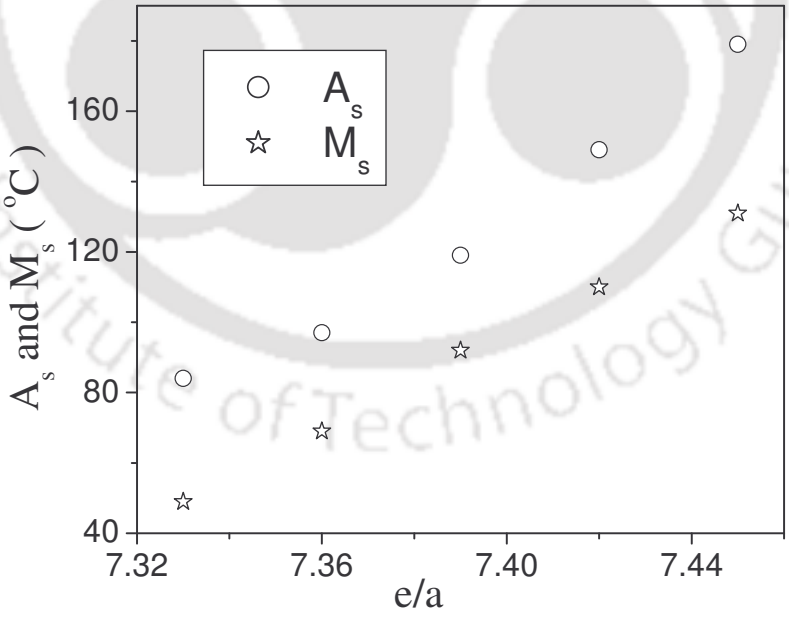

Fig. 3.2.2: Variation of A_s and M_s of $Co_xNi_{25}Ga_{75-x}$ ($43 \leq x \leq 45$) alloys with e/a ratio

It was observed that both M_s and A_s increased with an increase in e/a value (Fig.3.2.2). The e/a value is the ratio of total number of valence electrons in s+d orbitals and total number of atoms present in the system. The details of the e/a calculations have been discussed in Section 1.2.3 p.26 of this thesis. The calculated value of e/a for all the Co-Ni-Ga alloys are listed in Table 3.2

Change of entropy during the structural phase transition (ΔS) is a thermodynamic parameter which gives useful insight on the nature of the phase transition. It can be estimated using the relation

$$\Delta S = \Delta H/T_0 \qquad (3.2.1)$$

and $$T_0 = (A_f + M_s)/2 \qquad (3.2.2)$$

where ΔH is the average enthalpy change during M→A and A → M transformations [64], and T_0 is the equilibrium temperature at which the Gibbs' free energy of the martensite and the austenite phases are the same. The values of ΔS calculated for these alloys are listed in the Table 3.2. ΔS increases as the Co 45 at % in t the alloys is increased. The total change of entropy can be expressed for martensitic transition as

$$\Delta S = \Delta S_{vib} + \Delta S_{el} + \Delta S_{mag} \qquad (3.2.3)$$

It has been generally observed [64, 121] that the vibrational (ΔS_{vib}) and electronic (ΔS_{el}) contributions to the total entropy change ΔS do not vary much significantly when the composition of the alloys is varied. So, the increase in ΔS is generally attributed to the increase in the magnetic contribution (ΔS_{mag}). Hence it can be inferred that, the magnetic anisotropy increases in this alloy series as the Co at% is increased.

3.3. MASS DENSITY MEASUREMENT

The results of mass density measurement made on $Co_xNi_{25}Ga_{70-x}$ ($43 \leq x \leq 45$) alloys are given in Table 3.3. Density was also theoretically calculated by considering the individual contributions of mass density to the formula unit using the following empirical relation:

$$\rho_c = \{ x * \rho(Co) + 25 * \rho(Ni) + (75 - x) * \rho(Ga) \} / 100 \qquad (3.3)$$

where, ρ(Co), ρ(Ni) and ρ(Ga) are mass density of Co, Ni and Ga respectively

The calculated values are presented in Table 3.3 for the sake of comparison. The results obtained from individual calculation of density using the empirical relation are slightly lower than the experimental result. However, the closeness of the theoretical values with the experimental values suggests that the empirical rule provides reasonably good estimates of the density of the alloys as a function of composition.

Table 3.3: Mass Density (ρ_A) of $Co_xNi_{25}Ga_{75-x}$ ($43 \leq x \leq 45$) alloys

Co at.% (x)	Measured density ρ_A (g/cm^3)	Calculated density ρ_c(g/cm^3)
43	8.062 ± 0.004	7.944
43.5	8.160 ± 0.004	7.959
44	8.386 ± 0.004	7.974
44.5	8.463 ± 0.004	7.989
45	8.616 ± 0.004	8.004

Here ρ_A was measured by using Archimedes principle and ρ_c was calculated from the individual contribution of the constituent elements of the alloys. It is seen that density

increases with the increase in Co at % and decease of Ga at%. This is due to the lower mass density of the Ga as compared to Co.

3.4. MAGNETIC PROPERTIES

3.4.1. Temperature dependent AC susceptibility (ACS):

ACS data of $Co_xNi_{25}Ga_{75-x}$ ($43 \leq x \leq 45$) alloys obtained as a function of temperature are depicted in Fig. 3.4.1. The abrupt drop in the value of the real part of the susceptibility observed in the case of all the plots is the signature of the ferromagnetic to paramagnetic phase transition. The ACS data was used to find the Curie temperature of the as prepared samples at the initial stage of the alloy processing. T_C values have been measured from the local minimum point of the derivative of ac susceptibility versus temperature graph and are listed in the table 3.4.1 It is seen that T_C values increase with the increase of Co at % (x). It is expected as Co has the highest magnetic moment among the constituent element of this alloy series. The T_C value obtained by this method has been verified with the results obtained from magnetization measurement using vibration sample magnetometer.

Table 3.4.1: Currie temperature of $Co_xNi_{25}Ga_{75-x}$ ($43 \leq x \leq 45$) alloys

x	43	43.5	44	44.5	45
T_C [^oC]	-2	39	77	107	119

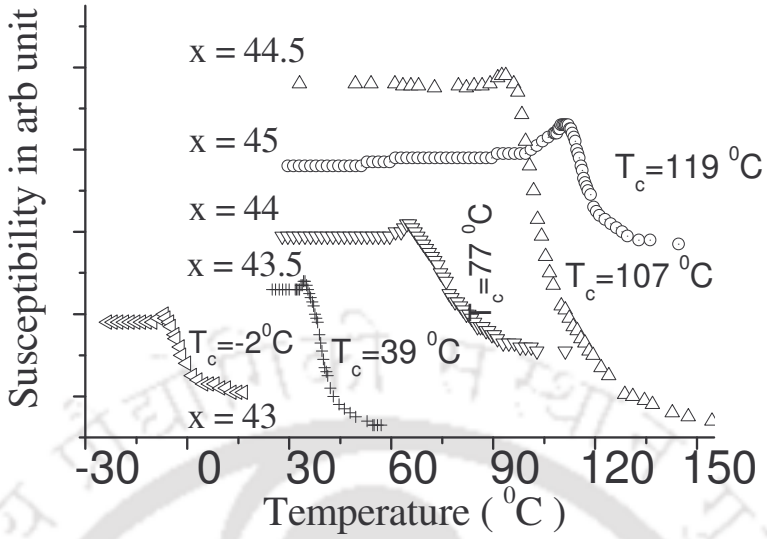

Fig.3.4.1: ac susceptibility of $Co_xNi_{25}Ga_{75-x}$ ($43 \leq x \leq 45$) alloys

3.4.2. Magnetization measurement as a function of temperature using VSM

Magnetization (M) of $Co_xNi_{25}Ga_{75-x}$ ($43.5 \leq x \leq 45$) alloys was measured at very low field (50 Oe) as a function of temperature using VSM. The M-T data are shown in Fig. 3.4.2. The alloy with the highest Co at % (x = 45) has the highest magnetization at 50 Oe field. The alloy with 43 at% Co exhibited very low magnetization typical of paramagnetic materials at room temperature. Referring to the ACS data presented in Table 3.4.1, it can confirmed that the T_C of this alloy is -2 ˚C. T_C value corresponding to each alloy composition was determined from the local minimum point of the derivative graph. T_C value obtained for various alloy compositions are listed in Table 3.4.2. It has been observed that magnetic moment and Curie temperature (T_C) of the magnetic materials linearly vary with the magnetic valence number *(Z_m)* [74]. A similar trend has been observed in this alloy system

also. The Z_m values calculated for $Co_xNi_{25}Ga_{75-x}$ $(43 \leq x \leq 45)$ alloys are listed in Table *3.4.2.* The details of the calculation of Z_m have been already discussed in section *1.2.5.*

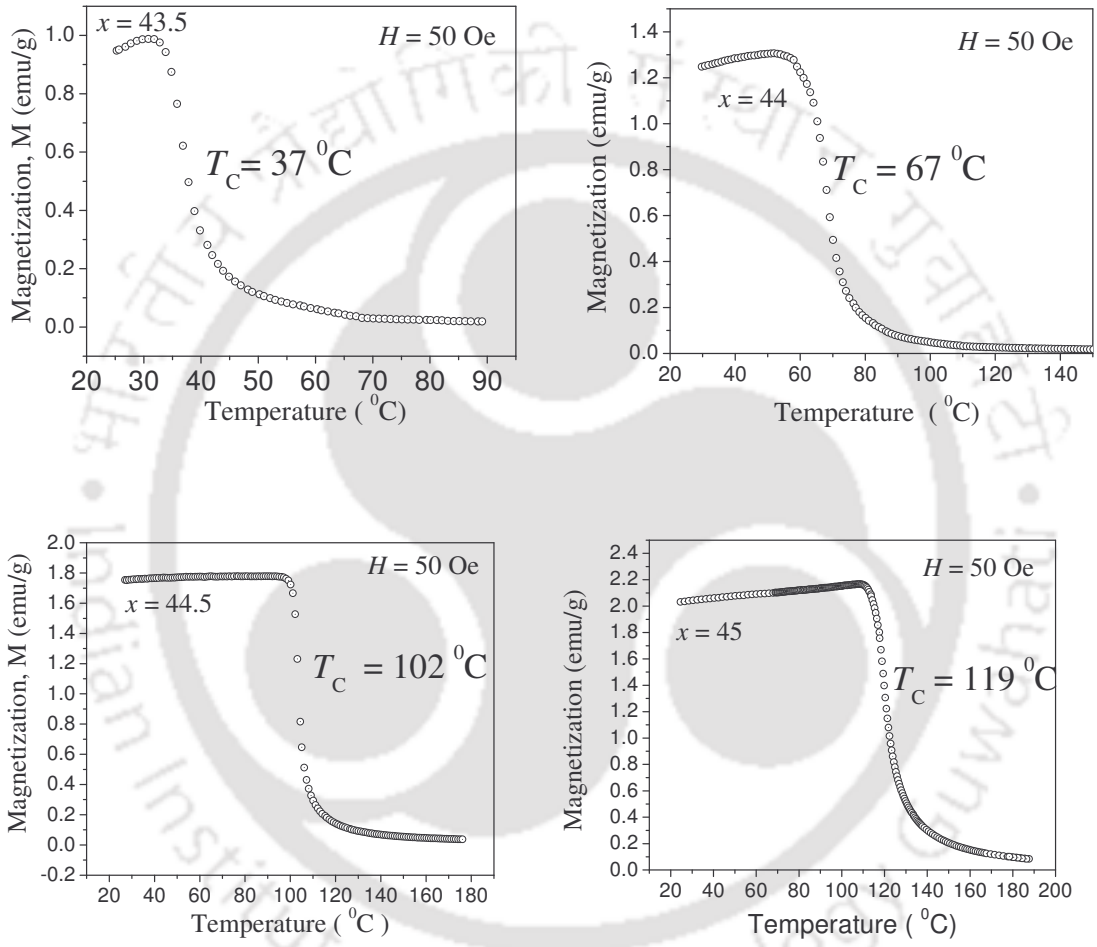

Fig. 3.4.2: Variation of magnetization of $Co_xNi_{25}Ga_{75-x}$ $(43 \leq x \leq 45)$ alloys with respect to temperature at constant field .

Table 3.4.2: Curie temperature (T_C) and magnetic valence number (Z_m) of $Co_xNi_{25}Ga_{75-x}$ ($43 \leq x \leq 45$) alloys

Composition of the alloy (x)	T_C (°C)	Z_m
$x = 43.5$	37	-0.51
$x = 44.0$	67	-0.49
$x = 44.5$	102	-0.47
$x = 45.0$	119	-0.45

The T_C values obtained from ACS measurement are close to the magnetization measurement by using VSM. The small differences in the T_C values obtained from the two measurements have been observed are due to the nature of the two measurements, and differences in the sensor type and temperature control employed in the two set-ups. While the ACS data was collected continuously using a small temperature ramp in the indigenous instrument, data was recorded at discrete temperature intervals and controlled by a PID temperature controller in the commercial VSM. So, the ACS measurements were rapid, whereas the VSM measurements were relatively slower. However, the latter yielded data with traceable accuracies when compared to the former. All the data presented in the table have been recorded during the heating cycle. Since the reverse martensitic transformation temperature (A_s) for all the alloys in this series are higher than its T_C value, no signature of the martensitic ttransofrmation has been observed in the data presented in Fig. 3.4.2.

3.4.3. Magnetization as a function of applied field at constant temperature using VSM

Magnetization measurement was carried out on $Co_xNi_{25}Ga_{75-x}$ ($43 \leq x \leq 45$) alloys at 25 °C at different applied field values. The M-H plots are depicted in Fig. 3.4.3a. The alloys with x =

44, 44.5 and 45 exhibit almost the same magnetic moment at an applied field of 20 kOe, but alloys with $x = 43.5$ and 43 exhibit lower magnetic moment at this field. It can also observed from the graphs that alloys x = 43, 43.5 and 44, attain saturation faster than the other two alloys. This gives the inference that the magneto crystalline anisotropy of the alloys increases with increasing Co at. %.

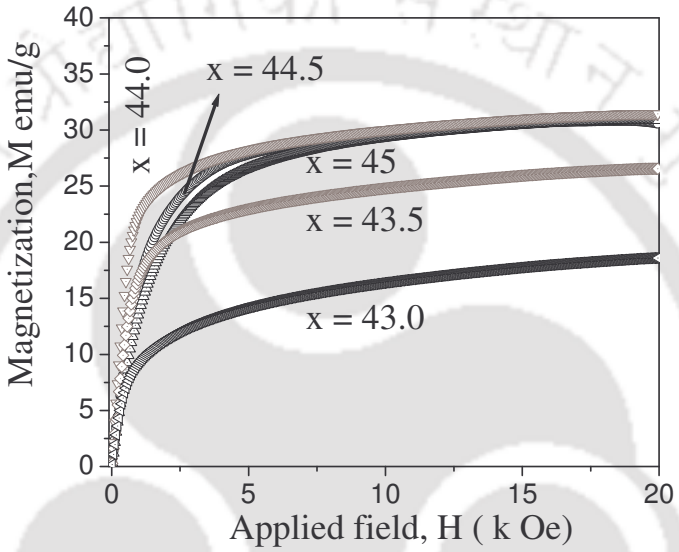

Fig. 3.4.3a: Variation of magnetization of $Co_xNi_{25}Ga_{75-x}$ ($43 \leq x \leq 45$) alloys with applied field.

The effective magnetic anisotropy constant K_{eff} of the alloys can be calculated by fitting the magnetization curves using the equation 3.4.3a

$$M = M_{sat}\left(1 - \frac{b}{H^2}\right) \qquad (3.4.3a)$$

The co-efficient b is related to the magnetocrystalline anisotropy by the equation.

$$K_{eff} = \sqrt{\frac{15b}{4}}\,\mu_0 M_{satt} \quad [Ref.109] \qquad (3.4.3b)$$

It can be observed from Fig. 3.4.3a that the applied field of 20 kOe is not sufficient to saturate the magnetic moment of the alloys with x = 44, 43.5 and 43. Careful observation of the data between 9 kOe and 18 kOe would reveal that apart from ferromagnetic contribution some paramagnetic contributions are also present in these alloys. The saturation magnetization was estimated from M-H curve after subtracting the paramagnetic component from the curve. This was done by fitting the following equations separately to the observed M-H data in the high field region.

$$M = M_{sat} + \chi_p H \qquad (3.4.3c)$$

$$M = M_{sat}\left(1 - \frac{a}{\sqrt{H}}\right) + \chi_p H \qquad (3.4.3d)$$

$$M = M_{sat}\left(1 - \frac{b}{H^2}\right) + \chi_p H \qquad (3.4.3e)$$

Each fit yielded very close values of the high field susceptibility, χ_p from which a good estimate of the same was obtained. Paramagnetic contributions were eliminated from the experimental M-H curve by the subtracting linear ($\chi_p H$) contribution from it. The subtracted data was then fitted to equation 3.4.3a. to obtain the best values of M_{sat}, a and b value. Fig. 3.4.3b shows the experimental (unsubtracted) M-H data (represented by darkened triangles), M-H data with the paramagnetic component subtracted (open circles) and the least squares fit of the high field data to eqn. 3.4.3d (solid line) corresponding to each alloy. The gradual decrease in the paramagnetic component in the M-H data as a function of Co at % is evident from Fig. 3.4.3(iii). The parameters obtained from the least squares fitting procedure are listed in Table 3.4.3.

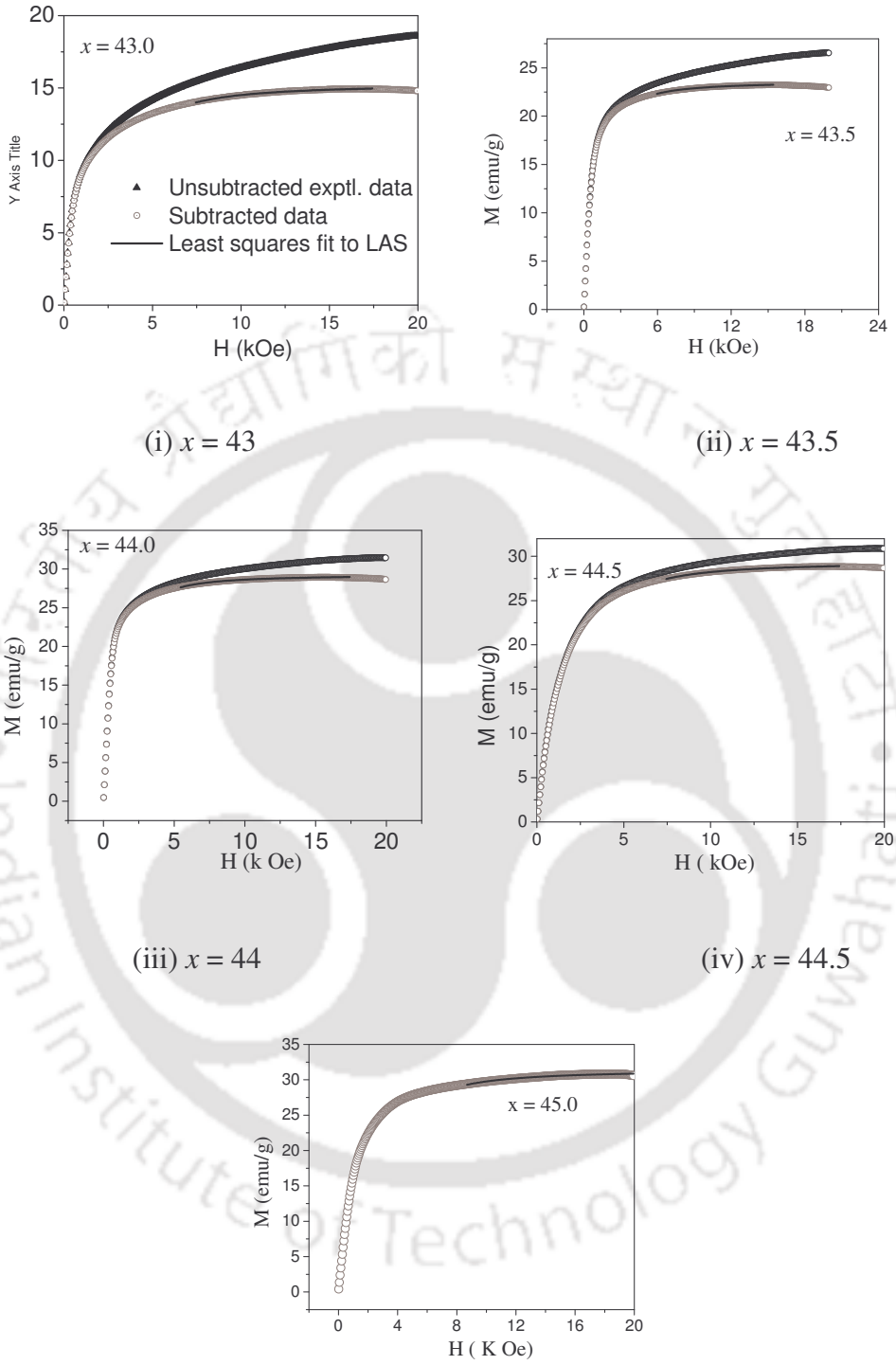

Fig. 3.4.3b:. M-H graph of $Co_xNi_{25}Ga_{75-x}$ alloys fitted to the equation of law of approach to saturation. The black dark lines are the fit line to the observed data

The value of b was converted from Oe to A/m to get K_{eff} value in terms of J/m^3. Likewise, M_{sat} value was also converted to volume magnetization (A/m) by multiplying corresponding mass density of the alloy. Taking $\mu_0 = 4\pi \times 10^{-7}$ N/A^2 (or $J/m\ A^2$) , he value of K_{eff} was obtained. The Estimated K_{eff} values corresponding to the different alloys are listed in Table 3.4.3. K_{eff} increases in these alloys as the Co at.% is increased. This indicates that the magneto crystalline anisotropy increases in this series of Co-Ni-Ga alloys as the Co at. % is increased.

Table: 3.4.3: M_{sat} and K_{eff} of $Co_xNi_{25}Ga_{75-x}$ ($43 \le x \le 45$).

Co at% in alloy (x)	Volume M_{sat} (Am^2/kg)	Density (kg/m^3)	$M_{sat} \times 10^5$ (A/m)	$b \times 10^6$ $(Oe)^2$	$\chi_p \times 10^{-6}$ (m^3/kg)	$K_{eff} \times 10^5$ (J/m^3)
43.0	15.52 ± 0.04	8062 ± 10	1.251	3.39 ± 0.10	2.38	0.45
43.5	23.84 ± 0.03	8160 ± 10	1.945	2.0 ± 0.07	2.01	0.53
44.0	29.69 ± 0.03	8386 ± 10	2.490	1.84 ± 0.07	1.51	0.65
44.5	29.37 ± 0.04	8463 ± 10	2.486	3.13 ± 0.07	1.23	0.85
45.0	30.96 ± 0.15	8616 ± 10	2.626	4.82 ± 0.07	0.25	1.24

Saturation magnetization (M_{sat}) obtained by J. Liu et.al [39] for almost similar composition of the alloys {$Co_x(Ni_{25}Ga_{30})$; x = 43.5, 44,44.5,45}are in reasonable agreement with the values obtained in this study. Chernenko et.al [42] observed a higher saturation magnetization (≅ 40 emu/g) at room temperature and comparatively smaller field of 10 kOe in single crystals of $Co_{49}Ni_{22}Ga_{29}$. The higher M_{sat} observed could be attributed to the single crystal nature of the sample and the higher at % of Co present at the alloy. A similar value (≅ 40 emu/g) has been reported by M. Zhang et.al [54] at room temperature at an applied field

of 50 kOe applied field in melt-spun ribbons of $Co_{50}Ni_{20}Ga_{30}$. Room temperature M_{sat} and K_{eff} of 52.1 A-m^2/kg and 1.01 $\times 10^5$ J/m^3, respectively has been reported [122] in polycrystalline $Ni_{50}Mn_{30}Ga_{20}$ ($\mu_0 H$ = 20 mT) at applied field of 20 kOe. Appreciable increase in M_{sat} and K_{eff} has been reported near the stoichiometric composition in [122]. Though M_{sat} of these alloys is much lower than that of Ni-Mn-Ga alloy, K_{eff} of these alloys is comparable to that of Ni-Mn-Ga alloys. The K_{eff} of polycrystalline $Ni_{49}Fe_{18}Ga_{27}Co_6$ alloy has been reported as 1.2×10^6 erg/cm^3 (M_{sat} = 40 emu/g) at 300 K [94]. For inducing magnetic field induced strain (MFIS), a large magnetocrystalline anisotropy energy is required to move the twin boundary [14,23]. Higher values of M_{sat} and K_{eff} value are expected with the increase of Co at % in Co-Ni-Ga alloys.

3.5. SUMMARY:

To realize the shape memory effect it is initially necessary to determine the correct alloy composition. The most promising means by which a substantial shape and dimensional change can be achieved in an FSMA is through the application of a magnetic field. In the case of FSMA in which martensitic and magnetic transformations occur closely, application of magnetic field can induce large MFIS. Thus, it is necessary to determine the main physical parameters of these alloys.

XRD and SEM studies revealed that single phase martensite phase exists in $Co_xNi_{25}Ga_{75-x}$ alloys when $x < 45$. The martensitic phase has been structurally identified as bct or $L1_0$ and the austenite phase as $A2$ by Rietveld analysis. It has been observed that in the case of $Co_xNi_{25}Ga_{75-x}$ alloys, the MT temperatures are higher than room temperature, but the Curie temperature (T_C) of all the alloys are below MT. All but one of the alloys have

ferromagnetic martensite structure at and above room temperature. It has been found that both *MT* and T_C decrease with the reduction of Co at%. Thus there is no chance to prepare alloy with close *MT* and T_C values by adjusting the alloy composition in this series. The magnetic anisotropy constant has been estimated for the alloys. The saturation magnetization (H = 20 kOe) observed at room temperature for these alloys are almost 1.5 times lower than the prototype Ni-Mn-Ga alloys [122] but K_{eff} of the alloy with x = 45 is comparable to the reported value of other alloys. It has been observed that magnetization increases with the increase of Co at %. Thus, by maintaining Ga at % constant, Co and Ni content can be adjusted to achieve higher saturation magnetization. Oikawa et al. observed [19] that T_C and *MT* temperature variation exhibit opposite trends when Ni at% is varied for constant Ga at%. Considering the Oikawa et al.'s results as a guideline, new series of alloys exhibiting higher saturation magnetization and magneto crystalline anisotropy can be prepared.

INVESTIGATION ON $Co_{70-x}Ni_xGa_{30}$ ($20 \leq x \leq 25$) ALLOYS

In this chapter, investigations performed on a series of Co-Ni-Ga alloys with compositions $Co_{70-x}Ni_xGa_{30}$ ($20 \leq x \leq 25$) are presented. In this series, Ga content is held constant and the concentration of the two transition metals in the alloys is varied.

4.1. PREPARATION AND PROCESSING OF THE ALLOYS

The alloy ingot of each composition was prepared by arc melting method, following the procedures already outlined in chapter 2. Quenching medium and annealing temperature are two crucial factors that influence the properties of the FSMAs. In order to comprehensively understand the influences of these factors on Co-Ni-Ga FSMAs, these alloys were processed in different ways. Alloys discussed here are mainly ingots annealed at 1150 °C and quenched in ice water. However, in order to investigate the effect of annealing temperature on the properties of $Co_{70-x}Ni_xGa_{30}$ alloys, ingots of one alloy composition were annealed individually at different temperatures such as 1230 °C, 1150 °C, 1000 °C and 900 °C and subsequently quenched in ice water. Moreover, for understanding the influence of quenching rate on this series of Co-Ni-Ga alloys, ingots of one alloy compositions were annealed at 1150 °C and individually quenched in liquid nitrogen, ice water or air. Alloys annealed at 1150 °C were brittle. In order to prepare alloys of large sizes suitable for mechanical property measurements, ingots of all the alloy compositions were cast in a cylindrical shape, annealed at 1000 °C and quenched in ice water.

The composition of the master alloys was determined by SEM-EDS analysis. A typical EDS spectrum is displayed in Fig. 4.1a. Table 4.1 lists the nominal starting and final (after annealing and quenching stages) alloy compositions. It can be seen that the measured composition values are very close to the starting composition. The martensitic microstructure observed in these alloys is also shown with the corresponding SEM micrograph in Fig.4.1b.

Table 4.1: Composition of $Co_{70-x}Ni_xGa_{30}$ obtained from EDS observations.

Starting alloy composition			Composition of the final processed alloys		
Co at%	Ni at%	Ga at%	Co at%	Ni at%	Ga at%
50	20	30	50.41	19.87	29.72
49	21	30	49.49	20.73	29.78
48	22	30	48.18	21.67	30.15
47	23	30	46.80	22.92	30.28
46	24	30	46.03	24.13	29.84
45	25	30	44.67	24.79	30.54

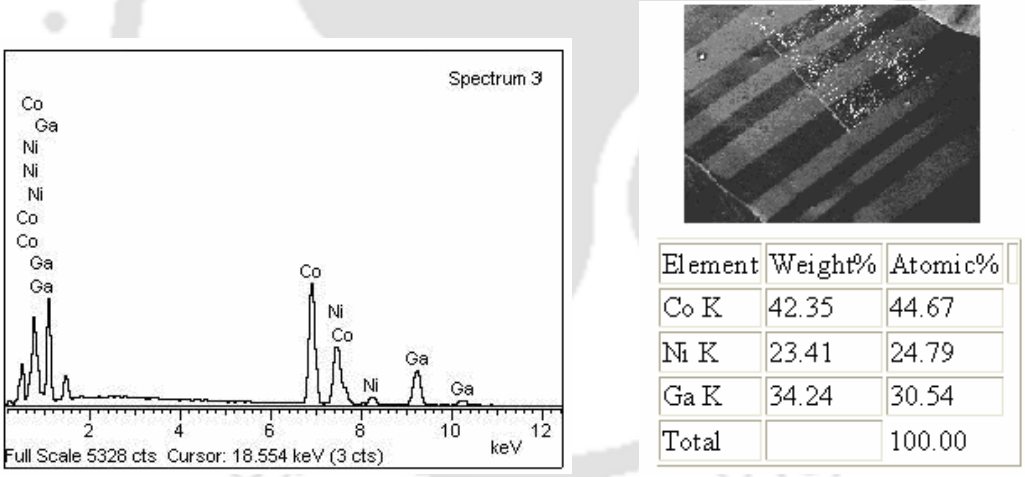

(a) (b)

Fig. 4.1. (a): EDS spectrum of $Co_{45}Ni_{25}Ga_{30}$ is shown as a typical example, (b): SEM micrograph of the martensite twins in the alloy and the corresponding SEM-EDS data.

4.2. CRYSTAL STRUCTURE AND MICROSTRUCTURE

4.2.1. Structure of alloys quenched from 1150 ˚C

X-ray diffraction (XRD) patterns of $Co_{70-x}Ni_xGa_{30}$ ($20 \leq x \leq 25$) alloys are shown in the Fig. 4.2.1a. The XRD patterns of alloys with $x = 20$ and the rest (with $x \geq 21$) exhibit different features. Alloys with $x \geq 21$ seem to exhibit a single phase structure. Microstructural analyses of these alloys support this observation. The twin microstructure observed in the optical micrograph is a typical signature of the martensite phase (Fig.4.2.1b). For alloys with $x < 21$, the intensity of the XRD peaks corresponding to the martensite phase was found to be weak and the presence of additional peaks was also observed. The optical micrograph of the alloy with x=20 reveal only weak features of the austenite phase, clearly showing that the major phase is austenite in this alloy. Unlike the alloys investigated in the previous chapter, γ-phase was observed only in the optical micrograph of the alloy with $x = 20$. The big black spots observed in some optical micrographs are porosities, which are common in cast alloys.

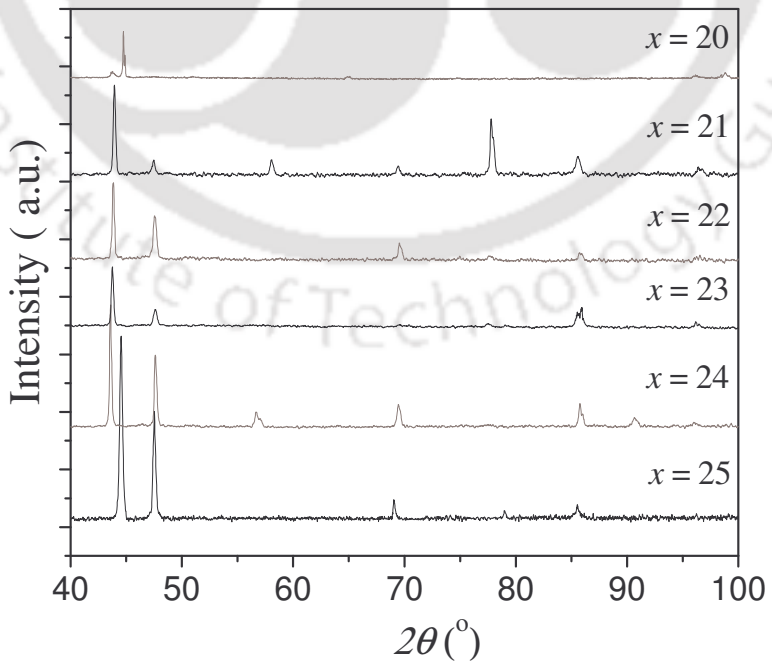

Fig. 4.2.1a: XRD patterns of $Co_{70-x}Ni_xGa_{30}$ ($20 \leq x \leq 25$) alloys.

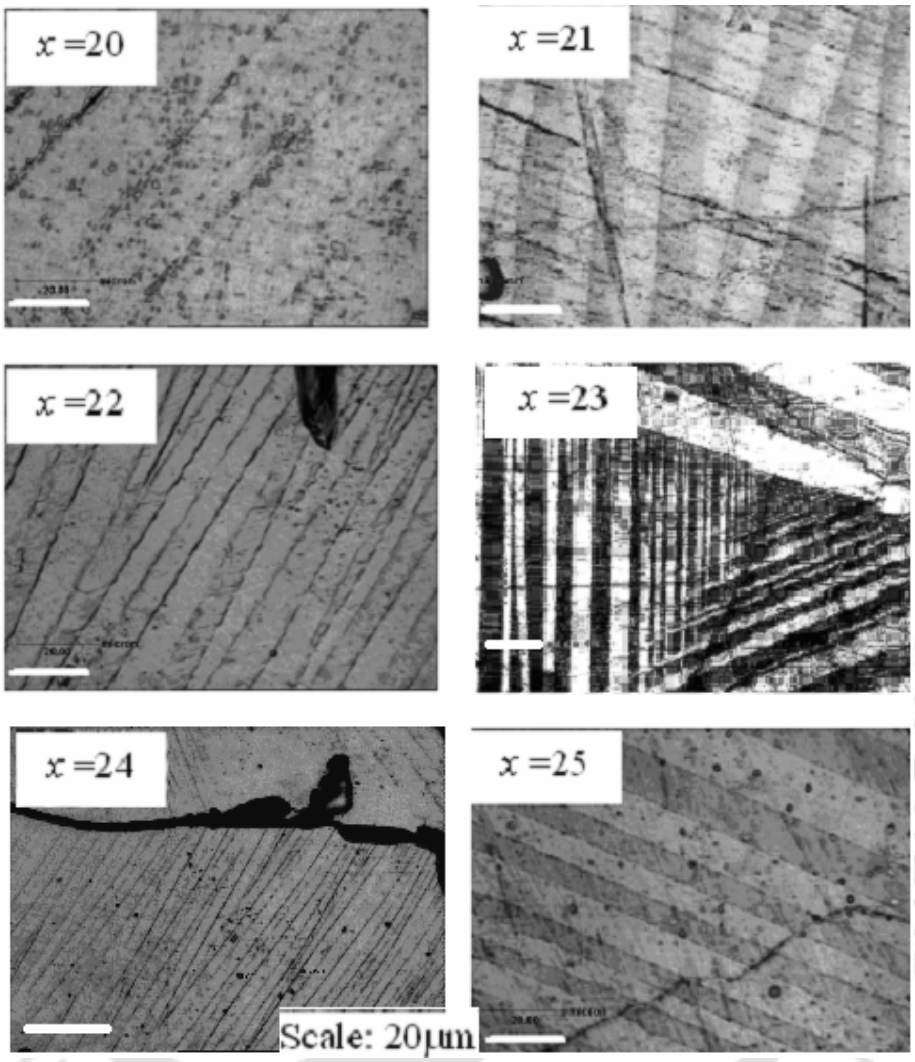

Fig. 4.2.1b: Optical micrograph of $Co_{70-x}Ni_xGa_{30}$ ($20 \leq x \leq 25$) alloys annealed at 1150 °C.

To determine the crystal structure of the alloys, the Rietveld refinement technique was employed. Both *I4/mmm* (bct) and *P4/mmm* (fct) models were used to refine the crystallographic parameters. Typical least squares fit to the data of alloy with x = 24 for both the model are shown as in the Fig.4.2.1c and Fig.4.2.1d, respectively. The XRD pattern of alloy with x = 20 exhibits a three phase structure (Fig.4.2.1e). The phases have been identified as bct martensite (β') phase, *A2* austenite (β)-phase and fcc γ-phase. The lattice parameters and atom positions in the unit cell for both the models are listed in Table 4.2.1.

Table 4.2.1: Crystallographic data of $Co_{70-x}Ni_xGa_{30}$ ($20 \le x \le 25$) alloys annealed at 1150 ˚C.

Space Group	*P4/mmm*							*I4/mmm*						
Wyckoff Position →	Ga: 1a (0.0, 0.0, 0.0) Ni: 1c (0.5, 0.5, 0.0) Co: 2e (0.0, 0.5, 0.5)							Ga: 2a (0, 0, 0) Ni: 2a (0, 0, 0) Co: 2a (0, 0, 0)						
Ni at. % (*x*) ↓	*a* (Å)	*c* (Å)	*c/a*	*V* (Å)^3	χ^2	R_{wp}	R_B	*a* (Å)	*c* (Å)	c/a	V (Å)^3	χ^2	R_{wp}	R_B
25	3.816	3.254	0.853	47.384	1.8	17	21	2.698	3.254	1.206	23.687	2.4	9	14
24	3.819	3.245	0.850	47.328	0.8	10	15	2.701	3.245	1.201	23.674	2.0	16	16
23	3.829	3.225	0.842	47.300	3.5	18	25	2.708	3.225	1.191	23.649	4.8	8	13
22	3.827	3.224	0.842	47.215	4.2	20	22	2.706	3.224	1.191	23.608	5.2	10	15
21	3.837	3.205	0.835	47.180	3.0	18	21	2.713	3.205	1.181	23.590	4.0	7	14

x = 20	*a* (Å)	*c* (Å)	*c/a*	*V* (Å)^3	χ^2	R_{wp}	R_{Bragg}
Martensite phase (β′) *Space group: I4/mmm*	2.713	3.213	1.184	23.649	1.92	20	23
Austenite phase (β) *Space group:* $Im\bar{3}m$	2.887	2.887	1.000	24.062		18	11
γ- phase *Space group:* $Fm\bar{3}m$	3.605	3.605	1.000	46.850		17	18

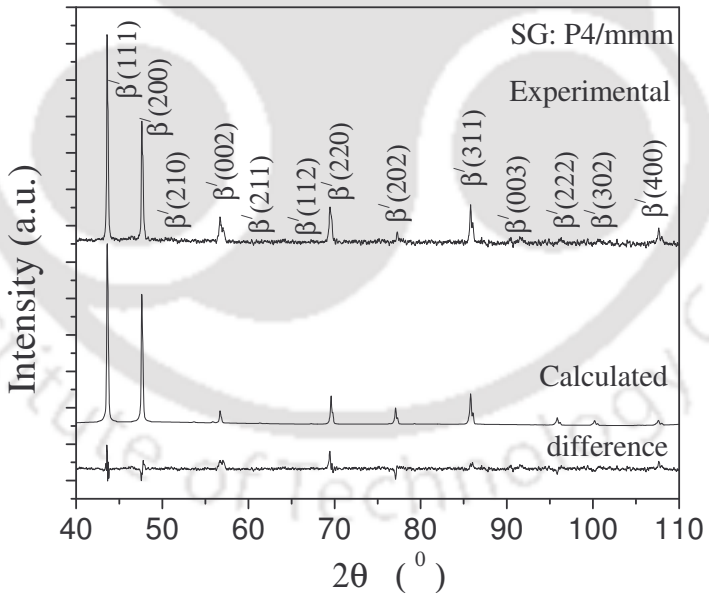

Fig. 4.2.1c: Rietveld fit to XRD pattern of $Co_{46}Ni_{24}Ga_{30}$ alloy annealed at 1150 °C showing the fit to *P4/mmm* space group.

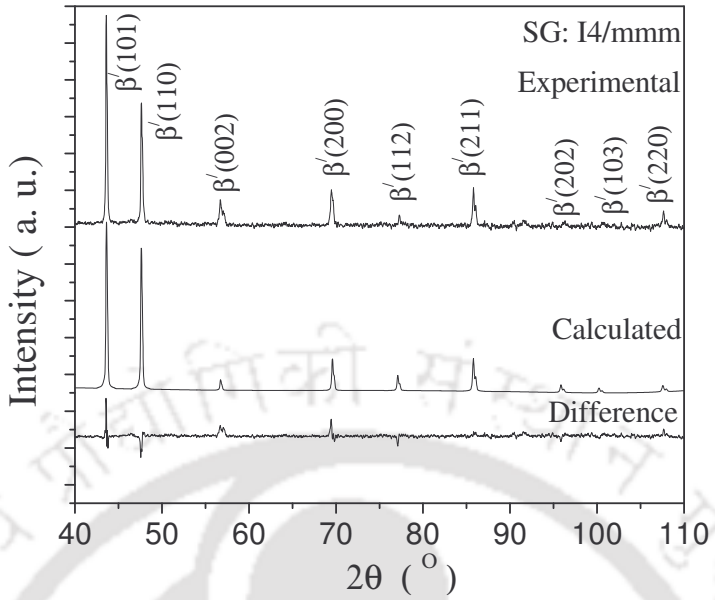

Fig. 4.2.1d: Rietveld fit to XRD patterns of $Co_{46}Ni_{24}Ga_{30}$ alloy annealed at 1150 °C showing the fit to *I4/mmm* space group.

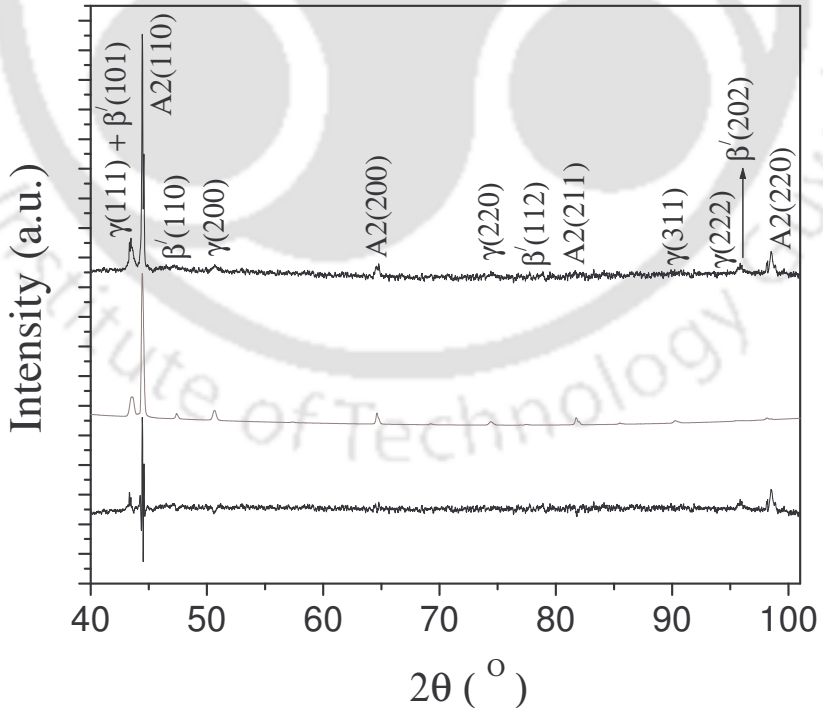

Fig.4.2.1e: Rietveld fits to XRD patterns of $Co_{50}Ni_{20}Ga_{30}$ alloy annealed at 1150 °C.

It can be seen from the data presented in Table 4.2.1 that the unit cell volume does not change appreciably with the change of Ni and Co at%. Since the atomic radius of Co and Ni are comparable, no appreciable change in unit cell volume is expected when these two atoms replace each other. A small change of *c/a* ratio has been observed with the decrease in *e/a* ratio. But the *e/a* ratio changes with the change of Ni and Co at %. The lattice parameters reported by Brown *et al*. from their neutron diffraction studies [32] and by Chernenko *et al.* from TEM observations [55] are in reasonable agreement with our results. The percentage of martensite, austenite and γ-phases in $Co_{50}Ni_{20}Ga_{30}$ at room temperature alloy was found from the Rietveld analysis to be 17.56%, 43.36% and 39.08%, respectively. M. Zhang et al. [54] reported the crystal structure of the austenite phase in $Co_{50}Ni_{20}Ga_{30}$ ribbons as B2 and that of the low temperature structure as tetragonal. However, no space group was assigned by them for the two crystal structures. Lattice parameter for austenite structure has been reported as a = 5.80 Å and that for martensite as a = 6.05 Å and c = 5.79 Å. It seems that a double unit cell has been considered for indexing the XRD pattern. We could not fit our XRD data using these lattice parameters.

4.2.2. Effect of annealing temperature on the crystal structure

Co-Ni-Ga and Co-Ni-Ga FSMAs have certain advantages over the prototype Ni-Mn-Ga FSMA [19] Compositions of Co-Ni-Ga(Al) alloys can be selected in such a way that they are located near the two-phase (β + γ) region [19], which facilitates the introduction of appropriate amounts of the cubic γ-phase in the β-matrix by proper choice of alloy composition and heat treatment conditions. The hot workability and room temperature ductility of these alloys are significantly improved by the introduction of the γ-phase, which is a great advantage for practical applications [38]. These alloys melt near 1200 ˚C. Alloy samples quenched in ice water from 1230 °C were ductile and hence could not be powdered well by grinding with a pestle and mortar. The alloys when quenched in liquid nitrogen were less ductile which facilitated grinding of the alloy pieces with minimal effort. Hence, pieces of alloys were sealed

under vacuum in a fused silica tube, annealed at 1230 °C and quenched at liquid nitrogen. As-quenched pieces were carefully crushed into a coarse powder. Certain amount of strain is expected to be present in the powders due to the rapid cooling as well as grinding done on the quenched sample pieces. No further heat treatment was given to the alloy powders prior to the X-Ray diffraction (XRD) measurements. The reason for this is the lack of complete information on the ageing behaviour of this alloy system [34,123], and there is a possibility of inducing γ-phase precipitation during heat treatment. The XRD patterns of $Co_{70-x}Ni_xGa_{30}$ ($20 \leq x \leq 25$) alloys quenched from 1230 °C are shown in Fig.4.2.2a.

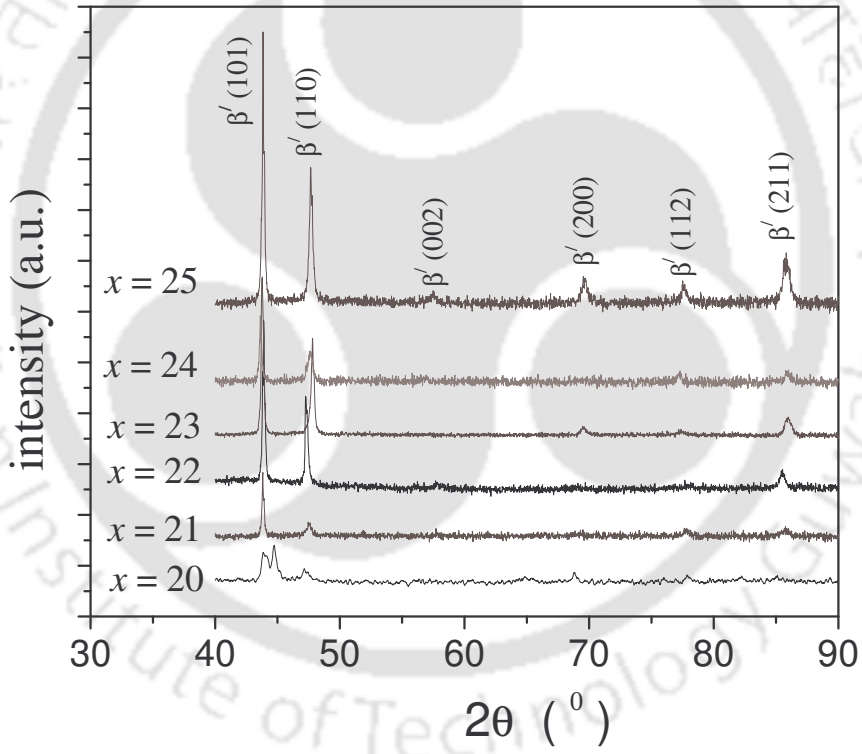

Fig.4.2.2a: XRD patterns of the $Co_{70-x}Ni_xGa_{30}$ alloys annealed at 1230 °C.

Table 4.2.2a: Structural data of bct unit cell and characteristic temperatures of $Co_{70-x}Ni_xGa_{30}$ alloys annealed at 1230°C.

x (Ni at.%) and lattice type	*a* (Å)	*c* (Å)	*V* (Å)^3	*c/a*
25 (tetragonal)	2.692	3.239	23.473	1.206
24 (tetragonal)	2.696	3.235	23.513	1.200
23 (tetragonal)	2.704	3.228	23.602	1.194
22 (tetragonal)	2.706	3.224	23.608	1.191
21 (tetragonal)	2.709	3.215	23.593	1.187
20 (cubic)	2.875	2.875	23.764	1.000
20 (tetragonal)	2.733	3.166	23.648	1.158

Lattice parameter corresponding to the fct unit cell ($L1_0$ –type structure) can be easily calculated by using the formula, $a_{L1_0} = \sqrt{2}a_{bct}$ and $c_{L1_0} = c_{bct}$ [46]. It is observed that the lattice parameters of the alloys quenched from 1150 °C and 1230 °C do not show appreciable differences. Only the FWHM (full width at half maximum) of the Bragg peaks of the alloys quenched from 1230 °C are more than those of the alloy quenched from 1150 °C. This is due to the smaller crystallite size of the alloy quenched from 1230 °C, the temperature at which the alloy is in molten state. However, alloys processed under both these quenching conditions were brittle. To make the alloys more ductile by introducing the γ-phase, the alloys were annealed at 1000 °C for six hours and quenched in ice water. XRD patterns of the alloys quenched from 1000 °C did not show any appreciable difference from the ones quenched from higher temperatures, except for the alloy with $x = 20$. Since the percentage of secondary (γ) phase developed during annealing at 1000 °C was very small, Bragg peaks due to the γ-phase were very weak. The intensity of the primary (martensite) phase peaks were also reduced due to the presence of the secondary phase. For the alloy with $x = 20$, a two phase structure ($A2 + \gamma$) was observed (Fig. 4.2.2a). It is to be noted that $\beta + A2$ phase structure was observed for this alloy ($x = 20$) when it was quenched from 1230 °C. A three-phase structure was observed for the same alloy when it was quenched from 1150 °C. Fig. 4.2.2b shows the XRD patterns of $Co_{50}Ni_{20}Ga_{30}$ alloy annealed from (i) 1230°C and (ii) 1000 °C.

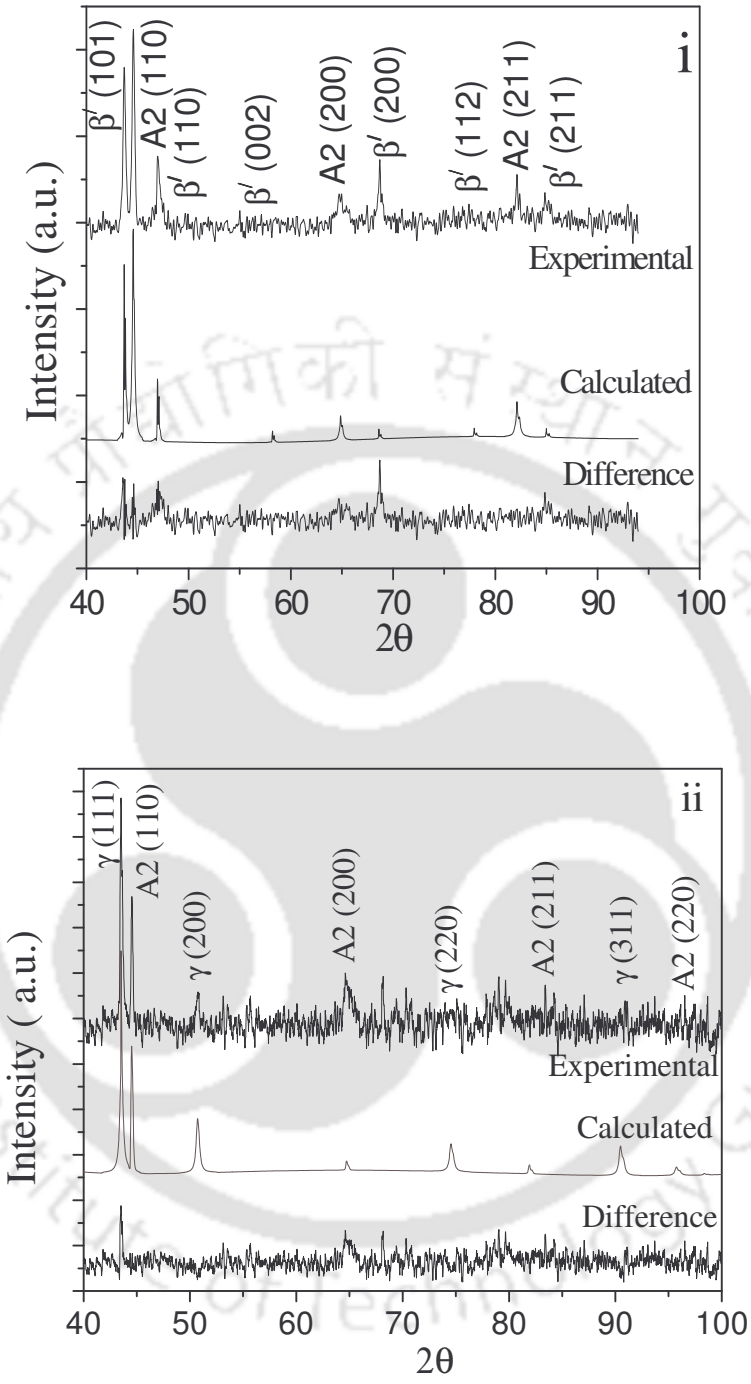

Fig.4.2.2b: XRD patterns of the $Co_{50}Ni_{20}Ga_{30}$ alloy annealed at (i) 1230°C and (ii) 1000 °C.

The evolution γ-phase due to the low temperature annealing has been observed clearly in the optical micrographs shown in (Fig.4.2.2c). The gray spots in the micrographs represent

the secondary phase developed due to the annealing at 1000 °C. The presence of secondary phase was verified with the help of compositional analysis using SEM-EDS measurement.

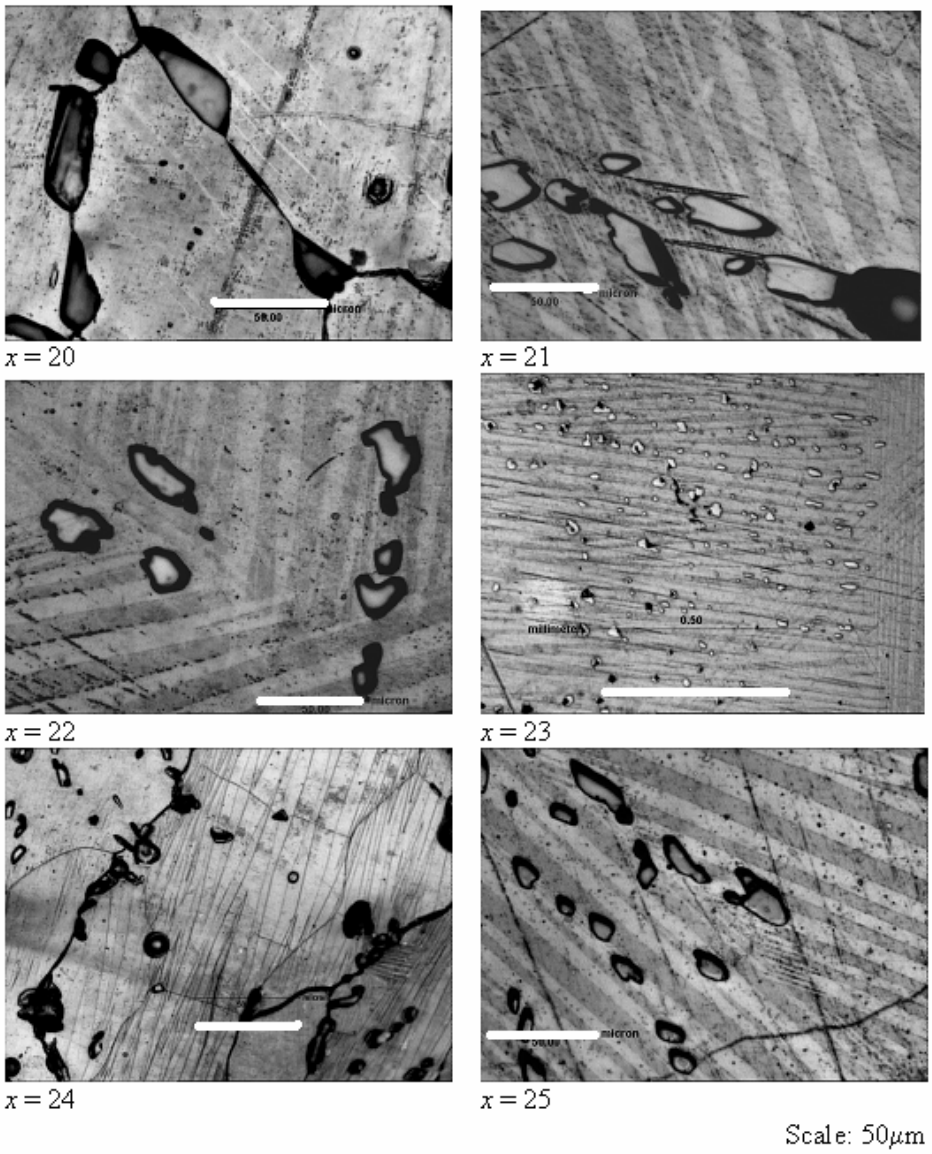

Fig. 4.2.2c: Optical micrographs of $Co_{70-x}Ni_xGa_{30}$ ($20 \leq x \leq 25$) alloys annealed at 1000 °C.

Batches of the pre-homogenized and ground powders of $Co_{47}Ni_{23}Ga_{30}$ alloy were separately annealed at 1230 °C, 1150 °C, 1000 °C and 900 °C for 6 hours each, and then quenched in ice water. No further heat treatment was performed on the quenched powders since the ageing characteristics of this alloy system are not well documented. The percentage

of γ phase present in the alloys annealed below 1150 ^{0}C was estimated from the optical micrographs using a commercial software package based on area scan method.

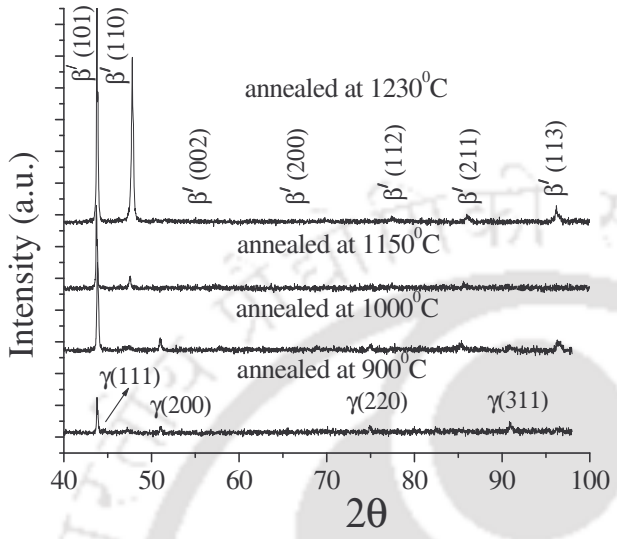

Fig. 4.2.2d: XRD patterns of $Co_{47}Ni_{23}Ga_{30}$ alloy annealed at different temperatures.

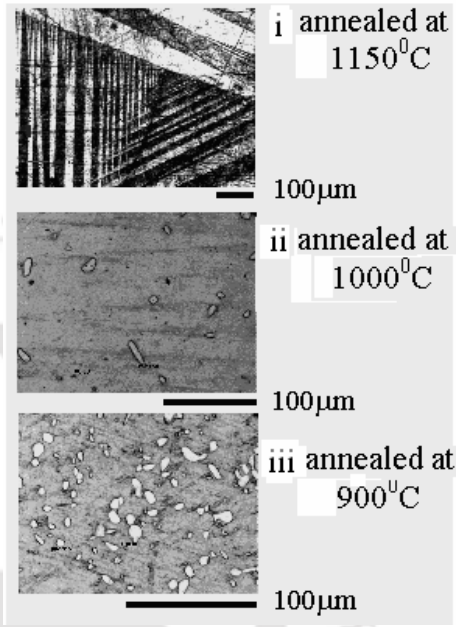

Fig.4.2.2e**:** Optical micrographs of the alloy annealed at various temperatures.

XRD patterns of the alloys annealed at 1150 °C and 1230 °C exhibited a single-phase martensite structure (bct β'-phase) at room temperature, whereas, presence of a face centered cubic γ-phase along with the martensite phase was observed in alloys annealed at 900 °C and 1000 °C (Fig.4.2.2d).

Rietveld refinement method was used to refine the lattice parameters of the two phases present in different samples. Lattice parameters of the martensite (β') phase were found to be $a = b = 2.71$ Å, $c = 3.23$ Å and the unit cell volume was 23.55 Å^3. Lattice parameters of the γ phase were found to be $a = 3.59$ Å and the unit cell volume was 46.27 Å^3. The unit cell parameters did not show much variation with change in annealing temperature as inferred from the unit cell volume change of 0.15 Å^3 between alloys annealed at 1230 °C and 900 °C. Liu *et al.* [40] claimed to have observed a change of 0.4 Å^3 in unit cell volume when the annealing temperature was changed from 1200 °C to 900 °C. Though the martensite structure

of Co-Ni-Ga alloys was reported by them [40] as tetragonal, it is evident that the lattice parameters, Miller indices of the peaks and the angular position of peaks in the reported XRD patterns did not fit in the indexing scheme of tetragonal crystal system. Hence, our observation on the unit cell volume change in alloys annealed at different temperatures is expected to be more reliable than the high value reported by Liu *et al*. The percentage of γ phase present in the alloy annealed at different temperatures was estimated from the least squares fit to the appropriate XRD data. The estimates obtained were 4.0% and 13.8% for the alloys annealed at 1000 °C and 900 °C, respectively.

Optical micrographs of polished $Co_{47}Ni_{23}Ga_{30}$ alloy samples annealed at 1150 °C, 1000 °C and 900 °C are shown in Fig. 4.2.2e(i - iii), respectively. The characteristic twinned structure of a single martensitic microstructure can be seen in the micrograph shown in Fig.4.2.2e.i. The white spots in Fig. 4.2.2e.ii and Fig. 4.2.2e.iii represent the γ phase precipitated during the annealing treatment at lower temperatures. The small black spots in the micrographs have been identified as porosities, which are usually present in cast alloys. It is clearly seen from Fig. 4.2.2e.ii and Fig. 4.2.2e.iii the amount of γ phase precipitated in the alloy increases as the annealing temperature is lowered. The percentage of γ phase estimated from optical microscopy was 4.4% and 16% for the alloys annealed at 1000 °C and 900 °C, respectively. This result is in close agreement with those obtained from the analysis of XRD data. The compositions of single martensite (β') phase and combined $\beta' + \gamma$ phases determined by EDS analysis are given in Table 4.3.2. It is evident from Table 4.3.2 that the composition of the β' phase varies slightly in samples annealed at lower temperatures. This variation in the composition of the β' phase is due to the precipitation of the γ phase. As a consequence of this change in the composition of the β' phase, the *e/a* ratio of the β' -matrix decreases when annealed below 1150 °C. Liu *et al.* [40] have also observed the precipitation of γ-phase in alloys annealed below 1120 °C. However, our results refute their claim that the amount of γ-

phase precipitates does not change with annealing temperature. In fact, a closer look at the XRD data presented by them [Fig. 5 in ref. 40] clearly shows the enhancement of the γ-phase reflections of the sample annealed at 900 °C when compared with that of the sample annealed at 1200 °C.

4.2.3. Effect of quenching rate on the crystal structure

The normal procedure for preparation of these alloys involves preparation of the master alloy ingots by arc melting (or induction melting) followed by homogenization at high temperature and quenching into cold temperature. This is done to retain a high temperature phase at room temperature and to avoid precipitation some intermediate phase normally present in the system. The effect of quenching rate on the crystal structure of one alloy composition was investigated. Ground powders of $Co_{45}Ni_{25}Ga_{30}$ alloy and three small discs cut out from the slowly cooled alloy were sealed in three different fused silica ampoules at a pressure ~10^{-5} mbar, annealed at 1150 °C for 4 hours and then quenched separately into liquid nitrogen, ice cold water and air, respectively. In this manner, three alloys were prepared under different cooling rates.

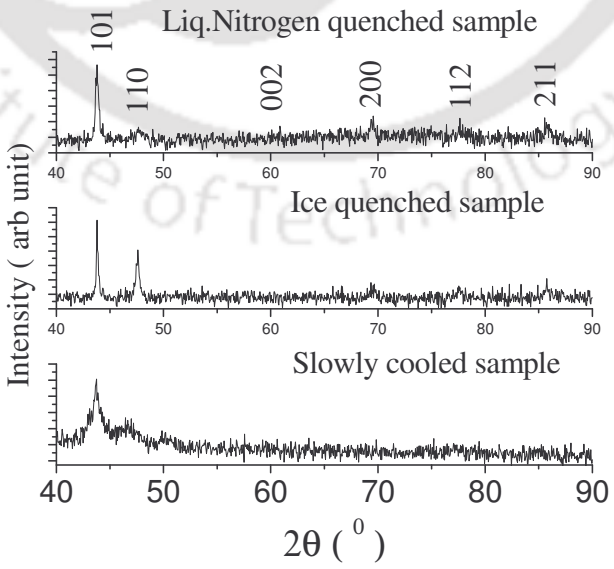

Fig. 4.2.3.a**:** XRD patterns of $Co_{45}Ni_{25}Ga_{30}$ alloys prepared with different quenching rate.

The XRD patterns of the alloy sample quenched under three different conditions are shown in Fig. 4.2.3a. The XRD pattern of the slowly cooled alloy showed a mixed phase structure. The extra peaks present in this XRD pattern is due to the presence of some other phase in the slowly cooled alloy. The surface relief due to martensitic transformation was observed in optical microscope for all the three quenched samples (Fig.4.2.3b). The thickness of the twin lines increased for samples cooled at higher rates. This is probably due to the larger displacement of lattice points required to accumulate higher elastic energy in samples quenched at higher rate. The twin lines are not distinct in the air cooled sample.

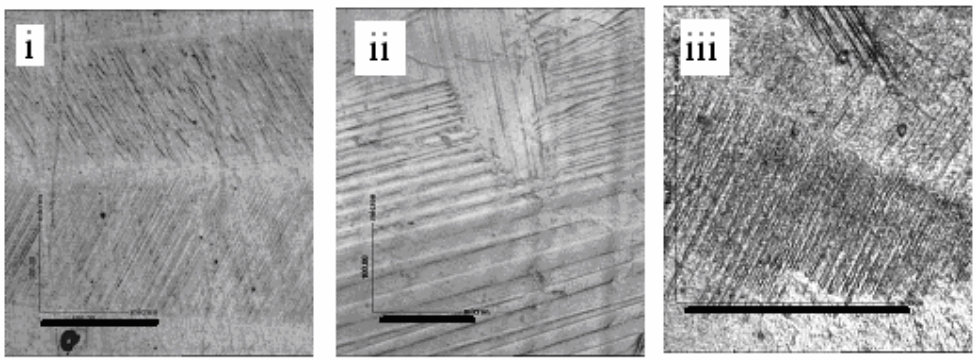

Liquid nitrogen quenched Ice quenched Air cooled

Fig. 4.2.3b: Optical microscope images of $Co_{45}Ni_{25}Ga_{30}$ alloy prepared under three different quenching rates.

4.3. THERMAL PROPERTIES

4.3.1. DSC studies of alloys quenched from 1150 ˚C

DSC thermograms depicting martensitic transformation temperatures corresponding to various compositions of $Co_{70-x}Ni_xGa_{30}$ alloys are shown in Fig.4.3.1a. Each DSC thermogram involving a heating and cooling cycle shows an endothermic and an exothermic peak corresponding to and $A \rightarrow M$ transformations, respectively. The $M \rightarrow A$ and $A \rightarrow M$ transformation temperatures for each alloy composition is different (cf. Table 4.3.1).

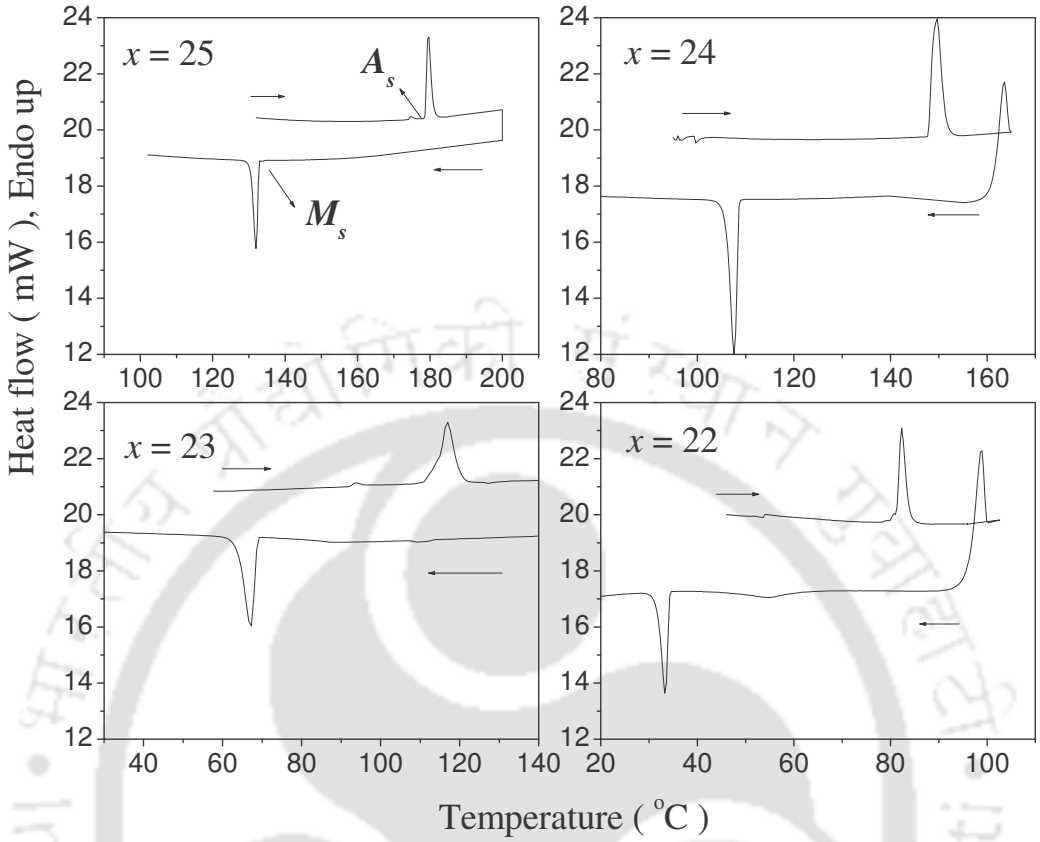

Fig. 4.3.1a: DSC thermograms of $Co_{70-x}Ni_xGa_{30}$ ($22 \leq x \leq 25$) alloys.

Table 4.3.1**:** Martensite transformation parameters (M_s, M_f, A_s, A_f and T_0) of $Co_{70-x}Ni_xGa_{30}$ ($22 \leq x \leq 25$) alloys.

Ni (at %)	M_s [°C]	M_f [°C]	A_s [°C]	A_f [°C]	T_0 [°C]	e/a
25	133	125	178	187	160.0	7.45
24	103	100	147	149	126.0	7.44
23	69	61	111	120	94.5	7.43
22	37	35	78	81	59.0	7.42
21*	15	18	44	49	32	7.41
20*	0	-38	6	15	7.5	7.40

* Martensitic transformation (MT) temperatures of alloys with x = 21 and 22 were near room temperature or below it. These data were obtained from low temperature AC susceptibility measurements.

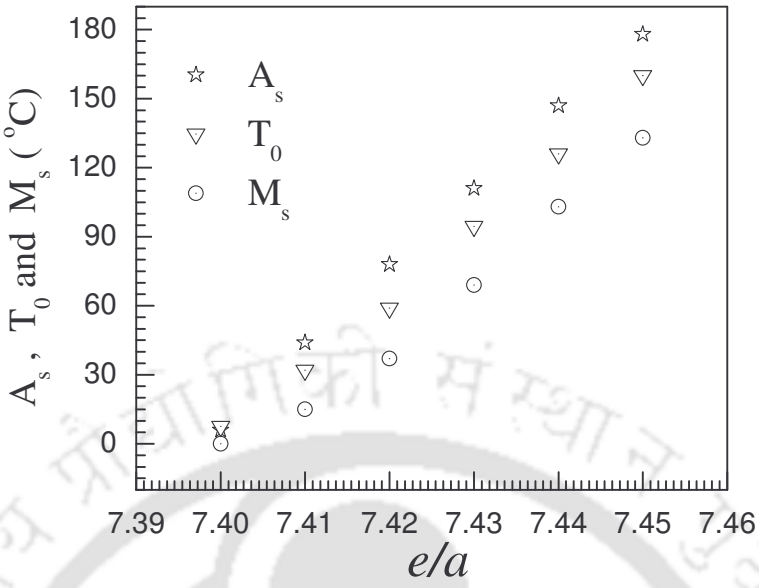

Fig. 4.3.1b**:** Variation of A_s , T_0 and M_s with e/a ratio of $Co_{70-x}Ni_xGa_{30}$ ($0 \leq x \leq 25$) alloys.

It can be seen from Fig. 4.3.1b that A_s, T_0 and M_s increase linearly with an increase in *e/a* value. The calculated value of *e/a* for all the Co-Ni-Ga alloys are listed in Table 4.3.1. Oikawa *et al.* [19] reported phase equilibrium between β and γ phases in this alloy system and pointed out similar variation of M_s, A_s and T_C of $Co_{70-x}Ni_xGa_{30}$ alloys in the $\beta + \gamma$ region. M_s and A_f were shown to decrease with increasing Co content. M_s and A_s values can be read from the data by them in graphical form for $Co_{45}Ni_{25}Ga_{30}$ alloy as $M_s \cong 130$ °C and $A_s \cong 160$ °C. Our observations are in close agreement with their results. Dadda *et al.* [124] reported the M_s and A_s temperature from AC susceptibility (ACS) measurements for $Co_{49}Ni_{21}Ga_{30}$ single crystal alloy as -5.3 °C and 6.3 °C, respectively. We observed higher A_s and M_s in our sample with x = 21. This may be due to the different processing condition under which single crystal and polycrystalline alloys are prepared. Zhang *et al.* [54] reported the MT temperature from ACS measurement for $Co_{50}Ni_{20}Ga_{30}$ ribbons as -3 °C (270 K) and 2 °C (275 K). But the graph shown in their paper reveals that A_s and M_s values are lower than the reported result. From ACS measurements, we observed A_s and M_s as 6 °C and 0 °C, respectively for this alloy. Dai *et al.*

[25] reported martensitic and reverse martensitic transformation temperatures of melt spun ribbons from ACS measurement as -18 °C and -8 °C, respectively. The low value obtained by them may be due to the smaller grain size of the melt spun alloys. Liu *et al.* [40] reported the A_s and M_s for alloy with *e/a* = 7.42 as 42 °C and 39 °C, respectively. Our M_s value is closer to their reported value but our A_s is higher than their reported value. This may be due to the fact that alloy prepared by them exhibited two phase ($\beta + \gamma$) structure after annealing at 700 °C and the presence of γ-phase has influenced the reverse martensitic transformation. For Co-Ni-Ga alloys, *MT* is so sensitive to composition that a decrease of 1 at% Ga leads to about 50 °C increases in M_s [125].

4.3.2. Effect of annealing temperature on martensitic transformation temperature

Properties of FSMAs have been found to be sensitive to alloy composition, homogenization (or annealing) temperature, cooling rate during preparation and post-preparation heat-treatment [40]. $Co_{47}Ni_{23}Ga_{30}$ alloy was taken up for study to investigate the influence of different annealing temperatures on the transformation temperature. Small pieces of the alloy was vacuum sealed in three fused silica tubes and separately annealed at 900 °C, 1000 °C and 1150 °C for 6 hours each and then quenched in ice water. DSC curves of $Co_{47}Ni_{23}Ga_{30}$ alloy annealed at 1230 ^{0}C, 1150 °C, 1000 °C and 900 °C are shown in Fig. 4.3.1a. The transformation parameters, namely, M_s and A_s, corresponding to the alloy annealed at different temperatures are listed in Table 4.3.1. The decrease in M_s and A_s observed in alloys annealed at lower temperatures can be understood on the basis of the change in the *e/a* ratio of the β'-matrix in the respective samples. It is now established [20, 40] that M_s and A_s of FSMAs vary linearly with *e/a* value. Hence, the decrease in M_s and A_s in alloys annealed at lower temperature is due to the decrease in the *e/a* ratio of the β'-matrix. The *e/a* ratio of the β'-matrix of the alloy annealed 900 °C is very close to 7.30 (cf. Table 4.3.1). This shows that annealing below 900 °C may not yield sufficient amount of martensite phase in $Co_{47}Ni_{23}Ga_{30}$ alloy.

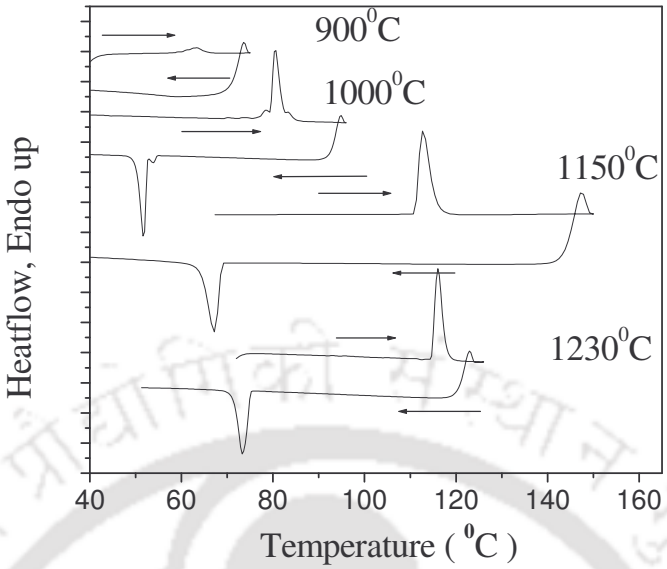

Fig. 4.3.2a: DSC curves of alloy samples annealed at different temperatures.

Table 4.3.2: Composition of constituent phases and characteristic temperatures of $Co_{47}Ni_{23}Ga_{30}$ alloy annealed at different temperatures.

Annealing temperature of alloy (ºC)	Composition of β´ matrix (at.%) from EDS measurements			*e/a* ratio	Composition of γ phase (at.%) from EDS measurements			A_s (°C)	M_s (°C)	T_C (°C)
	Co	Ni	Ga		Co	Ni	Ga			
1230	47.5	22.6	29.9	7.432	0	0	0	114	77	100
1150	46.9	23.1	30.0	7.431	0	0	0	111	69	105
1000	46.3	23.5	30.2	7.423	54.8	28.8	16.4	79	57	94
900	44.5	24.0	30.5	7.320	64.2	22.1	13.7	60	– 47	64

4.3.3. Effect of quenching rate on the martensitic transformation temperature

Three small discs of $Co_{45}Ni_{25}Ga_{30}$ alloy were sealed in three different fused silica ampoules at a pressure ~10^{-5} mbar, annealed at 1150 °C for 4 hours and then quenched separately into liquid nitrogen, ice cold water and air, respectively. The DSC curves of the three quenched samples are shown in Fig. 4.3.2a The transformation parameters, namely, M_s, M_f, A_s, A_f and the enthalpy involved in the transformations (ΔH_A and ΔH_M) are listed in Table 4.3.2. No evidence

of $M \rightarrow A$ and/or $A \rightarrow M$ transformations was observed in furnace-cooled sample. This indicates that the martensite phase could be formed in this alloy only by rapidly cooling the homogenized master alloy.

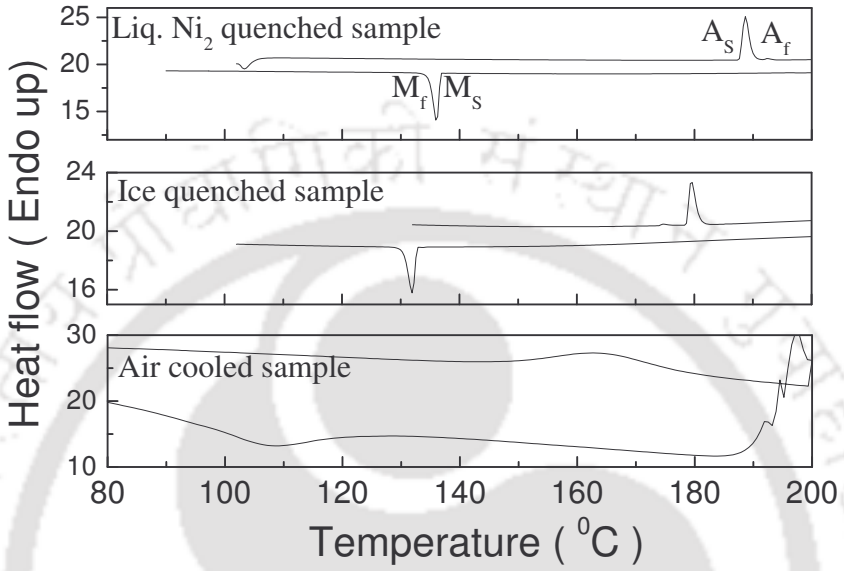

Fig. 4.3.3a: DSC curves of $Co_{45}Ni_{25}Ga_{30}$ alloy prepared under different quenching rates.

Table 4.3.3: DSC data of $Co_{45}Ni_{25}Ga_{30}$ alloy prepared under different quenching rate.

Quenching medium	Transformation parameter						
	A_s (°C)	ΔH_A ($=A_s \sim A_f$) (°C)	ΔH_A (J/g)	M_s (°C)	ΔM ($=M_s \sim M_f$) (°C)	ΔH_M (J/g)	Hysteresis ($=A_f \sim M_s$) (°C)
Liq. N_2	187	4	4.203	137	4	4.917	44
Ice water	178	4	4.588	133	5	4.306	33
Air	148	31	2.318	124	32	3.45	55

Analysis of the DSC data of the air cooled, ice quenched and liquid nitrogen quenched alloys showed higher A_s and A_f temperatures for the liquid nitrogen quenched sample. When samples were quenched from a high temperature to a very low temperature suddenly, the

elastic energy of the system can not be dissipated. Thus, the system accumulates (self accumulation of martensite) the elastic energy by displacive transformation of the lattice points. Thus, higher quenching rate introduces more elastic energy (or density of dislocation) in the system. To change from martensite state to austenite state, the SMA has to overcome more elastic energy and hence the transformation temperatures are higher for samples quenched at higher rates. Thus, it can be said that higher transformation temperatures can occur due to the presence of a higher concentration of defects in the martensite phase [126]. The same phenomenon causes larger thermal hysteresis, (A_f~M_s) in a sample quenched at higher rates. The elastic energy around the martensite resists the growth of the martensite unless a further driving force (i.e. cooling) is given [10]. The endothermic and exothermic peak of air cooled sample is very weak and wide. Thus, the $M \leftrightarrow A$ transformation in air cooled sample is not sharp and hence the cooling rate is not sufficient for the formation of shape memory alloys. The $M \leftrightarrow A$ transformation of ice quenched and liquid nitrogen quenched samples are very sharp. However, very high rates of quenching introduce more thermal strain into the system and cracks develop in the bulk sample. Taking account of these, one can say that the ice quenching method is more suitable for the preparation of Co-Ni-Ga alloys.

4.4. MASS DENSITY MEASUREMENT

The results of mass density measurement from Archimedes principle are given in Table 4.4. Here ρ_A was measured on the alloy samples. ρ_c (= 8.003 g/cm^3) was calculated from the individual contribution of the constituent elements of the alloys. It is seen that density does not vary with the change of Co at % and Ni at %. It is due to the fact that density of Co and Ni are almost same.

Table 4.4: Mass Density of $Co_{70-x}Ni_xGa_{30}$ ($20 \leq x \leq 25$) alloys.

Ni at% (x) in the alloy	Measured density ρ_A (g/cm^3)
20	8.583 ± 0.004
21	8.608 ± 0.004
22	8.587 ± 0.004
23	8.606 ± 0.004
24	8.620 ± 0.004
25	8.616 ± 0.004

4.5. MAGNETIC PROPERTIES

4.5.1. AC susceptibility as a function of temperature:

Temperature dependence of the AC susceptibility data of all the samples are shown in Fig. 4.5.1a. All samples show a characteristic decrease in the real component of ACS near the ferromagnetic to paramagnetic phase transition. The ferromagnetic to paramagnetic transition temperature (T_C) of $Co_{70-x}Ni_xGa_{30}$ alloys was determined from the magnetic susceptibility versus temperature data recorded while heating the sample (Fig. 4.5.1a) and the corresponding values are given in Table 4.5.1.

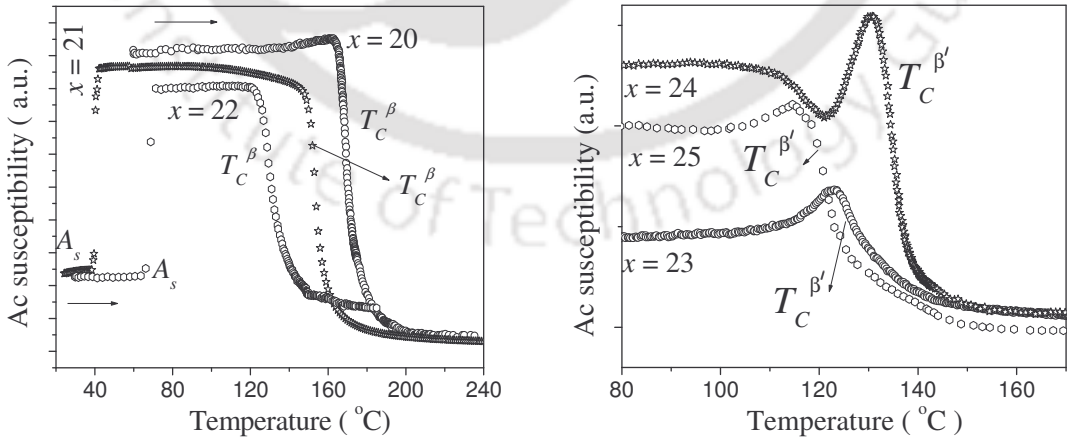

Fig. 4.5.1a: AC susceptibility of $Co_{70-x}Ni_xGa_{30}$ ($20 \leq x \leq 25$) alloys.

Table 4.5.1: Curie temperature of $Co_{70-x}Ni_xGa_{30}$ ($20 \leq x \leq 25$) alloys.

x	20	21	22	23	24	25
T_C [^oC]	169	151	129	125	133	119

T_C values have been measured from the local minimum point of the derivative AC susceptibility vs temperature graph and are listed in the Table 4.5.1 Curie temperature for the austenite state is conventionally written as T_C^{β} and that of the martensite state as $T_C^{\beta'}$. It is seen that T_C^{β} value is highest for x = 20 (50 at % Co), which decreases with an increase of x. A discontinuity is observed at x = 23, where T_C^{β} changes to $T_C^{\beta'}$. A similar trend has been reported in Ni-Mn-Ga [59], Fe-Ni-Ga [22], Co-Ni-Ga and Co-Ni Al [19] alloys (Ref. Chep1. page 27). The discontinuity has been observed for the alloys having close MT and T_C values. As the sample is heated, a sudden increase in magnetic susceptibility is observed at A_s followed by a sharp decrease in susceptibility at T_C. In the case of the alloy with x = 23, A_s (111 °C) and T_C (125 °C) are very close. At A_s, the susceptibility tries to rise sharply, whereas at T_C it tries to drop down. Due to the proximity of A_s and T_C values, precise measurement of T_C is difficult for this alloy. This could have been the cause for the difficulty faced by Oikawa *et al*. [19] in precisely determining the T_C of the $Co_{47}Ni_{23}Ga_{30}$ alloy quenched from 1150 °C on the heating cycle. A detailed investigation has been carried out on this sample to find T_C and the influence of different annealing and conditions on T_C.

4.5.2 Effect of annealing temperature on the Curie temperature

Some small pieces of alloys was vacuum sealed in three fused silica tubes and separately annealed at 900 °C, 1000 °C and 1150 °C for 6 hours each and then quenched in ice water. No further heat treatment was performed on the quenched powders. T_C was determined from the ACS data.

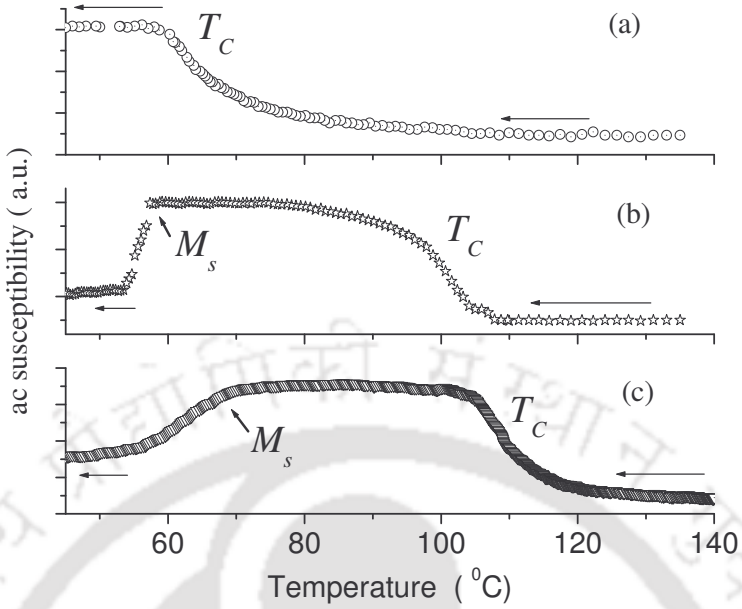

Fig. 4.5.2a: ACS data of $Co_{47}Ni_{23}Ga_{30}$ alloy annealed at (a) 900 °C (b) 1000 °C & (c) 1150 °C.

The ACS data of $Co_{47}Ni_{23}Ga_{30}$ alloy annealed at 1150 °C, 1000 °C and 900 °C are shown in Fig. 4.5.2a. The plots correspond to data collected on the cooling cycle. A small difference of ≤ 5°C was observed in T_C of the investigated alloys obtained during heating and cooling cycle. This difference was minimized by slowly heating or cooling the samples. As the sample is cooled, a sudden increase in magnetic susceptibility is observed at T_C followed by a decrease in susceptibility at M_s. Since M_s (69 °C) and T_C were far away there was no influence of the MT on T_C of this alloy. For this reason, we have presented the susceptibility data obtained on the cooling cycle.

T_C of the alloy decreases as the annealing temperature is decreased, except for the case of the sample annealed at 1230 °C. When the sample is quenched below 1120 °C, a secondary (γ) phase develops with the primary β-phase. The presence of γ phase introduces some crystallographic disorder in the alloys. Increased crystallographic disorder tends to shift T_C to lower temperatures. The lower T_C exhibited by the alloy quenched from 1230 °C can be understood as follows. Lowering of T_C has been observed in ribbons quenched at higher

cooling rates [127]. The alloy melts near 1220 °C. When the alloy is quenched from 1230 °C in molten condition, the grain size of the resultant alloy is considerably reduced than those quenched from the solid state. This smaller grain size and higher cooling rate results in shifting the T_C towards low temperature side with respect to the alloy quenched from 1150 °C.

4.5.3. Effect of quenching rate on the Curie temperature

The ferromagnetic to paramagnetic transition (Curie) temperature (T_C) was measured by ACS for $Co_{45}Ni_{25}Ga_{30}$ prepared under different cooling rate and the T_C values are given in Table 4.5.3. T_C was lower for samples prepared with higher cooling rate (i.e. samples quenched in liquid nitrogen). T_C is sensitive to local crystallographic environment. When the sample is quenched from high temperatures, the solidification is not under equilibrium conditions and this introduces some crystallographic defects in the sample. These defects create a local disorder in their vicinity. Faster cooling rates introduce more defects in the sample. Thus, the degree of disorder in the sample prepared by quenching in liquid nitrogen is more than in the other two samples. The increased crystallographic disorder is manifested in decreased grain size. T_C value shifts to lower temperature side with the reduction of grain size. Hence, lower T_C value of alloys quenched at higher rate is an expected result. Similar results have been reported in rapidly solidified Nd -Fe-B samples [127].

Table 4.5.3: Curie temperature of $Co_{45}Ni_{25}Ga_{30}$ alloy prepared under different cooling rate.

Quenching medium	Liq. N_2	Ice water	Air cooled
T_C (°C)	98	119	131

4.5.4. Magnetization as a function of temperature using VSM:

Magnetization vs temperature (*M-T*) graphs corresponding to the alloys annealed at 1150 °C and 1000 °C are shown as in Fig. 4.5.4a and Fig. 4.5.4b, respectively T_C was measured from the local minimum point of the derivative curve of *M-T* (*H* = 50 Oe) data.

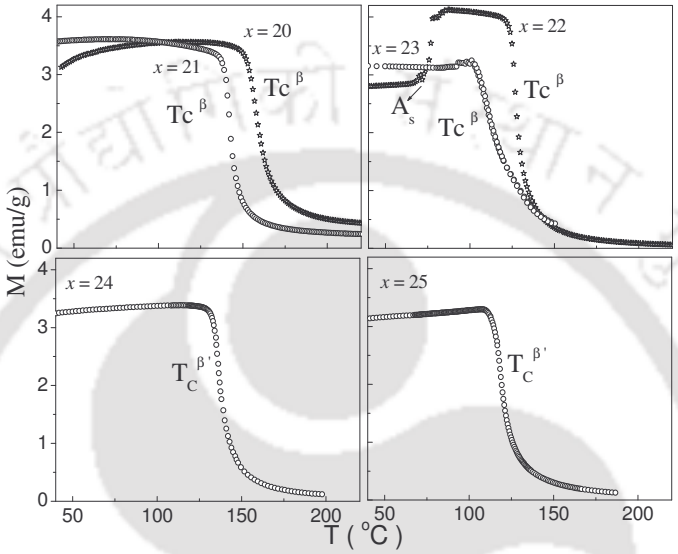

Fig.4.5.4a: Variation of magnetization of with respect to temperature at constant field. $Co_{70-x}Ni_xGa_{30}$ ($20 \le x \le 25$) alloys annealed at 1150 °C.

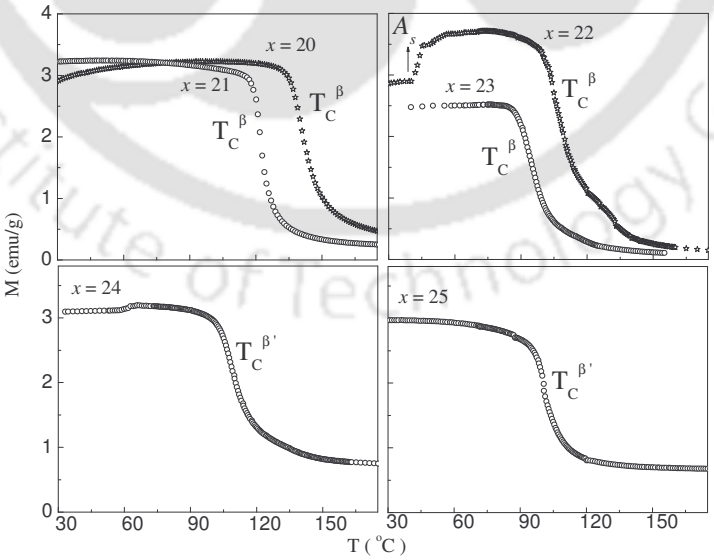

Fig.4.5.4b: Variation of magnetization of with respect to temperature at constant field. $Co_{70-x}Ni_xGa_{30}$ ($20 \le x \le 25$) alloys annealed at 1000 °C. The term 'β' and 'β/' are used for cubic phase and martensite phase respectively.

Table 4.5.4: Curie temperature (T_C) of $Co_{70-x}Ni_xGa_{30}$ ($20 \leq x \leq 25$) alloys obtained by quenching from different temperatures along with magnetic valence number (Z_m).

Composition of the alloy (x)	T_C (alloy annealed at 1150 °C)	T_C (alloy annealed at 1000°C)	Z_m
20	156 °C	139 °C	-0.40
21	141 °C	121 °C	-0.41
22	126 °C	105 °C	-0.42
23	109 °C	92 °C	-0.43
24	135 °C	107 °C	-0.44
25	117 °C	100 °C	-0.45

T_C values obtained from AC susceptibility measurements are close to the values obtained from magnetization measurements. All the data presented have been recorded on the heating cycle. A higher value of T_C was observed for the alloy annealed at higher temperature (1150 °C) than the alloy annealed at 1000 °C. The lower T_C exhibited by the alloy annealed at 1000 °C may be due to the presence of the γ-phase precipitates in the β - matrix. The magnetic ordering is likely to be disturbed due to the presence of the cubic secondary phase. A linear dependence of T_C and T_0 with annealing temperature has been reported [38] in $Co_{38}Ni_{34}Al_{28}$ alloy with two (β+ γ) phase structure. In the present studies, T_C of the alloys annealed at 1150 °C and 1000 °C decreases with the decrease in magnetic valence number Z_m as shown in Fig. 4.5.4c. The slope and y-intercept of the T_C vs Z_m graph changes at $x = 23$. This is because the Curie temperature of martensite phase ($T_C^{\beta'}$) is higher than that of the austenite phase (T_C^{β}) [17, 22]. For the alloys with $x = 24$ and 25, the reverse martensitic transformation temperature (A_s) is higher than the T_C. Thus, the ferromagnetic to paramagnetic transition of these two alloys occurs in the martensite phase during the heating cycle, whereas, the other alloys (i,e., $20 \leq x \leq 23$) undergo the magnetic transition in the austenite phase.

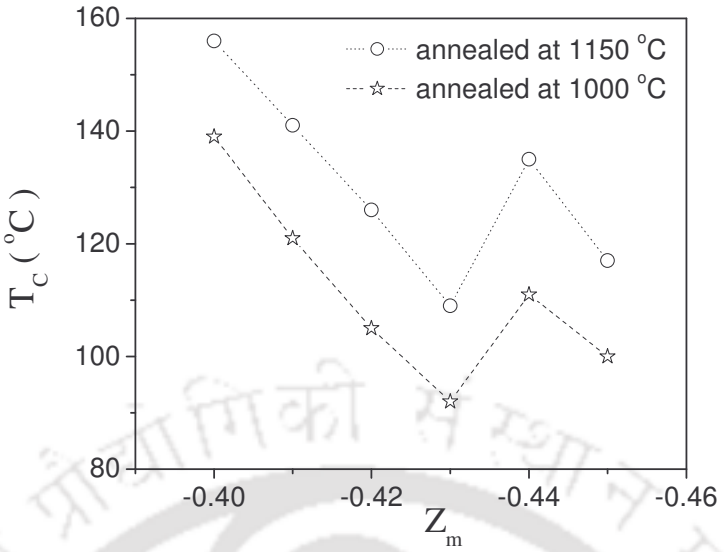

Fig.4.5.4c: Variation of T_C of $Co_{70-x}Ni_xGa_{30}$ ($20 \leq x \leq 25$) alloys with Z_m.

4.5.5. *M-H* measurements at constant temperature:

The magnetization (*M-H*) loops of $Co_{70-x}Ni_xGa_{30}$ ($20 \leq x \leq 25$) alloys show very small coercively (<100 Oe) at room temperature. This shows that the sample is soft magnetic both in austenite and martensite phases. The variation of magnetization with applied field for all the alloys annealed at 1150 °C and 1000 °C are shown as in Fig. 4.5.5a and Fig. 4.5.5b, respectively. Magnetization was measured at room temperature (25 °C). It can be observed from the insets in the two figures that the alloy with composition $x = 20$, annealed from 1150 °C saturates much faster than the other alloy compositions. A similar behavior has been observed for the alloys with composition $x = 20$ and 21, annealed at 1000 °C. This behaviour is due to the lower magneto crystalline anisotropy of these alloys as they are in the austenite state (cubic phase). The martensite phase has higher magneto crystalline anisotropy energy.

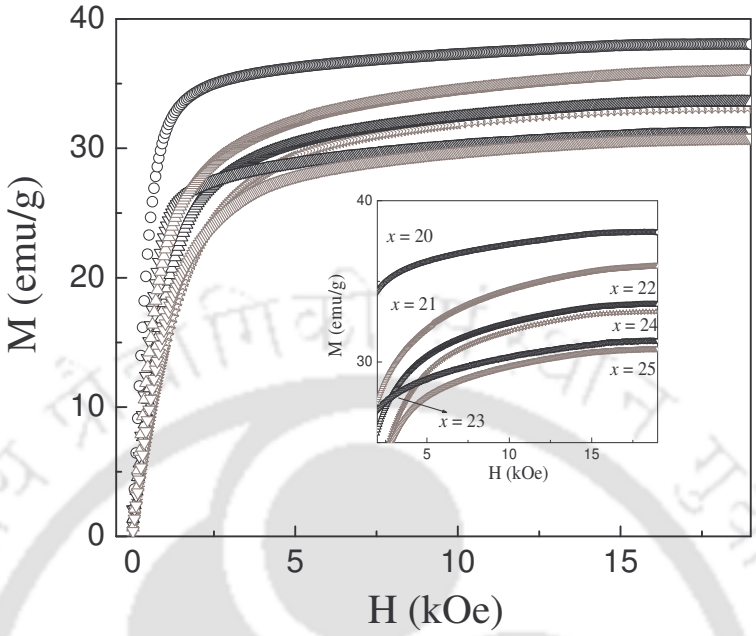

Fig. 4.5.5a: *M-H* curves of $Co_{70-x}Ni_xGa_{30}$ ($20 \leq x \leq 25$) alloys annealed at 1150 °C.

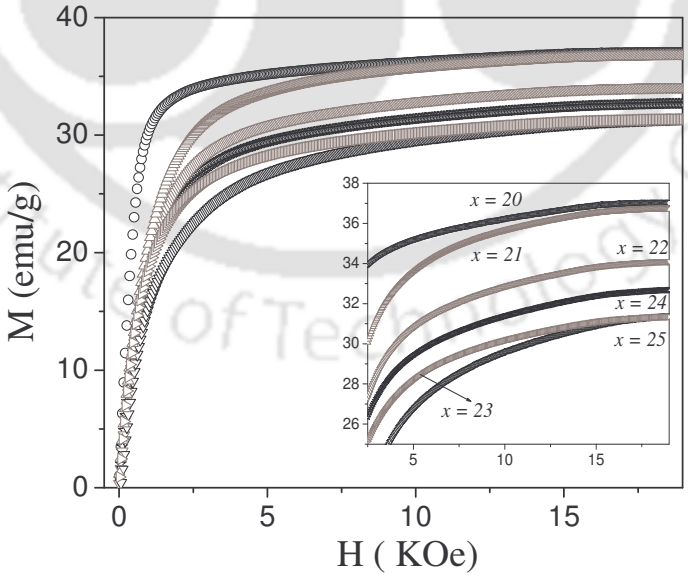

Fig. 4.5.5b: *M-H* curves of $Co_{70-x}Ni_xGa_{30}$ ($20 \leq x \leq 25$) alloys annealed at 1000 °C.

A higher magneto crystalline energy is required for a good FSMA. The anisotropy constants at room temperature have been estimated for these alloys from their *M-H* curve using law of approach to saturation (LAS).The equation used for non linear curve fit is

$$M(H) = M_{sat}[1 - \frac{b}{H^2}] \qquad (4.5.5a)$$

The saturation magnetization, co-efficient b and the K_{eff} estimated from it are listed in the Table 4.5.5a.

Table: 4.5.5.a: Magnetization and magneto crystalline anisotropy constants for $Co_{70-x}Ni_xGa_{30}$ ($20 \le x \le 25$) alloys obtained by quenching from 1150 °C.

Composition of Alloy (x)	$*M_{sat}$ (A-m^2/kg)	$*M_{sat}$ (A/m)	$** b \times 10^6$ (Oe)^2	$*** K_{eff} \times 10^5$ (J/m^3)
20	38.66 ± 0.01	332476	0.42 ± 0.03	0.4
21	37.14 ± 0.04	319404	5.04 ± 0.02	1.39
22	34.26 ± 0.01	294636	5.95 ± 0.03	1.39
23	31.94 ± 0.01	274684	5.84 ± 0.05	1.29
24	33.86 ± 0.01	291196	5.72 ± 0.03	1.34
25	30.96 ± 0.01	266256	4.82 ± 0.03	1.25

** emu/g ≅A-m^2/kg; M_{sat} is multiplied by corresponding density to obtain it in A/m.*

***Coefficient 'b' was estimated in Oe^2 and converted to A/m (1 Oe = $10^3/4\pi$ A/m)*

*** $K_{eff} = \sqrt{\frac{15b}{4}}\,\mu_0 M_{sat}$ [109] *for tetragonal structure.*

In order to minimize the demagnetization field, samples of very small cross sectional area (cylindrical sample with very small diameter) were placed perpendicular to the applied field during the experiment. Demagnetization field was also estimated for few samples from

the initial susceptibility (χ_{in}) of the initial magnetization curves. Demagnetizing factor (N_d) is expressed [128, 129] as,

$$N_d = 1/\chi_{in} = dH/dM \mid_{H=0} \qquad (4.5.5b)$$

The actual field (H_{ac}) inside the material can be obtained from the applied field from the relation,

$$H_{ac} = H_a - N_d M \qquad (4.5.5c)$$

These estimates showed that the difference in M_{sat} and K_{eff} values with and without demagnetization correction was very small.

Table 4.5.5b: Magnetization and magneto crystalline anisotropy constant of $Co_{70-x}Ni_xGa_{30}$ ($20 \leq x \leq 25$) alloys obtained by quenching from 1000 °C.

Composition of Alloy (x)	M_{sat} (A-m^2/kg)	M_{sat} (A/m)	$b \times 10^6$ (Oe)^2	$K_{eff} \times 10^5$ (J/m^3)
20	35.52 ± 0.01	305472	0.80 ± 0.03	0.52
21	35.72 ± 0.01	307192	2.33 ± 0.02	0.90
22	34.80 ± 0.01	299280	6.21 ± 0.03	1.44
23	32.32 ± 0.01	277780	6.56 ± 0.03	1.38
24	33.33 ± 0.01	286638	6.53 ± 0.02	1.42
25	31.95 ± 0.01	274684	6.18 ± 0.03	1.32

It was observed that M_{sat} was highest for the alloy with x = 20 (38.66 emu/g which corresponds to 1.72 μ_B / formula unit). Figure 4.5.5c shows the variation of M_{sat} with magnetic valence number (Z_m). M_{sat} of the alloy with x = 20 and 21 decreases with decrease in quenching temperature. When quenched from 1150°C, alloy with x = 20 exhibits austenite (cubic) structure, whereas, the alloy with x= 21 exhibits martensite structure. When quenched from 1000 °C, a secondary fcc (γ) phase developed along with the austenite (bcc,β) phase which causes some crystallographic disorder in the system. The decrease of saturation magnetization

may be due to the presence of γ-phase in β-matrix, which lowers the magnetic interaction between the atoms.

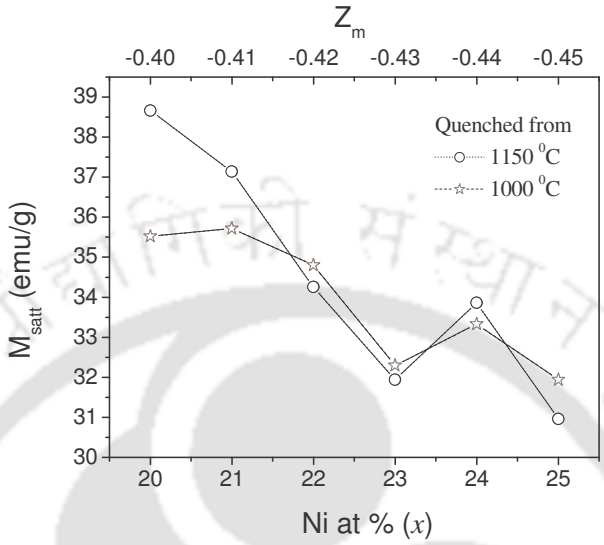

Fig. 4.5.5c: Variation of M_{sat} with Z_m for $Co_{70-x}Ni_xGa_{30}$ ($20 \leq x \leq 25$) alloys obtained by quenching from 1150 °C and 1000 °C.

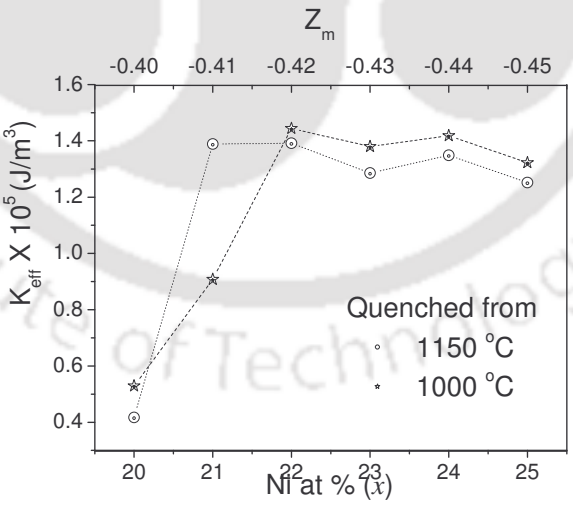

Fig. 4.5.5d: Variation of K_{eff} with Z_m for $Co_{70-x}Ni_xGa_{30}$ ($20 \leq x \leq 25$) alloys obtained by quenching from 1150 °C and 1000 °C.

K_{eff} is higher for the ferromagnetic martensite phase than the ferromagnetic austenite phase. The alloy with $x = 20$ quenched from 1150 °C and alloys with $x = 20, 21$ quenched from

1000 °C have the austenite phase at room temperature. Thus, K_{eff} for these alloys are much lower than that of the other alloys as shown in Fig. 4.5.5c. K_{eff} of polycrystalline $Ni_{49}Fe_{18}Ga_{27}Co_6$ alloy has been reported as 1.2×10^6 erg/cm^3 (M_{sat} = 40 emu/g) at 300 K [94]. K_{eff} estimated in the present studies are close to this value. The variation of M_{sat} and K_{eff} with different quenching temperatures for the alloy with x = 23 is presented in Fig. 4.5.5.d. Due to the increase in the amount of γ-phase (fcc) precipitates in the β matrix in samples quenched from lower temperatures, K_{eff} increases with decrease in quenching temperature. Since alloy melts near 1230 °C, homogenization at this molten state and subsequent quenching from this temperature into ice water results in smaller grains in the sample. Magnetic interaction enhances with smaller grain size and decreases with an increase in the amount of secondary phase.

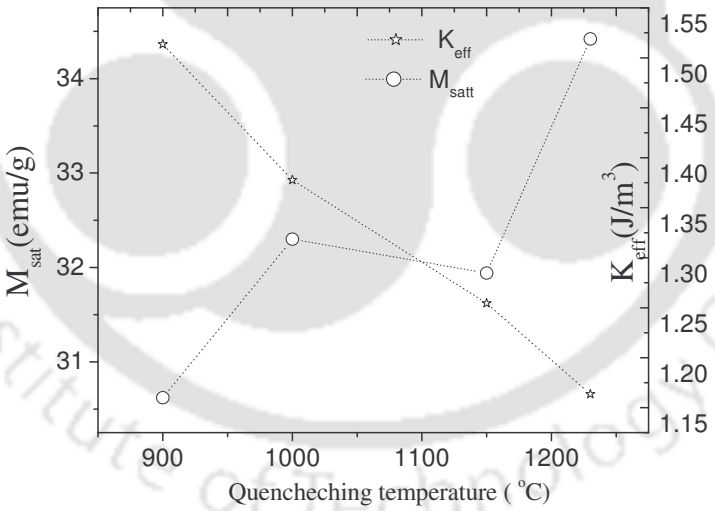

Fig. 4.5.5.e: Variation of K_{eff} and M_{sat} for $Co_{47}Ni_{23}Ga_{30}$ alloy quenched from different temperatures.

For the accurate determination of the Curie temperature from *M-T* curves curves, the applied field needs to be as low as possible. The task becomes tough especially when high magnetocaloric materials are involved. The Arrott plot is the most appropriate method for

determining the projected Curie temperature since this method is not susceptible to external factors such as influence of the applied magnetic field and thermal effects. Moreover, the critical constants corresponding to the ferromagnetic to paramagnetic transition can be determined from the modified Arrott plot. In order to obtain these plots, *M-H* data were recorded near T_C (= 100 °C in this case). The *M-H* isotherm for $Co_{45}Ni_{25}Ga_{30}$ alloy (annealed at 1000 °C) from 95 °C to 107 °C at an interval of 1 °C is shown in the Fig. 4.5.5f. Saturation of magnetization is not fully attained at this applied field. Such behavior also found in other compounds [116,117], is characteristic of the samples without true long-range order ferromagnetism. These data were used to determine the critical exponents β and γ corresponding to the exponents for the temperature dependence of the spontaneous magnetization (M_{sat}) and inverse initial susceptibility (χ_0^{-1}), respectively.

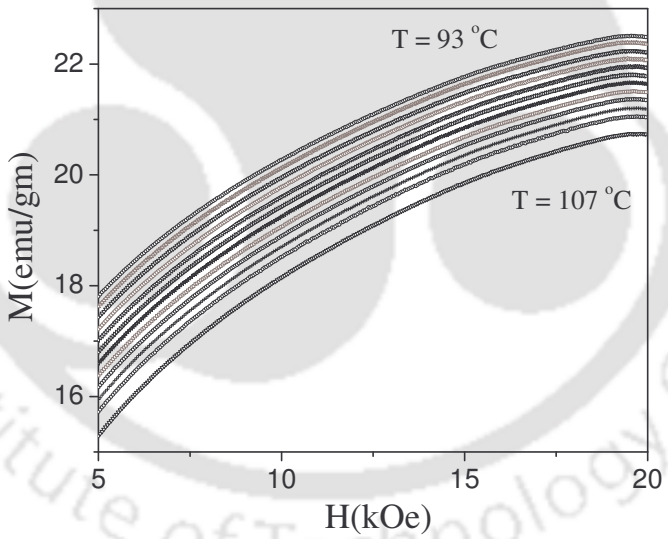

Fig.4.5.5f: *M-H* curves of $Co_{45}Ni_{25}Ga_{30}$ alloy (annealed at 1000 °C) taken near T_C. Only a truncated part of the graph is shown for the sake of clarity.

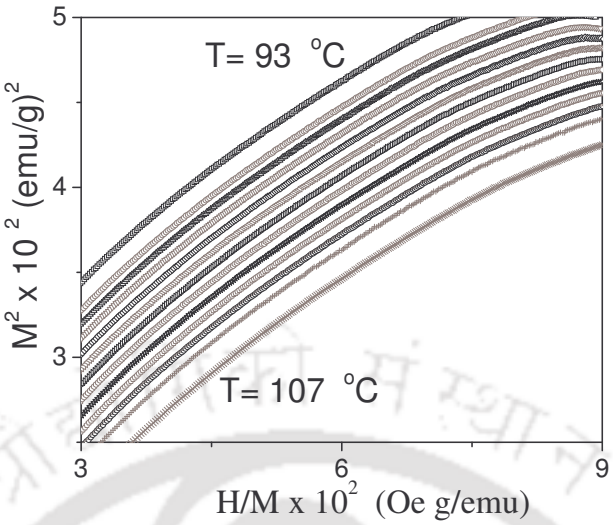

Fig. 4.5.5g: Arrott plot of $Co_{45}Ni_{25}Ga_{30}$ alloy near T_C.

As the first step in the process of obtaining accurate T_C, M^2 versus H/M plots were created from the data (Fig. 4.5.5g). The nonlinear curves obtained for the data close to the magnetic phase transition indicate that the mean field theory is not applicable to this data [113]. It is to be noted that a standard Arrott plot uses mean field theory exponents, $\gamma = 1$, $\beta = 0.5$ and $\delta = 3$, which are the characteristics of a system with long range interaction. Therefore, modified Arrott plots, i.e. $M^{1/\beta}$ versus $(H/M)^{1/\gamma}$ plots, which are based on Arrott-Noakes equation of state were obtained from the data. This modified Arrot [i.e., $M^{1/\beta}$ versus $(H / M)^{1/\gamma}$] plot with correct values of the exponents yields isotherms near the Curie temperature that are linear and parallel over a wide range of H/M values. Fig. 4.5.5h shows the $M^{1/\beta}$ versus $(H / M)^{1/\gamma}$ plots obtained for $Co_{45}Ni_{25}Ga_{30}$ alloy with optimized β and γ values. M_{sat} (0) was obtained from the positive y-intercept and χ_0^{-1} was obtained from the positive x-intercept of the above graph and the same are shown in Fig. 4.5.5i. The fitting equations used to obtain the plot are:

$$M_{sat}(0) = M_0(T_C - T)^{\beta} \; ; \quad T < T_C \tag{4.5.5d}$$

$$\chi_0^{-1} = (h/M_0)(T-T_C)^{\gamma} \quad ; \quad T > T_C \tag{4.5.5e}$$

where M_0 and h/M_0 are proportionality constants.

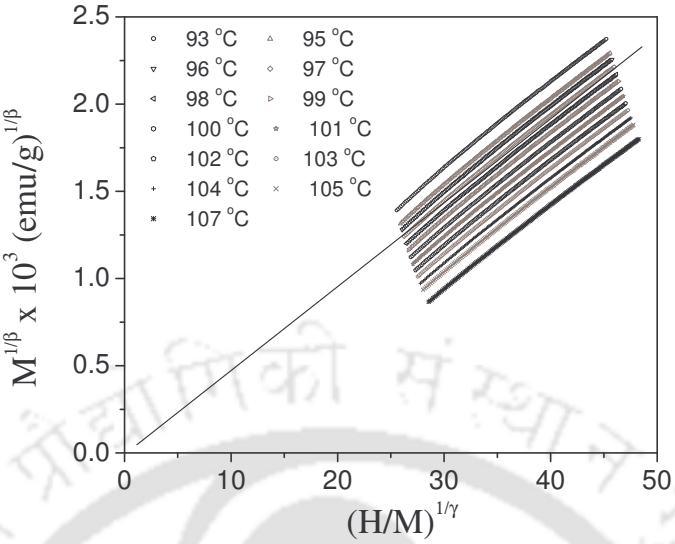

Fig. 4.5.5h: Modified Arrott [$M^{1/\beta}$ vs. $(H / M)^{1/\gamma}$] plot for $Co_{45}Ni_{25}Ga_{30}$ alloy. Data in the applied field range of 4 kOe ≤ H ≤ 15 kOe have been considered.

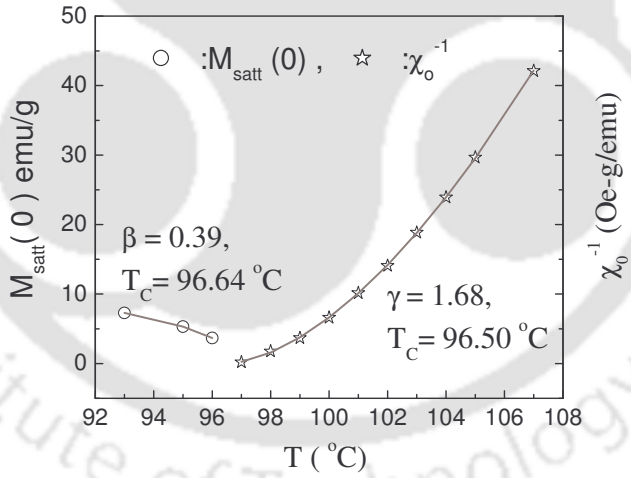

Fig. 4.5.5i: Variation of spontaneous magnetization and zero field inverse susceptibility with temperature close to T_C. Solid lines are least squares fit to eqn. (4.5.5d) and (4.5.5e), respectively.

T_C values obtained from nonlinear curve fitting are 96.50 °C and 96.64 °C, respectively. It can be seen that T_C obtained from both the fitting equations are reasonably close. The best (fitted) values of β and γ are 0.39 and 1.68, respectively. The critical constant δ was

determined from the scaling law, $\beta + \gamma = \beta\delta$, as 5.31. *M-H* data taken at 97 °C was plotted and fitted to the equation $M = C_1 H^{1/\delta}$ (where C_1 is proportionality constant) in order to extract the value of δ. This procedure yielded a value of 5.34 for δ, which is close to 5.31 obtained from the earlier method. The difference in δ is most likely due to the difference in the T_C used in the two procedures; the earlier was 96.57 °C (average of 96.50 °C and 96.64°C) and the latter was 97 °C. The critical exponents predicted by the 3-*d* Heisenberg model are $\beta = 0.367$, $\gamma = 1.388$ and $\delta = 4.78$ [130]. The values of the critical exponents depend on the range of exchange interaction *J(r)*. Fisher et.al [131] has performed a renormalization group analysis of systems with an exchange interaction of the form $J(r) = 1/r^{d+\sigma}$ (where *d* is the dimension of the system and σ is the range of interaction). If $\sigma > 2$, then Heisenberg exponents ($\beta = 0.365$, $\delta = 4.8$ and $\gamma = 1.386$) are valid. The mean field exponents ($\beta = 0.5$, $\delta = 3$ and $\gamma = 1$) are valid for $\sigma < ½$. There are no reports on the critical constants of FSMAs reported in the literature for comparison with our results. The critical constants estimated for $Fe_{29}Ni_{49}P_{14}B_6Si_2$ magnetic alloys ($\beta = 0.44$, $\delta = 5.25$ and $\gamma = 1.7$) [132] are very close to our estimated value for $Co_{45}Ni_{25}Ga_{30}$ alloy. For Ni, it has been found to be $\beta = 0.42$ $\gamma = 1.35$ and $\delta = 4.22$ [133]. Critical exponents estimated [116] for $La_{0.9}P_{0.1}MnO_3$ sample are $\beta = 0.498$, $\gamma = 1.456$ and $\delta = 3.92$ and it was concluded that at temperature below T_C the ferromagnetic (*FM*) order orientation of spin results in the β exponent being close to the value of the mean field theory. However, tenacious existence of the *FM* phase even above T_C has given rise to the γ-exponent value close to the 3-*d* short range isotropic Heisenberg model value. This conjecture is reasonable for unconventional ferromagnets where FM-PM transition is not sharp. The *FM-PM* transition of this present alloy is also not sharp (Fig.4.5.4b). The γ-exponent value estimated for the Co-Ni-Ga alloy is found to be higher than the value predicted by the Heisenberg 3-*d* model. Hence, it is proposed that the presence of *FM* phase above T_C might have caused the

shift of γ value toward the value which is higher than the one predicted by the Heisenberg 3-*d* model.

4.6. MECHANICAL PROPERTIES

It has been observed that the alloys under investigation annealed at 1150 °C have single phase structure and are brittle for machining. When they are annealed at 1000 °C, small amounts of the secondary (γ) phase precipitates in the martensite phase (β), thereby enhancing the ductility of the alloys. In order to obtain ductile $Co_{70-x}Ni_xGa_{30}$ ($20 \leq x \leq 25$) alloys, the respective homogenized alloys were molded in a copper cylinder to obtain cylindrical sample of diameter 7 mm and length ~ 11 to 15 mm. These samples were then annealed at 1000 °C for six hours and quenched in ice water so that sufficient amount of γ-phase precipitates in the β matrix. The martensitic transformation temperatures (A_s and M_s) and Curie temperature (T_C) of the alloys processed at 1000 °C are listed in the Table 4.6 in order to facilitate comparison. It may be noted that low temperature ACS and VSM were used for the determination of A_s and M_s for the alloy with composition x = 20 and 21, due to the limited low temperature range of the DSC. Suitable sizes of these samples obtained in the form of cylinders were used for mechanical testing.

Table 4.6: A_s, M_s and T_C of $Co_{70-x}Ni_xGa_{30}$ ($20 \leq x \leq 25$) alloys

Alloy composition (x)	25	24	23	22	21	20
A_s (°C)	145	119	79	40	-13*	- 43*
M_s (°C)	107	87	57	-6*	-38 *	-60*
T_C (°C)	100	107	92	105	121	139

* Data obtained using low temperature ACS

4.6.1 Microhardness (VHN)

Small discs of 7 mm diameter and 1mm thick were cut from the cylindrical samples, mounted on resin and polished for microhardness measurement. The results obtained from the Vickers microhardness measurement are listed in Table 4.6.1a. A typical indentation is shown in Fig. 4.6.1a as viewed under an optical microscope.

Table 4.6.1a: Microhardness of $Co_{70-x}Ni_xGa_{30}$ ($20 \leq x \leq 25$) alloys. Load applied for the indentation is 100gf

x	20	21	22	23	24	25	Steel ball*	Al bar *
VHN (GPa)	386	347	313	287	275	300	1770	167

*VHN of stainless steel ball bearing used in the rear wheel of Maruti 800^{TM} car and commercial aluminum bar are also listed in the table for the sake of comparison.

It has been observed that the VHN of the alloys are low as compared to stainless steel automobile ball bearing. But the alloys were almost twice harder than commercial aluminum. Thus, cutting, drilling or polishing can be done on these alloys with relative ease as compared to the same alloys processed at higher temperatures. It can be seen from the data presented in the table that the alloy with x = 20 exhibited the highest VHN and the alloy with x = 23 displayed the lowest VHN. Hardness for the alloy with x = 20 was measured for different indenter loads and the results obtained are listed in the Table 4.6.1b.

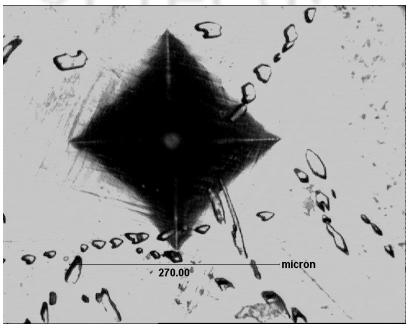

Fig. 4.6.1a: A typical pyramidal indentation obtained on Co-Ni-Ga alloy surface. The small spots seen in the optical micrographs are the γ-phase precipitates.

Table 4.6.1b: Microhardness of $Co_{50}Ni_{20}Ga_{30}$ alloy at different indentation load.

Indentation load (gf)	100	200	300	500	2000
VHN (GPa)	386	340	397	349	343

Yan *et al.* employed the dimensional analysis and the finite element approach to study the spherical indentation hardness of SMAs [77]. It has been observed by them that the indentation hardness increases with the maximum indentation depth. Therefore, they concluded that the measured indentation hardness cannot be treated as a material property of SMAs. It can be found from Table 4.6.1b that VHN of Co-Ni-Ga alloys does not depend on the applied load or indentation depth. Hence, systematic variation of the property can be expected in a series of FSMA which are subjected to identical loads. The highest VHN obtained for the alloy with x = 20 is due to the austenite (*bcc*) structure of this alloy. It can be observed from Table 4.6.1.b that the VHN decreases from its highest value for the alloy with x = 20 to the lowest value for the alloy with x = 24. An increase in VHN is observed for the alloy with x = 25. Although the VHN has a complicated dependence on the elastic moduli [119] of the material, it also provides a clue to the amount of γ-phase introduced into the β matrix. A careful comparison of the VHN of the alloys processed at different temperatures could provide a simple and indirect means of estimating the amount of γ-phase introduced into the β matrix during the processing stage.

4.6.2. Stress-strain behavior

To determine the mechanical strength of the alloys under investigation, samples of 7 mm diameter and 10.5 mm length were used for compression test in a servo hydraulic universal testing machine. Load was applied on the sample along its length till its mechanical failure point. Stress-strain (*S-S*) curves obtained from the compression test are shown as in Fig.4.6.2a.

It can be observed that alloys with x = 20 and 21, which are in the austenite phase (highest symmetry in crystal structure) have more ultimate compression strength than the alloys in martensite phase (lower symmetry crystal structure). J. Liu *et al.* [98] reported a very high compressive strength (2000 MPa) of $Co_{50}Ni_{22}Ga_{28}$ polycrystalline alloy as compared to our result for $Co_{50}Ni_{20}Ga_{30}$ alloy. The high compressive strength obtained by them may be due to the lower annealing temperature (900 °C) used and higher Ga content in their alloy. It is possible that the percentage of γ-phase is very high in their sample processed at 900 °C. Similar higher ultimate compressive strength (~1600MPa) has been reported [134] for samples near the stoichiometric composition and annealed at 800 and 900 °C. Since the MT peaks observed in DSC curves were very weak for the alloys annealed at lower temperature, SME is also expected to be low for these alloys. So, we did not investigate *S-S* behavior of alloys annealed lower than 1000 °C.

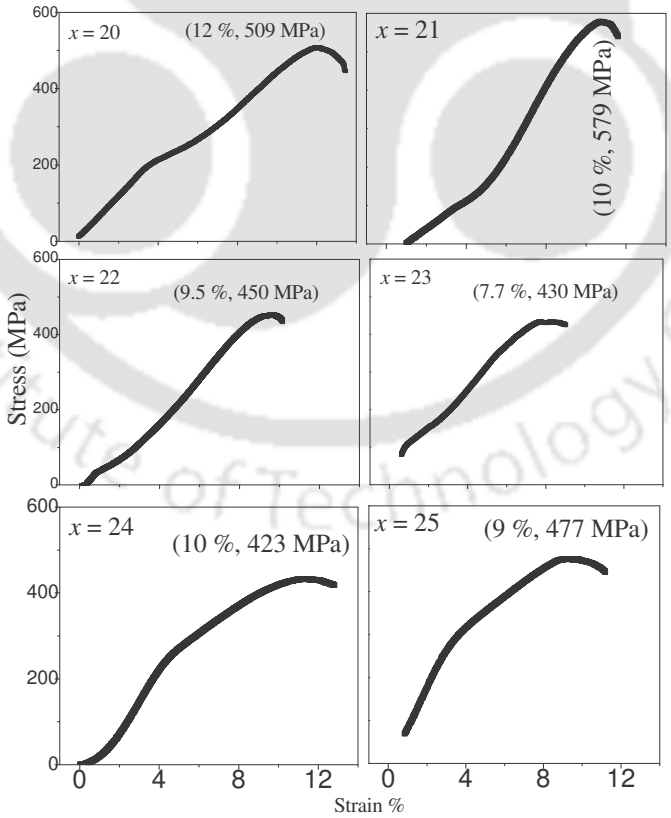

Fig. 4.6.2.a: Stress-Strain curve of $Co_{70-x}Ni_xGa_{30}$ ($20 \leq x \leq 25$) alloys obtained from compression test.

SME of the alloys was estimated by measuring the length of the sample before and after compression and then after the recovery of the residual strain after heating the load cycled alloy above the austenite finish temperature. The stress-strain data was recorded during compression loading and during the release of the load. The corresponding data are shown in Fig. 4.6.2b. The pre-strain (ε_p) value for ~ 200 MPa compressive load, residual strain (ε_r), strain recovery percentage (ε_{SME}) and the recovery ratio and strain permanently left with the samples (ε_{per}) are listed in Table 4.6.2

Table 4.6.2: Shape memory effect in $Co_{70-x}Ni_xGa_{30}$ ($20 \leq x \leq 25$).

x	ε_p %	Pressure(MPa)	ε_r %	ε_{SME} %	Recovery ratio	ε_{per} %
20	4.19	220	0	0	Super elastic	0
21	5.4	201	3	3.3	86.7	0.5
22	4.4	215	3	2	67.3	1
23	2.65	209	2	1	48.1	1
24	4.2	209	3	2	65.4	1
25	2.29	200	0.5	0	0	0.5

The alloy with x = 20 shows the pseudo elastic behavior i.e., after releasing the compressive load, it reverts back to the original length. This behavior is expected from this sample since the austenite finish temperature of this alloy is lower than room temperature. All the other alloys exhibited some residual strain after releasing the applied load (compression) and recovery of the length (ε_{SME} %) was observed for these alloys after heating them to temperatures above A_f. The alloy with x = 25 exhibited very small residual strain on application of 200 MPa pressure and the recovery of the length of the sample was also very small. This may be due to the higher A_s temperature of this alloy, requiring a higher applied pressure to induce SME in it.

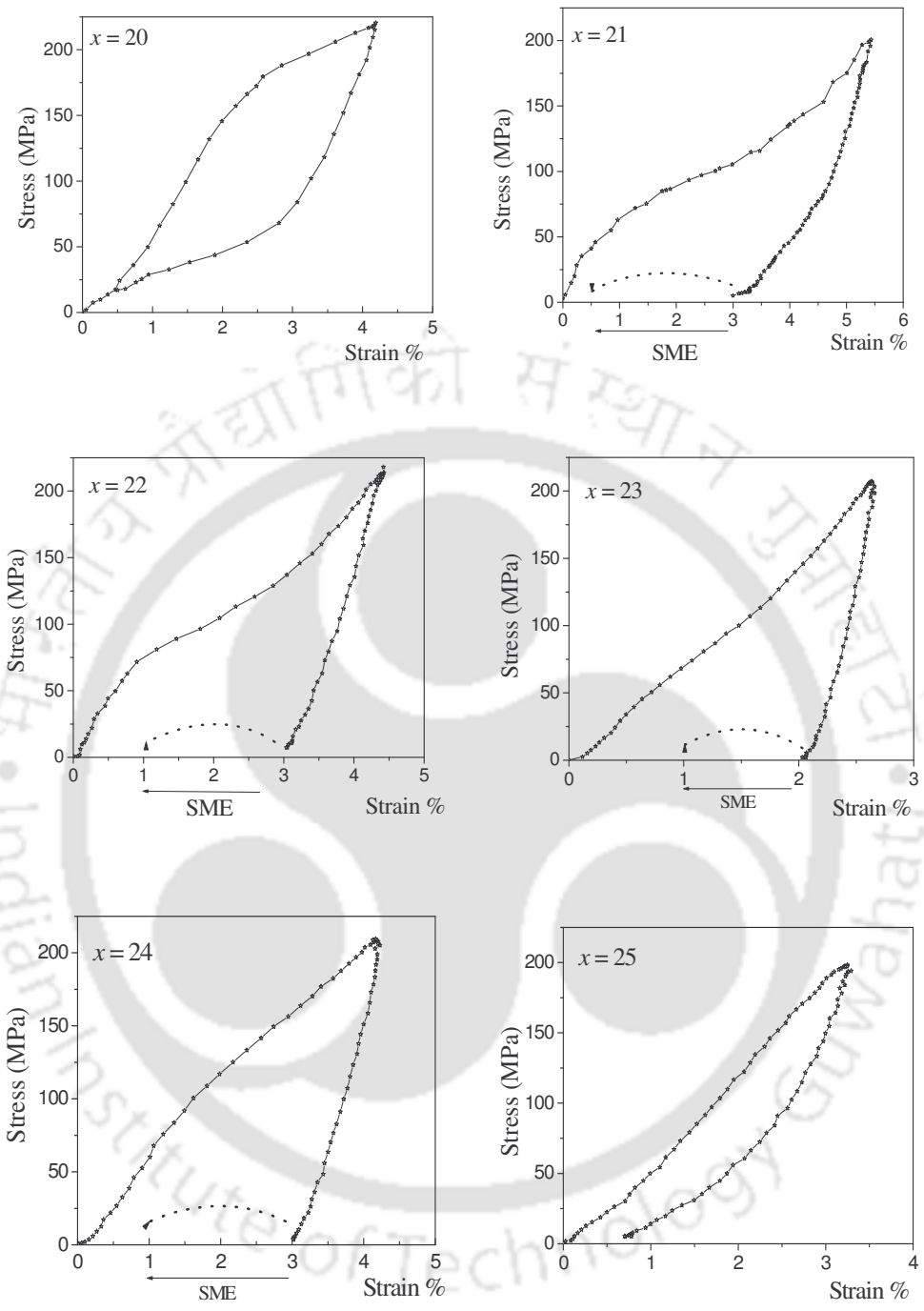

Fig. 4.6.2b: Shape memory effect of $Co_{70-x}Ni_xGa_{30}$ ($20 \leq x \leq 25$) alloys.

The pseudo elastic behavior of $Co_{49}Ni_{21}Ga_{30}$ single crystal has been observed by Dadda *et al.* [124] under compression with maximum recoverable pseudo-elastic strain of 4%. Chernwenko *et al.* [42] compressed $Co_{49}Ni_{22}Ga_{29}$ single crystal alloy to 200 MPa and after releasing the load, 3.7% residual strain was observed. A complete recovery of the residual

strain was observed after heating the sample above the austenite finish temperature (~ 360K). Y. Chumlyakov et al [134] observed 4.5 % shape memory effect at room temperature for $Co_{49}Ni_{21}Ga_{30}$ single crystal alloy. We observed 3.3 % shape memory effect with $Co_{49}Ni_{21}Ga_{30}$ polycrystalline alloy at room temperature after releasing the load (stressed to 200 MPa , ε_p = 5.4%). The smaller SME observed with our sample may be due to the polycrystalline nature of the alloy. A recovery of 86.7% residual strain on heating to a temperature above A_f has been observed for this sample.

4.7. SUMMARY

$Co_{70-x}Ni_xGa_{30}$ ($20 \leq x \leq 25$) alloys were processed under different conditions in order to understand the variation in the structure and properties of the alloys. Different processing conditions such as annealing temperature, quenching temperature and quenching rate were adopted. The alloys were structurally, thermally, magnetically and mechanically characterized. The highlights of the results obtained from these studies are listed below:

- All alloys, except the one with x =20, when quenched above 1150 °C, show single phase martensite (tetragonal) structure at room temperature.
- A secondary phase develops along with the primary martensite/austenite phase, when quenched below 1150 °C.
- The percentage of γ-phase precipitation increased with the decrease of quenching temperatures.
- All the alloys except the alloys with x = 20 and 21, exhibit MT above room temperature.
- M_s and A_s vary linearly with *e/a* ratio.
- M_s and A_s shift to lower temperatures with a decrease in quenching temperature.
- All the alloys are ferromagnetic at room temperature.
- T_C decreased with a decrease in quenching temperature.
- T_C was lower for samples prepared with higher cooling rate.

- The highest M_{sat} was observed in the alloy with x = 20 at 20 kOe. M_{sat} of this series of alloys was higher than that of $Co_xNi_{25}Ga_{75-x}$ alloys.
- K_{eff} estimated for these alloys in martensite phase are comparable to Ni-Mn-Ga alloy and $Ni_{49}Fe_{18}Ga_{27}Co_6$ alloys.
- K_{eff} increases with a decease in quenching temperature whereas, M_{sat} shows the opposite trend.
- Critical exponent β estimated near the magnetic phase transition in $Co_{45}Ni_{25}Ga_{30}$ alloy yielded a value close to the one predicted by the 3-*d* Heisenberg model. The γ-exponent's value was slightly higher than the value predicted by the model.
- The ultimate compressive strength of these alloys ranged from 423 to 579 MPa.
- The alloy with x = 20 exhibited perfect super-elastic behavior.
- Alloys with $x > 21$ showed shape memory effect. Residual strain of 3% was observed in the alloy with x = 21 after applying a strain of 5.4% (200 MPa) at room temperature. Recovery of strain due to SME has been observed for this sample is 4.2%; shape recovery percentage of this alloy has been observed as 86.7%.

INVESTIGATION ON $Co_{48-x}Ni_{22}Ga_{30-y}T_{x+y}$ (T = Fe, Mn and $x + y = 1$, 3 and 6) ALLOYS

It has been reported [135] that partial substitution of Mn by Fe in Ni-Mn-Ga alloy enhances the magnetic properties of the alloys. Fe substitution increases the Ni magnetic moment from the value of 0.33 μ_B [86] for the Heusler composition to 0.41 μ_B. The local magnetic moment of Mn in Ni-Mn-Ga alloy is very high compared to the other constituent elements. In this work, small amount of Fe or Mn has been substituted for Co and Ga in $Co_{48}Ni_{22}Ga_{30}$ alloy in order to change the magnetic and mechanical properties of the alloy. The e/a ratio decrease rapidly with the addition of Fe/Mn atom. From the results obtained in the last two chapters of this thesis, it is evident that the *e/a* has to be greater than 7.42 for ensuring that the *MT* occur above room temperature in Co-Ni-Ga alloys. This was kept in mind and substitution was done in such a way that e/a value was between 7.42 and 7.46 in the $Co_{48-x}Ni_{22}Ga_{30-y}T_{x+y}$ (T = Fe, Mn and $x + y = 1$, 3 and 6) alloys.

5.1. PREPARATION AND PROCESSING OF THE ALLOYS

The alloy ingot of each composition was prepared by arc melting method, as per procedures already outlined in chapter 2. Subsequently, the alloy ingots were cast in a cylindrical shape, annealed at 1150 °C and quenched in ice water. Alloys annealed at 1150 °C were found to be suitable for machining. Cylindrical shaped samples of ~10 mm diameter and ~ 7.5 mm length were cut out for compression testing. Samples of the same

diameter but smaller length were used for microhardness measurement. The composition of the master alloys was determined by SEM-EDS analysis as per procedure described in chapter 2. The EDS data presented are the mean of at least three independent observations. Table 5.1 shows the compositions of the starting and finally processed alloy samples.

Table 5.1: Compositions of various quaternary alloys obtained from EDS observations

Starting alloy compositions (at. %)					Composition.of the processed alloys (at.%)				
Co	Ni	Ga	Fe	Mn	Co	Ni	Ga	Fe	Mn
48	22	29	1	0	47.69	21.63	29.35	1.33	0
46	22	29	3	0	45.68	21.99	28.90	3.43	0
43	22	29	6	0	42.47	21.83	29.32	6.38	0
48	22	29	0	1	47.27	22.71	28.73	0	1.29
46	22	29	0	3	46.06	21.87	29.41	0	2.66
44	22	28	0	6	43.72	21.60	28.47	0	6.21

It can be seen from that data presented in Table 5.1 that the mean composition values of the processed alloys are very close to the starting compositions. These studies show that with the addition of the fourth element, Ni concentration reduces slightly, whereas, Ga concentration varied slightly. As a result, the *e/a* value decreases with respect to that of the starting composition. Here after, alloys substituted with 1 at.%, 3

at.% and 6 at.% Fe will be designated as Fe1, Fe3 and Fe6, respectively. Similarly, the Mn substituted alloys will be designated as Mn1, Mn3 and Mn6, respectively.

5.2. CRYSTAL STRUCTURE AND MICROSTRUCTURE

5.2.1. Crystal Structure

It was difficult of make fine powders of the processed alloys for XRD measurement due to their highly ductile nature. Thus, coarse powders of Fe1 and Mn1 samples, and polished plates of bulk Mn6 and Fe6 samples were used for recording the XRD patterns. XRD patterns of Fe1 and Mn6 alloys are shown in the Fig. 5.2.1.a and Fig. 5.2.1.b, respectively. It can be seen from the typical XRD patterns shown in the two figures that the quality of the data obtained is not suitable for Rietveld refinement. Hence, these XRD patterns were merely used to identify the phases present in various samples and no least squares refinement was attempted with the data. The XRD pattern of Fe1 alloy is similar to the unsubstituted parent $Co_{48}Ni_{22}Ga_{30}$ alloy (*cf.* Fig.5.2.1a) and could be indexed to *bct* structure (martensite phase). The peak near $2\theta = 51°$ indicates that some amount of γ- phase is present in both Fe1 and Mn1 alloys. In the case of Mn6 sample (Fig. 5.2.1b), one broad peak at $2\theta = 44°$ and one weak peak at $2\theta = 65°$ have been observed. XRD patterns recorded under slow scan near the Bragg peak at $2\theta = 44°$ is shown as inset in Fig. 5.2.1.b. The inset reveals the presence of two overlapping peaks at this 2θ value. These two peaks have been identified as $\gamma(111)$ and *A2* (110) when compared with the XRD data on $Co_{50}Ni_{20}Ga_{30}$ alloy (*cf.* Fig.4.2.1e). Similarly, the peak at $2\theta = 65°$ has been assigned to *A2* (200) plane.

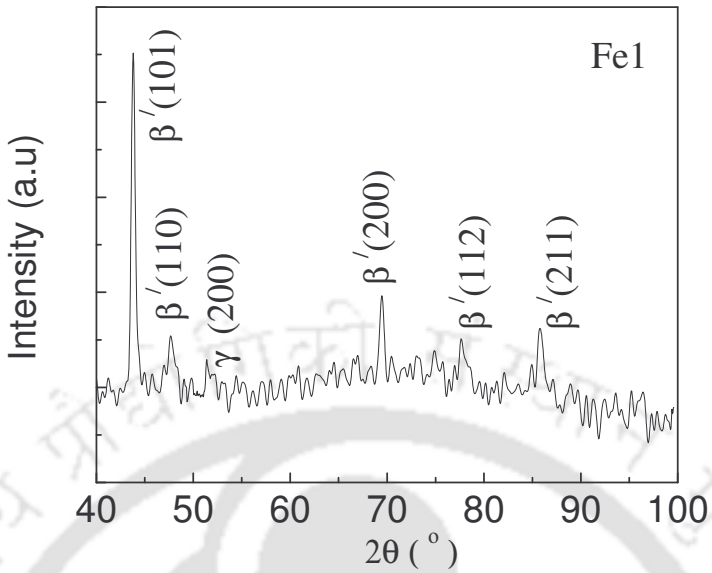

Fig. 5.2.1.a: XRD pattern of Fe1 alloy

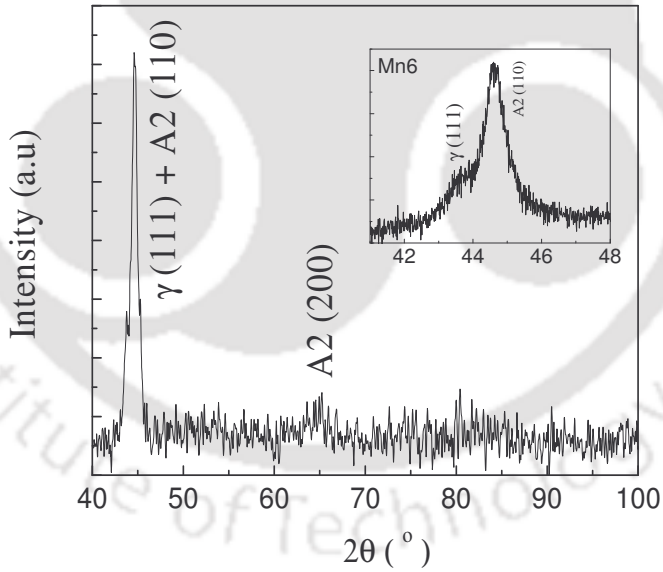

Fig. 5.2.1.b: XRD pattern of Mn6 alloy

Thus, the XRD studies on the quaternary alloy samples established that Fe1 and Mn1 alloys have martensite structure at room temperature, whereas, the rest, *viz*., Fe3,

Mn3, Fe6 and Mn6 alloys have austenite structure at room temperature. All the alloys contained small amount of γ-phase precipitates. The presence of the γ-phase has resulted in the high ductility of the samples. The presence of the γ-phase precipitates in all the alloys clearly shows that the alloys have to be processed at temperatures higher than 1150 °C for preventing the precipitation of the additional phase.

5.2.2. Microstructure

Optical micrographs of the quaternary alloys are shown in Fig.5.2.2.a-f. Micrographs of Fe1 and Mn1 alloys contained all the features of parent alloy of (Fig. 4.2.1.a) with one difference, *viz*., the additional presence of the white (γ-phase). It is interesting to note that addition of just 1 at.% of Fe/Mn to Co-Ni-Ga can induce γ-phase precipitat ion in this series of alloys. This merely confirms that the structure and properties of Co-Ni-Ga FSMAs are strongly influenced even by a small compositional and constituent variation. The twins present in the micrographs (Fig. 5.2.2.a & d) are the characteristics of the martensite phase. In the micrographs of Fe3 and Mn3 alloys, the secondary γ- phase is present along with the primary phase. But no twins are visible in these micrograph which means that the martensitic transformation temperatures of Fe3 and Mn3 are lower than room temperature. Thus, the optical micrographs of Fe3, Fe6, Mn3 and Mn6 alloys provide visual confirmation of the austenite structure revealed by XRD studies.

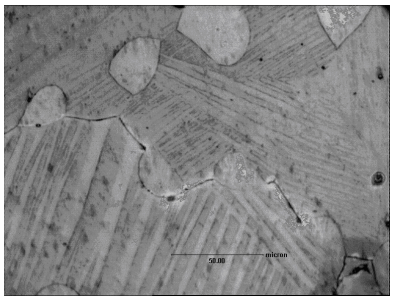

(a) Fe1; Full Scale bar represents 50µm

(d) Mn1; Full Scale bar represents 50µm

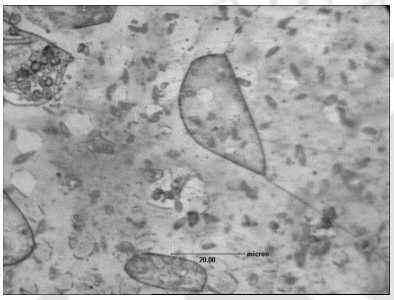

(b) Fe3; Full Scale bar represents 20 µm.

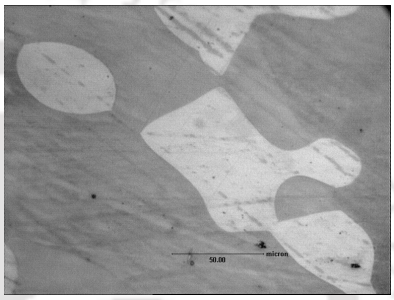

(e) Mn3; Full Scale bar represents 50 µm.

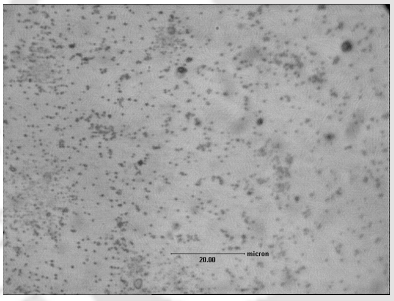

(c) Fe6 Full Scale bar represents 20µm.

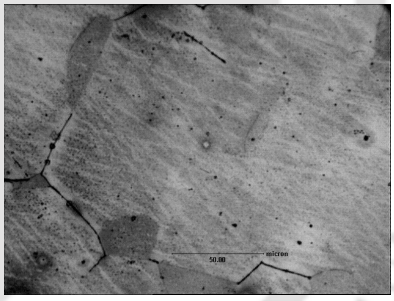

(f)Mn6; Full Scale bar represents 50 µm.

Fig. 5.2.2: Optical micrographs of (a) Fe1, (b) Fe3, (c) Fe6, (d) Mn1 (e) Mn3, and (d) Mn6 alloys. Thick dark lines and dark spots in (d) represent minor cracks and porosities present in the sample.

5.3. THERMAL CHARCTERIZATION

DSC curves obtained for Fe1 and Mn1 alloys are shown in Fig.5.3. The DSC curve of the parent alloy is also shown in the figure for comparison. Fig. 5.3 shows that Fe1 and Mn1

alloys have martensitic transformation (MT) temperatures above room temperature. DSC curves of Fe3, Fe6, Mn3 and Mn6 alloys recorded above room temperature did not show any endothermic peak on the heating cycle, which confirmed that the MT of Fe3, Fe6, Mn3 and Mn6 alloys is below room temperature. The same was confirmed by low temperature magnetization measurements (since the working range of the available DSC was from room temperature to 660 ˚C). It is evident from the DSC results that addition of Fe / Mn shifts the MT temperatures to higher temperature. However the shift caused by Mn addition is less than Fe addition. The DSC peaks of Fe1 and Mn1 alloys are wide and spread over a wide temperature range. This is the signature of existence of other phase(s) along with the martensite phase. XRD and optical microscopy studies have already confirmed the presence of γ-phase along with the martensite phase in these alloys. The MT temperatures of Fe1 and Mn1 determined from the DSC curves are listed in Table 5.3.

Table 5.3: Martensitic transformation temperature of Fe1 and Mn1 alloys

Composition of alloy	e/a	A_s (°C)	A_f (°C)	M_s (°C)	M_f (°C)
Parent alloy ($Co_{48}Ni_{22}Ga_{30}$)	7.42	78	81	37	35
Fe1	7.44*	91	120	57	40
Mn1	7.44*	86	111	78	50

* *e/a* ratio is calculated from the composition obtained from EDS measurements.

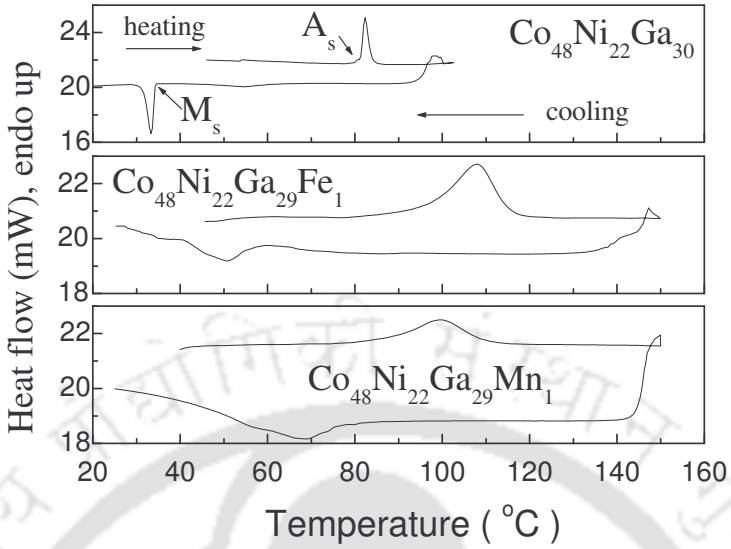

Fig. 5.3. DSC curves of Mn1, Fe1 and the parent alloy.

The *e/a* ratio of Fe3, Fe6, Mn3 and Mn6 calculated from the compositions determined from EDS measurement are 7.43, 7.39, 7.40 and 7.38, respectively. Hence, MT temperatures of these alloys must be lower than Fe1 and Mn1 alloys. Substitution of Ga (instead of Co) with Mn/Fe would yield alloys with higher e/a ratio which would have MT higher than room temperature. In the previous chapter, it was seen that the alloy with e/a = 7.43, yields A_s = 111 °C and M_s = 69 °C. In the case of Fe3, e/a = 7.43, A_s has been found as 12 °C (from low temperature magnetization measurement as shown in Fig.5.5.1.a below). This shows that though the MT temperatures vary linearly with e/a for SMAs, the slope of the *e/a* versus M_s or *e/a* versus A_s plots are different for different sets of SMAs. Similar observations have been made by Krenke et al [63] with respect to different Ni-Mn based Heusler alloys.

5.4. MASS DENSITY

Density of the quaternary alloys is listed in Table 5.4. Density decreases with an increase in Fe/Mn at%. This composition dependence of density is due to the relatively smaller mass density of the substituting atoms Fe (7.87 g/cm^3) and Mn (7.4 g/cm^3) as compared to that of Co.

Table 5.4: Mass Density of Fe1, Mn1, Fe3, Mn3, Fe6 and Mn6 alloys

Alloy sample	Measured density ρ_A (g/cm^3)	Alloy sample	Measured density ρ_A (g/cm^3)
Fe1	8.603 ± 0.004	Mn1	8.596 ± 0.004
Fe3	8.378 ± 0.004	Mn3	8.298 ± 0.004
Fe6	8.108 ± 0.004	Mn6	8.142 ± 0.004

5.5. MAGNETIC PROPERTIES

5.5.1 Variation of magnetization with temperature (M-T) at low temperatures

DSC curves of Fe3, Mn3, Fe6 and Mn6 recorded from room temperature onwards did not show any signature of the martensitic transformation (*MT*) in these alloys. In order to locate the *MT* in these alloys, magnetization measurements were performed on these samples from 100 K to 300 K (on the heating cycle) at a constant applied field of 50 Oe. The *M-T* curves for the Fe and Mn alloys are shown in Fig. 5.5.1.a and Fig. 5.5.1.b, respectively. Austenite phase has higher magnetocrystalline anisotropy than the martensite phase. Thus, an increase in magnetization is observed during reverse martensitic transformation as depicted in Fig. 5.5.1.a and Fig. 5.5.1.b.

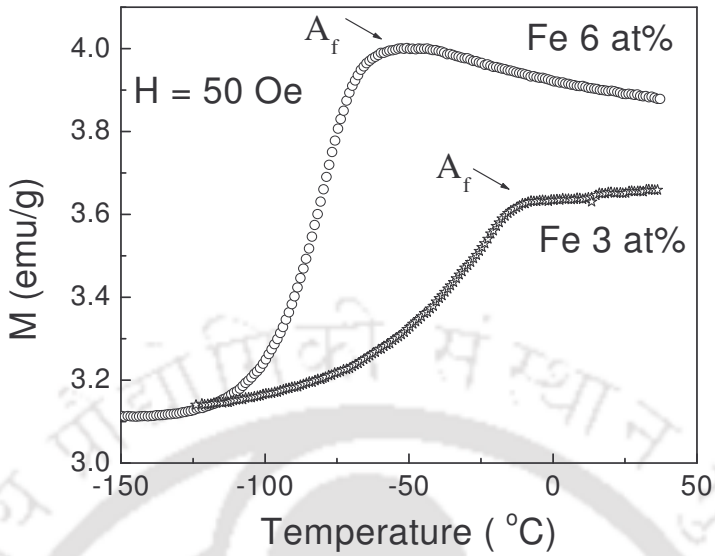

Fig. 5.5.1.a:. M-T graph of Fe3 and Fe6 alloy

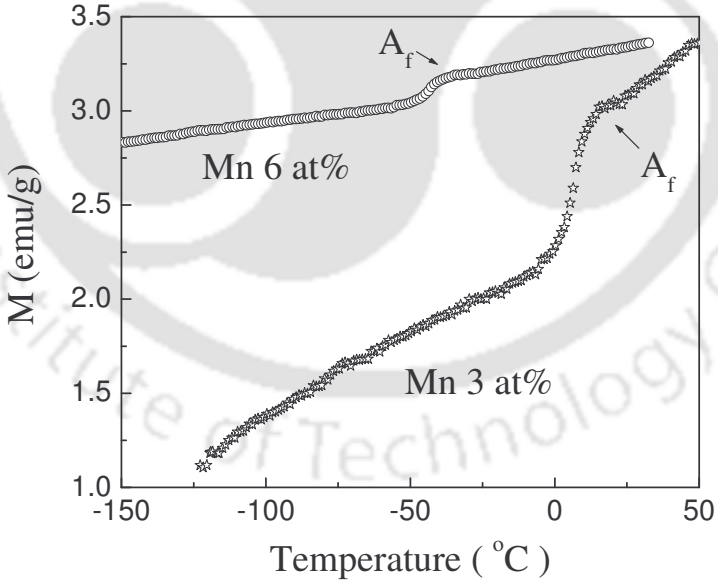

Fig. 5.5.1.b: M -T graph of Mn3 and Mn6 alloys.

The increase in magnetization at the structural transitions is not very sharp for all the samples. This gentle increase in magnetization conveys the same information as the broad peaks observed in the DSC curves of Fe1 and Mn1 samples (Fig. 5.3), namely, the presence of the additional phase along with the primary phase in these alloys. Due this broad nature of the reverse maternsitic transformation, we have estimated only the austenite finish temperature A_f from this data. A_f for Mn3, Fe3, Mn6 and Fe6 measured from the *M-T* graphs are 15 °C, -10 °C, -40 °C and -59 °C, respectively.

5.5.2 Variation of magnetization with temperature (M-T) at high temperatures

All the alloys were ferromagnetic at room temperature. In order to determine the Curie temperature of the alloys, *M-T* measurements were carried out from room temperature onwards under a constant applied field of 50 Oe. *M-T* plots of Fe1, Fe3, Fe6 and Mn1, Mn3, Mn6 alloys are shown in Fig. 5.5.2.a and Fig. 5.5.2.b, respectively. T_C estimated from the local minimum point in the *dM/dT vs. T* plots and listed in Table 5.5.2.

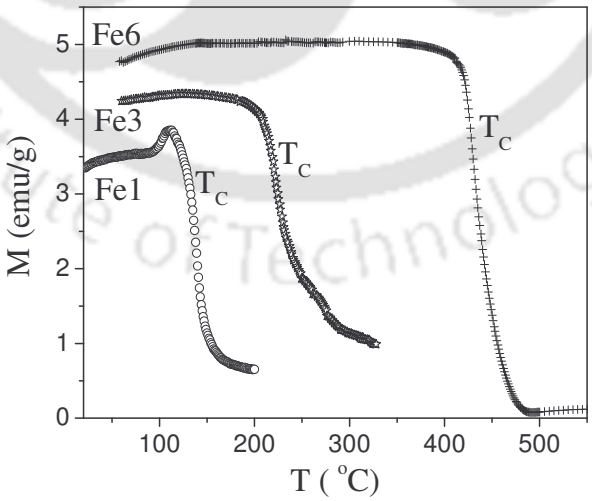

Fig. 5.5.2a: Variation of magnetization with temperature of Fe1, Fe3 and Fe6 alloys

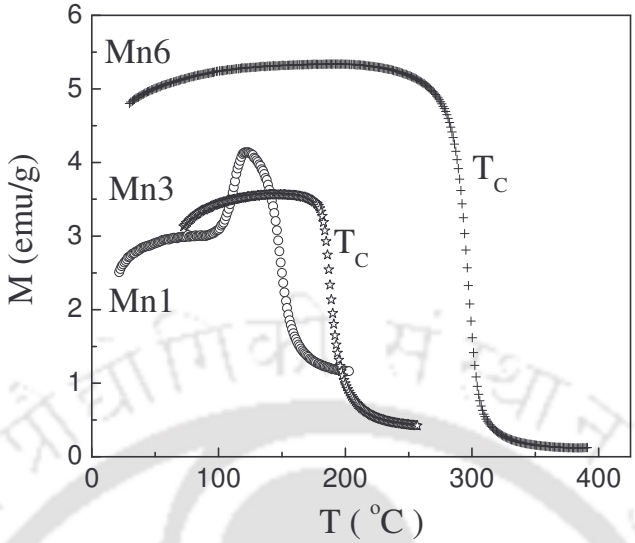

Fig. 5.5.2b: Variation of magnetization with temperature of Mn1, Mn3 and Mn6 alloys.

Table 5.5.2: Curie temperature (T_C) of Fe1, Mn1, Fe3, Mn3, Fe6 and Mn6 alloys

Alloy	T_C (°C)	Z_m	Alloy	T_C (°C)	Z_m
Fe1	139	-0.37	Mn1	141	-0.36
Fe3	219	-0.35	Mn3	185	-0.32
Fe6	428	-0.32	Mn6	288	-0.22

It has been observed that T_C of the quateranry samples are higher than the T_C of $Co_{48}Ni_{22}Ga_{30}$ (T_C = 126 °C). This increase in T_C may be attributed to the high magnetic moments of Fe and Mn [135]. Wu *et.al* [86] have reported that $Ni_{52}Mn_{16}Fe_8Ga_{24}$ has a higher T_C (381 K) than $Ni_{52}Mn_{24}Ga_{24}$ (348K). Substitution of Fe for Mn strengthens the magnetic exchange interactions, thereby increasing the Curie temperature to 381 K. It can be seen from Table 5.5.2 that T_C increases with the increase of Fe/Mn concentration. This

is expected as the magnetic valence number increases with the increase in Fe/Mn concentration. However, Z_m for Mn3 and Mn6 are higher than Fe3 and Fe6, respectively. Thus T_C of Mn3 should be higher than Fe3, and that of Mn6 should higher than Fe6. The opposite behavior observed in this study may be due to the antiferromagnetic alignment of the moments of neigbouring Mn atoms. It has also been pointed out [74] that magnetization of Mn alloys obeys the Slater-Pauling curve only for very dilute concentrations of Mn, which helps us in re-concluding the above results.

5.5.3. Variation of magnetization with field (M-H) at room temperature

The *M-H* data recorded at room temperature for the alloys under investigation are shown as in Fig. 5.5.3.a and Fig. 5.5.3.b. Magnetization increases with an increase of Fe/Mn concentration due to the higher magnetic moments of the Fe or Mn atoms as compared to that of Co and Ga atoms. The saturation magnetization (M_{sat}) of Fe1 was found to be 48 emu/g, corresponding to the magnetic moment 2.12 μ_B per formula unit and that of Mn1 has been observed to be 39 emu/g, corresponding to 1.73 μ_B per formula unit (*cf.* Table 5.5.3). However, Fe6 and Mn6 samples were found to have the same magnetic moment of 2.44 μ_B per formula unit. Room temperature M_{sat} of polycrystalline $Ni_{50}Mn_{30}Ga_{20}$ at an applied field of 20 kOe has been reported as 52.1 emu/g [122]. A comparison will show that Co-Ni-Ga with Fe/Mn substitution can yield alloys with M_{sat} values comparable with the prototype Ni-Mn-Ga alloy. K_{eff} was estimated for each alloy using law of approach to saturation. M_{sat} and K_{eff} estimated for the quaternary alloys are listed in Table 5.5.3. K_{eff} of polycrystalline $Ni_{50}Mn_{30}Ga_{20}$ at room temperature has been reported [122] to be 1.01×10^5 J/m^3. .

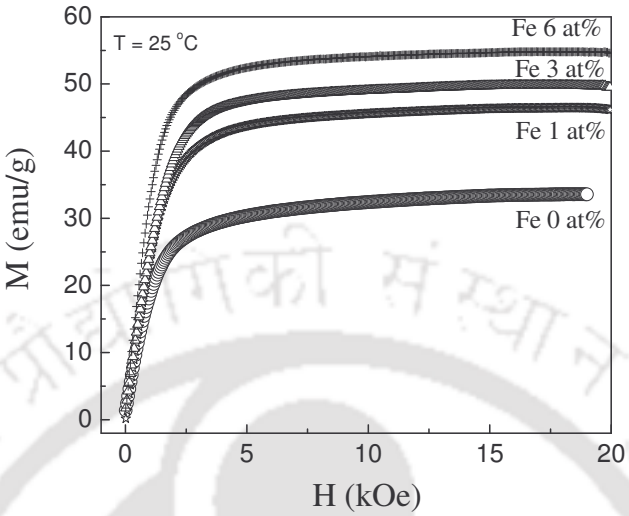

Fig. 5.5.3a: Room temperature *M-H* plots of $Co_{48}Ni_{22}Ga_{30}$ (Fe0), Fe1, Fe3 and Fe6 alloys.

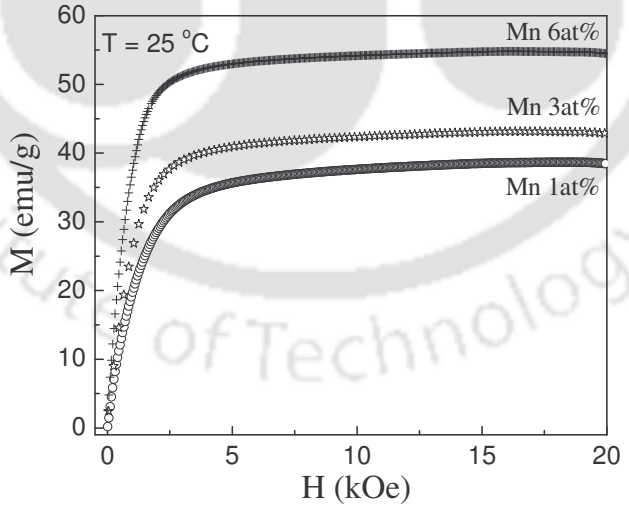

Fig. 5.5.3b: Variation of magnetization with applied field of Mn1, Mn3 and Mn6 alloys.

Table 5.5.3: M_{sat} and K_{eff} of Fe1, Mn1, Fe3, Mn3, Fe6 and Mn6 alloys

alloy	M_{sat} (Am^2/kg)	K_{eff} x 10^5 (J/m^3)	alloy	M_{sat} (Am^2/kg)	K_{eff} x 10^5 (J/m^3)
Fe1	47.82	1.28	Mn1	39.10	1.25
Fe3	50.14	1.20	Mn3	43.63	1.04
Fe6	55.10	1.16	Mn6	55.12	1.13

** emu/g ≅A-m^2/kg; M_{satt} is multiplied by corresponding density to obtain it in A/m.*

Density values of the alloys are listed in Table5.4

*** the coefficient 'b' was estimated in $(Oe)^2$ and converted to A/m (1 Oe = $10^3/4\pi$ A/m)*

*** $K_{eff} = \sqrt{\frac{15b}{4}}\,\mu_0 M_{sat}$ [109] *for tetragonal structure.*

5.6 MECHANICAL PROPERTIES

5.6.1 Microhardness (VHN)

The results obtained from microhardness measurement on the quaternary alloys are listed in Table 5.6.1. It is seen that microhardness (VHN) increases with an increase in the concentration of Fe/Mn. The soft martensite primary phase in Fe1 and Mn1 alloy is expected to exhibit lower hardness as compared to the cubic austenite phase alloys. The increased hardness of the alloys with higher Fe/Mn also shows that the amount of γ-phase decreases as the Fe/Mn concentration is increased. Liu et.al [98] has reported a gradual disappearance of γ-phase with an increase in Fe concentration in $Co_{50}Ni_{22-x}Ga_{28}Fe_x$ alloys.

It has to be pointed out that high VHN is a not desirable attribute for a good shape memory alloy.

Table 5.6.1: Microhardness of Fe1, Fe3, Fe6, Mn1, Mn3 and Mn6 alloys. Load applied for the indentation is 100 gf in all the cases.

x ⟶	Fe1	Fe3	Fe6	Mn1	Mn3	Mn6
VHN (GPa)	312	384	439	308	360	409

5.6.2 Compressive strength

Alloys of cylindrical shape (~10 mm diameter and 7.5mm length) with flat ends were used for the tests. Compressive stress was applied vertically in a UTM till failure. The stress-strain curves of Fe1, Mn1, Fe3, Mn3, Fe6 and Mn6 alloys are shown in Fig.5.6.2. It can be seen from Fig. 5.6.2 that Mn addition yields higher compressive strength than Fe addition. The mechanical strength of Mn6 alloy was so high that even for 1200 MPa load (~80 kN force), it could not be cracked. Mn3 alloy has been found to have the highest strain before failure. A very high compressive strength (~2000 MPa) and corresponding strain (~20 %) has been reported for $Co_{50}Ni_{21}Ga_{28}Fe_1$ alloy [98]. We observed a similar strain at very low compressive stress in Mn1 and Mn3 samples. The high compressive strength reported in $Co_{50}Ni_{21}Ga_{28}Fe_1$ alloy may be due to the low annealing and quenching temperature (900 °C) used to prepare the alloy. The strain exhibited by Fe1, Mn1, Fe3 and Mn3 for 400 MPa stress are 7.8%, 6.7%,, 8.8% and 6.9%, respectively. But strain exhibited by Fe6 and Mn6 alloys is very low (4% and 3.5%, respectively). Thus, addition of Fe or Mn beyong 3 at% will not help to enhancing the SME of these alloys.

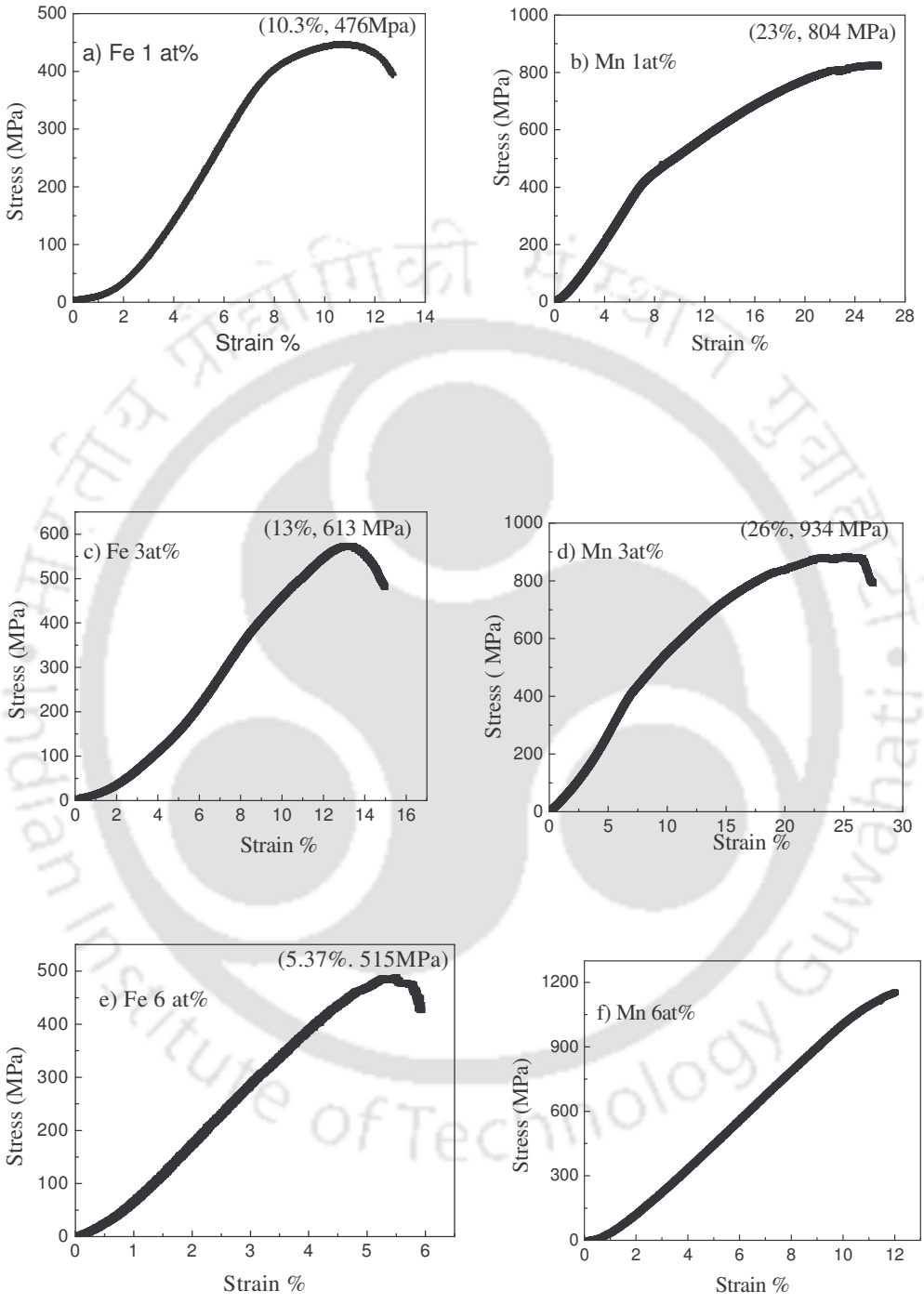

Fig.5.6.2: Compressive strength of (a) Fe1, (b) Mn1, (c) Fe3, (d) Mn3, (e) Fe6, and (f) Mn6 alloys

5.6.3. Shape memory effect and pseudo-elasticity

Stress-strain data of the alloys recorded during loading (to ~ 400 MPa) and unloading cycles are shown in Fig. 5.6.3.a-f. SME was estimated from the recovery of the residual strain by heating the sample above A_f after one cycle of loading and unloading. The pre-strain (ε_p %) due to loading, residual strain (ε_r %), shape memory effect (ε_{SME} %), recovery ratio due to heating and permanent strain (ε_{per} %) left on the sample determined from experiments are listed in Table 5.6.3. Residual strain and ε_{SME} % for the parent (*i.e.* $Co_{48}Ni_{22}Ga_{30}$) alloy is also listed again to facilitate comparison. The alloys Fe1 and Mn1 show SME% of 1.9% with recovery ratio of almost 60. The Fe3 and Mn3 alloys exhibit comparatively smaller SME% but recovery ratio is 100. Thus, it can be inferred that Fe3 and Mn3 behave more like psudo-elastic materials. No residual strain was observed for Fe6 and Mn6 alloys and hence they have pseudo–elastic behavior.

Table 5.6.3: Shape memory effect in Fe1, Fe3, Mn1 and Mn3 alloys.

alloy	ε_p %	Stress (MPa)	ε_r %	ε_{SME} %	Recovery ratio	ε_{per} %
Parent	4.4	215	3.0	2.0	67.3	1
Fe1	8.8	445	3.0	1.9	60	1.2
Mn1	7.39	417	3 .6	2.2	59.2	1.5
Fe3	7.1	354	1.6	1.6	100	0
Mn3	8.9	423	1.9	1.9	100	0

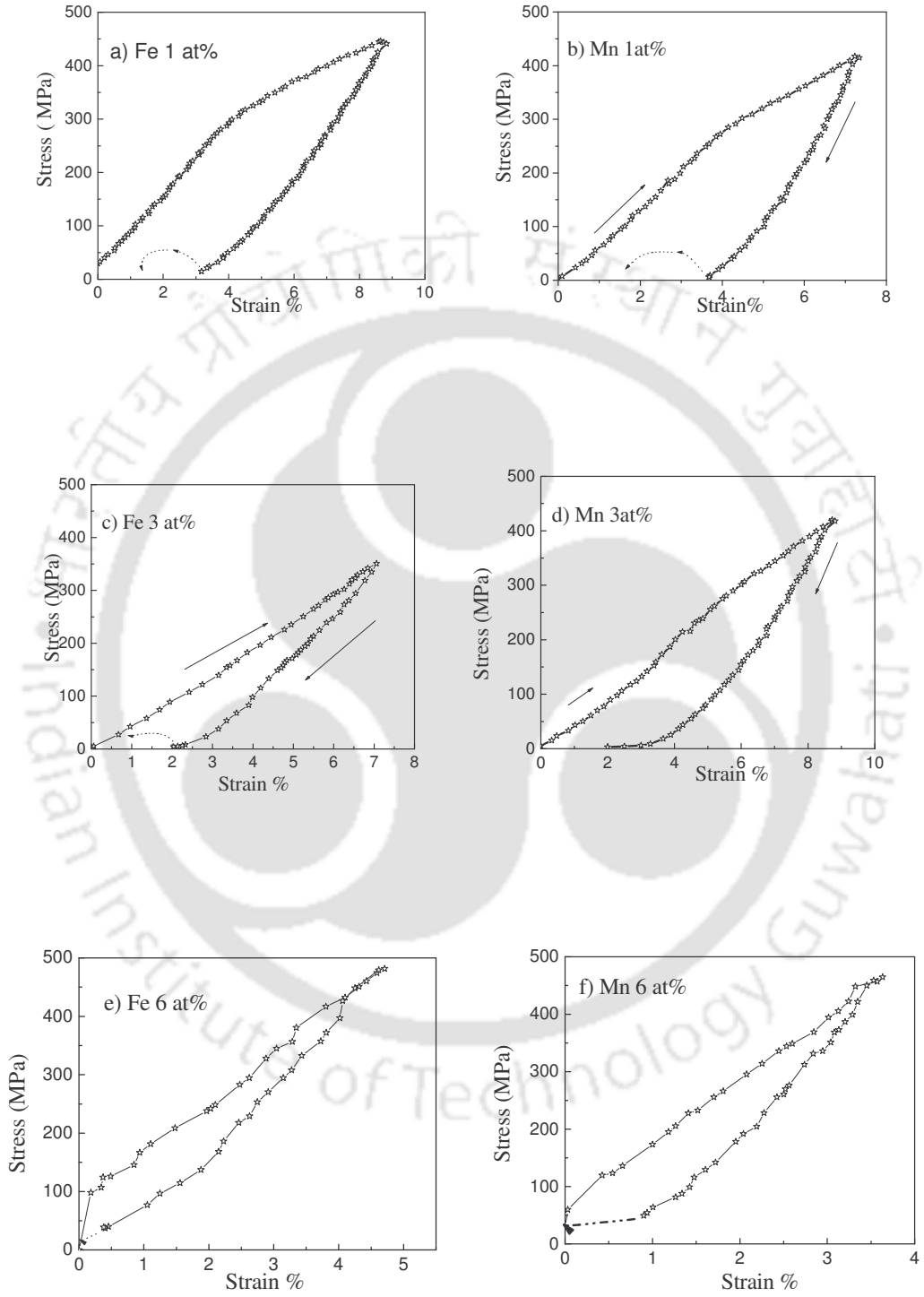

Fig. 5.6.3: Shape memory and pseudo-elastic of Fe_x and Mn_x (x = 1, 3, and 6) alloys.

The ε_{SME} % reported for $Co_{49}Ni_{21}Ga_{30}$ single crystal was 4.9% to 6.7% [134], for Ni-Mn-Ga was 2.8% to 6.1% [57] and for Ni-Fe-Ga was 5.1% to 8.1% [57]. The ε_{SME} % values obtained in the present samples are much lower than the reported values on other FSMAs. The low ε_{SME} % obtained in the current investigations may be attributed to the polycrystalline nature of the alloys.

5.6.4 Magnetic Field Induced Strain (MFIS)

Magnetic field induced strain (MFIS) measurement at room temperature was carried out without the application of any mechanical load. Samples of disc shape with diameter ~ 10 mm and length ~ 3 mm were used for the measurement. MFIS measurements were performed on four samples, out of which two are in the martesite phase (Fe1 and Mn1) and the two are in austenite phase (Fe3 and Mn 3). MFIS was measured for the samples as a function of magnetic field using the MFIS set-up described in chapter 2. In each measurement, magnetic field was raised up to 5000 G and then lowered back to zero. The results are shown as in Fig. 5.6.4. The graphs show that the strain% increases as a function of magnetic field and attains the maximum value near 5 kG. For the unsubstituted sample MFIS was found to be very small (~ 0.0035% at B = 5 kG). With the addition of Fe/Mn, the maximum MFIS increased to 0.012 % (for Fe3), and 0.011% (for Mn3).

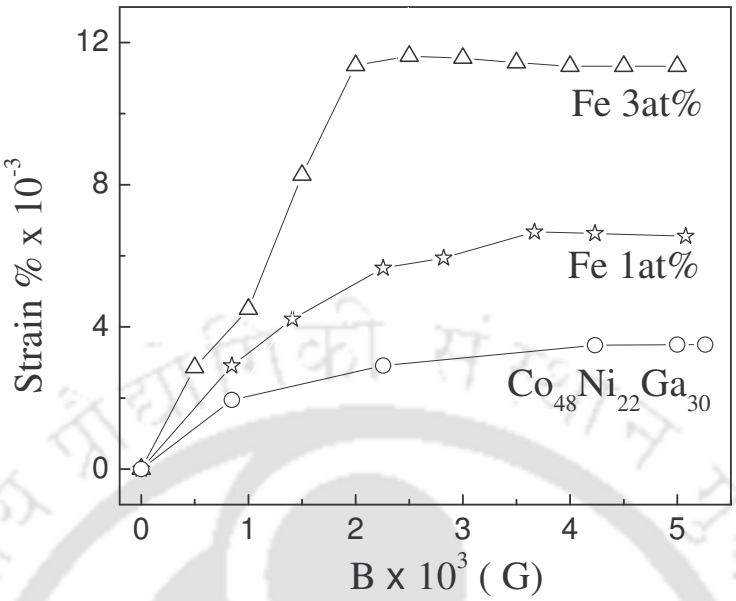

Fig. 5.6.4a: MFIS of $Co_{48}Ni_{22}Ga_{30}$, Fe1 and Fe3

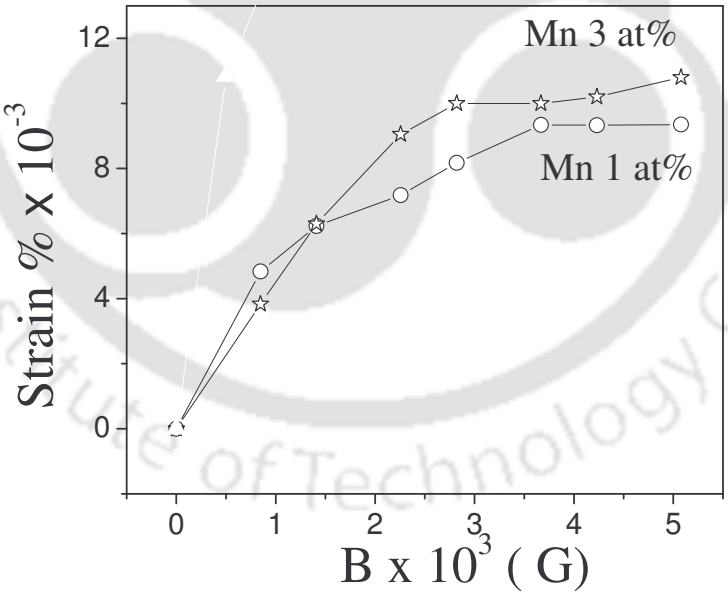

Fig. 5.6.4b: MFIS of Mn1, Mn3 and Mn6 alloys

MFIS of ~ 0.19% has been reported in unstressed single crystals of Ni_2MnGa with magnetic fields of 8 kG applied at 265 K [23], whereas in Fe_3Pt FSMA, MFIS of 0.6%

has been reported at 4.2K [43]. MFIS in polycrystalline samples was much smaller than that observed in single crystal samples. Soonjong Jeong *et. al*. [80] observed MFIS in $Ni_{19.5}Mn_{27}Ga$ polycrystalline alloys at different temperatures. They obtained maximum MFIS of 0.01% at ~ 37˚C under 1 kG applied magnetic field in the martensite phase. Our results (0.009 % at 5 kG for Mn1) are comparable to their reported value. The higher MFIS observed for austenite Fe3 and Mn3 alloys may be due to the magneto-super-elastic effect [80, 137]. This effect is the magnetic analogue of the mechanical super-elastic effect. When magnetic field is applied well above the A_f, all martensitic transition temperatures, e.g. M_s, M_f, A_s and A_f shift to higher temperature side. With this feature, it is possible to induce a structural phase transformation which can be reversed by withdrawing the magnetic field. In the case of $Ni_{54}Mn_{21}Ga_{25}$, the rate of shift of the transformation temperatures on application of a magnetic field is reported to be only about ~1 K/T [137-138]. But for $Ni_{50.3}Mn_{33.8}In_{15.9}$, it has been reported to be as high as ~10 K/T [137]. Thus, field induced structural transformation may be possible in Fe3 (A_f = -10 °C) and Mn3 (A_f = 15 °C) alloys. In magnetic field induced super-elasticity, the maximum field induced strain relies on the difference of crystallographic dimensions in the martensite and austenite state. When a field of sufficient strength is applied at a temperature corresponding initially to the austenitic state, the shift in all characteristic temperature can be large enough to stabilize the martensitic state is stabilized.

To observe FSME, one has to deform the alloy in martensite state by applying external mechanical stress before measuring the strain in magnetic field. The highest MFIS of 10% has been reported [78] for mechanically stressed Ni-Mn-Ga alloy. It may be possible to achieve higher MFIS in the quaternary alloys by a applying a mechanical

stress. Directionally solidified or single crystal Co-Ni-Ga samples would also help in achieving higher uniaxial strains.

5.7. SUMMARY

A series of $Co_{48-x}Ni_{22}Ga_{30-y}T_{x+y}$ (T = Fe, Mn and $x + y = 1$, 3 and 6) alloys have been prepared and their properties have been investigated in this chapter. The basic interest of substitution of Ga and Co by Fe or Mn is to enhance the saturation magnetization and magneto-crystalline anisotropy of these alloys, so that better FSMAs could be obtained.

1. XRD and optical micrograph show that Fe1 and Mn1 alloys exhibit tetragonal martensite structure with precipitation of some amount of γ - phase. Fe6 and Mn6 exhibit a mix structure of bcc austenite and fcc γ - phase.

2. Martensitic transformation temperature was observed for Fe1 and Mn1 alloys above room temperature whereas it was observed lower than room temperature for Fe3, Fe6, Mn3 and and Mn6 alloys

3. T_C of the alloys increased with an increase in Fe/Mn concentration. M_{sat} also increased substantially (almost twice) with the increase of Fe/Mn concentration.

4. Microhardness increased with the increase of Fe/Mn concentration.

5. Compressive strength of the alloy increases with an increase in Mn concentration. A very high compressive strength was observed for the Mn6 alloy.

6 Shape memory effect has been observed in Fe1, Fe3, Mn1 and Mn3 alloys. The other two alloys exhibited pseudo-elastic properties.

7. MFIS of polycrystalline Co-Ni-Ga alloys has been measured for the first time. Our results reveal that MFIS of Fe1 and Mn1 alloys are comparable to the reported value of the unstressed polycrystalline Ni-Mn-Ga alloys.

8. Since MFIS was measured without applying mechanical load on the samples, the strain observed in Fe1 and Mn1 alloys are very low. A high MFIS is expected from these alloys on application of external stress before exposing them to magnetic field.

Three key parameters controlling the magnetic SME are (i) magnetic anisotropy of the martensite, (ii) twinning stress (macroscopic parameter reflecting resistance of martesitic microstructure to rearrangement) and (iii) distortion of lattice. In non-modulated tetragonal martensite, higher compressive stress is required as compared to the modulated structure for radical re-arrangement of martensite microstrucrure by the motion of twin boundaries. Thus, comparatively lower FSME effect is expected in the non-modulated structure alloys. Still from ductility point of view, these quaternary alloys have some potential for actuator application.

CONCLUSION AND SCOPE FOR FUTURE WORK

6.1. Conclusion

A systematic investigation on Co-Ni-Ga ferromagnetic shape memory alloys has been presented in this thesis. Four series of alloys have been prepared and their structural, magnetic and mechanical properties have been discussed. In the first series, Co and Ga contents were varied, maintaining the Ni content constant. In the second series, Ni and Co contents were varied keeping Ga content constant. $Co_{48-x}Ni_{22}Ga_{30-y}Fe_{x+y}$ (where $x+y$ = 1, 3, 6) and $Co_{48-x}Ni_{22}Ga_{30-y}T_{x+y}$ (where $x+y$ = 1, 3, 6) are the last two series of alloys.

In the first series studied, *viz.*, $Co_xNi_{25}Ga_{75-x}$ ($43 \leq x \leq 50$) alloys, single phase martensite phase were exhibited at room temperature by alloys with $x \leq 45$. Alloys with $x \geq 45.5$ exhibited a two phase ($\beta+\gamma$) structure at room temperature. T_C of all the alloys in this series was found to be lower than M_s and A_s. M_{sat} and K_{eff} of these alloys increased with increase in Co at %.

In the second series, viz., $Co_{70-x}Ni_xGa_{30}$ ($20 \leq x \leq 25$), all alloys with $x \geq 21$ exhibited martensitic phase at room temperature. The alloy with $x = 20$ showed austenite structure at room temperature. An increase in M_s and A_s, and a decrease in T_C have been

observed as Co is gradually substituted by Ni in this series of alloys. $Co_{47}Ni_{23}Ga_{30}$ alloy has A_s and T_C very close to each. Such alloys are expected to show giant magneto caloric effect.

M_{sat} was found to be smaller for Co-Ni-Ga than Ni-Mn-Ga alloys. However, K_{eff} estimated for the Co-Ni-Ga alloys was comparable to Ni-Mn-Ga and Fe-Ni-Ga alloys. A considerable increase in M_{sat} and T_C has been observed when small amounts of Fe or Mn are added to Co-Ni-Ga alloys.

Apart from investigating the influence of changes in the constituent elements of Co-Ni-Ga alloys, the studies performed in this thesis have also showed that the structure of the alloys is sensitive to the preparative conditions. Presence of a secondary (γ) phase has been observed when the alloy is quenched from temperatures below 1150 °C. This γ-phase is responsible for the enhancement of ductility of the samples. However, large amounts of γ-phase adversely affects the SME. Thus, an optimum annealing and quenching conditions is required to obtain alloys with good ductility and SME.

The ultimate compressive strength of these alloys ranged from 423 to 579 MPa. Very high compressive strength has been observed in Mn substituted alloys. Highest recovery of strain (3.3 %) was observed in $Co_{49}Ni_{21}Ga_{30}$ alloy. Pseudo-elastic effect was in $Co_{50}Ni_{20}Ga_{30}$ which was pre-strained to 4.2%. MFIS in Co-Ni-Ga has been reported for the first time in this thesis. MFIS values of the investigated alloys are comparable to reported values of polycrystalline Ni-Mn-Ga alloys. Higher MFIS has been observed in Fe/Mn substituted Co-Ni-Ga alloys. However, with the substitution of Fe/Mn, MT

temperatures shifted to lower temperatures. Pseudo–elastic behavior has been observed at room temperature in alloys with higher Fe/Mn substitution.

6.2. Scope for future work

Giant magneto-caloric effect has been reported in various magnetic materials including Ni-Mn-Ga alloys in which magnetic and structural transformations co-occur. The magneto-caloric effect is gaining at lot of attention due to its potential in magnetic refrigeration. We observed very close magnetic and reverse martensitic structural transitions (tetragonal to cubic) in $Co_{47}Ni_{23}Ga_{30}$ alloy prepared by quenching ingots annealed at 1150 °C.

We have observed that the Co-Ni-Ga alloys are very sensitive to ageing. Stabilization of the martensite and precipitation of s secondary phase have been observed in some Co-Ni-Ga samples upon ageing in the martensite or austenite phase. Due to time constraint this work could not be completed and hence did not form part of this thesis. Since the ageing behaviour of these alloys has not well documented, the same is worthy of study.

MFIS observed in this work is comparable to that of polycrystalline Ni-Mn-Ga. Higher MFIS can be achieved in the present alloys by applying mechanical stress on them before exposing them to magnetic field. Recovery of shape can also be observed by deforming the alloys in the martensite phase and then exposing them to magnetic field. Samples in ribbon form may be more suitable for such measurements. Ribbons of these alloys can be prepared by melt spinning technique. Enhancement of magnetic properties

has been observed in Co-Ni-Ga alloys substituted with small amounts of Fe and Mn. It would be interesting to verify whether the properties of Co-Ni-Ga alloys can be further enhanced by the substitution of other elements.

REFERENCES

[1] A. Lendlein and S. Kelch: *Angew. Chem. Int. Ed.* **41** (2002) 2034.

[2] T. Okano and A. Kikuchi: *Proceedings of Third International Conference on Intelligent Materials*, *Third European Conference on Smart Structures and Materials*, Lyon, France, 3–5 June 1996, Edited by P. F. Gobin and J. Tatibouët, 34–41.

[3] B. Culshaw: *Smart Structures and Materials*, San Diego, CA, Artech House Publisher, 1996, 1–16.

[4] J. Hu: *Shape memory polymers and textiles*, Woodhead Publishing Limited, Cambridge, 2007.

[5] L. N. Christophorov: *Proceedings of the Third International Conference on Intelligent Materials*, *Third European Conference on Smart Structures and Materials*, Lyon, France, 3–5 June 1996, Edited by P.F. Gobin and J. Tatibouët, 58–65.

[6] V. V. Varadan, L. C. Chin, and V. K. Varadan: *Proceedings First European Conference on Smart Structures and Materials*, Glasgow, 12–14 May 1992, Edited by B. Culshaw, P. T. Gardiner and A. McDonach, 1–6.

[7] http://en.wikipedia.org/wiki/Shape_memory_alloy

[8] G. B. Kauffman and I. Mayo: *Invention Tech. Magazine* **9** (1993) (available at www.americanheritage.com/articles/magazine/it/1993/2/1993_2_18.shtml).

[9] http://www.scielo.br/scielo.php

[10] K. Otsuka and C. M. Wayman (editor): *Shape Memory Materials*, Cambridge University Press, UK (1998).

[11] K. Otsuka and X. Ren: *Intermetallics* **7** (1999) 511.

[12] L.G. Machado and M.A. Savi: *Braz. J. Med. Biol. Res.* **36** (2003) 683.

[13] P. J. Webster, K. R. A. Ziebeck, S. L. Town and M. S. Peak: *Philos. Mag.B* **49** (1984) 295.

[14] R.D. James and M. Wutting: *Philos. Mag. A* **77** (1998) 1273.

[15] T. Kakeshita, T. Takeuchi, T. Fukuda, T. Saburi, R. Oshima, S. Muto and K. Kishio: *Mater. Trans. JIM* **41** (2000) 882.

[16] F. Gejima, Y. Sutou, R. Kainuma and K. Ishida: *Matell. Mater. Trans.* **30** (1999) 2721.

[17] K. Oikawa, L. Wulff, T. Iijima, F. Gejima, T. Ohmori, A. Fujita, K. Fukamichi, R. Kainuma and K. Ishida: *Appl. Phys. Lett.* **79** (2001) 3290.

[18] R. Kainuma, M. Ise, C. -C. Jia, H. Ohtani and K. Ishida: *Intermetallics* **4** (1996) S151.

[19] K. Oikawa, T. Ota, F. Gejima, T. Ohmori, R. Kainuma and K. Ishida: *Mater. Trans.* **42** (2001) 2472.

[20] M. Wuttig, J. Li and C. Craciunescu: *Scripta Mater.* **44** (2001) 2393.

[21] K. Oikawa, T. Ota, Y. Sutou, T. Ohmori, R. Kainuma and K. Ishida: *Mater. Trans.* **43** (2002) 2360.

[22] K. Oikawa, T. Ota, T. Ohmori, Y. Tanaka, H. Morito, A. Fujita, R. Kainuma, K. Fukamichi and K. Ishida: *Appl. Phys. Lett.* **81** (2002) 5201.

[23] K. Ullakko, J.K. Huang, C. Kantner, R.C. O'Handley and V.V. Kokorin: *Appl. Phys. Lett.* **69** (1996) 1966.

[24] V.V. Khovalio, T. Takagi, A.N. Vasilev, H. Miki, M. Matsumoto and R. Kainuma: *Phys. Stat. Sol.(a)* **183** (2001) R1-R3.

[25] S. Banik, R. Ranjan, A. Chakraborti, S. Bhardwaj, N.P Lalla, A.M. Awasthi, V. Sathe, D.M. Phase, P.K. Mukhopadhyay, D. Pandey and S.R. Barman: *Phys. Rev. B* **75** (2007) 104107.

[26] X. F. Dai, H. Y. Wang, G. D. Liu, Y. G. Wang, X.F. Duan, J.L. Chen and G. Wu: *J. Phys.D: Appl. Phys.* **39** (2006) 2886.

[27] D.Canadinc, J. Dadda, H. J. Maier, I. Karaman, H. E Karaca and Y. I-Chumlyakov: *Smart Mater. Struct.* **16** (2007)1006.

[28] V. A. Chernenko, E. Cesari, V. V. Kokorin and I. N. Vitenko: *Scripta Metall. Mater.* **33** (1995) 1239**.**

[29] Y. Li, Y. Xin, C. Jiang and H. Xu: *Scripta Mater.* **51** (2004) 849.

[30] W. H. Wang, F. X. Hu, J. L. Chen, Y. X. Li, Z.Wang, Z. Y. Gao,Y. F. Zheng, L. C. Zhao, G.H.Wu and W. S. Zan: *IEEE Trans. Magn.* **37** (2001) 2715.

[31] P. J. Brown, J. Crangle, T. Kanomata, M. Matsumoto, K-U Neumann, B. Ouladdiaf and K. R. A. Ziebeck: *J. Phys: Condens. Matter* **14** (2002) 10159.

[32] P. J. Brown, K. Ishida, R. Kainuma, T. Kanomata, K-U Neumann, K Oikawa, B. Ouladdiaf and K. R. A. Ziebeck: *J. Phys: Condens. Matter* **17** (2005) 1301.

[33] *A*. Planes, L. Mañosa, X. Moya, T. Krenke, M. Acet and E.F. Wassermann: *J. Magn. Magn. Mater.* **310** (2007) 2767.

[34] R. Santamarta, J. Font, J. Muntasell, F. Masdeu, J. Pons, E. Cesari and J. Dutkiewicz: *Scripta Mater.* **54** (2006) 1105.

[35] K. R. Priolkar, P. A. Bhobe, S. D. Sapeco and R. Paudel: *Phys. Rev. B* **70** (2004) 132.

[36] S. Majumdar, V. K. Sharma, M. Manekar, R. Kaul, K. J. S. Sokhey, S. B. Roy and P. Chaddah: *Sol. Stat. Com.* **136** (2005) 85.

[37] S. Kustov, M. Corró and E. Cesari: *Appl. Phys. Lett.* **91** (2007) 141907.

[38]Y. Tanaka, K. Oikawa, Y. Sutou, T. Omori, R. Kainuma and K. Ishida: *Mater. Sci. Engg. A* **438** (2006) 1054.

[39] J. Liu, H. X. Zheng, M. X. Xia, Y. L. Huang and J. G. Li: *Scripta Mater.* **52** (2005) 935.

[40] J. Liu, M. Xia, Y. Huang, H. Zheng and J. Li: *J. Alloys Compd.* **417** (2006) 96.

[41] P. Müllner,V. A. Chernenko, M. Wollgarten and G. Kostorz: *J. Appl. Phys.* **92** (2002) 6708.

[42] V. A. Chernenko, J. Pons, E. Cesari and A. E. Perekos: *Mater. Sci. Engg. A* **378** (2004) 357.

[43] T. Sakamoto, T. Fukuda, T. Kakeshita, T. Takeuchi and K. Kishio: *Sc. Tech. Adv. Mater.* **5** (2004) 39.

[44] V. V. Martynov: *J. Phys. IV* **5** (1995) C8-91.

[45] B. Wedel, M. Suzuki, Y. Murakami, C. Wedel, T. Suzuki, D. Shindo and K. Itagaki: *J. Alloys and Compd.* **290** (1999)137.

[46] J. Pons, V. A. Chernenko, R. Santamarta and E. Cesari: *Acta Mater.* **48** (2000) 3027.

[47] R. Ranjan, S. Banik, S. R. Barman, U. Kumar, P. K. Mukhopadhyay and D. Pandey: *Phys. Rev. B* **74** (2006) 224443.

[48] H. X. Zheng, M. **X**. Xia, J. Liu and J. G. Li: *J. Alloys Compd.* **385** (2004) 144.

[49] G. D. Liu, Z. H. Liu, X. F. Dai, S. Y. Yu, J. L. Chen and G. H. Wu: *Sc. Techn. Advan. Mater.* **6** (2005) 772.

[50] Y. Sutou, N. Kamiya, T. Omori, R. Kainuma, K. Ishida and K. Oikawa: *Appl. Phys. Lett.* **84** (2004) 1275.

[51] Y. Murakami, D. Shindo, K. Oikawa, R. Kainuma and K. Ishida: *Acta Mater.* **50** (2002) 2173.

[52] Z. H. Liu, X. F. Dai, Z. Y. Zhu, H. N. Hu, J. L. Chen, G. D. Liu and G. H. Wu: *J. Phys. D: Appl. Phys.* **37** (2004) 2643.

[53] J. Liu, H. Xie, Y. Huo, H. Zheng and J. Li: *J. Alloy Compd.* **420** (2006) 145.

[54] M. Zhang, E. Brück, F. R. de Boer and G. Wu: *J. Phys. D: Appl. Phys.* **38** (2005) 1361.

[55] V. A. Chernenko, J. Pons, E. Cesari and I. K. Zasimchuk: *Scripta Meter.* **50** (2004) 225.

[56] P. Müllner, V. A. Chernenko and G. Kostorz: *J. Magn. Magn. Mater.* **267** (2003) 325.

[57] Y. Ma, C. Jiang, Y. Li, H. Xu, C. Wang and X. Liu: *Acta Mater.* **55** (2007) 1533.

[58] M. Matsumoto, M. Ebisuya, T. Kanomata, R. Note, H. Yoshida and T. Kaneko: *J. Magn. Magn. Mater.* **239** (2002) 521.

[59] S. Banik, A. Chakrabarti, U. Kumar, P. K. Mukhopadhyay, A. M. Awasthi, R. Ranjan, J. Schneider, B. L. Ahuja and S. R. Barman: *Phys. Rev. B* **74** (2006) 085110.

[60] M. Wuttig, L. Liu, K. Tsuchiya and R. D. James: *J. Appl. Phys.* **87** (2000) 4707.

[61] S. K. Wu and S.T. Yang: *Mater. Lett.* **57** (2003) 4291.

[62] V. A. Chernenko: *Scripta. Mater.* **40** (1999) 523.

[63] T. Krenke, X. Moya, S. Aksoy, M. Acet, P. Entel, L. Mañosa, A. Planes, Y. Elerman, A. Yücel and E.F. Wassermann: *J. Magn. Magn. Mater.* **310** (2007) 2788.

[64] V.V. Khovalio, K. Oikawa, T. Abe, T. Tagaki, arXiv.cond-mat:0302352 v1 (2003)1.

[65] S. Miura, S. Maeda and N. Nakanushi: *Philos. Mag.* **30** (1974) 56.

[66] Y. Nakajima, S. Aoki, K. Otuka and T. Ohba: *Mater. Lett.* **21** (1994) 271.

[67] H. Sakamoto, K. Otsuka and K. Shimizu: *Scripta Mater.* **11** (1977) 607.

[68] L. Dai, M. Wuttig and E. Pagounis: *Scripta Mater.* **55** (2006) 807.

[69] C. Seguí, E. Cesari, J. Font, J. Muntasell and V.A. Chernenko: *Scripta Mater.* **53** (2005) 315.

[70] V. A. Chernenko, V. A. L'vov and E. Cesari: *J. Magn. Magn. Mater.* **196** (1999) 859.

[71] V. A. L'vov, E. V. Gomonaj and V. A. Chernenko: *J. Phys: Condens. Matter* **10** (1998) 4587.

[72] S. V. Andreev, M. I. Bartashevich, V. I. Pushkarsky, V. N. Maltsev, A. Pamyatnykh, E. N. Tarasov, N. V. Kudravatykh and T. Goto: *J. Alloys and Compd.* **260** (1997) 196.

[73] A. Arrott and J. Noakes: *Phys. Rev. Lett.* **19** (1967) 786.

[74] A. R. Williams, V. L. Moruzzi, A. P. Malozemoff and T. Terakura: *IEEE Trans. Magn.* **19** (1983) 1983.

[75] G. Li, Y. Liu and B. K. A. Ngoi: *J. Magn. Magn. Mater.* **303** (2006) 261.

[76] C. Biswas, R. Rawat and S. R. Barman: *Appl. Phys. Lett.,* **86** (2005) 202508.

[77] W. Yan, Q. Sun and H.Y. Liu: *Mater. Sci. Engg. A* **425** (2006) 278.

[78] A. Sozinov, A. A. Likhachev, N. Lanska and K. Ullakko: *Appl. Phys. Lett.* **80** (2002) 1746.

[79] S. J. Murray, M. Marioni, R. C. O'Handley and T. A. Lograsso: *Appl. Phys. Lett.* **77** (2000) 886.

[80] S. Jeong, K. Inoue, K. Koterazawa, M. Taya, K. Inoue: *Mater. Sci. Engg. A* **359** (2003) 253.

[81] T. Kakeshita, J.-H. Kim and T. Fukuda: *Mater. Sci. Engg. A* **481** (2007) 40.

[82] Z. Q. Zhao, W. Xiong, S. X. Wu and X. L. Wang: *J. Iron Steel Res.* **111** (2004) 55.

[83] Z. Q. Zhao, S. X. Wu, F. S. Wang, Q. Wang, L. P. Jiang and X. L. Wang: *Rare Met.* **23** (2004) 241.

[84] L. Gao, W. Cai, A. L. Liu and L. C. Zhao: *J. Alloys Compd.* **425** (2006) 314.

[85] L. Gao, J. H. Sui and W. Cai: *J. Magn. Magn. Mater.* **320** (2008) 63.

[86] G. H. Wu, W. H. Wang, J. L. Chen, L. Ao, Z. H. Liu, W. S. Zhan, T. Liang and H. B. Xu: *Appl. Phys. Lett.* **80** (2002) 634.

[87] D. Kikuchi, T. Kanomata, Y. Yamaguchi, H. Nishihara, K. Koyama, K. Watanabe: *J. Alloys Compd.* **383** (2004) 184.

[88] H. Zheng, M. Xia, J. Liu, Y. Huang and J. Li: *Acta Mater.* **53** (2005) 5125.

[89] K. Oikawa, Y. Imano, V.A. Chernenko, F. Luo, T. Omori and Y. Sutou: *Mater. Trans.* **46** (2005) 734.

[90] Imano, T. Omori, K. Oikawa, Y. Sutou, R. Kainuma and K. Ishida: *Mater. Sci. Engg.* A **438** (2006) 970.

[91] H. Zheng, J. Liu, M. Xia and J. Li: *Mater. Sci. Engg.* A **438** (2006) 1011.

[92] H. X. Zheng, J. Liu, M. X. Xia and J. G. Li: *J. Alloys Compd.* **387** (2005) 265.

[93] H. Morito, K. Oikawa, A. Fujita, K. Fukamichi, R. Kainuma and K. Ishida: *Scripta Mater.* **53** (2005)1237.

[94] H. Morito, K. Oikawa, A. Fujita, K. Fukamichi, R. Kainuma and K. Ishida*: J. Magn. Magn. Mater.* **290** (2005) 850.

[95] Z. H. Liu, H. Liu, X. X. Zhang, X. K. Zhang, J. Q. Xiao and Z. Y. Zhu: *Appl. Phys. Lett*. **86** (2005) 182507.

[96] H. Morito, A. Fujita, K. Oikawa, K. Ishida, K. Fukamichi and R. Kainuma: *Appl. Phys. Lett.* **90** (2007) 062505.

[97] C. Picornell, J. Pons, E. Cesari and J. Dutkiewicz: *Intermetallics* **16 (** 2008) 751.

[98] J. Liu and J. G. Li: *Scripta Mater.* **56** (2007) 109.

[99] B. D. Cullity and S. R. Stock: *Elements of X-ray Diffractions*, 3rd ed., Prentice Hall, Upper Saddle River, N J (2001).

[100] H.M Rietveld: *Acta Cryst.* **22** (1967) 151.

[101] H. M Rietveld: *Acta Cryst.* **2** (1969) 65.

[102] D. Louer: *Acta Cryst*. **A 54** (1998) 922.

[103] T. Hatakeyama and Z. Liu (editor): *Hand Book of Thermal Analysis*, John Wiley & Sons , Chichister (1998).

[104] H. Sehitoglu, C. Efstathiou, H. J. Maier and Y. Chumlyakov: *Mech. Mater.* **38** (2006) 538.

[105] W. R. Abel, A. C. Anderson and J. C. Wheatley: *Rev. Sci. Instrum.* **35** (1964) 444.

[106] S. Sarma, M. P. C. Kalita, A. Perumal and A. Srinivasan: *Proc. National Workshop Adv. Tech. Material Characterization*, M. S. University of Baroda, Vadodara (2006) 19.

[107] D. J. Griffith: *Introduction to Electrodynamics*, 2nd ed., Prentice hall, NewDelhi (1995).

[108] M. Fähnle and H. Kronmüller: *J. Magn. Magn. Mater.* **8** (1978) 149.

[109] Z. -Q. Jin, W. Tang, J. -R Zhang, H. -X. Qin and Y. -W. Du: *Eur. Phys J.B* **3** (1998) 41.

[110] J. P. Wang, D. -H. Han, H. -L. Luo, Q. -X. Lu and Y.-W. Sun: *Appl. Phys. A* **61** (1995) 407.

[111] C. D. Graham and M. R. J. Gibbs: *IEEE Trans. Magnet.* **29** (1993) 3457.

[112] A. Arrott and J. Noakes: *Phys. Rev. Lett.* **19** (1967) 786.

[113] J. S. Kovel and M. E. Fisher: *Phys. Rev. B* **136** (1964) A1626.

[114] S. N. Kaul: *Phys. Rev. B* **22** (1980) 278.

[115] S. N. Kaul: *J. Magn. Magn. Mater.* **53** (1985) 5.

[116] T. L. Phan, S. G. Min, S. C. Yu and S. K. Oh: *J. Magn. Magn. Mater.* **304** (2006) e-778.

[117] K. Ghosh, C.J. Lobb, R. L. Greene, S.G. Karabashev, D.A. Shulyatev, A. A. Arsenov and Y. Mukovskii: *Phys. Rev. Lett.* **81** (1998) 4740.

[118] A. S. Khan and X Wang: *Stress measurement and Strain anlysis*, Prentice Hall, Upper Saddle River (2001).

[119] M. Yamane and J. D. Mackenzie: *J. Non-Cryst. Solids* **15** (1974) 153.

[120] A. D. Helfrick and W. D. Cooper: *Modern Electronic Instrumentation and Measurement Techniques*, Prentice Hall, New Delhi (1996).

[121] A. Planes, L. Manosa, D. Rios-Jara and J. Ortin: *Phys. Rev. B* **45** (1992) 7633.

[122] C. Jiang, Y. Muhammad, L. Deng, W. Wu and H. Xu: *Acta Mater.* **52** (2004) 2779. [123] J. Pons, C. Segui, V. A. Chernenko, E. Cesari, P. Ochin and R. Portier: *Mater. Sci. and Engg. A* **273** (1999) 315.

[124] J. Dadda, H. J. Maier, I. Karaman, H. E. Karaca, Y. I. Chumlyakov: *Scripta Mater.* **55** (2006) 663.

[125] C. Craciunescu, Y. Kishi, T. A. Lograsso and M. Wuttig: *Scripta Mater.* **47** (2002) 285.

[126] J. S. Koehler, F. Seitz and J. E. Bauerle: *Phys. Rev. B* **107** (1957) 1499.

[127] L. H. Lewis, M. J. Kramer, R.W. McCallum and D. J. Branagan: *Proc. III Intel. Workshop Mater. Sci.*, Hanoi (1999) BNL-66785.

[128] H. Grimm and K. Kronmoller: *Phys. Stat. Solid b* **117** (1983) 663.

[129] O. Heczko and P. Ruuskanen: *IEEE Trans. Magnet.* **30** (1994) 513l.

[130] S. Blundell: *Magnetism in Condensed Matter* (Oxford Univ. Press, Oxford, 2001) 119.

[131] M. E. Fisher, S-K. Ma and B. G. Nickel: *Phys. Rev. Lett.* **29** (1972) 917.

[132] R. Malmhall, G. Backstrom, K. V. Rao, S. M. Bhagat, M. Meichle and M. B. Salamon : *J. Appl. Phys.* **49**(1978) 1727.

[133] H. E. Stanley: *Intr. Phase Transitions and Critical Phenomena* (Oxford Univ. Press, Newyork (1987) 47.

[134] Y. Chumlyakov, E. Panchenko, I. Kireeva, I. Karaman, H. Sehitoglu, H. J. Maier, A. Tverdokhlebova and A. Ovsyannikov: *Mater. Sci. Engg. A* **481** (2008) 95.

[135] T. Krenke, X. Moya, S. Aksoy, M. Acet, P. Entel, Ll. Mañosa, A. Planes, Y. Elerman, A. Yücel and E. F. Wassermann: *J. Magn. Magn. Mater.* **383** (2004) 184.

[136] T. Sakamotoa,T. Fukudaa,T. Kakeshitaa,T. Takeuchib and K. Kishioc*: Sci. Tech. Adv. Mater.* **5** (2004) 39.

[137] T. Krenke, E. Duman, M. Acet, E. F. Wassermann, X. Moya, L. Mañosa, A. Planes, E. Suard and B.Ouladdiaf: *Phys. Rev. B* **75** (2007) 104414.

[138] I. E. Dikshtein, D. I. Ermakov, V. V. Koledov, L.V. Koledov, T.Tagaki, A. A. Tulaikova, A. A. Cherechukin and V. G. Shavrov: *JETP Lett.* **72** (2000) 373.

PUBLICATIONS

Paper published/communicated in Journals:

1. **Sidananda Sarma** and A. Srinivasan, Development of Co-Ni-Ga ferromagnetic shape memory alloys with enhanced properties, Mater. Sci. Forum **587** (2008) 650.
2. **Sidananda Sarma** and A. Srinivasan, Influence of annealing temperature on the properties of Co-Ni-Ga ferromagnetic shape memory alloy, Advance Mater. Res. **52** (2008) 63.
3. **Sidananda Sarma** and A. Srinivasan, Structural characterization of $Co_{70-x}Ni_xGa_{30}$ ferromagnetic shape memory alloys, Advance Mater. Res. **52** (2008) 103.
4. A. Srinivasan and **Sidananda Sarma**, Co-Ni-Ga alloys with room temperature ferromagnetic martensite phase, Advance Mater. Res. **52** (2008) 95.
5. **Sidananda Sarma** and A. Srinivasan, Influence of cooling rate on the properties of ferromagnetic shape memory alloy, Indian J. Phys. **82** (2008) 701.
6. **Sidananda Sarma**, Study of structural and magnetic phase transformations in Co-Ni-Ga alloys. Research Journal of Contemporary Concern, Cotton College Research Council, Research Journal of Cotton College (accepted for publication).

Paper published in Conference Proceedings:

1. **Sidananda Sarma**, A Perumal and A. Srinivasan, The nature of ferromagnetic phase transition in Co-Ni-Ga alloys, Proc. of International Workshop and Conference on Statistical Physics Approaches to Multi-disciplinary Problems, 2007, I.I.T. Guwahati, India.
2. **Sidananda Sarma** and A. Srinivasan, Magnetic and thermal characterization of Co-Ni-Ga ferromagnetic shape memory alloys, Proc. of National Conference on Sensors and Actuators: Emerging Technological challenges (NCSA-06), 2007, CGCRI, Kolkata, India.
3. **Sidananda Sarma** and A. Srinivasan, Investigation of shape memory effect in Co-Ni-Ga alloy using differential scanning calorimeter, Proc. of National Workshop on Advance Techniques for Material characterization, 2006, M.S. University, Baroda, India.
4. **Sidananda Sarma**, Manos P.C. Kalita, A. Perumal and A. Srinivasan, Development of a high temperature and low-field ac susceptometer, Proc. of National Workshop on Advance Techniques for Material characterization, 2006, M.S. University, Baroda, India.
5. **Sidananda Sarma** and A. Srinivasan, Preparation and characterization of Co-Ni-Ga ferromagnetic shape memory alloys, Proc. of National Conference of Material Science, 2006, Periyar University, Salem, India.

-----^-----

PREPARATION AND CHARACTERIZATION OF Co-Ni-Ga FERROMAGNETIC SHAPE MEMORY ALLOYS

A thesis submitted

by

Sidananda Sarma
Roll 004604

to

Indian Institute of Technology Guwahati

in
partial fulfillment of the requirement for the award of the degree of
Doctor of Philosophy in Physics

Department of Physics

Indian Institute of Technology Guwahati

Guwahati – 781039, Assam, India

August 2008

Statement

The work contained in the thesis entitled “Preparation and characterization of Co-Ni-Ga ferromagnetic shape memory alloys” has been carried out by me under the supervision of Prof. A. Srinivasan, Department of Physics Indian Institute of Technology Guwahati. This work has not been submitted elsewhere for the award of any degree.

August 29, 2008

(Sidananda Sarma)

Roll No: 004604

Department of Physics

Indian Institute of Technology Guwahati

Guwahati - 781039

Certificate

It is certified that the work contained in the thesis entitled “Preparation and characterization of Co-Ni-Ga ferromagnetic shape memory alloys” by Sidananda Sarma, a Ph. D. student of the Department of Physics, Indian Institute of Technology Guwahati for the award of degree of Doctor of Philosophy has been carried out under my supervision. This work has not been submitted elsewhere for the award of any degree.

August 29, 2008

(Dr. A. Srinivasan)
Professor
Department of Physics
Indian Institute of Technology Guwahati
Guwahati - 781039

To my Parents …

and

daughter Jumon

Acknowledgements

First of all, I would like to thank my thesis supervisor Prof. A. Srinivasan for introducing me into the world of Shape memory alloys. I am grateful to him for his endless effort, constant encouragement and keen interest in the progress of my work. He made all the arrangement for me in advance to prepare and analysis of my samples. His guidance turned me into an independent research worker.

I would like to thank my doctoral committee members, Dr. S. Ravi, Dr. P. Agarwal and Prof. P. S. Robi for their suggestions to improve my research work. I would like to express my appreciation to Prof. Robi for permitting me to work freely in the material science laboratory of Mechanical Engineering Department after office hours and on holidays.

I am thankful to Prof Alika Khare for her constant encouragement and mental support during my Ph.D. work. I'm grateful to the Department of Physics and the Institute for allowing me to carry out research as a part-time research scholar. My thanks are due to all faculty members of our Department for their help and suggestion. It is my pleasure to record my gratitude to my colleague Lokesh Chakraborty, Atul Ch. Deka, Pankaj Goswami, Madan Deka, Bimal Kr. Sarma, Basab B. Purakayastha and Jyoti P. Borah for their mental support during my research work.

My sister's friend Ms. Ranju Bhuyan used to write me letters in my college days describing how the research workers work in laboratories. I was motivated towards research with her letters in those days itself. I sincerely acknowledge her at this moment. I am grateful to Ms. A. Janaki for inspiring me to carry out the research sincerely without unnecessarily worrying for results. She used to say me that work is like an insurance policy and it never goes waste. My sincere thanks are due to Mr. Chandan Borgohain, Mr. Kula Kamal Senapati, Mr. Rituraj Saikia, late Ramananda Das and Mr. Sanjib Sarma for extending technical help at Central Instrumentation Facility and Material Science Laboratory, ME. During my work, I have benefited from the mechanical workshop in the

fabrication of the instrumental set up. I would like to thank all the members in the workshop. I express my special gratitude to my co-research workers and friends for their affection and encouragement. My special thanks go to Manos, Rajendra, Debabrata, Amal, Anto, Munima, Indrajit, Manoranjan, Amit, Panchanan, Anil Bora, Sandeep, Pramod and Ardhendu. I'm thankful to them for many useful discussions I had with them. The help extended by Manos, Rajendra, Debabrata and Mr. L.N. Sharma during printing and arrangement of my thesis is unforgettable.

I am deeply indebted to my parents, my mother-in law, sisters and brothers for their constant encouragement and moral support. My brother-in-law Mr. Dijen Goswami and sister Beuty are next to my parents. They have been taking responsibilities of my parents in many critical situations and helped me to carry out my research work freely. I'll remember this help throughout my life. My uncles, aunties and cousins have always been sources of inspiration to me. Particularly, Mr. Biren Sarma and Ms. Rina Sarma often used to phone me up and advise me not to deviate from research work until it is completed. I'm indebted to all of them.

Last but not least, I would like to offer my sincere gratitude to my wife Sumi and daughter Jumon.

Finally, I express my sincere thanks to all who helped me in whatever manner during my Ph.D. work some of whom I may have inadvertently forgotten to mention in this acknowledgement.

- Sidananda.

PRFECAE

Shape memory alloys (SMA) have been engineered for various applications and devices since the first discovery of the shape memory effect in the 1930s. The advent of Nitinol (a Ni-Ti alloy) in 1962 established SMAs as a major area of research and development. . Unlike most conventional metals that recover less than 1% of the strain before plastic deformation, SMAs undergo a diffusionless thermo-elastic martensitic phase transformation that enable them to deform *via* the movement of twins or self accommodation process rather than by conventional dislocation slip mechanism and thereby allow recovery of strain as large as 8%. Diffusionless phase transformation in an SMA can be triggered by temperature change or application of stress or magnetic field. In conventional SMA, shape change or mechanical strain is achieved by applying a mechanical stress or by temperature variation. These inherently slow processes put an upper limit on the actuation speed of the SMA. Faster change of shape / volume or mechanical strain can be achieved in some magnetic alloys by applying an alternating magnetic field. Such alloys are called ferromagnetic shape memory alloys (FSMAs). Current research activities on FSMAs are mainly aimed at understanding the properties of FSMAs and developing FSMAs with properties desirable for actuator applications.

Quite a few FSMAs had been developed and many of them have been proposed as potential candidates for sensor and actuator applications. But till now, no practical device has been reported with these FSMAs and the material is still being investigated

intensively. Practical application of prototype Ni-Mn-Ga alloy is limited because of its extreme brittleness in polycrystalline state. Co-Ni-Ga solidifies in a peritectic reaction and forms a composite structure with fcc γ-phase and bcc β matrix. Thus, controlled amount of γ-phase can be introduced in the β-matrix by proper choice of composition and suitable heat treatment conditions. The hot workability and room temperature ductility of these alloys are significantly improved by the introduction of the γ-phase, which is a great advantage for practical applications.

Understanding the evolution of various crystalline phase in FSMAs by different processing conditions and the resulting changes in properties of the alloys is crucial for evaluating these materials for actuator applications. Although the prototype FSMA, Ni-Mn-Ga has been well studied, other FSMAs such as Co-Ni-Ga, Ni-Fe-Ga etc. have not yet been investigated with so much rigour. In this thesis work, a systematic investigation of the processing conditions and physical properties of several Co-Ni-Ga alloys has been carried out.

Three series of Co-Ni-Ga alloys have been prepared by a process consisting of arc melting technique followed by the homogenization at high temperature and quenching to low temperature. Care was taken to prepare alloys with ferromagnetic martensite near room temperature. The samples were characterized by powder X-ray diffractometer, energy dispersive spectrometer attached to a scanning electron microscope, optical microscope, differential scanning calorimeter, magnetic ac susceptometer, vibration sample magnetometer, Vickers microhardness tester, Universal testing machine (UTM) and strain gauge setup couple to an electromagnet, etc.

The present thesis work has been presented in six chapters, namely, (1) introduction, (2) experimental technique and methodology, (3) investigations on

$Co_xNi_{25}Ga_{75-x}$ ($43 \leq x \leq 50$) alloys, (4) investigations on $Co_{70-x}Ni_xGa_{30}$ ($20 \leq x \leq 25$) alloys, (5) investigations on $Co_{48-x}Ni_{22}Ga_{30-y}T_{x+y}$ (T = Fe, Mn and $x + y = 1$, 3 and 6) alloys, and (6) conclusions and scope for future work.

Chapter 1 serves as a brief introduction to shape memory alloys. A brief review of earlier work done on ferromagnetic shape memory alloys and the motivation behind the thesis work are given here.

Chapter 2 discusses the experimental techniques used in the present investigations. The basic principle and the theory behind the experiments, the experimental set up and the measurement / methodology leading to the determination of the physical properties are discussed here. Instrumentation developed for the specific needs of this research work are also discussed in this chapter.

In chapter 3, the experimental studies on $Co_xNi_{25}Ga_{75-x}$ ($43 \leq x \leq 50$) alloys are presented. It starts with the determination of crystal structure of the alloys. Rietveld refinement technique was used for crystal structure refinement of single phase alloys. The variation of martensitic transformation temperatures, Curie temperatures saturation magnetization and magneto-crystalline anisotropy of the alloys with the change of composition are discussed. The salient features of the present studies on $Co_xNi_{25}Ga_{75-x}$ alloys are summarized at the end of the chapter.

Chapter 4 is devoted to the studies on $Co_{70-x}Ni_xGa_{30}$ ($20 \leq x \leq 25$) alloys. This chapter is arranged in the same sequence as chapter 3. But the influence of quenching temperature and quenching rate on the crystal structure, microstructure, martensitic transformation temperatures Curie temperature and other properties are discussed in

details. Use of modified Arrott plot for accurate measurement of Curie temperature and critical constants involved during ferromagnetic to paramagnetic phase transition of this FSMAs is discussed using $Co_{45}Ni_{25}Ga_{30}$ as a typical sample. The optimum processing conditions for the improvement of ductility of the alloys without disturbing martensitic transformation is found. Mechanical properties such as microhardness, strength, strain induced by the mechanical compressive stress and its recovery due to shape memory or pseudo-elastic effects of ductile samples are discussed.

Effort was made to enhance the magnetic properties of Co-Ni-Ga alloys by the addition of a fourth element. Small amounts of Fe or Mn were substituted for Co and Ga in $Co_{48}Ni_{22}Ga_{30}$. The resulting modifications in various properties such as crystal structure, microstructure, magnetic and mechanical properties are discussed in chapter 5. Magnetic field induced strain in some selected samples has been measured and results are discussed in this chapter.

Chapter 6 is the concluding chapter which attempts to summaries the results obtained on the present studies on Co-Ni-Ga ferromagnetic shape memory alloys. Scope for future work on these FSMAs is also briefly touched upon at the end of this chapter.

References cited in the thesis are listed at the end of the thesis.

Contents

INTRODUCTION

Materials that respond dynamically to environmental stimuli are generally called as 'intelligent' or 'smart' materials [1-3]. Most materials are responsive to some stimuli and in this (conventional or simple) sense can be termed as 'smart'. But, it is doubtful whether all these materials can respond in an adaptive way. A 'very smart' adaptive response is exhibited by a material if it can respond dynamically to a number of input stimuli and in a repeatable manner. Thus, a simple pressure transducer that produces a voltage output dependent on the input pressure could be regarded as 'smart' in a simple way. Then, a pressure transmitter incorporating a thermocouple that measures both temperature and pressure and corrects the pressure in response to the sensor's temperature coefficient is to be regarded as 'very smart'. Fig. 1.1 summarizes the responses of different transducer materials to different stimuli.

According to the general definition of a smart material [4], the material must also respond to more than one variable. If the material can be engineered to exhibit a particular response due to a sum of inputs, then it fulfills the definition of being 'very smart'. The term 'very smart' also used to refer to materials that can (1) respond reversibly to the changes in the surrounding environment, and (2) contribute an optimal or useful response by either changing its physical properties, geometry, mechanical

properties, or electromagnetic properties. The physical change is usually a significant one which can easily be observed and detected. In recent years, these 'very smart' materials are being intensely investigated because of their ability to change their physical properties usefully when they are triggered by environmental stimuli [5]. In all cases, very smart materials are expected to provide a reversible and useful response to a change in the adapted environment [6]. Shape memory materials belong to a class of 'very smart' materials, which have the ability to remember their original shape.

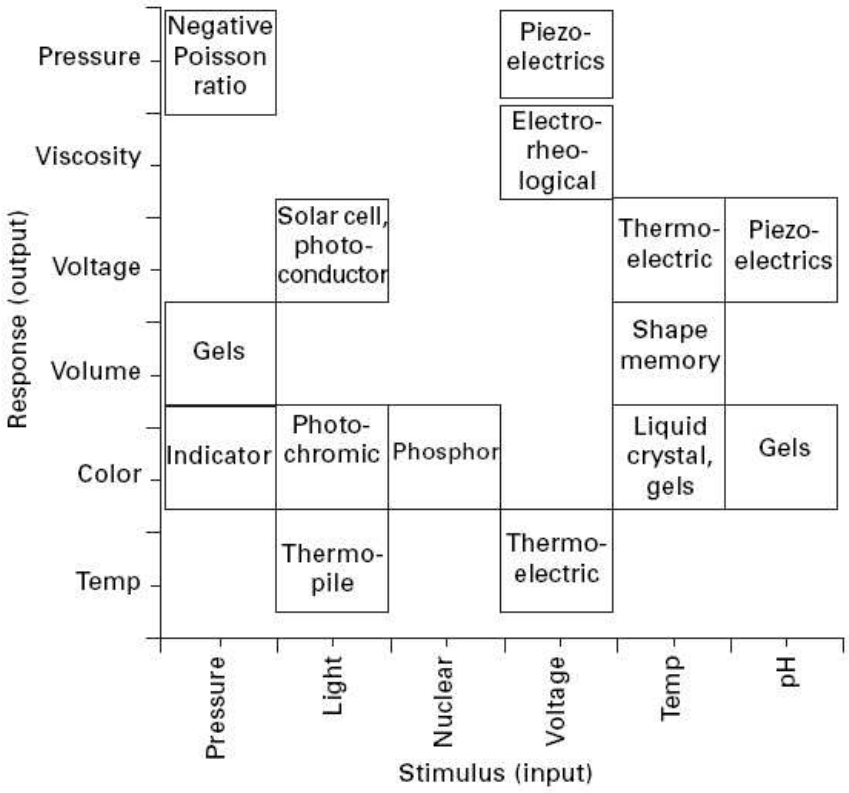

Fig. 1.1: Response of some sensor materials. These materials are often referred to as 'smart' [from reference 4].

Shape memory alloys (SMA) have been engineered for various applications and devices since the first discovery of the shape memory effect in the 1930s [7]. The advent of Nitinol (a Ni-Ti alloy) in 1962 [8] established SMAs as a major area of research and

development. Since then more than 10,000 patents have been issued for applications using SMAs. Unlike most conventional metals that recover less than 1% of the strain before plastic deformation, SMAs undergo a diffusionless thermo-elastic martensitic phase transformation that enables them to deform *via* the movement of twins or self accommodation process rather than by conventional dislocation slip mechanism and thereby allow recovery of strain as large as 8%. Diffusionless phase transformation in an SMA can be triggered by temperature change or application of stress or magnetic field. In a conventional SMA, shape change or mechanical strain is achieved by applying a mechanical stress or by temperature variation. These inherently slow processes put an upper limit on the actuation speed of the SMA. Faster change of shape / volume or mechanical strain can be achieved in some magnetic alloys by applying an alternating magnetic field. Such alloys are called ferromagnetic shape memory alloys (FSMAs) or magnetic shape memory alloys. It is generally believed that FSMAs have the potential to be the next generation 'very smart' actuator materials. The phenomenon of coupled magnetic and structural phase transitions observed in FSMAs is rare in condensed matter physics. Such systems with coupled phase transformation can exhibit many interesting properties including giant magneto-caloric effect, magneto-resistance and magneto-striction, and consequently have great technological potential. Current research activities on FSMAs are mainly aimed at understanding the properties of FSMAs and developing FSMAs with properties desirable for actuator applications. Since this thesis is concerned with the preparation and properties of Co-Ni-Ga FSMAs, a brief account of some general aspects of SMAs and FSMAs is given in the following sections.

1.1. SHAPE MEMORY ALLOYS

Shape memory alloys (SMAs) are metallic alloys that "remember" their original shapes. SMAs exhibit two unique properties, *viz*., shape memory effect and pseudo-elasticity (or super-elasticity). The remarkable properties of SMA have been known since the 1930's [9-12]. Ölander discovered the pseudo-elastic behavior of the Au-Cd alloy in 1932 and the shape memory effect was first observed in 1951 by Chang and Read in an Au-47.5 at% Cd alloy [10]. However, SMA attracted some technological interest only after the discovery of Nitinol. In 1962, Buehler and co-workers [9], of the U.S. Naval Ordnance Laboratory, discovered shape memory effect in an equiatomic Ni-Ti alloy which began to be known as NITINOL. These discoveries led to the development of a considerable number of shape memory alloys (SMAs), some of which are listed below:

Table 1.1: Different types of shape memory alloys [10].

- Ag - 44/49 at.% Cd
- Au - 46.5/50 at.% Cd
- Cu -14/14.5 wt.% Al-3/4.5 wt.% Ni
- Cu - approx. 15 at.% Sn
- Cu -38.5/41.5 wt.% Zn
- Cu - Zn-X (X = Si, Al, Sn)
- Ti-Pd in various concentrations
- Ni -Ti
- Ni-Mn-Ga
- Fe-Pd
- Fe_3 Pt
- Ni-Mn-Al
- Ni-Mn-In
- Ni-Fe-Ga
- Co-Ni-Al
- Co-Ni-Ga

The widely researched, as well as the most prominent SMA currently used in various applications is Ni-Ti. Ni-Ti alloys are generally more expensive; however they

possess superior mechanical properties when compared to copper-based SMAs. Because of their unique properties, SMAs can be utilized as 'multifunctional' materials in structural, sensing, and actuating applications.

1.1.1. The Shape Memory Effect

When temperature of an SMA is lowered below its transformation temperature, it has very low yield strength and can be deformed quite easily into new shape which it can retain. However, when the material is heated above a specific (characteristic) temperature, it undergoes a change in crystal structure which causes it to return to its original shape. If the SMA encounters any resistance during the transformation, it can generate extremely large forces to counter it [10]. The high temperature phase is called austenite phase and low temperature phase is called martensite phase. To give the so-called 'original' shape to an SMA which it can remember, the alloy is stressed or heat treated for a long time in the parent (austenite) phase. When the SMA in the parent phase is cooled down to some critical temperature called M_s (martensitic start temperature), its structure changes into martensitic (low temperature and low symmetry) phase. In this stage, multiple formations of martensites with the same structure in different orientations are possible. These are called 'variants' of martensite. These structural domains have well defined boundaries and they are called 'twin variants'. The line joining the two variants is known as the 'twin boundary'. Due to easy movement of twin boundaries, the sample can be deformed easily in the martensitic phase. Thus, a sample with a parent shape could be deformed in the martensite phase by the application of stress. The SMA retains the deformed shape after removal of the stress. The schematic diagram of temperature

induced martensitic transformations and shape memory effect is shown in Fig. 1.1.1a and Fig. 1.1.1b.

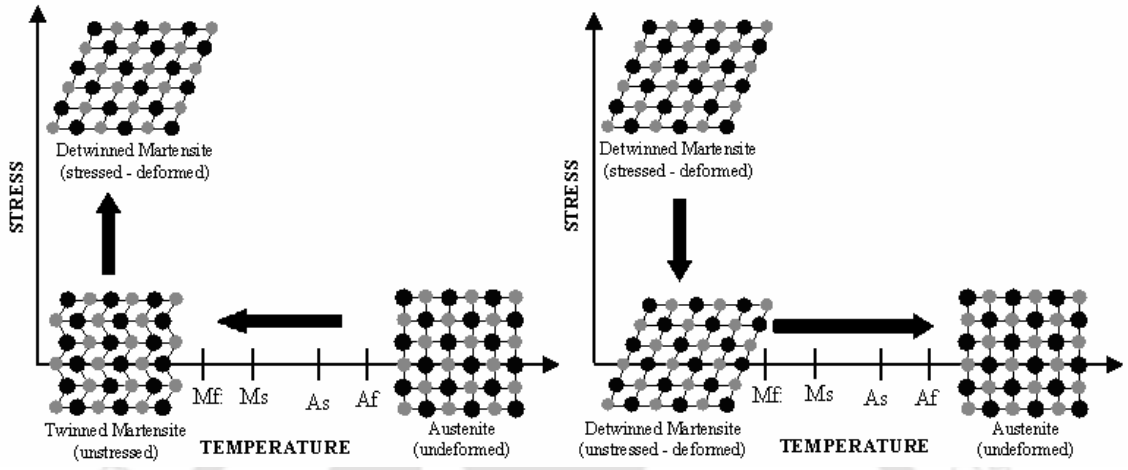

Fig. 1.1.1a: Temperature and stress induced phase transformations.

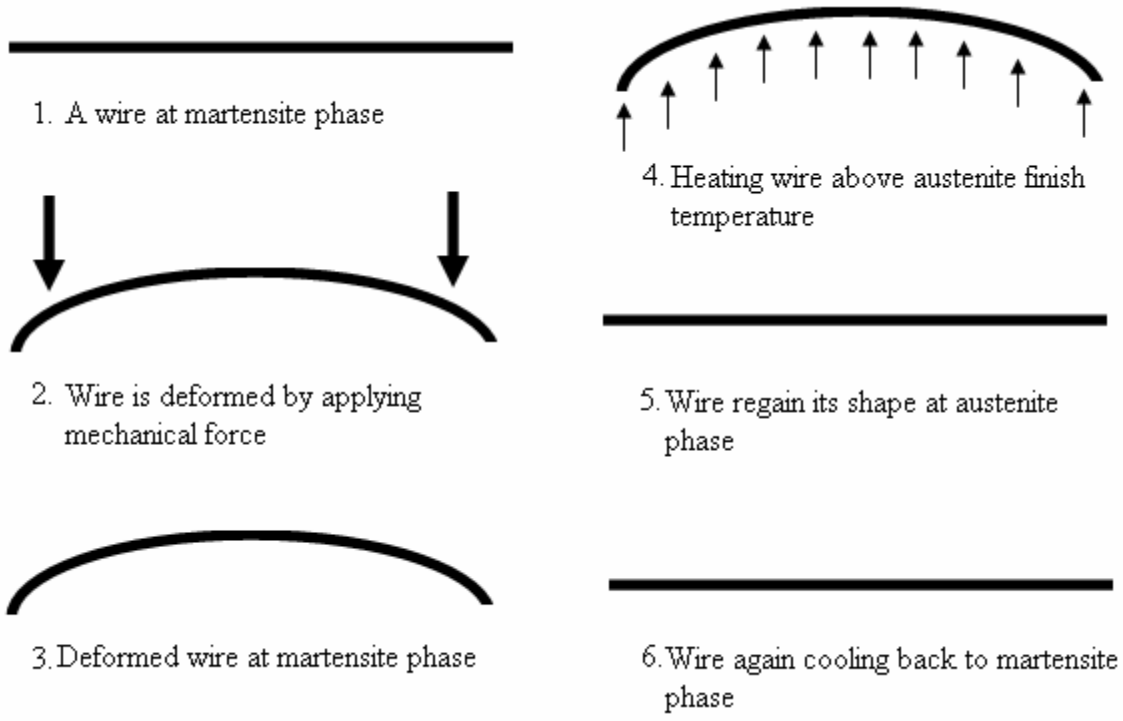

Fig. 1.1.1b: Shape Memory Effect in a straight wire.

However, when the sample is heated back to the austensite phase, the sample will recover to its original shape, *i.e*., it will 'remember' the shape it had before being cooled to the martensite phase. Hence, the sample can be claimed to possess a memory of its parent shape and has the ability to revert back to the parent shape if it is heated back to the austenite phase. The temperature at which the SMA changes its crystallographic structure which is called the martensitic transformation temperature, is characteristic of the alloy, and can be tuned by varying the elemental ratios in the alloy.

A typical differential scanning calorimeter (DSC) curve showing the transformation temperatures obtained under constant heating and cooling rates is shown in Fig. 1.1.2.

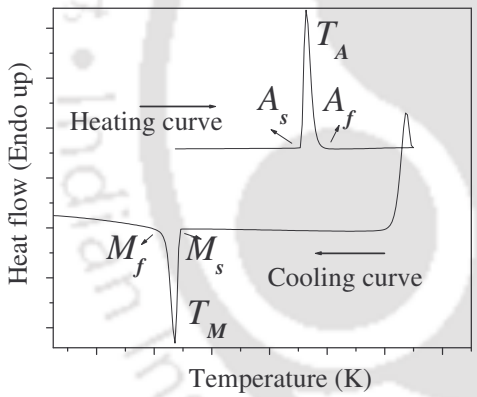

M_s: Martensite start temperature upon cooling
M_f: Martensite finish temperature upon cooling
T_A: Martensite peak temperature upon cooling
A_s: Reverse transformation start temperature upon heating
A_f: Reverse transformation finish temperature upon heating
T_M: Reverse transformation peak temperature upon heating

Fig. 1.1.2: DSC curve showing the martensite and austenite transformations.

1.1.2. Martensitic transformations

Martensite is a crystal structure that is formed by displacive transformation, as opposed to the common diffusive transformations, which is much slower. The martensitic phase transformation is diffusionless, cooperative and shear-like motion of atoms from a high

symmetry phase to a lower symmetry phase, as shown schematically in Fig 1.1.1a. For a reversible martensitic transformation to occur, the following conditions must be satisfied:

1) the driving force for the transformation should be very small,
2) the interface between the martensite and the austenite phases has to be very mobile upon heating and cooling, and
3) the transformation should be crystallographically reversible, *i.e*., the martensite should revert back to the austenite in its original orientation rather than re-nucleating into austenite in different orientations.

Martensitic transformations that satisfy these conditions are also known as thermo-elastic martensitic transformations. The following are the salient properties of this transformation.

1) Martensitic transformations are usually first order solid state structural phase transitions which are diffusionless and dislplacive.
2) Their kinetics and morphology are dictated by the strain energy arising from shear displacement.
3) The atoms move in an organized manner relative to their neighbours and therefore they are known as 'military' transformations in contrast to diffusional 'civilian' transformations. and
4) The displacement can be described as a homogeneous lattice deformation.

1.1.3. One-way and two-way shape memory effects

SMAs are known to display two different types of shape memory effects, *viz*., the one-way and the two-way shape memory effects. A schematic view of the two effects is given

in the Fig. 1.1.3. When a SMA is in its martensitic state, it can be bent or stretched into a variety of new shapes (Fig.1.1.3b) and will retain that shape until it is heated above the transition temperature. Upon heating, the shape changes back to its original shape (Fig.1.1.3c), regardless of its shape in the martensitic state. When the SMA is cooled again, it will remain in the hot shape (Fig.1.1.3c), until deformed again. Such an SMA is said to have 'one-way' shape memory. With the one-way effect, cooling from high temperatures does not cause a macroscopic shape change. A deformation is necessary to create the low-temperature shape.

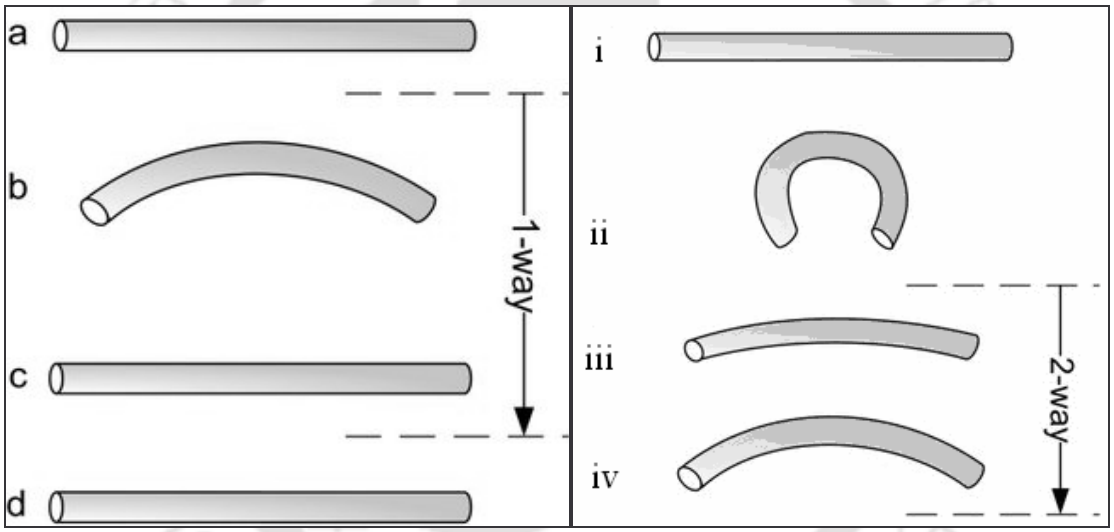

Fig. 1.1.3: One-way and two-way shape memory effects.

A material that shows a shape memory effect during both heating and cooling is called two-way shape memory. In the two-way shape memory effect, the material remembers two different shapes: one at low temperatures (*cf.* Fig. 1.1.3ii), and the other at the high temperature (*cf.* Fig. 1.1.3iv). This effect can also be obtained without the application of an external force (intrinsic two-way effect). The reason the material

behaves so differently in these situations lies in its 'training'. Training implies that an SMA can 'learn' to behave in a certain way. Under normal circumstances, a shape memory alloy 'remembers' its high-temperature shape. But upon heating to recover the high-temperature shape, it immediately 'forgets' the low-temperature shape. However, it can be 'trained' to leave some reminders of the deformed low-temperature condition in the high-temperature phase. There are several ways of doing this. If an SMA is heated up to very high temperatures (after it has been trained), then it may lose the two-way memory effect. Hence this process is said to induce 'amnesia'.

1.1.4. Pseudo-elastic effect

SMAs show almost rubber-like flexibility. This is called 'pseudo-elasticity' or 'super elasticity'. Due to this property, phase change of SMAs from austenite to martensite can be achieved by applying pure mechanical load (without varying temperature). Stress-Strain diagram corresponding to pseudo-elastic effect in an SMA is shown in Fig.1.1.4a.

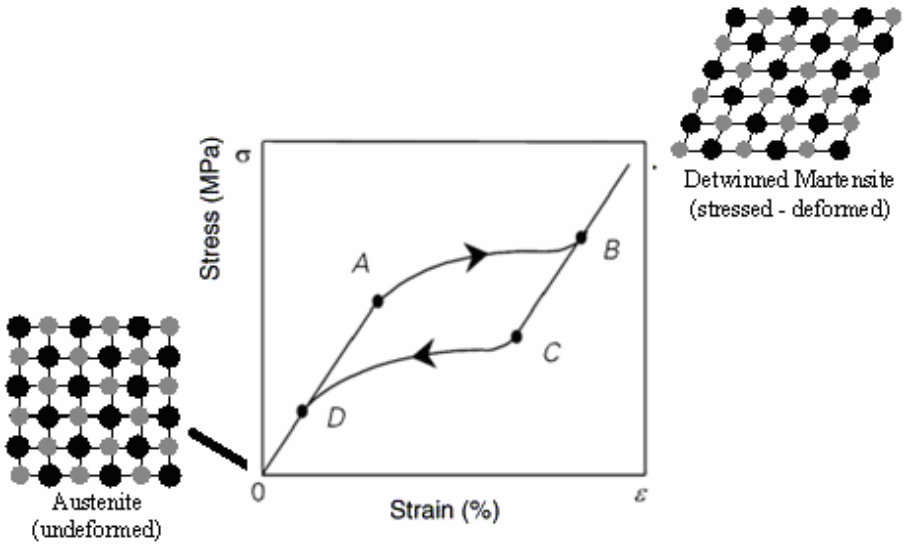

Fig. 1.1.4a: Stress-Strain diagram of the pseudo-elastic effect in an SMA.

Pseudo-elasticity occurs in SMAs when the alloy is completely composed of austenite phase (for $T > A_f$). Unlike the shape memory effect, pseudo-elasticity occurs without a change in temperature. The load on the shape memory alloy is increased until the austenite transforms into martensite, simply due to the loading (Fig.1.1.4b). The loading is absorbed by the softer martensite. But as soon as the loading is decreased, the martensite begins to transform back to austenite since the temperature of the alloy is still above A_f, and it has to regain its original shape.

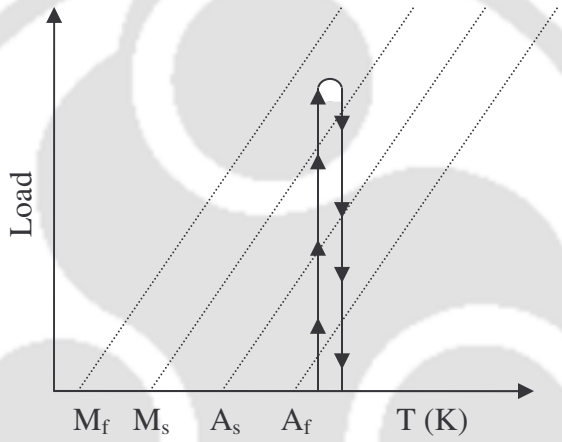

Fig. 1.1.4b: Stress induced martensitic transformations.

1.1.5. Applications of shape memory alloys

Shape memory alloys are used in a variety of applications [10-12] such as military, medical, safety, and robotics. The United States military has been using Nitinol couplers in F-14 fighter planes since the late 1960s. Many of the current applications of Nitinol have been in the field of medicine. Tweezers to remove foreign objects through small incisions were invented by NASA, U.S.A. Anchors with Nitinol hooks to attach tendons

to bone were used for Orel Hershiser's shoulder surgery. Orthodontic wires made out of Nitinol reduce the need to retighten and adjust the wire. Nitinol eyeglass frames can be bent totally out of shape and return to their parent shape upon warming. Nitinol localizers used to locate and mark breast tumors utilize the metal's shape memory property. Another successful medical application is Nitinol's use as a guide for catheters through blood vessels. Anti-scalding devices and fire-sprinklers utilizing SMAs are already in the market. Nitinol is being used in robotic actuators and micromanipulators to simulate human muscle motion. The main advantage of Nitinol is the smooth, controlled force it exerts upon activation. Other miscellaneous applications of shape memory alloys include use in household appliances, clothing and structures.

Future applications envisioned include components of engines in cars and airplanes and electrical generators utilizing the mechanical energy resulting from the shape transformations. Some of the main advantages of shape memory alloys include bio-compatibility of some SMAs and good mechanical properties (high strength, corrosion resistant). However, there are still some difficulties with SMAs that must be overcome before they can live up to their full potential. These alloys are still relatively expensive to manufacture and machine as compared to other materials such as steel and aluminium. Most SMA's have poor fatigue properties which mean that under the same loading conditions (i.e. twisting, bending, compressing), a steel component may survive for more than one hundred times more cycles than an SMA element. Moreover, the response time of SMAs is slow as it is driven by temperature/mechanical stress. These inherently slow processes put an upper limit on the actuation speed of the SMA. Faster change of shape / volume or mechanical strain can be achieved in some magnetic alloys by applying an

alternating magnetic field. Such alloys are called ferromagnetic shape memory alloys (FSMAs).

1.2. FERROMAGNETIC SHAPE MEMORY ALLOY (FSMA)

Ferromagnetic shape memory alloys are very smart materials which can undergo large reversible deformations in an applied magnetic field. As such, they can function both as sensors and actuators. Compared to the ordinary (temperature driven) shape memory alloys, the magnetic field control offers faster response, since the heating and especially cooling process is slower than alternating a magnetic field. Also, the maximum deformation obtained in FSMAs is larger than that obtained in ordinary magnetostrictive materials. When an FSMA is cooled down, it undergoes a structural (so called martensitic) transformation from a cubic to a tetragonal (or modulated) structure. There are two or more equivalent directions for the tetragonal distortions, which results in a twinned microstructure. There are regions called twin variants which have the same structure but with tetragonal distortion occurring in different directions. The twin variants are separated by well defined boundaries. The ordinary shape memory effect is based on the relatively easy movement of the twin boundaries (resulting in large shape changes) and the recovery of the original structure when heated above the structural transition temperature.

In the magnetic shape memory alloys, there are also internal magnetic moments. In the absence of an external field, the magnetic moments are aligned with the easy directions of the magnetization which differ in the different twins [Fig. 1.2a (i)]. When external magnetic field is applied, the magnetic moments try to align with the field. There

are two possibilities, *viz*., the magnetic moments can just rotate within the twins, as it happens in the ferromagnetic shape memory effect [Fig.1.2a (ii)] the twins themselves can move so that the directions of the easy magnetizations align with the field (Fig.1.2a iii). The magnetic field induced redistribution of the twin variants gives the large shape changes observed in the FSMAs.

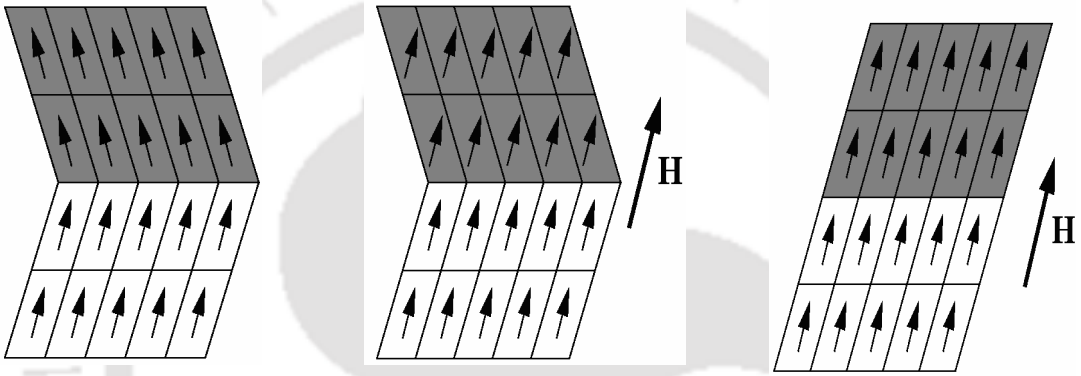

(i) Magnetic moments without external field.

(ii) Rotation of magnetic moments within the twins.

(iii) Redistribution of the twin variants

Fig. 1.2a: Rotation of magnetic moment on application of magnetic field.

The energy required to rotate the magnetization away from the easy directions is called the magnetic anisotropy energy (MAE). For better understanding, a brief discussion on MAE is included here. When the magnetic properties of a crystal are dependent on the direction in which they are measured, the crystal is said to have magneto-crystalline anisotropy. Magnetization has a certain preferable direction with respect to the crystal lattice, the so-called easy axis (the direction along which magnetization tends to align when an external magnetic field is applied). If the energy

required for rotating the magnetization out of the easy direction (i.e. MAE) is higher than the energy required to move a twin, then it is energetically more favorable to move the twin boundaries instead of rotating the magnetization. As a result, twin boundaries can move through the material to increase the volume fraction of the favorably oriented martensite variants and decrease the volume fraction of the unfavorably oriented variants, which lowers the total energy of the system. An interesting and advantageous result of this variant rearrangement is that a macroscopic strain can be induced in a FSMA by applying a magnetic field. If the applied magnetic field is reversed, the twin boundaries can move back to their original positions, recovering the magnetic field induced strain. This magnetic field induced shape memory effect is illustrated in Fig. 1.2a. In short, to be a useful FSMA, the alloy must have ferromagnetic martensite phase and a high uniaxial magneto-crystalline anisotropy.

The ferromagnetic shape memory effect is in a way analogous to super elasticity observed in traditional SMAs. The super-elastic effect occurs when a SMA in its austenitic state is stressed, resulting in the formation of a metastable martensite phase. The martensite forms because the applied stress lowers its total energy, which stabilizes the martensite even though the temperature is above the unstressed martensite-austenite transformation temperature. Analogous to stress-induced martensite, an applied magnetic field can also induce the formation of martensite. If a FSMA is in the austenitic state and an applied magnetic field lowers the total energy of the martensite, a metastable martensite can form. These materials are of particular interest as the magnetic response tends to be faster and more efficient than the temperature-induced response.

Ni-Mn-Ga [13] is the first ternary prototype FSMA developed. Subsequently, Fe-Pd [14], Fe_3Pt [15], Ni-Mn-Al [16], Co-Ni-Al [17-19], Co-Ni-Ga [19,20], Fe-Ni-Ga [21,22] FSMAs have also been developed. Among the FSMAs reported so far, Ni-Mn-Ga alloys are the most widely investigated due to their giant MFIS and excellent thermal stability. In 1996, Ullakko *et al.* [23] reported a large magnetic field induced strain of ~6% in Ni_2MnGa single crystal, which triggered a lot of interest in stoichiometric and off-stoichiometric Heusler alloys. Heusler alloys are ternary intermetallic compounds with a common composition form of X_2YZ. At high temperatures, the stable phase corresponds to a disordered body centered cubic (*bcc*) type structure, referred to as the *A2* phase, characterized by an arbitrary occupation of every site in the crystal lattice [24]. The *A2* phase undergoes a two-stage disorder–order transition on cooling to an ordered *B2* phase. In this phase, *X* atoms order themselves while *Y* and *Z* atoms occupy their sites in the crystal lattice randomly. On further cooling, the structure transforms to the ordered $L2_1$ phase, which is commonly known as the Heusler structure (Fig. 1.2b).

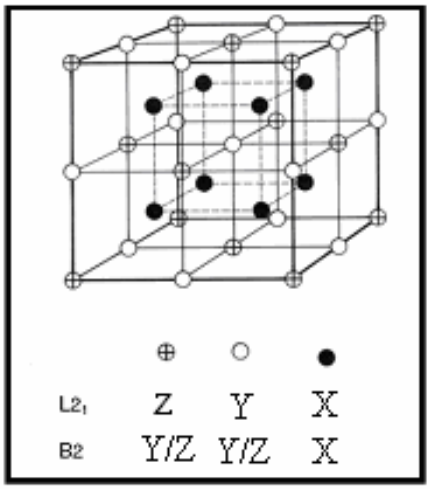

Fig. 1.2b: Atomic arrangement of Heusler alloy X_2YZ [25] for $L2_1$ and *B2* order.

Heusler alloys such as Ni_2MnGa, which are intrinsically inter-metallic compounds, suffer from a number of drawbacks as applicable to engineering materials, the most significant among them being the low toughness of the matrix. In this regard, efforts have been made to explore other systems, particularly, solid solution based alloy systems such as Co–Ni–Al [17, 18, 19] and Co-Ni-Ga [19,20].

1.2.1. Preparation

FSMAs are generally prepared by induction melting [16, 17], arc melting [19, 16, 22] or melt-spinning [26]. Single crystals of FSMAs have also been prepared from the polycrystalline material. Chernenko *et al*. [27, 28] prepared Ni-Mn-Ga alloys by repeated induction melting under argon atmosphere and casting into a cooper mold. Casting into copper mold was employed to get a regular shaped sample. Rod type sample obtained from cylindrical copper mold exhibited relatively small grain size as compared to the button ingot [29]. Wang *et al*. [30] prepared Ni-Mn-Ga alloys by arc melting constituent metals under argon atmosphere followed by the homogenization of the ingots by annealing at 827 °C for nine days in sealed quartz ampoules. Repeated melting causes weight loss of the cast sample which will change the composition of the sample from the desired value. Homogenization below melting point for long time periods yields a homogenous sample. Sometimes, annealing at high temperature is employed to get the desired single phase (*B2* or $L2_1$) sample [16]. Quenching from high temperature into ice water / liquid nitrogen is employed to avoid intermediate phase formation which may have adverse effect on shape memory properties.

The Gibbs free energy change (ΔG) of a system upon martensitic transformation (MT) may be written as a summation of change of chemical energy term (ΔG_c), surface energy term between austenite and martensite (ΔG_s) and elastic energy term around martensite (ΔG_e). In most MTs, the last two non-chemical parts ($\Delta G_{nc} = \Delta G_s + \Delta G_e$) are equally as large as the chemical energy term. Because of this, super-cooling is necessary for the nucleation of martensite [10]. So, shape memory effect will not be observed in the case of some alloys unless they are quenched into ice water or liquid nitrogen.

Often samples need to be processed in a specific way depending on experimental requirements. Brown *et al.* [31,32] prepared Ni-Mn-Ga, Co-Ni-Ga and Co-Ni-Al samples for X-ray and neutron diffraction by crushing the as cast alloys with steel pestle and mortar to a particle size of < 250 μm. The powder samples were sealed under reduced argon atmosphere in quartz ampoules and annealed at 800 °C for 40 hrs and after which they were quenched in ice water. For resistivity or thermoelectric power measurements, flat thin regular shaped samples were obtained by cutting the homogenized sample using low speed diamond cutter [33]. Oikawa *et al*. [17] prepared 2 mm thick ribbon by hot rolling the as-cast sample at 1300 °C. Further cold rolling was carried out to obtain samples of about 150 μm thick to investigate the thermally induced shape change of the Co-Ni-Al alloys. Similar methods have been adopted to obtain Fe-Ni-Ga FSMAs [34]. Martensitic transformations (MT) have been observed in Ni-Mn-Ga [35] and Ni-Fe-Ga [36, 37] in as-cast samples without the need for further processing. However, in the case of Co-Ni-Ga(Al) alloy samples, MT are observed only after rapid cooling or quenching the as-cast ingots homogenized at high temperatures.

Co-Ni-Ga solidifies in a peritectic reaction and forms a composite structure with *fcc* γ-phase and *bcc* β matrix. Thus, controlled amounts of γ-phase can be introduced in the β-matrix by suitable heat treatment procedure. The hot workability and room temperature ductility of these alloys are significantly improved by the introduction of the γ-phase, which is a great advantage for practical applications [19, 38]. So, Co-Ni-Ga(Al) alloys are prepared by arc (or induction melting) constituent metals, followed by homogenization near 1150 °C for 6 – 72 hrs [19, 39, 40] and quenching in ice water / oil bath / liquid nitrogen. Controlled amounts of γ-phase precipitates is introduced [40] by annealing the alloy samples below 1120 °C for 1 - 6 hrs time and then quenching the same in ice water. Single crystals of FSMAs are usually grown by Bridgmann or floating zone method. Müllner *et al*. [41] used single crystal of $Ni_{2.04}Mn_{1.12}Ga_{0.84}$ grown by Bridgman method to investigate the large cyclic deformation of Ni-Mn-Ga FSMAs induced by magnetic field. Chernenko *et al*. [42] also employed Bridgman method to grow $Co_{49}Ni_{22}Ga_{29}$ single crystal. Sakamoto *et al.* [43] used floating zone method to grow single-crystal rods of $Fe_{68.8}Pd_{31.2}$ and Fe_3Pt.

1.2.2. Crystal Structure of phases

The Heusler Ni_2MnGa and its non-stoichiometric compounds undergo a thermoelastic martensitic transformation from the $L2_1$-ordered cubic phase to monoclinic or tetragonal structure with 5*M* modulation or orthorhombic structure with 7*M* modulation [13]. Matrynov [44] described the stress induced martensite structure of $Ni_{2.04}Mn_{0.96}Ga$ as five layered periodic (5*M*- Monoclinic with a = 5.9 Å, b = 5.89 Å and c = 5.59 Å). Wedel *et al.* [45] determined the space group and the atomic coordinates of the stoichiometric and

non-stoichiometric low temperature Ni–Mn–Ga alloys with the help of Transmission electron microscope (TEM) and X-ray diffraction (XRD) data. The results reported by them are summarized in Table 1.2.2a along with the unit cell diagram.

Table 1.2.2a: Atomic parameters for the $Ni_{2.16}Mn_{0.84}Ga$ phase with tetragonal structure, $I4/mmm$ space group a = 3.88 Å; c = 6.48 Å; number of atom per unit cell, Z = 2; unit cell volume = 96.47 Å^3 [45].

Atom	Wyckoff position	*x*	*y*	*z*
Ga	2*a*	0	0	0
Mn[a]	2*b*	0	0	0.5
Ni1[a]	2*b*	0	0	0.5
Ni2[b]	4*d*	0	0.25	0.5

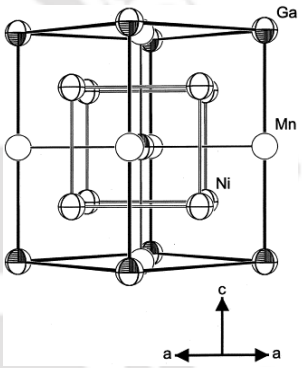

The crystal data and atomic parameters for Ni_2MnGa suggested by Webster [13] are presented in Table 1.2.2b. The crystal structure of the different martensitic phases observed in a wide variety of Ni–Mn–Ga alloy compositions have been studied in detail by Pons *et al.* [46]. A correlation of teragonality with martensite transformation start temperature M_s and *e/a* ratio was observed in the alloys undergoing MT. From Rietveld analysis of the neutron and X-ray powder diffraction data, Brown *et al.* [31] have shown that Ni_2MnGa in the martensitic phase has a 7*M* orthorhombic structure with *Pnnm* space group. Temperature-dependent powder X-ray diffraction studies were carried out by

Table1.2.2b: Crystallographic data of Ni_2MnGa. (1) high temperature cubic, (2) low temperature tetragonal, and (3) low temperature orthorhombic structures [13].

Parameter	(1)	(2)	(3)
Crystal system	Cubic	Tetragonal	Orthorhombic
Space group (atom/unit cell	$Fm\bar{3}m$ ($Z = 4$)	I_4/mmm ($Z = 2$)	$Fmmm$ ($Z = 4$)
Lattice constants (Å)	$a = 5.825$	$a = 4.18$ $c = 5.56$	$a, b = 5.92$ $c = 5.56$
Unit cell volume ($Å^3$)	192.34	97.46	194.93
Wyckoff position (x,y,z) Ni Mn Ga	 8*c*: 0.25,0.25,0.25 4*b*: 0.5, 0.5, 0.5 4*a*: 0, 0, 0	 4*d*: 0, 0.5, 0.25 2*b*: 0, 0, 0.5 2*a*: 0, 0, 0	 8*f*: 0.25,0.25,0.25 4*b*: 0. 0 0.5 4*a*: 0, 0, 0

Ranjan *et al*. [47] on $Ni_2Mn_{1.05}Ga_{0.95}$. With detailed LeBail and Rietveld analyses of powder XRD data, they concluded that the martensite phase belongs to the *Pnnm* space group with 7*M* modulation. However, the tetragonal phase did not exhibit any modulation. $Ni_{2+x}Mn_{1-x}Ga$ ($0.19 \leq x \leq$_0.35) alloys have been reported to be of non-modulated tetragonal structure at room temperature [30]. The lattice constants a and c were reported to linearly decrease and increase, respectively, as x was increased. A cubic austenite phase with $L2_1$ atomic ordering was observed at room temperature for compositions with $x \leq 0.07$. A composite austenite and martensite phase was observed for compositions in the range $0.1 \leq x \leq 0.15$. $Fm\bar{3}m$ space group was assigned to the cubic and *I4/mmm* space group was assigned for *bct* structures. It was found that modulation is

absent as Ni-Mn-Ga compositions with $c/a \geq 1$. A 7*M* modulated monoclinic phase was observed when the $x = 0.2$ alloy was annealed [25]. All the atoms have been reported to be present at fixed high-symmetry special positions. The Wyckoff positions of various atoms in the tetragonal structure are given in the Table 1.2.2b.

Unlike Ni-Mn-Ga alloy, systematic investigations have not been performed on the structure of other FSMAs. It has been reported [48, 49] that Ni_2FeGa alloy has $L2_1$ atomic ordering in its austenite phase and orthorhombic (*14M*) structure at low temperature (<142 K). Sutou *et al.* [50] concluded from stress-strain data that the $Ni_{54}Ga_{27}Fe_{19}$ alloy undergo stress induced martensitic transformation in the following sequence: $L2_1 \rightarrow 10M$, $10M \rightarrow 14M$ and finally, $14M \rightarrow L1_0$.

The crystal structures of the martensite and parent phases of Co-Ni-Al alloys have been identified as $L1_0$ and *B2*, respectively [18, 51 52] Brown *et al.* [32] determined the crystal structure and lattice constant of $Co_{38}Ni_{33}Al_{29}$ alloy from neutron powder diffraction measurements. According to them, the parent phase is the cubic *B2* structure with space group $Pm\bar{3}m$ and $a_{B2} = 2.8571$ Å at 177 °C, and the martensite phase is $L1_0$ with *P4/mmm* space group and $a_{bct} = 2.7139$ Å and $c_{bct} = 3.1311$ Å at −263 °C. Tanaka *et al*. [38] performed XRD measurements on $Co_{30}Ni_{39}Al_{31}$ alloy powder in the temperature range of −198 to 23 °C. The *a* and *c*-axis of martensite phase was found to decrease and increase, respectively, with decreasing temperature. No extra peak characteristic of modulated structure appeared in the Co–Ni–Al XRD data. The high temperature β phase in $Co_{39}Ni_{33}Al_{28}$ alloy could be retained at room temperature by rapid cooling *via* melt-spinning. The over-saturated β phase in the as-spun state exhibited a reversible

martensitic transformation to an $L1_0$ structure. A precipitate phase was formed from the over-saturated β phase upon heating to 673 K [26].

XRD studies have been performed by some researchers [26, 39, 40, 53, 54] to identify the structural phases in Co-Ni-Ga alloys. Though the martensite structure of Co-Ni-Ga alloys was reported [39-40] to be tetragonal, it became evident that the lattice parameters, Miller indices of the peaks and the angular position of peaks in the reported XRD patterns did not fit in the indexing scheme of tetragonal crystal system. The crystal structure of the austenite phase in $Co_{50}Ni_{20}Ga_{30}$ ribbons was reported [26, 54] as *B2*. However, no space group was assigned for the crystal structure. Brown *et al.* [32] analyzed the neutron diffraction data of $Co_{45}Ni_{23}Ga_{32}$ alloy and reported that its martensite phase has a bct unit cell with *I4/mmm* space group and the austenite phase belonged to the *A2*-type with $Im\bar{3}m$ space group. Oikawa *et al.* [19] preferred to designate the austenite and martensite phases of $Co_{45}Ni_{25}Ga_{30}$ alloy as *B2* and $L1_0$ (face centred tetragonal), respectively. Chernenko *et al.* proposed [55] that the martensite phase structure of $Co_{49}Ni_{21}Ga_{30}$ could be either non-modulated bct with lattice parameters $a = b = 2.7$ Å and $c = 3.2$ Å or $L1_0$ with $a = b = 3.8$ Å and $c = 3.2$Å after analyzing electron diffraction data. Selected area electron diffraction patterns revealed that the atomic order in the martensite phase was derived from *B2*-type rather than $L2_1$ type austenite phase [55]. From the above discussion, it is obvious that confusion prevails about the structure of the martensite phase of Co-Ni-Ga alloys. The inherent difficulty in obtaining fine powders suitable for diffraction experiments in this ductile system without inducing additional strain in the alloy poses considerable challenge in performing XRD measurements.

1.2.3. Effect of composition on the properties

The number of martensite phases, their structures and the sequence of their occurrence in FSMAs depend on the stoichiometry of the alloys. Chernenko *et al.* [28] investigated the variation of M_s, thermal hysteresis, Curie temperature (T_C) and transformation heat with composition in Ni-Mn-Ga alloys. Their results can be summarized as follows: (i) At a constant value of Mn content, Ga addition lowers M_s. (ii) Mn addition (instead of Ga) at constant Ni concentration causes M_s to increase. (iii) Substitution of Ni atoms by Mn at constant Ga content results in alloys with lower M_s and higher T_C. Based on these observations, Ni-Mn-Ga alloys have been classified into the following three groups. Group-I: alloys near stoichiometric composition (Ni_2MnGa), whose T_C ~ 370 K; premartensitic transition (T_{PM}) ~ 250K and martesitic transition (T_M) ~ 210K (*i.e.* $T_M < T_{PM} < T_C$). Group-II: off-stoichiometric alloys with T_M ~ 250 K and $T_M < T_C$. These alloys usually exhibit stress and thermally induced intermartensitc transition [56, 57]. Giant magnetic field induced strain is a common feature observed in these alloys. Group-III: alloys with $T_M > T_C$.

The magnetic properties and structural phase transformations of Heusler alloys $Ni_{2+x}Mn_{1-x}Ga$ and $Ni_{2-x}Mn_{1+x/2}Ga_{1+x/2}$ were investigated by Wang *et al*. [30]. It was found that the martensitic transformation temperature increases and the Curie temperature decreases with decreasing Mn concentration in the $Ni_{2+x}Mn_{1-x}Ga$ system, but the magnetic properties decrease faster than the $Ni_{2-x}Mn_{1+x/2}Ga_{1+x/2}$ system. This suggests that the influence of the conduction electron concentration and the distance between Mn atoms on the Curie temperature is stronger than the magnetic dilution effect. The

martensitic transformation temperature shows a peak value at x = 0.06 in the $Ni_{2-x}Mn_{1+x/2}Ga_{1+x/2}$ system. Similar behavior was observed by Matsumoto *et al.* [58] in $Ni_{2+x}Mn_{1-x}Ga$ alloys. They have also investigated the substitutional effect on martensitic transformation and Curie temperature of $Ni_{2+x}Mn_{1-x}Ga$ (x = 0 - 0.19) alloy system. In stoichiometric composition (x = 0), crystal transformation temperatures are around 200 K and Curie temperature is around 400 K. The transformation temperatures increased and Curie temperature decreased with an increase in Ni content. The magnetic transition and the crystal transformation occur simultaneously at the same temperature for the alloys with Ni composition $x \geq 0.18$, giving rise to a coupled magnetostructural transition. It has been found that for $x \geq 0.24$, $T_M > T_C$. In these alloys, a paramagnetic phase appears between paramagnetic cubic and the ferromagnetic tetragonal phase, and the martensitic transition occurs in the paramagnetic state [59]. Single phase martensite with tetragonal structure was observed in $Ni_{50+x}Mn_{25}Ga_{25-x}$ (x = 2 - 11) alloys for $x < 7$ [57]. When x changes from 2 to 7, a systematic change of the tetragonal structure has been observed which leads to the conclusion that unit cell volume reduces with the reduction in Ga content (or with the addition of Ni). The lattice parameters do not change for x = 7 to 11. It was inferred from the above results that 57% of Ni is the soluble limit of Ni atom in tetragonal structured martensite. A linear increase of martensitic transformation temperature with the decrease of Ga content was observed for alloys with $x \leq 7$. The variation of martensitic transformation temperatures with Ga content was correlated with electron concentration (*e/a*). Wuttig *et al*. [20] reported that the martensite start temperatures vary in the range 20 °C < T < 60 °C in $Co_2Ni_{1-x}Ga_{1+x}$, (x = 0.06, 0.09, 0.12, 0.15) alloys in their as-solidified state. Quenched $Co_2Ni_{1-x}Ga_{1+x}$, ($1 > x > 0.3$) alloys are

ferromagnetic when $x < 0.5$ and their saturation magnetization depends on the composition as well as the annealing treatment [20].

Wuttig *et al*. [60] predicted that the transformation temperatures should be higher for SMAs with higher electron/atom (*e/a*) ratio, which was also experimentally confirmed in the prototype Ni-Mn-Ga alloys [61]. The electron concentration (*e/a*) was calculated by assuming the following configurations of the valence electrons and their number per atom (in brackets): For Mn: core + $3d^5 4s^2$ (7); for Fe: core + $3d^5 4s^3$ (8); for Co: core + $3d^3 4s^1$ (9); for Ni: core + $3d^8 4s^2$ (10); for Ga /Al: core + $4s^2 4p^1$ (3); *etc*. These configurations are commonly used in band calculations of the electronic structure of Heusler alloys [62]. Krenke *et al*. [63] studied the linear variation of M_s with *e/a* for Ni–Mn–X Heusler systems, where X is a group III–group V element. It was observed that the linear dependence is not universal for all systems and that the slope of the linear behavior is different for the different X species. It increased either as X changes from Al to In (isoelectronic) or from In to Sb (increase in number of *p* electrons). The features in the M_s *versus e/a* plot and the relative stability of the various crystallographic phases of Ni–Mn based Heusler alloys have been analysed and reported.

The compositional dependence of martensitic transformation and Curie temperatures were systematically investigated for various FSMAs by Oikawa *et al*. [19] All FSMAs exhibit similar compositional dependence behavior. The compositional dependent phase diagram of Ni-Fe-Ga, Ni-Mn-Ga, Co-Ni-Ga and Co-Ni-Al alloys studied by them are shown in Fig. 1.2.3 (a-d).

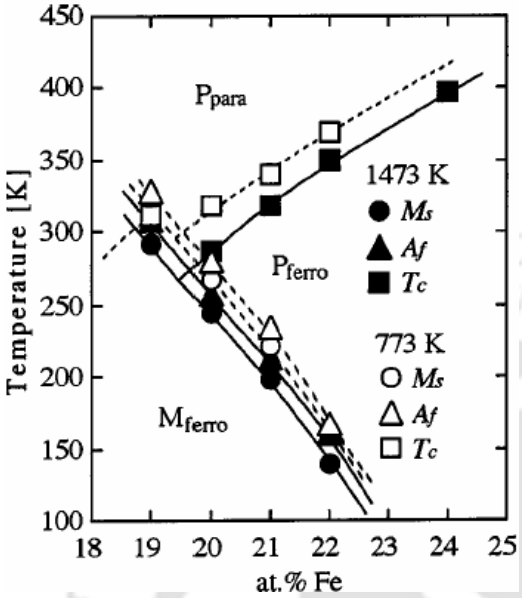

Fig.1.2.3a: T_C, M_s and A_f variation in Ni-Fe-27at%Ga annealed at 773 k and 1473 K [22].

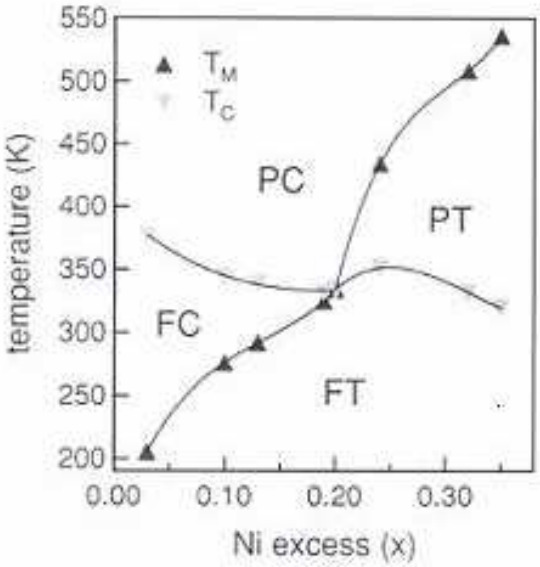

Fig.1.2.3b: T_C, M_s and A_f variation in Ni-Mn-Ga [59].

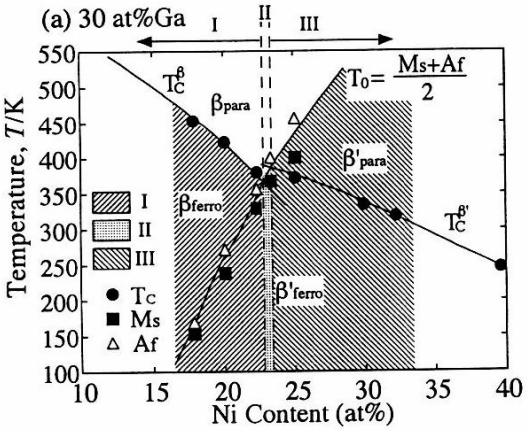

Fig.1.2.3c: T_C, M_s and A_f variation in Co-Ni-30at%Ga [19].

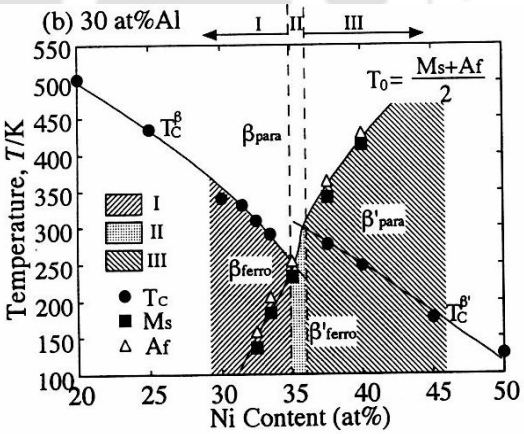

Fig.1.2.3d: T_C, M_s, A_f variation in Co-Ni-30at%Al [19].

Change of entropy at the martensitic transformation in $Ni_{2+x}Mn_{1-x}Ga$ was investigated by Khovalio *et al.* [64]. The entropy change was reported to increase with an increase in Ni content.

1.2.4. Effect of heat treatment

When dealing with high temperature shape memory alloys, thermal stabilization of martensite has to be considered. This phenomenon, consisting of the transient shift of the reverse transformation temperatures after direct quenching to martensite or after ageing in martensitic state, has been studied in depth for Cu–Zn–Al alloys [65]. Several other SMAs have been found to show some degree of martensite stabilization, including Au–Cd [66] and Cu–Al–Ni [67]. The mechanisms used to explain this phenomenon have been extensively discussed and include short-range atomic reordering and defect pinning of the martensite interfaces [67-68]. Although the relative importance of the role played by the different mechanisms in martensite stabilization is very much dependent on the alloy system and thermo-mechanical treatments, it has been clearly established that the stabilization brought about by martensite ageing is a diffusive phenomenon, hence thermally activated process. Therefore, stabilization can be promoted by ageing in martensite phase in high temperature shape memory alloys. Segui *et al.* [69] reported that in Ni-Mn-Ga, the martensite stabilization increases with ageing time and temperature. Santamarta *et al*. [34] observed the aging effect of polycrystalline $Ni_{53.5+x}Fe_{19.5-x}Ga_{27.0}$ alloys, with $x = 0$, 0.5, 1.5 by ageing at 520 K, 670 K and 770 K. All the alloys showed good long-term thermal stability after treatment at 520 K, but, ageing at 670 K and 770 K caused degradation of the martensitic transformation after ~10^5 s.

TEM studies revealed the appearance of small and mostly elongated precipitates after long ageing periods at 670 K and 770 K.

1.2.5. Magnetic properties

The magnetic properties relevant to FSMAs include variation of magnetization with applied field (*M-H* plot) at different constant temperatures, variation of magnetization with temperature (*M-T* plot) at low field, and variation of low field ac susceptibility with temperature (χ-*T*). It was experimentally observed that the martensitic transformation in the FSMAs is accompanied by (i) abrupt decrease of magnetization measured at non-saturated fields [70], (ii) nearly 40 times drop of the initial magnetic susceptibility [36], (iii) appearance of a maximum temperature dependence of the transversal magnetosriction, and (iv) an order of magnitude increase of magnetosriction. A phenomenological model relating the magnetization process in the twinned martensitic state of Fe and Ni based alloys to the strain-induced magnetic anisotropy has been analyzed by Cherenko *et al.* [70]. The lowering of point symmetry group during the austenite-martensite transformation results in a considerable enhancement of magnetocrystalline anisotropy of the martensite phase. Due to the magnetoelastic interaction, the elastic energy stored by the martensite gives rise to the magnetic anisotropy, which can dominate the magnetization process [71].

The effective magnetic anisotropy constant K_{eff} of the powders has been calculated from the initial magnetization curves using the law of approach to saturation [72]. The *M-H* data is fitted to the relation, $M = M_{sat}\left(1-\frac{a}{\sqrt{H}}-\frac{b}{H^2}-\right)$ and from it K_{eff}

could be estimated using the relation $K_{eff} = \sqrt{\frac{15b}{4}} \times M_{sat}$ .Here M_{sat} is called as saturation magnetization.

For ferromagnetic materials, at finite temperatures, M_{sat} will also depend on how well the dipole moments are aligned, as thermal vibration of the atoms causes misalignment of the moments and hereby reduction in M_{sat}. At Curie temperature (T_C), magnetization or ac susceptibility falls sharply with the increase/decrease of temperature during heating/cooling. Thus, T_C can be roughly estimated from the M-T or χ-T data. The modified Arrott plot obtained from the M-H plots yields more accurate T_C values. The M-T and χ-T behaviour close to the accurately determined T_C can be used to estimate the critical constants and nature of the ferromagnetic to paramagnetic transition. [73].

The variation of T_C with composition has been explained in terms of the magnetic valence number [38]. It was found that there is a strong correlation between saturation magnetization M_{sat} or T_C and the average magnetic valence number Z_m. The value of T_C increases with the increase of Z_m, as predicted in generalized Slater-Pauling model [74]. Magnetic valence like ordinary chemical valence is an integer for each column of the periodic table. The magnetization M (in the unit of μ_B) is given by as, $M = (N^{\uparrow} - N^{\downarrow} = 2N^{\uparrow} - Z)$; where Z is the chemical valence (atomic number – number of core electrons or $Z = N^{\uparrow} + N^{\downarrow}$). Thus, Z_m for 3d transition metal can be expressed as, $Z_m = 2N_d^{\uparrow} - Z$; where $N_d^{\uparrow}$ is the number of up spin electrons in the 3d shell. Using the above relation magnetic valence numbers for Mn, Fe, Co, Ni, ….., Zn, Ga, etc, are obtained as 3, 2, 1, 0, , -2, -3 respectively. The average magnetic valence number for an alloy of composition $A_xB_yC_z$ is calculated as

$$Z_m \text{ (average)} = \{x * (Z_m \text{ of } A) + y* (Z_m \text{ of } B) + z* (Z_m \text{ of } C)\}/100 \quad \text{--- (1.2.5)}$$

It should be noted that if the magnetic phase transition occurs in the martensite phase, the T_C values are systematically higher than the T_C in austenite phase [17, 19, 22]

1.2.6. Transport properties

Knowledge of thermal and electrical properties of FSMAs is very important because they can help us in understanding the mechanisms involved in the phase transformation process, including its electronic structures and scattering processes. The thermal stability is directly related to the thermal properties. Electron transport can be evaluated from the thermoelectric power (also known as Seebeck coefficient denoted by *S*) and electrical resistance (*R*) measurements. The temperature variation of electrical resistivity and thermoelectric power (TEP) of magnetic Heusler alloy $Ni_{2.19}Mn_{0.81}Ga$ has been investigated by Priolkar *et al.* [35]. Temperature dependence of the TEP of this alloy has been explained in terms of the crystal field splitting. The occurrence of the magnetic and martensitic transitions at almost the same temperature in $Ni_{2.19}Mn_{0.81}Ga$ has been explained from TEP data as a consequence of changes in the density of states at the Fermi level. Li *et al.* [75] measured the electrical and thermal properties of Ni–Mn–Ga FSMAs. They noticed a jump in electrical resistance and a maximum in *S* at the structural phase transformation were observed. Similar behavior of abnormal change of resitivity during the structural phase transition was also reported by other research groups [36]. The resistance jump near the transformation temperature is due to the scattering mechanism which is a result of formation of interfaces and twin boundaries during the structural transformation [75].

Magneto-resistance (MR) in the martensite phase shows different behavior as compared to the austenite phase due to the twinning and high magneto-crystalline anisotropy. A negative magneto-resistance of 5% has been reported in bulk $Ni_{2+x}Mn_{1-x}Ga$ alloys by C. Biswas *et al*. [76]. The variation of MR for different phases (austenite, martensite, intermartensite) in an alloy and as a function of alloy composition has been explained by spin disorder scattering and magnetic anisotropy.

1.2.7. Mechanical properties

Tensile and compression testing: Mechanical properties of FSMA can be determined from stress-strain (*S*-*S*) data obtained by compressing regular shaped sample or applying uniform tension to the both ends of the sample. Fig.1.2.7 shows *S*-*S* curve of a typical SMA. One can clearly see in the permanent strain after unloading (shown as curve OC in Fig.1.2.7), the recovery strain (shown as curve CD in Fig.1.2.7; shape memory strain, as indicated by the arrow) and the residual strain (irreversible strain, curve OD in Fig.1.2.7). The shape memory effect measurement using compression test involves the following steps: At the outset, the length of the samples is measured before loading (l_0), after unloading (l_1) and after heating it to a temperature higher than A_s (l_2). Residual strain after unloading (ε_r), strain recovered due to SME (ε_{SME}) and permanent strain (ε_{per}) are then obtained as: $\varepsilon_r = (l_0-l_1)/l_0 \times 100\%$, $\varepsilon_{SME} = (l_1-l_2)/l_1 \times 100\%$ and $\varepsilon_{per} = (l_0-l_2)/l_0 \times 100\%$ respectively. Recovery rate (R) is calculated as $R = \varepsilon_{SME} / (\varepsilon_{SME} + \varepsilon_{per}) \times 100\%$ [57].

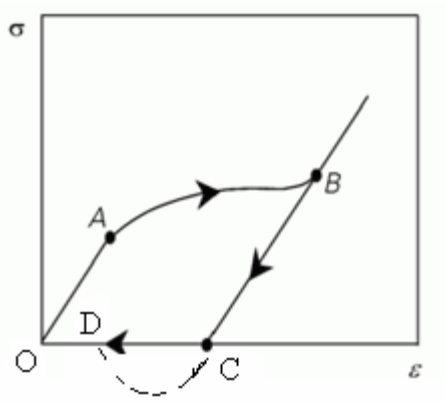

Fig.1.2.7: Stress-strain curve of a typical SMA.

It has been reported that the mechanical and shape memory characteristics of the polycrystalline $Ni_{54}Mn_{25}Ga_{21}$ high temperature shape memory alloys can be improved by grain refinement. It is known that the polycrystalline Ni-Mn-Ga alloys are extremely brittle. Li *et al*. [29] investigated the stress–strain behavior of polycrystalline NiMnGa alloys with high transformation temperature in compression mode and demonstrated the effectiveness of grain refinements. Better mechanical properties obtained for $Ni_{54}Mn_{25}Ga_{21}$ rod sample was explained in terms of its small grain size and finer martensitic twins. Super-elasticity (SE) in tensile loading of the Co–Ni–Al polycrystalline $\beta + \gamma$ alloys has been investigated by Tanaka *et al.* [38]. It was found that the SE properties in the $\beta + \gamma$ two-phase alloys strongly depend on the volume fraction of γ-phase present. In particular, the temperature dependence of the critical transition stress increased with increase in the volume fraction of γ-phase. Furthermore, the SE properties were enhanced by controlling the β-grain size. Consequently, the maximum recovery SE strain of about 6.3% was achieved in a sheet specimen with the large β. A pronounced super elasticity of ~6% was reported in single crystalline NiMnGa alloys [28].

Microhardness: Dimensional analysis and the finite element approach were employed to study the spherical indentation hardness of SMAs [77]. The reverse transformation stress does not affect the hardness of a super-elastic SMA. The scaling relationship between the hardness and other material parameters has been established through dimensional analysis. The influences of all the parameters on the spherical indentation hardness have been examined using the numerical analysis. The major conclusions are (1) hardness increases with the forward transformation stress, (2) higher Young's modulus of the martensite will lead to a larger hardness, (3) hardness decreases with an increase in the maximum transformation strain magnitude, and (4) indentation hardness increases with the maximum indentation depth. Therefore, the measured indentation hardness cannot be treated as a material property of SMAs. Contrary to the above conclusion it is found that Vickers microhardness (VHN) does not depend on the applied load or indentation depth. Thus, Vickers microhardness measurement can be used to obtain information about the ductility from the indentation fracture toughness data.

Magnetic field induced strain (MFIS): The main goal of research on FSMA is to find a magnetic alloy composition exhibiting martensitic phase transformation that would allow control of large displacements by application of a magnetic field at constant temperature. A martensitic phase generally accommodates the strain associated with the transformation by the formation of twin variants that pack together in compatible orientations to minimize strain energy. Alignment of these twin variants by the motion of twin boundaries can result in large macroscopic strains. Magnetic field control of the twin variant orientation requires that the magnetization energy $K_u = M_{sat}H_a/2$ (where M_{sat} is the saturation magnetization, H_a is the applied magnetic field) [23], be sufficient to induce

motion of the twin boundaries. This energy K_u is called magnetic anisotropy energy density. The mechanical energy required to move the twin boundaries can be obtained from stress-strain analysis using the relation $E_v = \sigma.\varepsilon/2$, σ is the critical stress required for the movement of twins and ε is the corresponding strain [23]. Here, E_v is the energy density essential for total alignment of all twin variants. σ represents the stress applied to the system and ε represents the corresponding strain. By equating K_u and E_v we can get the value of M_{sat} required to get appreciable strain induced by a given magnetic field. This input could be used to tailor sample compositions optimized for actuator applications.

Ni-Mn-Ga FSMAs exhibiting up to ~10% magnetic field induced strain [78] has led to the possibility of developing magnetic actuators with extremely fast response time. Murray *et al*. reported magnetic field induced strain of 6% [79] in single crystalline Ni-Mn-Ga martesite at room temperature. Jeong *et al*. [80] observed maximum MFIS of 0.01% at temperature ~ 37˚C under 10000 G applied magnetic field in the martensite phase of Ni-19.5at.% Mn-27at.% Ga polycrystalline alloy. Kakeshita *et al*. [81] reported MFIS in Fe–31.2 at. % Pd alloy at 77 K, Fe_3Pt at 4.2 K and Ni_2MnGa at 77 K. Magnetic field was applied along [0 0 1] direction and strain was measured along the same direction. It should be also noted that strain recovery of 0.6% observed in Fe_3Pt was not seen in Fe–31.2 at.% Pd and Ni_2MnGa. Similar results have been observed at other temperatures as well, with the highest value being ~1% at 20 K.

1.2.8. Effect of additive element

The addition of a fourth element can be an effective way to change the characteristics of the magnetic and structural transformations of Heusler (X_2YZ) and offstoichiometric Heusler alloys. The brittleness of Ni-Mn-Ga alloys is the biggest obstacle for practical applications. It is well known that proper addition of rare-earth elements can improve the mechanical properties of various alloys and intermetallic compounds. The martensitic transformation temperatures of Ni–Mn–Ga alloys are very sensitive to the presence of rare-earth elements. As reported, the substitution Tb for Ga in $Ni_{50}Mn_{29}Ga_{21}$ alloy enhanced the M_s, whereas the M_s of $Ni_{48}Mn_{33}Ga_{19}$ alloy decreased with the addition Sm [82-83]. Heavy rare-earth Gd is ferromagnetic and has the highest Curie temperature among the rare-earth elements. Addition of Gd affects the martensitic transformation temperatures, mechanical properties and magnetic properties of Ni–Mn–Ga alloys [84-85]. On adding Gd to $Ni_{50}Mn_{29}Ga_{21-x}Gd_x$, the martensitic transformation temperatures, bending strength and ductility increase remarkably. Refinement of the grains and strength of the grain boundaries resulting from the addition of Gd result in the improvement of the mechanical properties. Martensite structure changes from 5M in alloys with 0.1 at% Gd to 7M for alloys with 0.5 to 2 at.% Gd. Wu *et al*. have reported the magnetic properties and shape memory effect of Fe-doped $Ni_{52}Mn_{24}Ga_{24}$ [86]. On partly replacing Mn with Fe in $Ni_{52}Mn_{24}Ga_{24}$ with the $L2_1$ crystal structure, the material ($Ni_{52}Mn_{16}Fe_8Ga_{24}$) exhibits a large moment of $3.91\mu_B$ per *f.u.* (formula unit) and a high T_C of 381 K. Kikuchi *et al.* [87] studied the magnetic properties of the $Ni_2Mn_{1-x}Fe_xGa$ ($0 \leq x \leq 0.7$) alloys in order to investigate the electronic properties of FSMAs Ni_2MnGa and Fe–Ni–Ga. The martensitic and reverse martensitic transformation temperatures have been reported to

decrease with increasing x, whereas T_C increased with the increase of x. It is reported that μ^{total} is almost independent of x for $Ni_2Mn_{1-x}Fe_xGa$ ($0 \leq x \leq 0.7$). Assuming that the moments of Ni and Mn in $Ni_2Mn_{1-x}Fe_xGa$ ($0 \leq x \leq 0.7$) are $0.36\mu_B$ [31] and $3.08\mu_B$ [32], respectively, the moment of Fe is estimated to be about $3.0\mu_B$. This value is much larger than the moment of pure α-Fe ($2.217\ \mu_B$). The moment of Fe in $Ni_2Mn_{6/7}Fe_{1/7}Ga$ ($x \cong 0.14$) was reported to be $2.68\ \mu_B$ [87]. The large moments on Fe are brought through hybridization with the surrounding Ni atoms. Thus, the moment of Fe is enhanced when Fe is surrounded by transition elements with more *d*-electrons.

The effect of addition of many different elements has been studied in the Ni–Mn–Ga alloy. However, much less information exists on this topic in the new FSMA families. Effect of Co, In, Ag and Mn addition in Ni–Fe–Ga has been investigated [88-95]. Indium causes a strong decrease of the MT temperatures [91], while Co increases these temperatures [88]. Co substituting Ni causes a drop in T_M and an increase in T_C. The opposite behaviour occurs when Co substitutes Fe (in this case, the change of T_C is however very small) [89-90]. Finally, when Co substitutes Ga, the MT temperatures increase, while substitution of 1 at% Ni by Ag practically does not affect the transformation temperatures [92]. Besides the change of the transformation temperatures, some other effects have also been reported, such as an improvement of MFIS in alloys containing Co, increase in Curie temperature [93-94] and a large negative magneto-resistance effect in a $Ni_{50}Fe_{17}Ga_{25}Mn_8$ alloy [95]. Recently, very large MFIS (8.5% under a field of ~0.6 T) assisted by an external stress of 8 MPa applied to the sample has been reported in $Ni_{49}Fe_{18}Ga_{27}Co_6$ [96]. Picornell *et al.* [97] reported that the MT temperatures decrease and T_C increases slightly when 3 at.% Mn substitutes for Fe. Substitution of Fe

by Co causes an increase in MT temperatures, the effect being opposite when Co replaces Ni. In both cases, T_C increases, the effect being stronger in the alloy in which Ni is replaced by Co. The $L2_1 \rightarrow B2$ order–disorder transition temperatures are hardly affected by addition of Co, whereas Mn addition induces an increase of ~50 K with respect to the ternary alloy. Addition of Co or Mn to Ni–Fe–Ga alloys (substituting Ni or Fe) modifies the MT temperatures according to the changes produced in *e/a* ratio. However, the shift of MT temperatures is notably higher in the alloy in which Fe is substituted by Co, having the same change (in absolute values) of *e/a* than the others. These results suggest that, besides the density of conduction electrons, the change in the size of the atoms (and the corresponding unit-cell volume) also at play role in controlling the transformation temperatures. Although both elements additions increase T_C, the effect being stronger when Co is added, especially when it replaces Ni. The martensitic phases formed are also modified. Addition of Co (replacing either Fe or Ni) seems to increase the stability of the seven-layered martensite. Moreover, when Co substitutes Fe, the *2M* structure is also formed. Substitution of Fe atoms by Mn promotes the predominance of the six-layered phase and formation of the unusual four-layered structure.

Liu *et al.* [98] investigated the microstructure, super-elasticity and fracture behavior of $Co_{50}Ni_{22-x}Ga_{28}Fe_x$ ($x = 0,\ 1,\ 2,\ 5$) alloys. It was shown that the MT temperatures decrease as Ni is gradually substituted by Fe. The volume fraction of the second phase is also reduced with increasing Fe content, which impairs the mechanical properties. Two-phase Co–Ni–Ga–Fe alloys have been reported to exhibit complete super-elastic behaviour in a wide temperature interval between room temperature and 200 °C. Moreover, the stress hysteresis in two-phase alloy was found to be more sensitive

to temperature than the single-phase alloy. Zheng *et al* investigated [88] the effects of Co on the martensitic transformation and magnetic properties of Ni–Fe–Ga magnetic shape memory alloys. An unusual phenomenon of one martensitic transformation and two intermartensitic transformations was observed in the DSC curve of $Ni_{55.3}Fe_{17.6}Ga_{27.1}$ alloy. Addition of 3 at.% Co in $Ni_{55.3}Fe_{17.6}Ga_{27.1}$ alloy increases the M_s from 313 K to 405 K, improves the saturation magnetization from 21.64 to 97.67 emu/g and enhances the magnetocrystalline anisotropy constant from 1.253×10^6 to 4.035×10^6 erg/cm^3.

1.3. SOME FEATURES OF THIS WORK

As of now many FSMAs had been developed and many have been proposed as potential candidates for sensor and actuator applications. But till now, no practical device has been reported with these FSMAs. Practical application of Ni-Mn-Ga alloy is limited because of its extreme brittleness in polycrystalline state. The compositions of Co-Ni-Ga(Al) FSMAs are located near the two-phase (β + γ) region [19], which facilitates the introduction of appropriate amounts of the cubic γ-phase in the β-matrix by proper choice of alloy composition. Also Co-Ni-Ga solidifies in a peritectic reaction and forms a composite structure with fcc γ-phase and bcc β matrix. Thus, controlled amount of γ-phase can be introduced in the β-matrix by suitable heat treatment conditions. The hot workability and room temperature ductility of these alloys are significantly improved by the introduction of the γ-phase, which is a great advantage for practical applications [19].

Oikawa *et al.* [19] observed phase equilibrium between β and γ phases in these systems and the variation of martensitic phase transformation temperatures (M_s and A_s) and Curie temperature (T_C) of $Co_{70-x}Ni_xGa_{30}$ alloys in the β + γ region. It was observed

that the T_C increases while M_S and A_f decrease with increasing Co content. T_C and M_s plotted as a function of composition intersect near x = 23 in this series of alloys. Magnetization increases abruptly at the reverse martensite transformation temperature (A_s) and decreases sharply at T_C during heating. Similarly, magnetization increased sharply at T_C and decreased abruptly at the martensite transformation temperature (M_s) during cooling. Since T_C and M_s are very close in $Co_{47}Ni_{23}Ga_{30}$ alloy, the magnetic transition in this alloy composition could not be properly characterized by them. Properties of FSMAs have been found to be sensitive to alloy composition, homogenization (or annealing) temperature, cooling rate during preparation and post-preparation heat-treatment. Apart from tailoring the transformation temperatures, these heat-treatment procedures adopted during preparation and post-preparation stages help in understanding the stability and structural evolution in these alloys.

Understanding the structure of the crystalline phases present, the $M \leftrightarrow A$ structural transformations, magnetic properties and mechanical properties in the Co-Ni-Ga FSMA are crucial for evaluating these materials for actuator applications. Hence, an investigation on Co-Ni-Ga FSMAs was taken up in this thesis work.

Composition of alloys has been selected so as to obtain room temperature or high temperature ferromagnetic martensite samples on the basis of the *e/a* ratio. Wuttig *et al*. [60] have claimed that alloys exhibit martensitic transformations for *e/a* > 7.33. Two series of Co-Ni-Ga alloy compositions have been selected for the present investigations (Fig.1.3). In the first series ($Co_xNi_{25}Ga_{75-x}$), Co is replaced by Ga, and for each 0.5 at.% increment of x, *e/a* decreases by 0.03. It is expected that martensitic transformations will decrease when Co content in decreased at the cost of Ga. The magnetic valence number

Z_m will also decrease with the decrease of Co content. Consequently, T_C is expected to decrease. In the second series ($Co_{70-x}Ni_xGa_{30}$), Ni is replaced by Co and for each (x is changed by 1.0 at.%) decrement of x , e/a will decrease by 0.01. Thus, the transformation temperatures are expected to be lowered with the decrease of Ni. But as Z_m increases when Co content [74] is increased at the cost of Ni, T_C is expected to increase.

The variation of A_s, M_s and T_C with compositions in Co-Ni-Al(or Ga) was reported by Oikawa *et al.* [19] served as the basis for the of selection of Co-Ni-Ga compositions for the present investigation. The criteria to obtain a complete β - microstructure which transforms to martensite are (1) the β-phase must be stable across as a wide temperature range as possible (The less wide is this temperature range, the faster the cooling rate required to retain the β-phase without diffussional composition), (2) the transformation temperature must fall within a range that satisfies the requirement for shape memory application. With this choice of composition three groups of alloys has been prepared namely, Group I: $M_s < A_s < T_C$, Group II: $M_s < T_C < A_s$ and Group III: $T_C < M_s < A_s$.

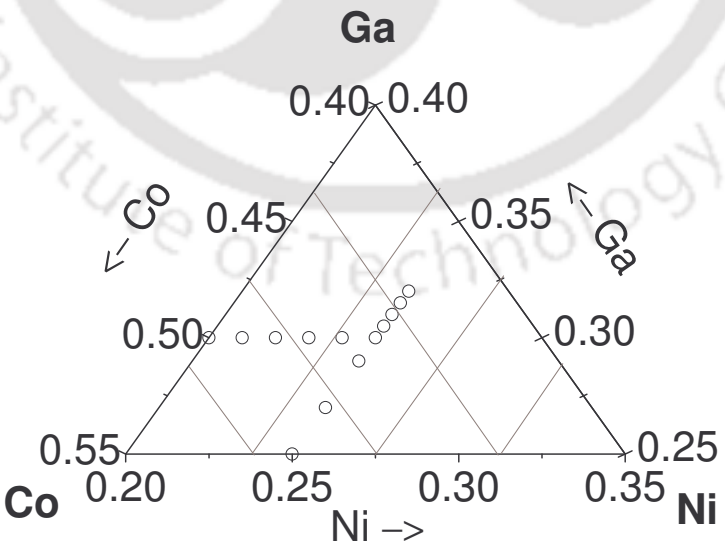

Fig. 1.3: Co-Ni-Ga compositions chosen for study in the present work.

It has been found that Co-Ni-Ga alloys have better ductility than Ni-Mn-Ga. However, saturation magnetizations (Msat) of Co-Ni-Ga are much lower than that of Ni-Mn-Ga alloys. An effort has been made to improve the M_{sat} of Co-Ni-Ga alloys without compromising the ductility by the additions of small amount of Mn or Fe to a chosen Co-Ni-Ga alloy composition with reasonably high M_s, T_C and M_{sat}.

EXPERIMENTAL TECHNIQUES AND PROCEDURES

The experimental techniques used and procedures adopted in the course of this experimental thesis work are described below:

2.1. SAMPLE PREPARATION

In the present work, the alloy ingots were prepared by arc melting the constituent elements. A commercial arc melting furnace (Vacuum Techniques, India) was used for preparing the alloy ingots. A schematic diagram of an arc melting furnace is given in Fig. 2.1.1 (A 200 A dc power supply used as electrical source is not shown here).

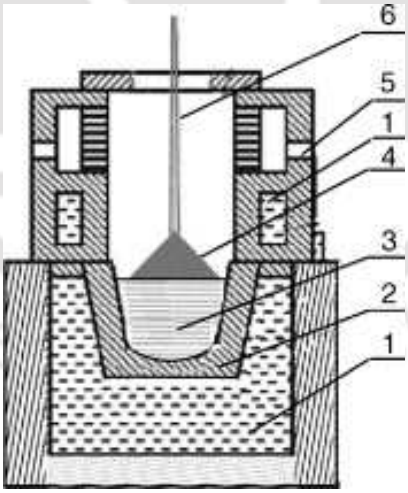

Fig. 2.1.1: Schematic diagram of water-cooled copper-hearth electric arc melting furnace used: Labels denote, (1) circulating water to cool the hearth, (2) copper hearth; (3)

compacted metal blend, (4) electric arc struck between the electrodes (5) gas inlet valve (6) water cooled flexible electrode with tungsten tip (anode).

Elemental powders of cobalt, nickel, gallium, manganese and iron, as per the requirement of the target composition, were weighed in a calibrated electronic balance of 0.01 mg resolution and blended thoroughly in an agate pestle and mortar. The blended alloy mixture was cold compacted in a stainless steel die under a pressure of 40 MPa. The compacted pellet weighing about 5 g was placed the water-cooled copper hearth of the arc furnace and the chamber was pumped down to ~ 10^{-5} Torr. The chamber was purged with argon gas to remove traces of oxidizing atmospheric gases and finally filled with argon gas pressure of 750 Torr. DC arc was then struck and the pellet was melted carefully so as to ensure that no material is lost from the pellet. The cast ingot was then flipped around and re-melted three or four times to ensure complete melting of the constituent elements.

The ingot obtained after melting was molded (re-melted) in a dismountable copper cylinder kept on the water cooled hearth in order to obtain a 10 mm diameter cylindrical sample. As-cast ingots with weight loss > 3% were rejected. The alloy ingots were processed under different conditions as required for various investigations. The different processing procedures are briefly described below.

The as-cast alloys were brittle and also needed to be homogenized further in order to obtain samples with consistent and reproducible properties. The metallic ingots cannot be heat treated in air since they might oxidize. So, the as-cast ingots were taken separately in fused silica ampoules, which were pumped down to 10^{-5} Torr using an oil

diffusion pump (Vacuum Techniques, India) and then flame-sealed. The vacuum-sealed ampoules containing the alloy ingots were placed inside a raising hearth furnace (70T-4, Okay, India), homogenized at 1150 °C for 24 hours and allowed to slowly cool inside the furnace. The slowly cooled samples did not show any signature of martensitic transformations in differential scanning calorimeter studies. So, the cylindrical ingots were cut into small discs (1mm or 8 mm thickness, as required) using a diamond saw (Isomet 2000, Buehler) and cleaned with acetone in an ultrasonic bath. The dried discs were again flame-sealed in fused silica ampoules at a pressure of 10^{-5} Torr, annealed separately at 1230 °C, 1150 °C, 1000 °C and 900 °C for six hours and quenched. Air, ice water and liquid nitrogen were used as quenching media for different investigations. The small discs ensured effective quenching of the homogenized alloy. Thick discs (8mm thickness) were annealed at 1000 °C and quenched in ice water for mechanical testing (Stress-strain studies). For the investigation of microstructure and microhardness, flat samples were mounted in resin using a thermostatic press (Simplet 2, Buehler) and polished using a polishing machine (Ecomet 6, Buehler). A mixture of 40 ml HNO_3 and 60 ml distilled water was used as etchant in order to, microscopically examine the twinned structure and secondary phase present in the samples. Liquid nitrogen quenched samples showed cracks and were very brittle. This provided a means to obtain coarse powder of the alloys for performing XRD measurements. It has to be pointed out that due to the high ductility of the Co-Ni-Ga alloys, fine powders ideally suited for good XRD measurements could not be obtained. The powdered alloys were taken in sealed fused silica ampoules, heat treated again at 1230 °C for 4 hours and quenched in ice water, so as to remove any strain induced while grinding the discs.

2.2. SCANNING ELECTRON MICROSCOPE

The scanning electron microscope (SEM) images the sample surface by scanning it with a high-energy beam of electrons in a raster scan pattern. The electrons interact with the atoms that make up the sample producing signals that contain information about the sample's surface topography, composition and other properties such as electrical conductivity. The types of signals produced by an SEM include secondary electrons, back scattered electrons, characteristic x-rays and light (cathodo-luminescence). These signals come from the beam of electrons striking the surface of the specimen and interacting with the sample at or near its surface. In its primary detection mode, *viz*., secondary electron imaging, the SEM can produce very high resolution images of a sample surface, revealing details about 1 to 5 nm in size. Due to the way these images are created, SEM micrographs have a very large depth of focus (commonly from about 25 times to 250,000 times) yielding a characteristic three-dimensional appearance useful for understanding the surface structure of a sample. Back-scattered electrons (BSE) that come from the sample may also be used to form an image.

In a typical SEM (schematically shown as in Fig.2.2.1), electrons are thermionically emitted from a tungsten filament cathode are accelerated towards an anode. The electron beam, with a typical energy of a few hundred eV to 40 keV, is focused into a very fine focal spot of 0.4 nm to 5 nm by one or two condenser lenses. The beam passes through pairs of scanning coils or pairs of deflector plates in the electron column, which deflect the beam horizontally and vertically so that it scans in a raster

fashion over a rectangular area of the sample surface. When the primary electron beam interacts with the sample, the electrons lose energy by repeated scattering and absorption. The size of the interaction volume depends on the electron's landing energy, the atomic number of the specimen and the specimen's density. The energy exchange between the electron beam and the sample results in the reflection of high-energy electrons by elastic scattering, emission of secondary electrons by inelastic scattering and the emission of electromagnetic radiation which can be detected to produce an image. The image may be captured by photography from a high resolution cathode ray tube, but in modern machines is digitally captured and displayed on a computer monitor.

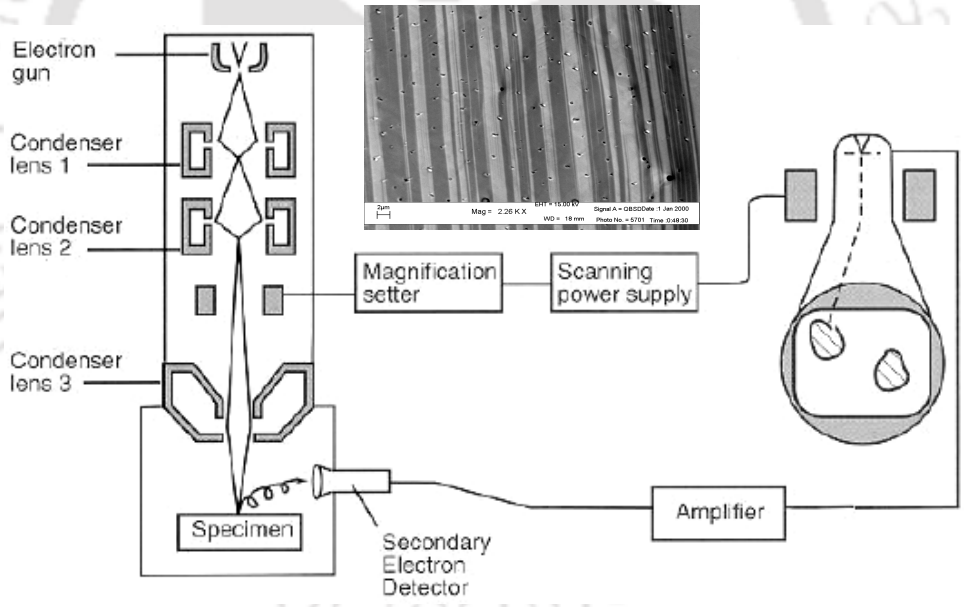

Fig. 2.2.1: A schematic diagram of a SEM.

In an SEM, as in scanning probe microscopy, magnification results from the ratio of the dimensions of the raster on the specimen and the raster on the display device. Assuming that the display screen has a fixed size, higher magnification results from reducing the size of the raster on the specimen, and vice versa. Magnification is therefore controlled by the current supplied to the *x*, *y*.

BSE images are often used in analytical SEM along with the spectra produced from the characteristic X-rays as clues to the elemental composition of the sample. The analytical technique used for the elemental analysis or chemical characterization of a sample is called energy dispersive X-ray spectroscopy (EDS, EDX or EDXRF). Its characterization capabilities are due in large part to the fundamental principle that each element has a unique atomic structure allowing X-rays that are characteristic of an element's atomic structure to be identified uniquely from each other. To stimulate the emission of characteristic X-rays from a specimen, a high energy beam of electrons is focused into the sample being studied. The incident beam may excite an electron in an inner shell, ejecting it from the shell while creating an electron-hole where the electron was. An electron from an outer, higher-energy shell then fills the hole, and the difference in energy between the higher-energy shell and the lower energy shell is released in the form of an X-ray. The X-ray released by the electron is then detected and analyzed by the energy dispersive spectrometer. There are four primary components of the EDS setup: the beam source; the X-ray detector; the pulse processor; and the analyzer. The schematic diagram of the EDS is shown as in Fig.2.2.2. A typical EDS graph is also shown in Fig.2.2.3.

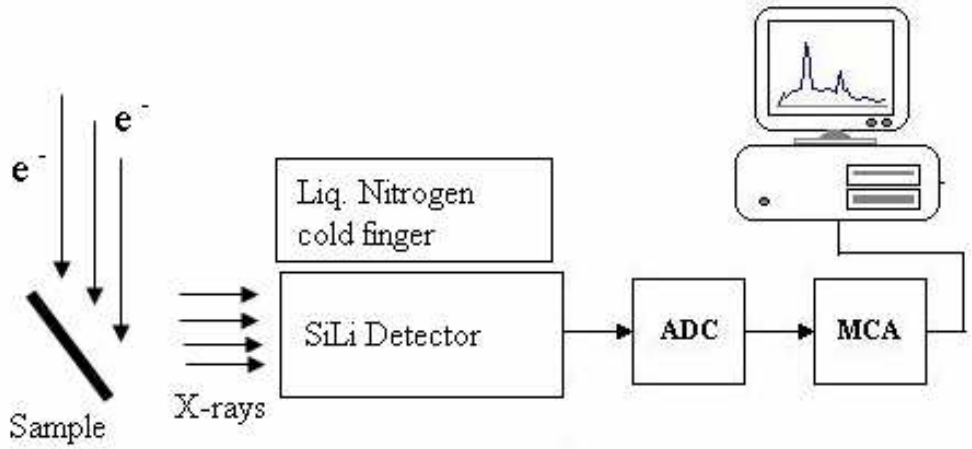

Fig. 2.2.2: A schematic diagram of the EDS attachment in a SEM

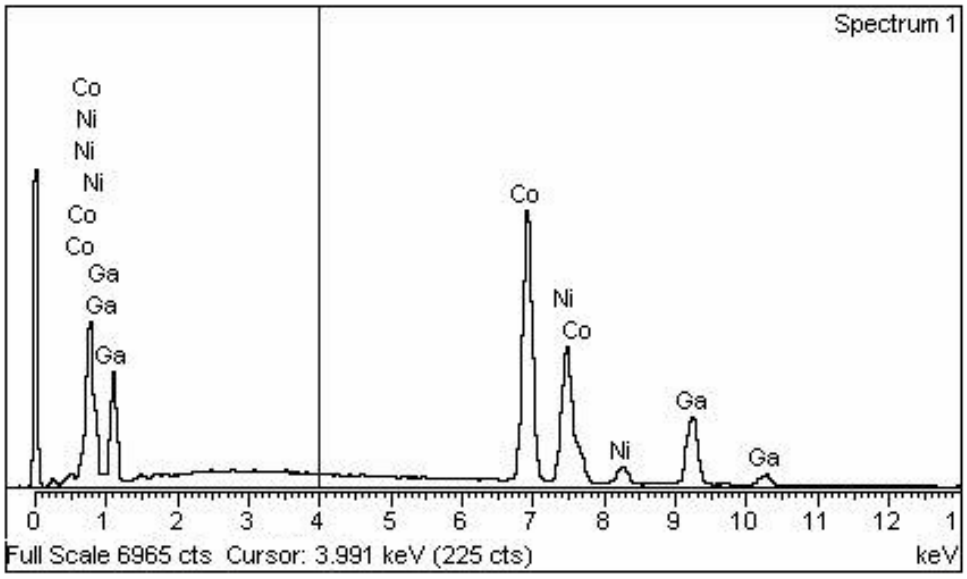

Fig. 2.2.3: A typical EDS graph of Co-Ni-Ga alloy

Emitted X-rays are allowed to fall on a radiation sensitive silicon semiconductor detector with a high impedance zone. Both, the detector and the field-effect transistor of the first stage of preamplifier are cooled to get an optimum of energy-resolution. Inside the detector, each absorbed X-ray quantum is converted into pairs of charge- carriers

(electrons and holes). With a charge-sensitive preamplifier (PA) the charge quantity is finally converted into a voltage-pulse. The pulses are digitized by the analog to digital converter (ADC) and a multi-channel analyzer (MCA), stores the digitized pulses as pulse height spectrum. Then, a pulse amplitude spectrum is developed, in which the stochastically measured discrete X-ray quanta are sorted according to the energy and are collected for different energy types. The X-ray spectrum of the EDS is thereby a histogram (energy distribution of all collected X-ray quanta).

Compositional analysis has been carried out on the prepared alloy samples using a commercial SEM (LEO 1430VP) equipped with an EDS attachment (Model 7353, Oxford Instruments) at Central Instrumental Facility (CIF), IIT Guwahati. Both spot and line analysis were performed on the samples using software provided with the instrument. The SEM-EDS was operated with an acceleration potential of 15 kV to 20 kV, and each spectrum was collected for about 100 s duration. The SEM photograph was taken for selected samples in order to study the martensite structure. A typical SEM micrograph is shown as an in-set in Fig. 2.2.1.

2.3. X-RAY POWDER DIFFRACTOMETER

A commercial X-ray powder diffraction system (Seifert XRD 3003 T/T) was used for the phase identification, quantitative measurement of secondary phase present in two-phase alloys and crystal structure determination of the FSMAs. Cu K_α radiation (1.541 Å) with a nickel filter was used. The X-ray tube was operated with an acceleration voltage of 40 kV and tube current of 30 mA. The theta-theta (θ-θ) goniometer was used in the reflection (Bragg-Brentano) geometry [99] as depicted in Fig. 2.3.1.

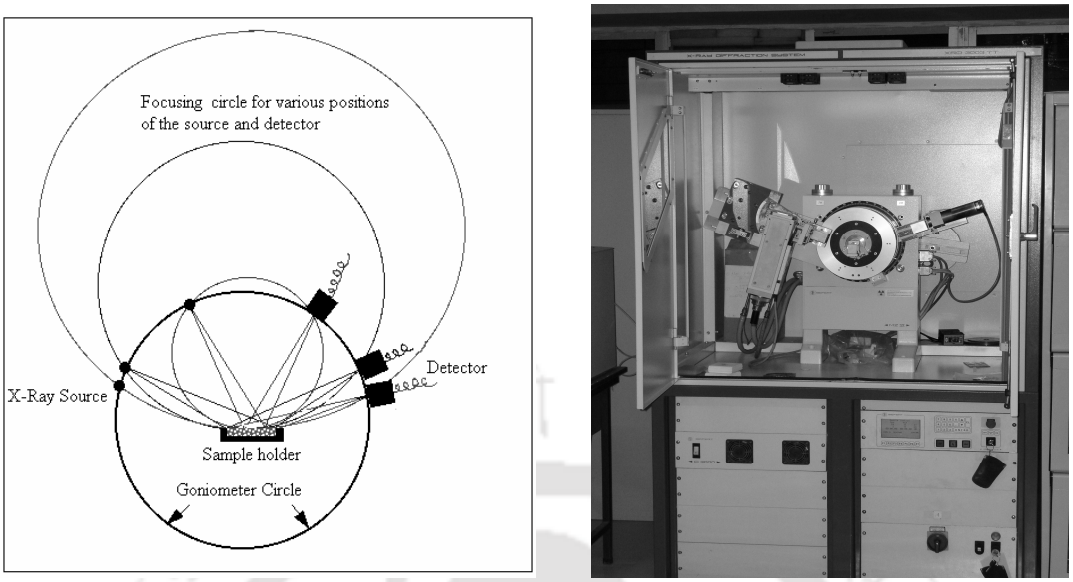

Fig. 2.3.1: A typical X-ray Diffractometer with Bragg- Brentano geometry

A polymetamethylacrylate (PMMA) plate with a square depression of dimensions 25 mm × 25 mm × 0.5 mm coated with a thin layer of high vacuum grease was used as sample holder for X-ray diffraction (XRD) measurements. A thick layer of coarsely powdered alloy sample (processed as mentioned earlier) was evenly spread over a square depression and mounted on the goniometer for recording the XRD patterns. The XRD data provides the variation of intensity / counts per second (cps), recorded by the scintillation detector as a function of 2θ, where θ is the glancing angle. A standard polycrystalline silicon (Si) sample, provided with the instrument was used for the calibration of the instrument. A typical (observed) XRD pattern of standard polycrystalline Si sample is shown in Fig. 2.3.2.

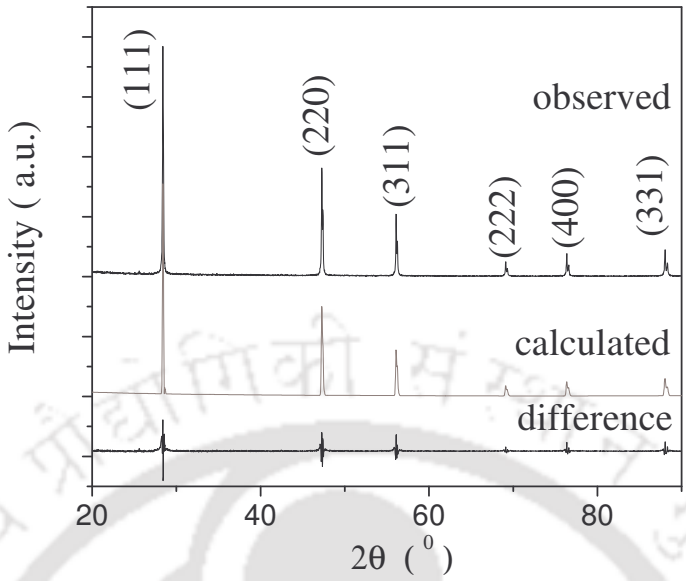

Fig. 2.3.2: XRD pattern of Si sample (observed). Calculated and difference data correspond to least squares fitting performed on the observed data.

Rietveld refinement technique has been employed to refine the crystal structures. The public-domain software, Fullprof, was used for Rietveld analysis [100-102] of X-ray powder diffraction data. There are two version of source code available. The first corresponds to a program written in FORTRAN 77 and can be used in multiple platforms. The second version developed from the previous one, is coded in FORTRAN 95. The two input files for this program are the '*.pcr' and '*. dat' files. The *.pcr file contains the title, type of analysis (X-ray, neutron or profile fitting), profile function used for fitting, number of phase present, wave length of the beam used for the collection of data along with the step size and 2θ range, number of iteration cycles, number of refined parameter and other crystallographic data. The *.dat file contains the intensity (cps) data. Some optional input files can also be used such as '*.bac' for specifying the

background at each step of the scattering variable, '*.irf' for incorporating the instrumental resolution function, *etc*. The two main output files are '*. out' and '*.sum' that contain all control variables and refined parameters. Another important output file is '*.prf' which contains observed and calculated profiles that are automatically used by another graphical interface program called *WinPLOTR*. A graph is obtained with calculated pattern from the input file (*.pcr) and observed pattern from (*.dat) and their differences. The control of the refined parameter is achieved by using a flag in the form of a code word. The sequences for refinement involves setting / optimising the following: (1) scale factor, (2). zero point of detector, first two background parameters and lattice constant(s), (3) overall Debye-Waller factor, (4) peak shape and asymmetry parameters, (5) atom occupancies, (6) individual isotropic thermal parameters, and (7) additional background parameters.

The quality of refinements are known based on the values of reliability factors such as R_p, R_{wp}, R_{exp}, R_{Bragg} , χ^2 and R_F and they are defined as follows:

Profile factor, $$R_P = 100 \frac{\sum_{i=1,n} \left| y_i - y_{c,i} \right|}{\Sigma_{i1,n} y_i} \qquad (2.3.1)$$

Here 'y_i' is the observed point (experimental), '$y_{c,i}$' is the calculated point and n represents the number of data points.

Weighted profile factor, $$R_{wp} = 100 \left(\frac{\sum_{i=1,n} \omega_i \left| y_i - y_{c,i} \right|^2}{\Sigma_{i1,n} \omega_i y_i^2} \right)^{1/2} \qquad (2.3.2)$$

Here $\omega_i = \frac{1}{\sigma_i^2}$; σ_i^2 is the variance of the observation y_i.

Expected weight factor, $$R_{\exp} = 100\left(\frac{n-p}{\Sigma_{i\,1,n}\omega_i y_i^2}\right)^{1/2} \quad (2.3.3)$$

Here (n - p) is the number of degrees of freedom. . 'p' is the number of refine parameters.

Reduced chi-square, $$\chi^2 = \left(\frac{R_{wp}}{R_{\exp}}\right)^2 \quad (2.3.4)$$

Bragg factor $$R_{\exp} = 100\left(\frac{\Sigma_h \left|I_{obs,h} - I_{cal,h}\right|}{\Sigma_h I_{obs,h}}\right)^{1/2} \quad (2.3.5)$$

Here 'h' levels the Bragg's reflections. The $I_{obs,h}$ is the observed integrated intensities and $I_{cal,\,h}$ is the calculated intensities.

The crystallographic R_F factor, $$R_F = 100\left(\frac{\Sigma_h \left|F_{obs,h} - F_{cal,h}\right|}{\Sigma_h F_{obs,h}}\right) \quad (2.3.6)$$

Here $F_{obs,h}$ and $F_{cal,h}$ are the observed and calculated structural factors respectively.

The χ^2, R_B and R_F values has been observed by fitting XRD data for Si std sample as 1.86, 10.2 and 6.2 respectively. A quantitative estimate of the percentage of secondary phase present with the primary phase (in case of alloys exhibiting two-phase structure) has been obtained from the *.out file.

2.4. DIFFERENTIAL SCANNING CALORIMETER (DSC)

DSC is a thermo-analytic technique [103] in which the difference in the amount of heat required to increase the temperature of a sample and a reference material is measured as a function of temperature. The DSC curves are recorded either under a constant heating (or cooling) rate or under isothermal conditions (time scan at a constant temperature).

A typical DSC consists of two isolated sealed pans, one containing the sample and the other a reference material (generally, Al_2O_3 or just the empty Al pan) (Fig. 2.4.1). The two pans are heated or cooled uniformly while the heat flow difference between the two is monitored. The basic principle underlying this technique is the following, when the sample undergoes a physical transformation such as phase transition, more or less heat will need to flow to it in comparison with the reference in order to maintain both at the same temperature. More or less heat flowing to the same would depend on the process being endothermic or exothermic. In the power compensation type DSC, heat is supplied to either of the pans so that both are maintained at the same temperature. The heat flow (dH/dt) is then estimated from this data. In a DSC based on the heat-flux technique, the temperature difference (ΔT) between the two isolated pans is measured from which the heat flow is estimated.

A commercial DSC (PerkinElmer, DSC7) based on the power compensation technique was used in the current investigations. Weighed quantities of Co-Ni-Ga sample pieces were crimped in Al sample pan and the thermal transformations occurring in the temperature range of 25 ^{o}C to 250 ^{o}C was studied during the heating and cooling cycles under a constant heating/cooling rate.

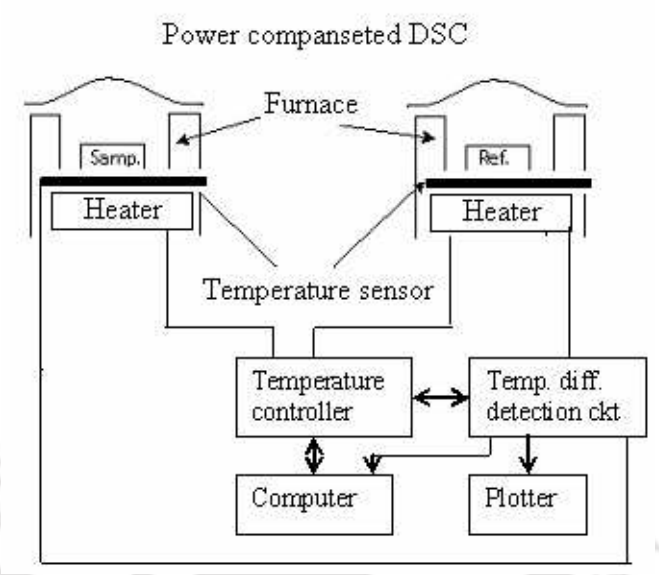

Fig. 2.4.1: A schematic diagram of a DSC

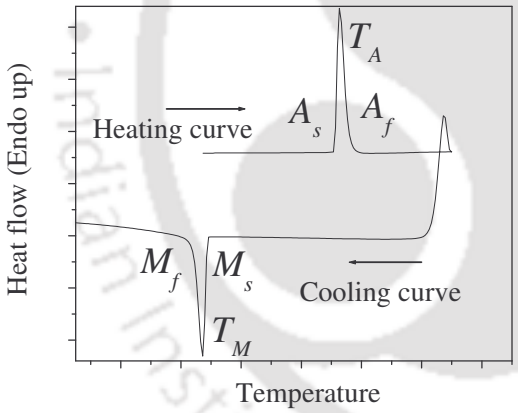

Fig. 2.4.2: Typical DSC curve obtained for an FSMA sample in the current studies.

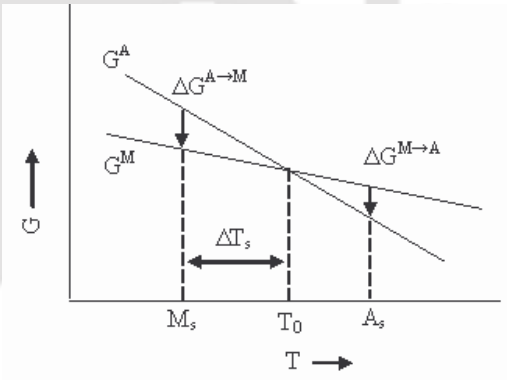

Fig. 2.4.3: Schematic representation of free energy curves of martensite and austenite phases [10]

The runs were programmed and the DSC curves (*dH/dt* versus *T* data) were recorded and analyzed using the Pyris™ software. Temperature and enthalpy calibrations

were performed using standard samples (In and Zn). High purity nitrogen gas was purged continuously throughout the runs.A typical DSC thermogram for of a shape memory alloy is shown as in Fig. 2.4.2. The endothermic peak during heating and exothermic peak during cooling represents the reverse martensitic phase transformation and forward martensitic phase transformation, respectively. The point at which the endothermic peak starts during heating is called austenite start (A_s) temperature and the point at which endothermic peak finishes is called austenite finish (A_f) temperature. Similarly the starting and finishing points of the exothermic peak during cooling are called martensite start (M_s) and martensite finish (M_f) temperature, respectively.

The free energy of the martensite phase is more than that of the austenite phase (Fig. 2.4.3). Thus, during the solid state phase transformation from martensite to austenite, energy is absorbed by the system (endothermic reaction). Similarly, during the transformation from austenite to martensite, energy is released from the system (exothermic reaction). The Gibbs free energy change of a system at $M \leftrightarrow A$ transformation may be written as,

$$\Delta G = \Delta G_c + \Delta G_s + \Delta G_e = \Delta G_c + \Delta G_{nc} \qquad (2.4.1)$$

where ΔG_c is a chemical energy term originating in the structural change from parent to martensite and ΔG_{nc} is the non chemical energy term contains a surface energy term (ΔG_s between austenite and martensite) and elastic energy term (ΔG_e around the martensite) [10]. In most martensitic transformations, ΔG_{nc} is equally large as ΔG_c. In the absence of elastic strain energy, the forward and reverse transformation temperatures (i.e. M_s and A_s) coincides with the thermodynamic equilibrium ($\Delta G = 0$) temperature T_0. This non-chemical energy term changes the driving forces and hence T_0 [104]. A further super-

cooling of ΔT_s from T_0 is necessary for inducing the martensitic transformation and superheating is necessary for the reverse martensitic transformation. The fact M_s is not the same as M_f can also be explained in a similar way. Elastic energy around the martensite resists the growth of the martensite unless a further driving force such as cooling is performed on the system.

2.5. AC SUSCEPTOMETER

AC susceptibility (ACS) technique was used to determine the ferromagnetic to paramagnetic transition (Curie) temperature in the Co-Ni-Ga samples [105]. However, ACS can also be used to determine the martensitic and reverse martensitic transformation temperatures. ACS is a useful technique in condensed matter physics since the typical magnetic fields used are very low and the relative ease with which the frequency and amplitude of the magnetic fields could be varied in the instrument. A high temperature low-field AC suseptometer with a temperature range of 25 °C to 300 °C, was designed and built in our laboratory [106]. The instrument is based on a three-coil mutual inductance bridge. The mutual inductance bridge consists of a primary coil and two Secondary coils as schematically shown in Fig. 2.5.1. The primary coil consisting of 930 turns was wound with 22 SWG copper (Cu) enameled wire on a nylon cylinder of inner diameter 15.6 cm, outer diameter 19.8 cm, and length 70 mm. The secondary coils containing ~1600 turns over a length of 13 mm, were wound with 42 SWG enameled Cu wire. A Cu plate of dimension $2\times5\times120$ mm^3 fitted with a resistive heater was used as the sample holder. The temperature of the sample was measured with a calibrated copper – constantan thermocouple. A Low pressure environment was maintained around

the sample holder with the aid of the fused silica sheath connected to a rotary pump. The primary coil was energized using an ac (sinusoidal) voltage fed from a lock-in amplifier. When a signal, $E = E_0 \sin(i\varpi t)$ is applied to the primary coil, a magnetic field of $B = B_0 \sin(i\varpi t)$ is generated along the axis of the solenoid (primary coil). When there is no sample present at the centre of the secondary coil, the induced voltage in both the secondary coils would be nearly equal and the difference output at the Lock-in Amplifier will be zero.

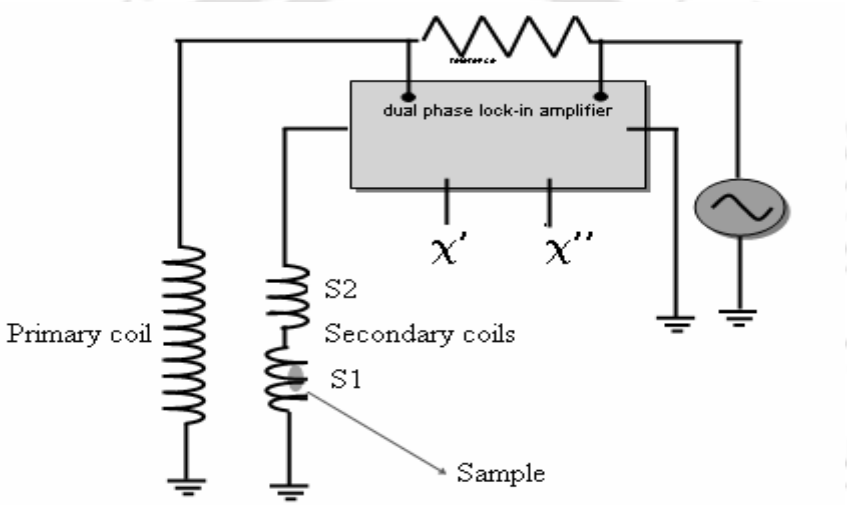

Fig. 2.5.1: Schematic diagram of the indigenously developed ACS. χ' and χ'' are in-phase and out-of-phase components of the magnetic susceptibility.

When a magnetic sample is inserted in the centre of one the secondary coils, the voltage induced in secondary coil *S1*(e_1) and *S2* (e_2) are $e_1 = NV\omega\mu_o H(1+\chi)$ and $e_2 = NV\omega\mu_o H$, where N is the number of turns / unit length in secondary coils, V is the volume of the sample, H is the applied magnetic field in the primary coil, and $\omega = 2\pi f$, where f is the frequency of the ac excitation voltage. Then, the differential output e_{rms} is $(NV\omega\mu_o$

$H\chi)/\alpha$, where the calibration constant $\alpha = [(10^8/8\pi^2 NL) - (L^2 + d^2)^{1/2}]$, where L is the length and d is the diameter of secondary coil. In the present case, $\alpha = 1.59$. Therefore, $\chi = [\alpha\, e_{rms} / V f H]$, where f is the frequency of the applied field. A small amount of sample (~20mg) is taken in the copper sample holder and the position of the rod is carefully adjusted such a way that the test sample stays at the centre of the secondary coil *S1*. A rotary pump was used to maintain an environment of low pressure (~10^{-1} Torr) around the sample. The sample is then heated to the paramagnetic phase. The phase angle of the locking amplifier is then adjusted to get almost zero value of χ''. χ'' is maximum during the ferro- to para magnetic transition and it is negligibly small at its paramagnetic phase. The sample is then cooled to room temperature. χ' and χ'' data are then recorded by heating the sample in a controlled way (@5 °C/ min) inside the coil *S1*. Temperature was measured using a calibrated Copper-Constantan (E-type, non magnetic) thermocouple connected to a 6½ digital multimeter (DMM, Hewlett-Packard 34401A). χ' and χ'' are measured using a Lock-in amplifier (Stanford Research Systems Model: SR830 DSP). Both the instruments were interfaced to a personal computer using Lab-View™ program to facilitate automatic data acquisition.

A typical graph of ac susceptibility data of a Co-Ni-Ga sample recorded as a function of temperature (heating cycle) is shown in Fig. 2.5.2. It was experimentally observed that the martensitic transformation in the FSMAs is accompanied by a sudden drop of the initial magnetic susceptibility [87]. Lowering of point symmetry group during the austenite-martensite transformation results a considerable enhancement of magneto-crystalline anisotropy of the martensite phase. Due to this difference in magneto-crystalline anisotropy, a sudden rise in ac susceptibility was observed during the reverse

martensitic transformations (or sudden fall during $A \rightarrow M$ transformation). At the ferromagnetic to paramagnetic transition, a sharp decrease in ac susceptibility is observed. The Curie temperature (T_C) is determined from the local minimum point of the derivative curve of ACS data taken near the magnetic transition region.

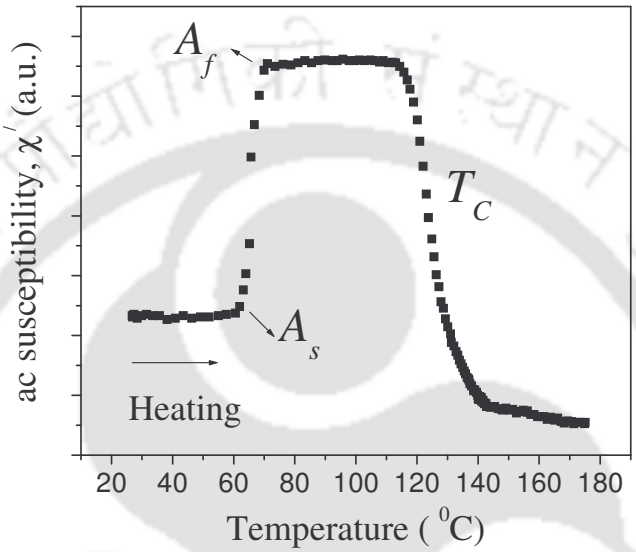

Fig. 2.5.2: Typical ac susceptibility data of an FSMA.

2.6. VIBRATION SAMPLE MAGNETOMETER

Magnetization as a function of applied field and temperature was measured for all the FSMA samples using a commercial Vibrating Sample Magnetometer (VSM, LakeShore model 7410). A block diagram of the VSM is shown in Fig. 2.6.1. The VSM operates on the principle of Faraday's law of induction, which tells us that a changing magnetic field will produce an electric field [107]. This electric field can be measured, which in turn can provide us information about the magnetic moment of the sample as magnetic field and temperature are varied. The VSM consists of nine major parts, *viz.*, 1) water cooled

electromagnet and power supply, 2) vibration exciter and sample holder (with angular position indicator), 3) sensing coils, 4) Hall probe, 5) amplifier, 6) control chassis, 7) lock-in amplifier, 8) Gauss meter, and 9) computer interface.

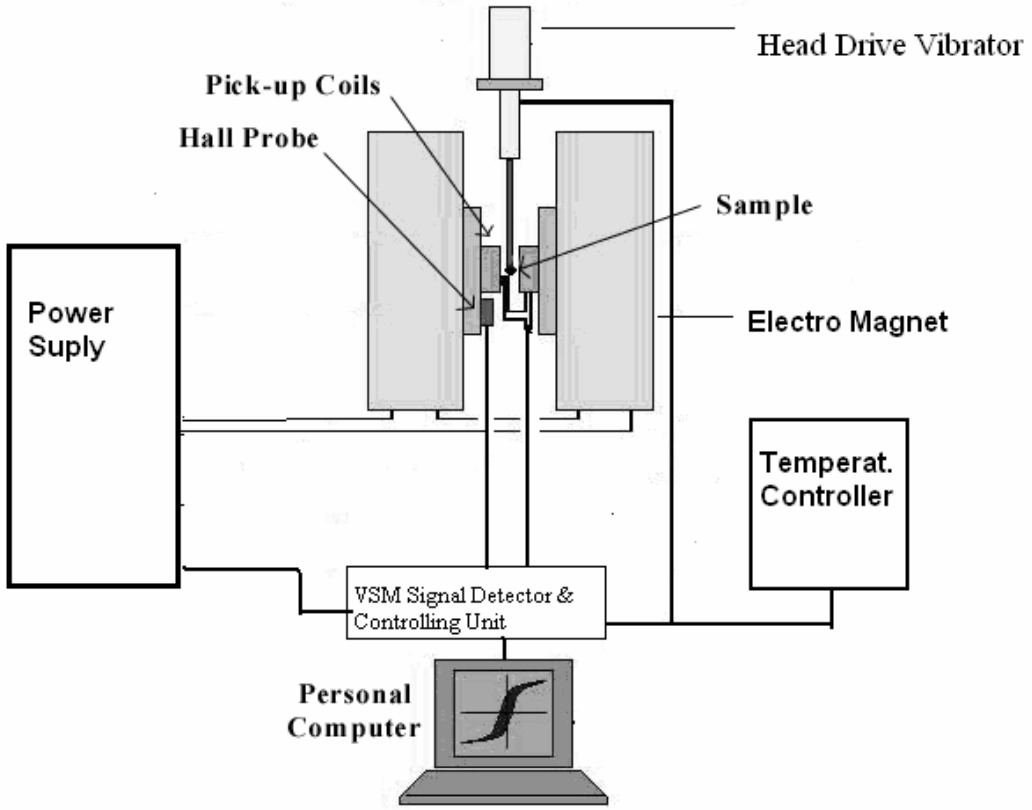

Fig. 2.6.1: A schematic diagram of a VSM.

The sample is fixed to the lower end of the quartz sample holder. The measurement sequence is then programmed using the software provided with the instrument. The vibration exciter is then started and the signal received from the probe and the pick up coils is converted into the magnetic moment value of the sample. Magnetic field up to 20,000 Oe can be applied to the sample. Normally, magnetic field is

automatically increased in steps at a constant temperature (*M-H* measurement) by setting the program. From this measurement, the value of magnetization at different applied magnetic fields is obtained in emu/g. These data provide M_{sat} value of the sample. Magnetization as a function of temperature at a constant applied field (*M-T* measurement) is recorded to obtain information of martensitic transformation temperatures and Curie temperature.

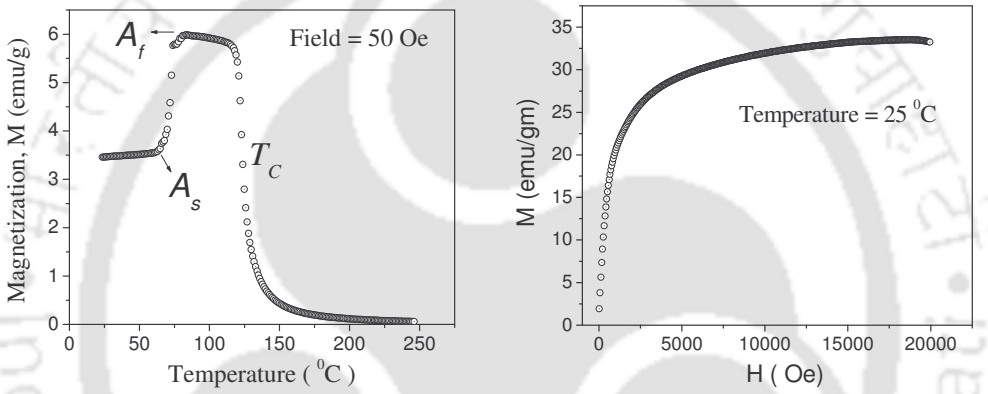

Fig. 2.6.2: Typical magnetization vs temperature (*M-T*) data at constant applied field (50 Oe) and magnetization vs applied field (*M-H*) data at constant temperature (25 °C) for a FSMA.

The martensitic transformation in the FSMAs is accompanied by an abrupt change in magnetization measured at unsaturated fields. This is due to the change of magnetocryctalline anisotropy of the material during structural phase transitions. A sharp decrease in magnetization has been observed at ferro- to paramagnetic phase transition and T_C was determined from the minimum point of its first derivative data.

The effective magnetic anisotropy constant K_{eff} of the alloys can be calculated from the magnetization curves using the law of approach to saturation [72]. Generally, the magnetization (M) as a function of applied field can be expressed as

$$M = M_{sat}\left(1 - \frac{a_{1/2}}{\sqrt{H}} - \frac{a}{H} - \frac{b}{H^2} - \cdots\right) + \chi_{hf} H + D\sqrt{H} \qquad (2.6.1)$$

where H is applied field in kOe, M_{sat} is a saturation magnetization in A/m, χ_{hf} is high field susceptibility and $a_{1/2}$, a, b, c are constant coefficients. The 'a' coefficients depend upon the amount of various structural defects and intrinsic fluctuations. According to Fähnle et.al [108], the second term $\frac{a_{1/2}}{\sqrt{H}}$ can arise from point-like defects, from intrinsic magneto-static fluctuations and from randomly distributed magnetic anisotropy (magneto-crystalline fluctuations). b is related to the magneto-crystalline anisotropy. The constant "D" arises from the partial suppression of thermal excited spin waves in magnetic field. The paramagnetic term $\chi_{hf}H$ causes an increase in spontaneous magnetization at high external magnetic fields. The straightforward method for obtaining the coefficients would be by fitting the experimental curve with this full expression. But because of the large amount of coefficients involved, the fitting procedure gives ambiguous results. To overcome this, an alternate expression [109] involving fewer coefficients given below is chosen as the fitting equation.

$$M = M_{sat}\left(1 - \frac{b}{H^2}\right) \qquad (2.6.2)$$

When applied field is increased to large values, domain wall movements become relatively unimportant and magnetization of the sample is primarily controlled by domain rotation. With the assumption that particles are oriented at random and strain distribution

is homogeneous, the above equation is the best fit equation at high fields [110]. Deciding on the appropriate low field limit is a hurdle in this procedure. Graham *et. al.* [111] discussed this problem and for the as cast metallic glass the lower field limit was set at 10 kOe.

When paramagnetic contribution is comparable with the ferromagnetic contribution, the data obtained form *M-H* measurement can not fit with the above equation. So, data are first fit to the equation,

$$M = M_{sat}(1-\frac{a}{H}) + \chi_{hf} H \qquad (2.6.3)$$

and the paramagnetic contribution χ_{hf} obtained from the above fit is subtracted from the magnetization data ($M_{sat} \rightarrow M$ - $\chi_{hf}H$) and the subtracted M_{sat} *vs* H data are again fitted with equation (2.6.2) to obtain the optimal b value. Once b value is estimated, magneto crystalline anisotropy constant, K_{eff} can be calculated using the relation,

$$K_{eff} = \sqrt{\frac{4b}{15}}\,\mu_0 M_{sat} \text{ [109]} \qquad (2.6.4)$$

In our VSM measurement M_{sat} is measured in emu/g ≅ A-m^2/kg and b is estimated from the non-linear fit has the unit (Oe)^2. Thus, by multiplying M_{sat} with its corresponding density (kg/m^3), it is converted to A/m. b is also converted to (A/m)^2 from Oe^2 (*1 Oe = 10^3/4π A/m*). Finally K_{eff} is obtained in J/m^3.

The nature of ferromagnetic transition was investigated by determining the critical constants involved in the magnetic phase transition. In order to get an accurate T_C value, *M-H* measurements was carried out at different temperature very close to T_C (0.5% above and below T_C). Arrott Noakes [112] plots were obtained to deduce the accurate value of T_C and critical constants were estimated using Kovel -Fisher method [113]. The nature of

the ferromagnetic to paramagnetic phase transition in the critical region may be characterized by a group of physical relations, *viz.*, [114-115]

$$M_{H\to 0} = A(-t)^{\beta} \text{ for } T < T_C \quad (2.6.5)$$
$$M = BH^{1/\delta} \text{ for } T = T_C \quad (2.6.6)$$

$$(M/H)_{H\to 0} = C(-t)^{-\gamma} \text{ for } T < T_C \quad (2.6.6)$$
$$= C\acute{t} \quad \text{for } T > T_C$$

with M as magnetization in the applied magnetic field, H. The parameters β, δ and γ are the critical exponents and A, B and C are the proportionality constants. The parameter t is the reduced temperature, $(T-T_C)/T_C$. The scaling law relation

$$\alpha = 2 - \beta(\delta+1) \quad (2.6.7)$$

enables us to evaluate the value of α, the specific heat exponent. In order to determine the critical constant, arbitrary β and γ value are selected and $M^{1/\beta}$ vs. $(H/M)^{1/\gamma}$ are plotted. The zero field $M_{sat}(0)$ at different temperature is determined from the intersection of the linearly extrapolated curve with $M^{1/\beta}$- axis. A similar process also performed for $\chi_0^{-1}(T)$ with the $(H/M)^{1/\gamma}$-axis. A graph is obtained $M_{satt}(T)$ vs.T and $\chi_0^{-1}(T)$ vs.T. New values of the critical exponents β and γ are obtained and they are re-introduced in the scaling of modified Arrott plot. All these processes are repeated until the iteration converges and lead to the optimum fitting values [116-117].

2.7. OPTICAL MICROSCOPE

Microstructural observation of polished samples was carried out using an upright reflected beam optical microscope (Carl Zeiss, Axiotech). The image of the specimen

was captured by a charged coupled device (CCD) camera fitted to the instrument. The image from the CCD camera is transferred to a computer memory and processed by KS-300 image analysis software.

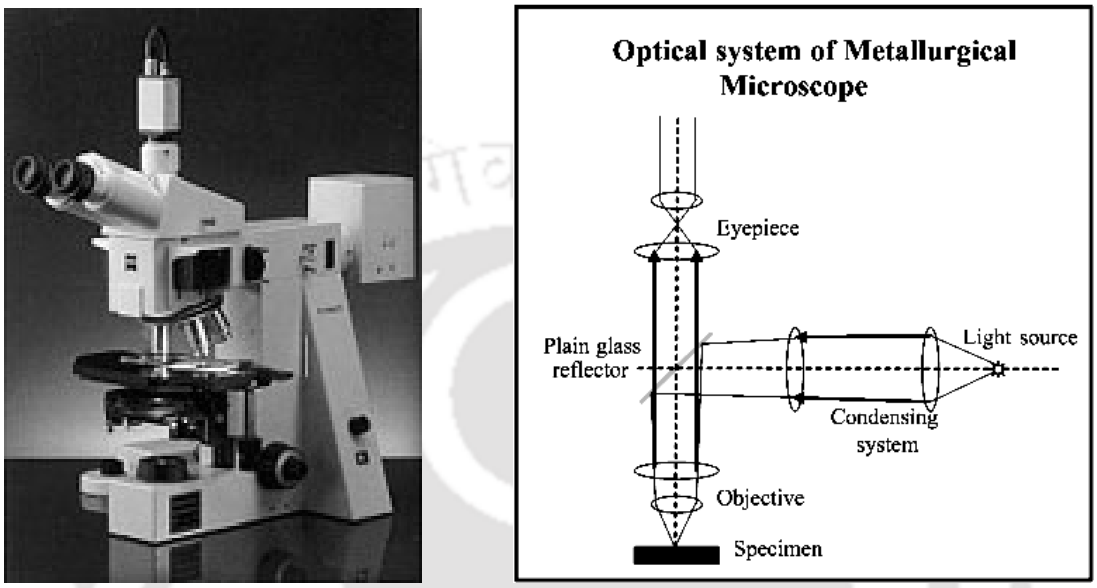

Fig. 2.7.1: Optical microscope with CCD camera.

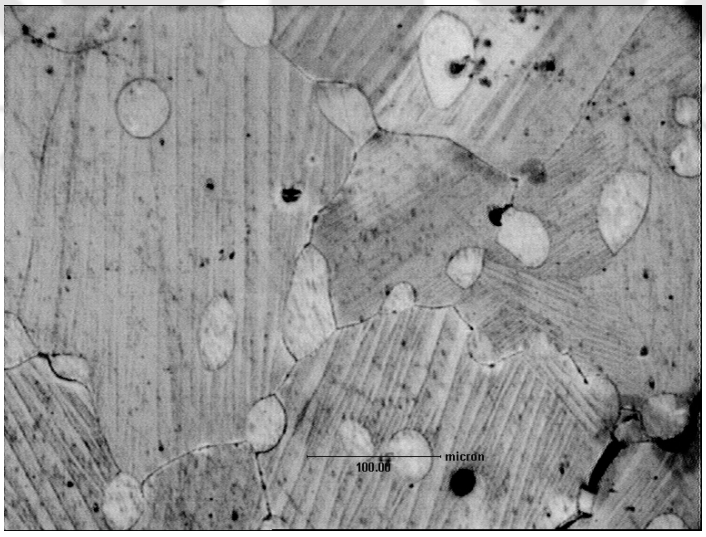

Fig. 2.7.2: A typical optical micrograph of CoNiGaFe alloy

A photograph and ray diagram of the microscope is shown as in Fig.2.7.1. The optically flat polished were carefully etched in dilute HNO_3 prior to observation. The graphical data recorded by the CCD camera was digitally stored in the computer (not shown in the figure). A typical optical micrograph of a FSMA specimen is shown in Fig. 2.7.2. The characteristic martensite twins along with secondary γ-phase precipitates are visible in the optical micrograph. The dark spots are porosities present in the cost sample

2.8. UNIVERSAL TESTING MECHINE

Stress-Strain analysis of the samples was performed using a universal testing machine (UTM, Instron 8801 Servohydraulic). A block diagram of a servohydraulic single-axis UTM is given in Fig. 2.8 [117]. The main controlling modes of the system are strain (up to 10 %), load (up to 100 kN) and position (up to 75 mm) with a loading and unloading frequency range from 0 to 200 Hz. The instrumental is equipped with a hydraulically actuated self-aligning gripping mechanism. The major parts of the instrument are 1) a load-cell based servo hydraulic system, 2) motor driven sample holder assembly for loading, 3) control system which controls the operation of the load-cells and collects data from the load-cells and extensometer, and 4) computer interface.

Since the FSMA samples could not be prepared in size and shape required for tensile testing, only compression test was performed on flat-ended cylindrical samples of diameter 7-10 mm and length of 11 – 7 mm. The samples were kept between the upper and lower grips of the machine and load was applied with proper monitoring. The data on the strain (in strain %) for a particular load (in MPa) was recorded in the computer using in-built software. From these data, stress-strain graph for the different samples were

plotted. For the sample with Mn, load up to 1200 MPa was applied, as where for the other samples, loads up to 500 MPa were sufficient to induce failure. From the graphs, strain ε (in %) corresponding to the critical stress σ (in MPa required to move the twins were found. From these calculations, the mechanical energy density $E_v = \sigma\varepsilon/2$ required for total alignment of the twin variants in the FSMA sample was determined. The compressive strength of the materials was assessed at the failure point of S-S graph.

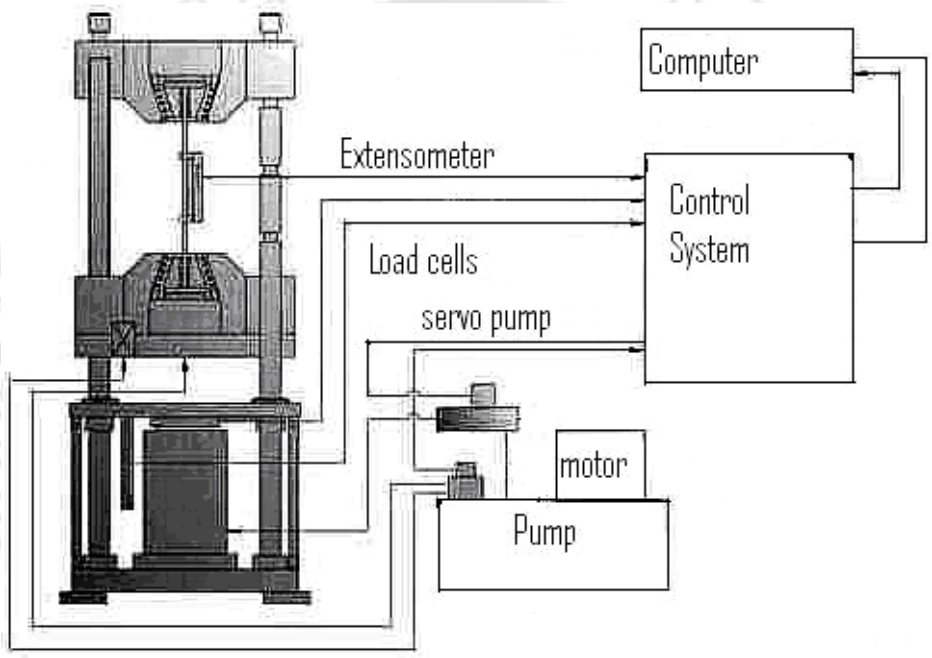

Fig. 2.8.1: A block diagram of a Universal Testing Machine.

Typical graphs of stress-strain behavior of shape memory alloys are shown as in Fig. 2.8.2. In Fig. 2.8.2a, stress was applied till failure occurred (load is released automatically after failure). The maximum stress accumulated taken by the sample without cracking is called the compressive strength of the material. In Fig. 2.8.2b,

residual strain in the sample after unloading is shown. On heating the sample above A_f, some part of the strain gets relaxed.

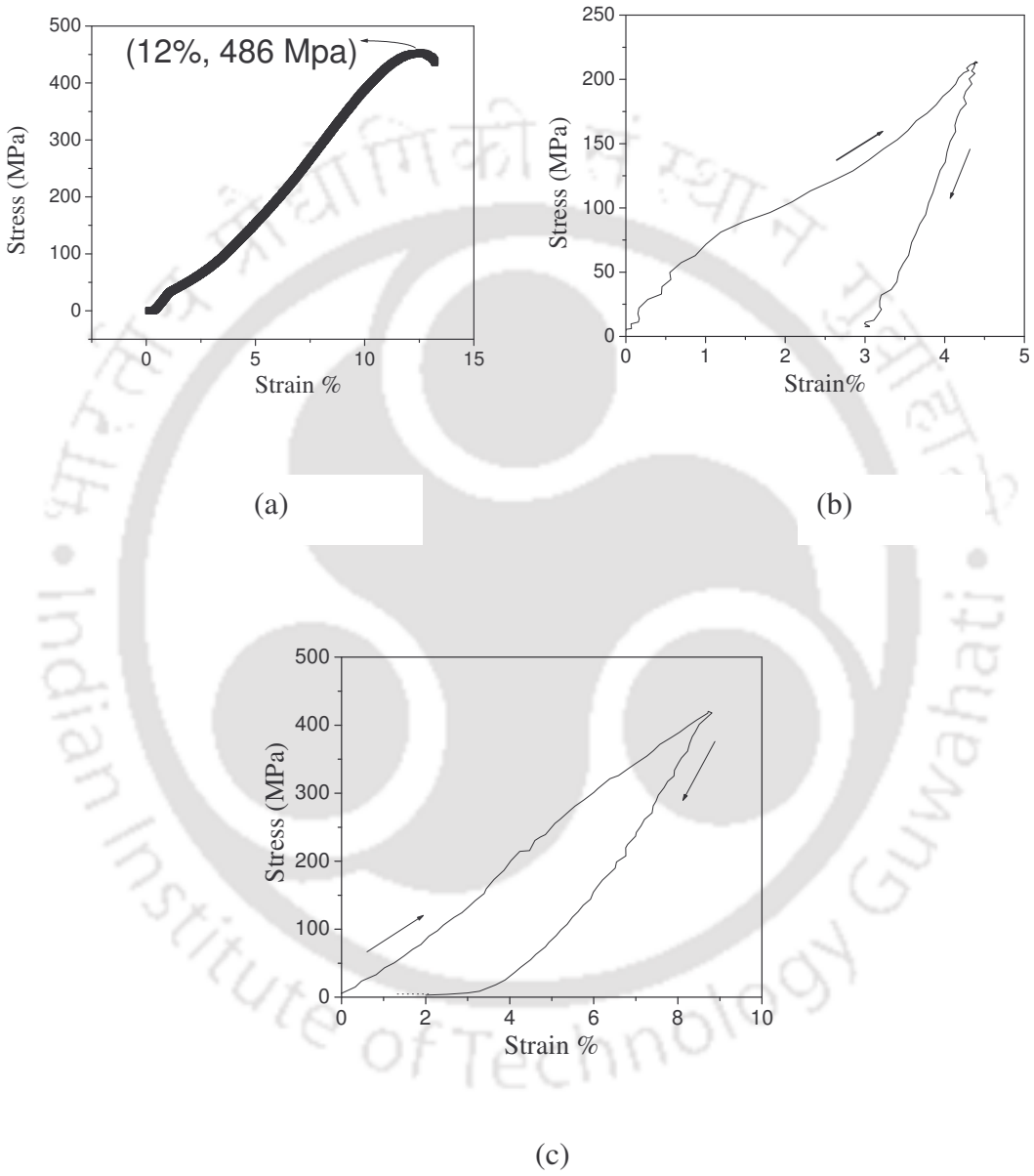

Fig. 2.8.2: Stress strain behavior of shape memory alloys.

This strain relaxation is due to the shape memory effect (SME). SME measurement using compression test involves the following steps: 1) At the outset, the length of the samples is measured before loading (l_0), after unloading (l_1) and after heating it beyond A_f (l_2). 2) Residual strain after unloading (ε_r), strain recovered due to SME (ε_{SME}) and permanent strain (ε_{per}) are then obtained using the raltions $\varepsilon_r = (l_0-l_1)/l_0 \times 100\%$, $\varepsilon_{SME} = (l_1-l_2)/l_1 \times 100\%$ and $\varepsilon_{per} = (l_0-l_2)/l_0 \times 100\%$, respectively. 3) Recovery rate (R) is calculated as $R = \varepsilon_{SME} / (\varepsilon_{SME} + \varepsilon_{per}) \times 100\%$ [57]. If 100% recovery of the strain is obtained after unloading as depicted in Fig. 2.7.2c, the sample is said to have exhibited 'super-elastic effect'.

2.9. MICROHARDNESS MEASUREMENT

Microhardness (or simply the hardness measured over a micrometer scale) is a characteristic property of solids. The hardness is a measure of the resistance of a material to being penetrated and eroded by another material's sharp projections [119].

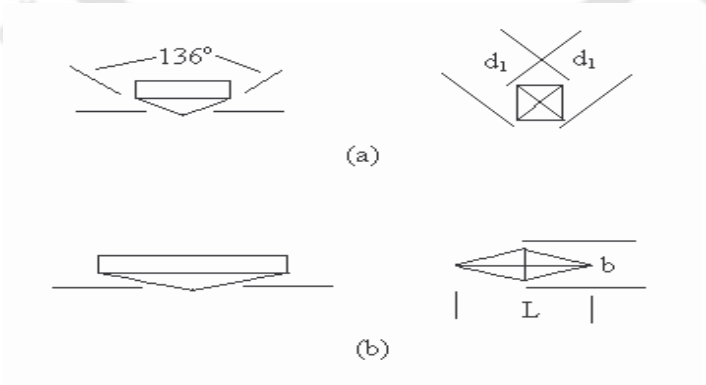

Fig. 2.9.1: Geometry of micro indenters of the (a) Vickers (b) Knoop type.

The measurement procedure involves the use of a diamond micro indenter either in the shape of a square pyramid (Vickers indenter) or an elongated pyramid (knoop indenter). Figure 2.9.1 explains the process of a small diamond indenter being pushed into the material under a known load. The size of the indentation is generally of the order of a few microns under 5 to 1000 g loads and hence the term 'microhardness'. For the Vickers indenter, the Vickers hardness number,

$$\mathrm{VHN} = \frac{\text{force}}{\text{area}} = \frac{2\mathrm{F}\sin\left(\frac{\theta}{2}\right)}{\mathrm{d}^2} \qquad (2.9.1)$$

where F is the force in kg, θ is the inclined angle of Vickers pyramid tip and d is the average diagonal of the impression in mm. Since $\theta = 136^0$ for the Vickers pyramid, VHN (expressed usually in units of kg/mm^2) may be written as

$$VHN = \frac{1.8544\,F}{d^2} \qquad (2.9.2)$$

In this work, microhardness of the alloys was evaluated from the average VHN. Generally, a total indentation time of 15-25 seconds was used for the measurement, which is sufficient for the load to gradually descend onto the surface and reach an equilibrium penetration depth. Careful preparation of the sample surface is necessary prior to indentation. For this, the samples are mounted on a thermosetting resin and polished to a mirror finish. The polished samples were then indented using a Vickers diamond pyramidal indenter and the length of the diagonals of the indents was measured

using a graduated microscope. A typical indent made on a polished Co-Ni-Ga sample is shown in Fig. 2.9.2. The indent corresponds to a load of 100 gm and loading time of 15 s. The microhardness (VHN) values reported in this thesis are the average values of at least 10 independent indents made on each sample composition under identical loading conditions. All measurements were made at room temperature.

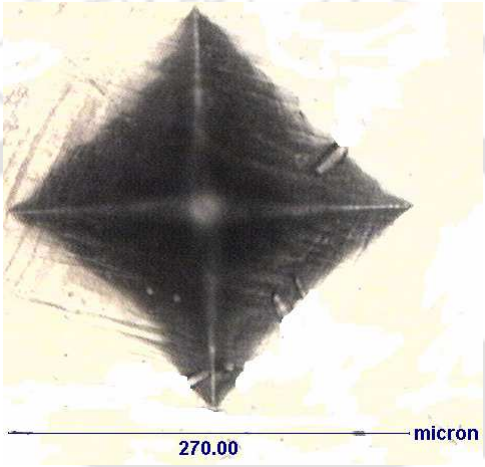

Fig. 2.9.2: Typical indent made on Co-Ni-Ga alloys using a Vickers pyramidal indenter.

2.10 STRAIN GAUGE SET-UP

A strain gauge based instrument (Hottinger Baldwin Messtechnik, Spider 8) was used to measure the magnetic field induced strain (MFIS) in the FSMA samples. The unit consists of a bonded resistance strain gauge connected to the Spider 8 unit and the data (resistance change) measured by the unit is sent to a computer through a universal serial bus. Strain gauges with gauge resistance of 120 Ω (±0.35%) and gauge factor G of 1.9 (±1.5%) were used in quarter Wheatstone bridge configuration to measure the strain produced in the samples under the application of magnetic field. Fig. 2.10.1 shows a typical bonded resistance strain gauge used as the MFIS sensor. An in-built Wheatstone

bridge circuit with the strain gauge in one of its arms forms the 'sensing part' of the instrument. If a strain gauge of resistance R_g (Fig. 2.10.2) is connected in one arm of the Wheatstone bridge, then the strain produced in the sample can be measured from the change in resistance (ΔR_g) of the strain gauge under the bridge balance condition, using the formula [120]

$$\text{Strain} = (\Delta R_g / R_g)/G \qquad (2.10)$$

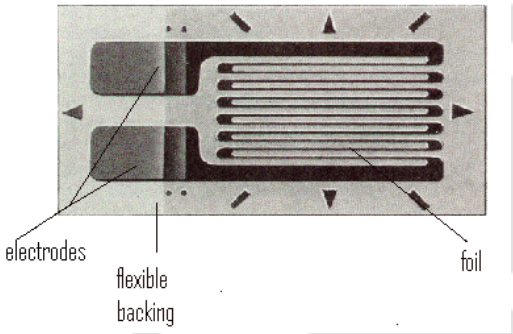

Fig. 2.10.1: A Strain Gauge. The resistive element (dark lines) is embedded on the the backing (gray) material.

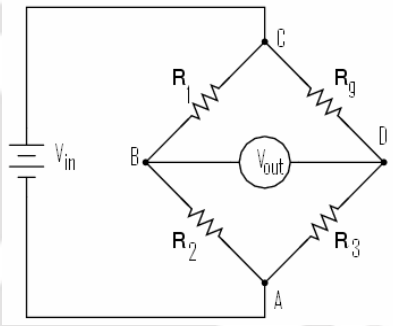

Fig. 2.10.2: Wheatstone bridge with measuring strain gauge (R_g).

Thick disk shaped samples were used for the strain measurement. The surface of the sample was cleaned in an ultrasonic bath containing acetone. The strain gauge was fixed on the sample surface with a strong adhesive (Araldite). The sample was placed in a Teflon capsule, which acted as the sample holder, and introduced between the pole pieces of an electromagnet. The software used for acquiring data requires the data acquisition channel no, the gauge constant, the bridge configuration and zero field data as inputs. The magnetic field was then turned on by energizing the electromagnetic with a variable DC power supply. The electromagnet coil current is increased in small steps and the

corresponding magnetic field at the sample is measured with a Hall probe placed close to the sample. At each field step, data was acquired for a fixed sampling time. After completing one cycle, the data was taken again by reversing the direction of the field and the data of the two runs are averaged. Fig. 2.10.3 shows a block diagram of strain gauge data acquisition procedure.

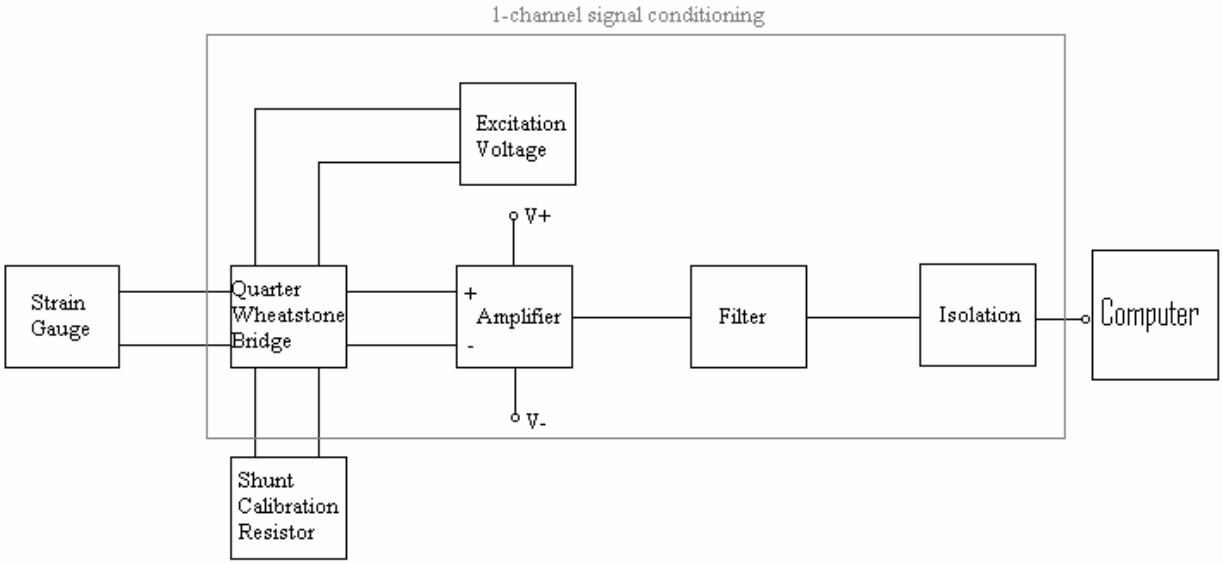

Fig. 2.10.3: Block diagram of strain gauge data acquisition system

The Spider 8 data is a processed strain gauge data. In order to obtain meaningful MFIS values from this data, the instrument has to be calibrated. Calibration of the Spider 8 strain gauge was done by simultaneous strain measurements on a standard nylon plate using the Spider 8 and the UTM extensometer (Instron 8801). Fig. 2.8.1 shows block diagram of a UTM. The details of this instrument are given in the section 2.8 of this chapter. Strain gauge was pasted on the nylon plate clamped to the UTM. The extension of the plate was measured by the extensometer in tensile mode and monitored by a computer. During the extension, Spider 8 data was also acquired simultaneously, and the

strain measured in steps of 0.005 mm, 0.01 mm and 0.1 mm extension. By comparing the Spider 8 data with the corresponding UTM extensometer data, a calibration graph was made Fig. 2.10.4. From this graph, the true MFIS (in %) could be obtained from the corresponding Spider 8 data.

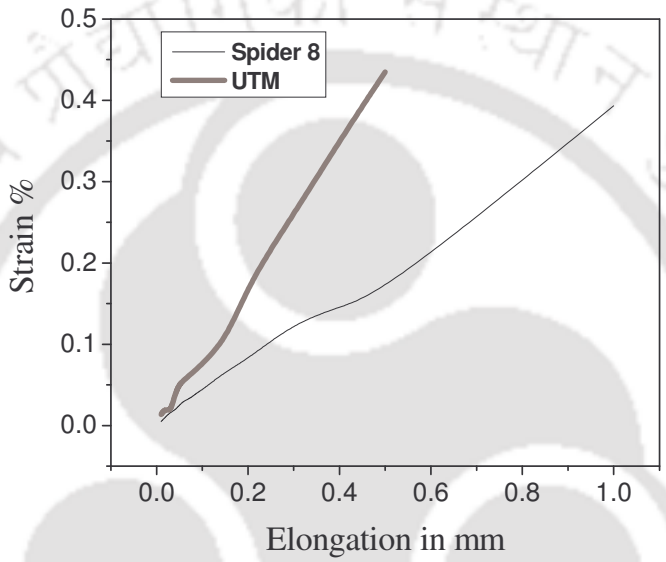

Fig. 2.10.4: Calibration of spider 8 with load strain gauge system using UTM.

2.11. DENSITY MEASUREMENT

Density is measured by weighing a suitably selected piece of alloy sample in air and delivering this weight by the buoyancy, when the sample is suspended in water. According to Archimedes principle, the buoyancy equals the weight of the displaced fluid, which, for water, equals the volume. If W_a is the weight of the specimen in air and W_b in water, then the buoyancy is (W_a-W_b) and density (assuming density of water is 1

gm/c.c),

$$\rho = \frac{W_a}{W_a - W_b} \qquad (2.11.1)$$

If W_1 is the weight of the density bottle filled with analytical grade xylene and W_2 is the weight of the density bottle with xylene and sample outside the density bottle, then the weight of the sample is (W_2-W_1). If W_3 is the weight of the density bottle with the sample immersed in xylene, then the sample weight loss in the immersion medium is (W_2-W_3). Then the specimen volume is,

$$V = \frac{W_2 - W_3}{\rho_m} \qquad (2.11.2)$$

where ρ_m is the density of xylene and the density of the specimen is,

$$\rho = \frac{W_2 - W_1}{W_2 - W_3} \times \rho_m \qquad (2.11.3)$$

Several pieces of the sample were taken in a 10 ml specific gravity bottle and the weighing was carried out in an electronic balance with 0.01 mg resolution. Each measurement was repeated at least three times and the average value was taken. Measurements were carried out in a room with temperature maintained at 24 ± 1 ˚C.

INVESTIGATIONS ON $Co_xNi_{25}Ga_{75-x}$ ($43 \leq x \leq 50$) ALLOYS

In this chapter, investigations performed on a series of Co-Ni-Ga alloys with compositions $Co_xNi_{25}Ga_{75-x}$ ($43 \leq x \leq 50$) are presented. The alloy ingots of each composition were prepared by arc melting method as per procedures explained in chapter 2. All the alloys discussed here are ingots annealed at 1150 °C and quenched in ice water. The composition of the alloys was determined by SEM-EDS. The results are listed in Table 3. It is clear from the table that the processed alloys exhibited compositions that are very close to the starting composition. The processed alloys were highly homogenous and yielded consistent results in various experiments. These consistent results were also used to optimize the annealing time so as to obtained alloys with the required homogeneity.

Table 3: Compositions of alloys obtained by SEM-EDS

Starting composition			Composition of the quenched alloys		
Co at%	Ni at%	Ga at%	Co at%	Ni at%	Ga at%
43	25	32	43.25	24.87	32.48
43.5	25	31.5	43.42	24.73	31.85
44	25	31	44.18	25.03	30.85
44.5	25	30.5	44.67	24.89	30.44
45	25	30	45.03	25.13	29.84
46	25	29	46.32	24.98	28.70
47	25	28	46.78	25.12	28.10
48	25	27	48.33	24.67	27.00
49	25	26	48.95	25.16	25.89
50	25	25	50.17	24.96	24.87

3.1. CRYSTAL STRUCTURE AND MICROSTRUCTURE

X-ray diffraction (XRD) pattern of the alloys of $Co_xNi_{25}Ga_{75-x}$ ($43 \leq x \leq 50$) alloys were recorded as per procedure outlined in the previous chapters. The XRD data are shown as in Fig.3.1.1a and c. Fig. 3.1.1b and d depict the microstructure of the various alloy compositions. Alloys with Co at % from 43 to 45 exhibited a single phase structure. The inset in Fig. 3.1.1a shows the expanded view of the XRD peaks between 2θ values of 42˚ and 48˚, which confirms the single phase nature of the alloys. Microstructure of the alloys observed under an optical microscope also exhibited the similar observation. The twinned microstructure observed in the optical micrographs of these alloys is the typical signature of the martensite phase (Fig.3.1.1b)

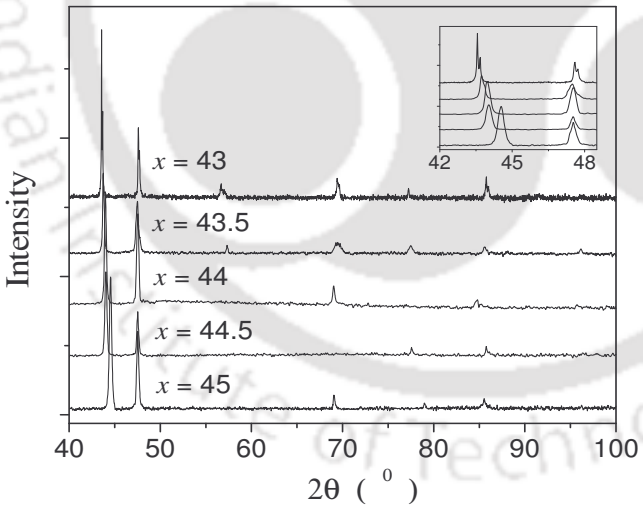

Fig. 3.1.1a: XRD pattern for $Co_xNi_{25}Ga_{75-x}$ ($43 \leq x \leq 45$) alloys

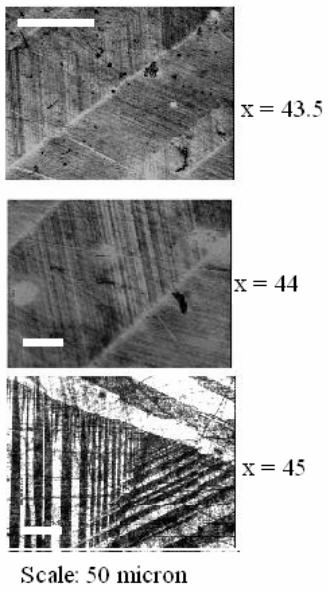

Fig. 3.1.1b: Twin microstructure of the alloys

When the amount of Co was increased above 45 at% in the $Co_xNi_{25}Ga_{75-x}$ alloys, a new phase starts appearing and at 50 at % Co, the new phase dominates over the primary phase. This can be observed from the clearly distinct XRD patterns obtained for the alloys with $x \geq 45$ shown in Fig. 3.1.1c. The optical micrographs of $x = 47$ and 50 alloys (Fig. 3.1.1d) show the dominance of this secondary phase over the primary phase. The black spots in the optical micrographs are porosities, which are common in cast alloys. Since single phase structure has been observed for the alloys with $43 \leq x \leq 45$, no further analysis has been carried out for the alloys with $46 \leq x \leq 50$.

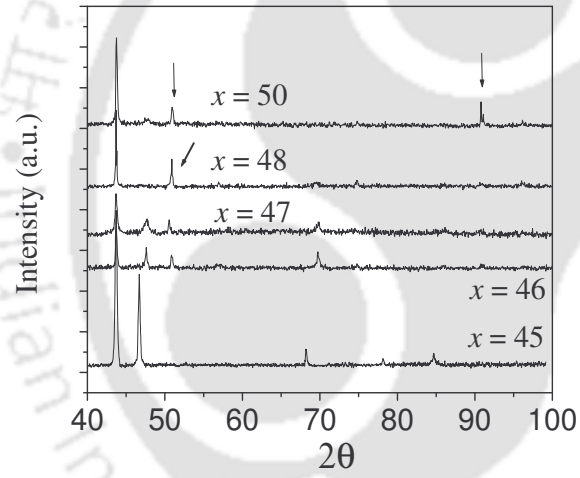

Fig. 3.1.1c: XRD pattern for $Co_xNi_{25}Ga_{75-x}$ ($46 \leq x \leq 50$) alloys

Fig. 3.1.1d: Presence of secondary phase in optical micrograph

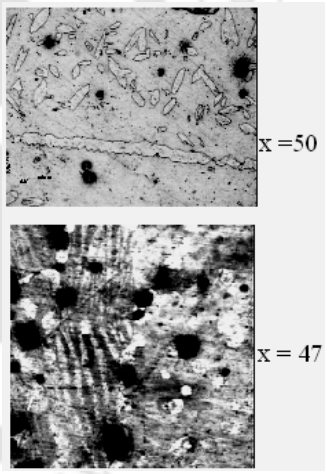

To determine the crystal structure of the single phase alloys (i.e. for alloys with Co at% $43 \leq x \leq 45$), a Rietveld refinement technique (FullProf software package) was employed (Ref. *Sec.2.3, page 52-54).* The models used in the literature for least squares fitting to the experimental diffraction data were all tested. Rietveld analysis showed that the

XRD data could be fitted well to two different models with space group I4/mmm (bct) and P4/mmm (fct), respectively. The lattice parameters and atomic positions in the unit cell for both the models are listed in Table 3.1. Typical least squares fit of both the models to the data corresponding to alloy with $x = 45$ are shown in Fig.3.1.2a and Fig.3.1.2b, respectively.

For the space group P4/mmm, the Wyckoff positions are Ga at 1a(0, 0, 0), Ni at 1c(0.5, 0.5, 0) and Co at 2e(0, 0.5, 0.5) (Fig. 3.1.2b). All the major (intense) peaks in the XRD pattern of the alloys could be fitted well with this model ($L1_0$ type structure). However, some weak peaks appeared in the calculated XRD patterns which were not observed in the experimental XRD patterns. Since these alloys were inherently very ductile, very finely powdered samples could not be prepared for XRD observation. Due to the coarseness of the samples used for XRD measurements and the upper limit of 40kV/30mA X-ray generator rating, highly noisy background was observed in the recorded XRD patterns. With these limitations, the presence of the weak peaks could not be ascertained in the observed XRD pattern. However, the lattice parameters reported by Chernenko *et a.l* from TEM observations [55] are in reasonable agreement with our results.

Table 3.1: Crystallographic data of the alloys obtained from Rietveld analysis

Space Gp.	*P4/mmm*					*I4/mmm*				
Wyckoff Position	Ga: 1a (0, 0, 0) Ni: 1c (0.5, 0.5, 0) Co: 2e (0, 0.5, 0.5)					Ga: 2a (0, 0, 0) Ni: 2a (0, 0, 0) Co: 2a (0, 0, 0)				
Co at % in alloy (x)	a (Å)	c (Å)	c/a	V (Å)^3	χ^2	a (Å)	c (Å)	c/a	V (Å)^3	χ^2
43.0	3.831	3.254	0.849	47.758	3.8	2.698	3.254	1.206	23.687	5.4
43.5	3.843	3.222	0.838	47.585	3.2	2.713	3.218	1.186	23.685	5.6
44.0	3.865	3.205	0.829	47.877	3.5	2.718	3.205	1.179	23.677	4.8
44.5	3.875	3.163	0.816	47.494	4.2	2.721	3.192	1.173	23.633	5.2
45.0	3.887	3.136	0.807	47.381	3.0	2.743	3.139	1.144	23.618	4.0

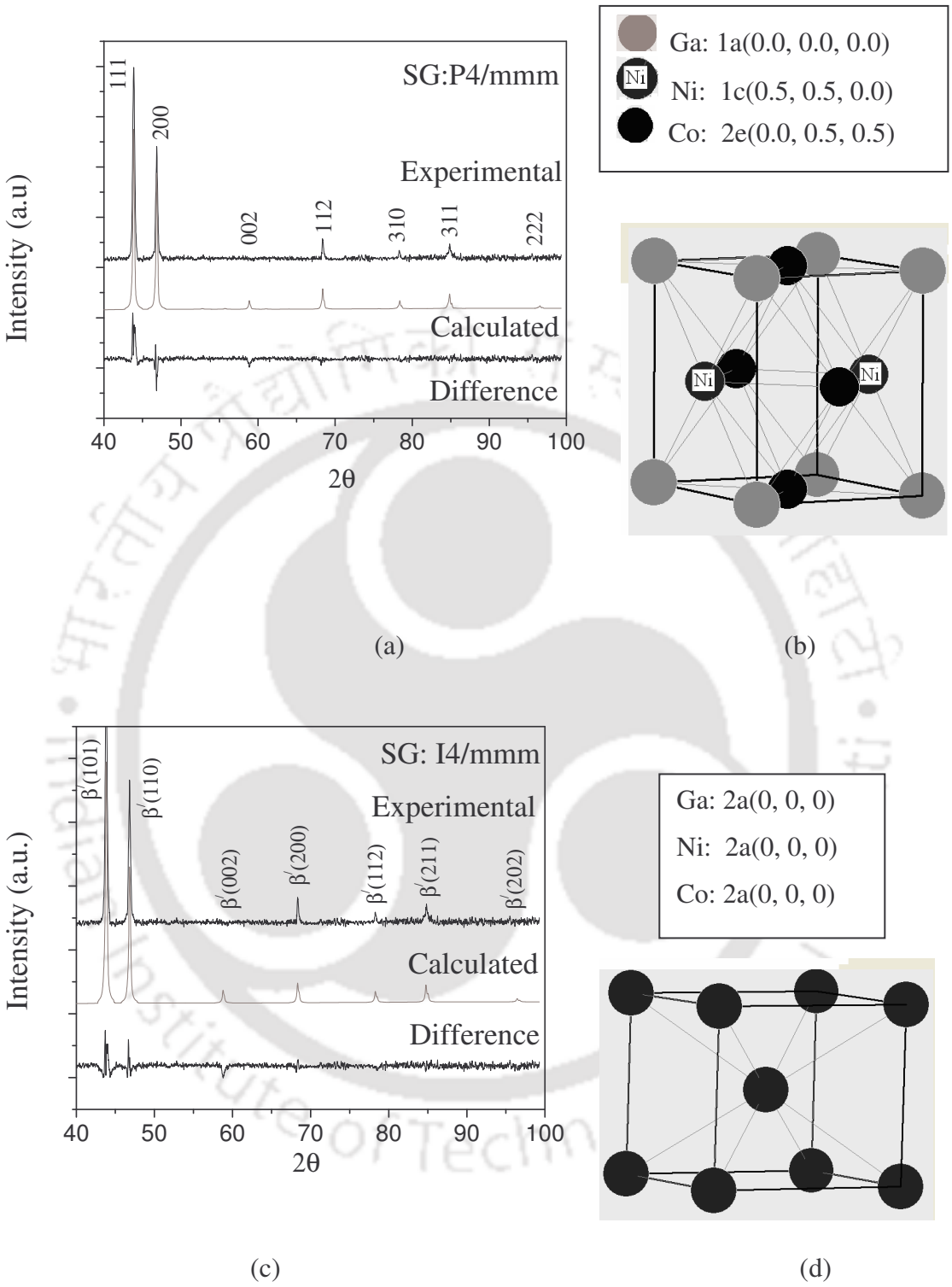

Fig. 3.1.2: Rietveld fit to the XRD data for $Co_{45}Ni_{25}Ga_{30}$ alloy considering SG (a) *P4/mmm* and (c) *I4/mmm*. (b) and (c) show the arrangement of atoms in $L1_0$ and bct unit cell respectively.

Pons *et al.* [46] pointed out that both bct and $L1_0$ unit cells can be obtained by appropriate choice of crystallographic axes. The lattice parameters of $L1_0$ and bct unit cells are related to each other by expressions, $a_{L1_0} = \sqrt{2}a_{bct}$ and $c_{L1_0} = c_{bct}$ [46]. Thus another model with *I4/mmm* space group was also considered. It was observed that if the Wyckoff position 2a (0,0,0) is assumed to be occupied by Co, Ni and Ga in an arbitrary manner (Fig.3.1.2d), the calculated pattern matched very well with the experimental XRD pattern. The lattice parameters reported by Brown *et al*. from their neutron diffraction studies [32] are in reasonable agreement with our results obtained using Rietveld analysis using this model. To solve the low temperature structure of Ni-Mn-Ga alloy, Wedel et al [45] used *I4/mmm* space group but with the Wyckoff position assigned as Ga at 2a(0,0,0), Mn at 2b(0, 0 , 0.5) and Ni at 4d(0. 0.5, 0.25). Attempts were made to fit the data using this model. Most of the peaks could be fitted well by considering the lattice parameter to be $a = b = 3.88$ Å and $c = 6.28$ Å. However, no Bragg peaks were observed below $2\theta = 40°$ in the experimental data, while two major peaks appeared at $2\theta = 28°$ and 32.5° in the generated pattern. Thus Wyckoff position mentioned above (i.e.2a, 2b and 4d) could not be assigned in case of Co-Ni-Ga system. Conversion to $L1_0$ unit cell using the relations given by Pons et.al [46] yielded lattice parameters $a = b = 5.49$ Å and $c = 6.28$ Å. This lattice parameters did not match with the results obtained by Brown et.al [32] or Chernenko et.al. [55]. Hence this model was not considered as appropriate for the fitting procedure. So, it is assumed that all Co, Ni and Ga atoms arbitrarily occupied the 2a(0,0,0,) position in the case of the bct unit cell. Khovailo et.al [24] has reported that at cooling from liquid phase Ni-Mn-Ga alloy solidify in disordered *A2* phase characterized by an arbitrary occupation of every site in the

crystal lattice. Thus an arbitrary occupation of crystal site may be possible for Co-Ni-Ga alloys quenching from 1150 °C.

3.2. THERMAL PROPERTIES

DSC curves corresponding to various compositions of $Co_xNi_{25}Ga_{75-x}$ alloys are shown in Fig.3.2.1. Each DSC run consisting of a heating and cooling cycle shows an endothermic and an exothermic peak corresponding to and A→M transformations, respectively. The M↔A transformation temperatures varied as a function of alloy composition (*cf* Table 3.2).

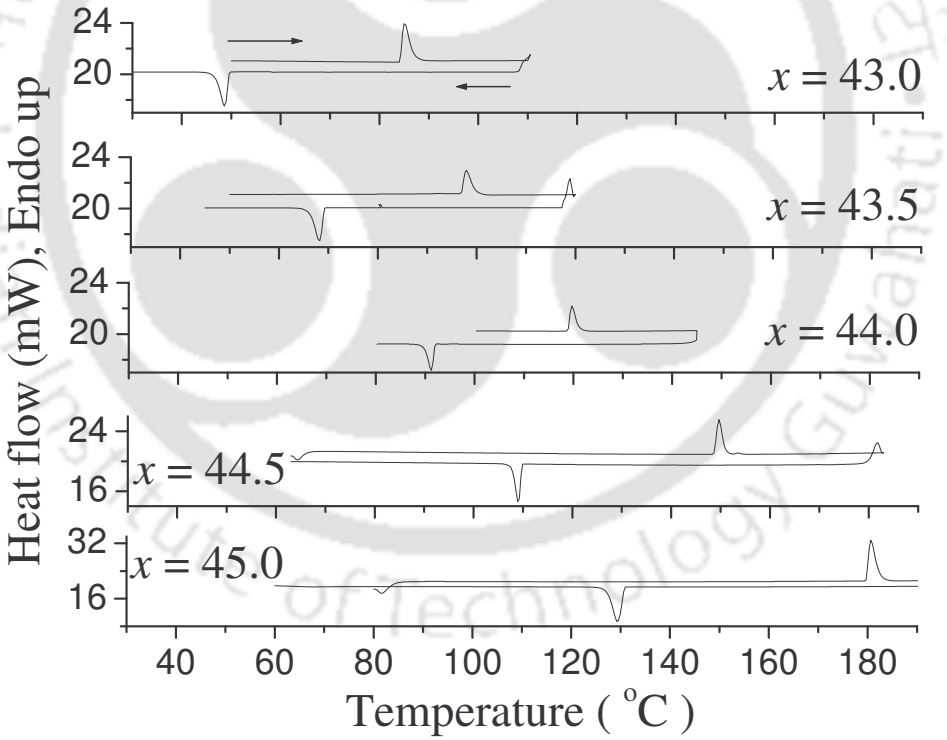

Fig. 3.2.1: DSC curves of $Co_xNi_{25}Ga_{75-x}$ ($43 \leq x \leq 45$) alloys

Table 3.2: DSC data (M_s, M_f, A_s, A_f, T_0 etc.) of $Co_xNi_{25}Ga_{75-x}$ ($43 \leq x \leq 45$) alloys

Co at % (x) ⟶	43.0	43.5	44.0	44.5	45.0
e/a	7.33	7.36	7.39	7.42	7.45
A_s [°C]	84	97	119	149	179
A_f [°C]	89	101	123	153	184
M_s [°C]	49	69	92	110	131
M_f [°C]	45	64	88	106	125
$T_0 = (A_f + M_s)/2$ [°C]	69	85	107.5	131.5	157.5
ΔH (J/g)	1.59	2.13	2.90	4.73	6.93
ΔS (mJ/g °C)	23	25	27	36	44
Hysteresis (A_f - M_s)	40	32	31	43	53

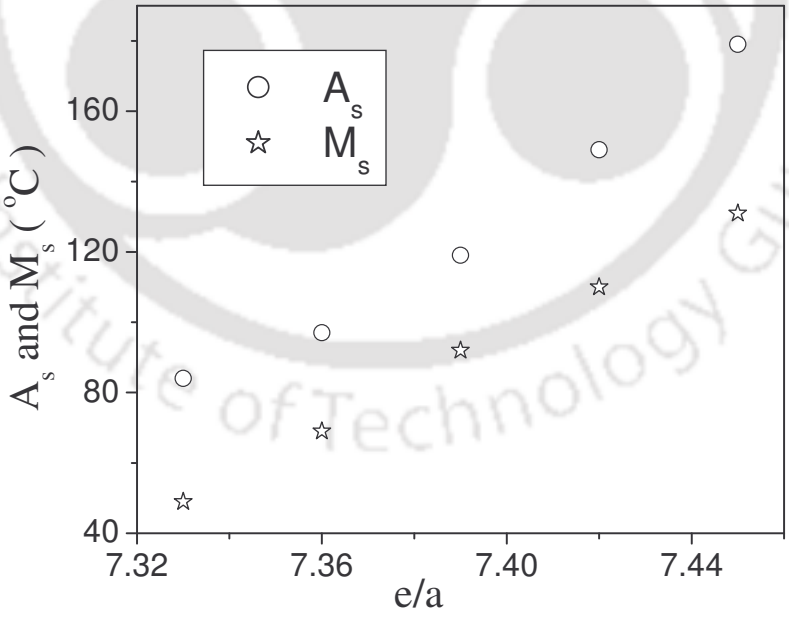

Fig. 3.2.2: Variation of A_s and M_s of $Co_xNi_{25}Ga_{75-x}$ ($43 \leq x \leq 45$) alloys with e/a ratio

It was observed that both M_s and A_s increased with an increase in e/a value (Fig.3.2.2). The e/a value is the ratio of total number of valence electrons in s+d orbitals and total number of atoms present in the system. The details of the e/a calculations have been discussed in Section 1.2.3 p.26 of this thesis. The calculated value of e/a for all the Co-Ni-Ga alloys are listed in Table 3.2

Change of entropy during the structural phase transition (ΔS) is a thermodynamic parameter which gives useful insight on the nature of the phase transition. It can be estimated using the relation

$$\Delta S = \Delta H/T_0 \qquad (3.2.1)$$

and $$T_0 = (A_f + M_s)/2 \qquad (3.2.2)$$

where ΔH is the average enthalpy change during M→A and A → M transformations [64], and T_0 is the equilibrium temperature at which the Gibbs' free energy of the martensite and the austenite phases are the same. The values of ΔS calculated for these alloys are listed in the Table 3.2. ΔS increases as the Co 45 at % in t the alloys is increased. The total change of entropy can be expressed for martensitic transition as

$$\Delta S = \Delta S_{vib} + \Delta S_{el} + \Delta S_{mag} \qquad (3.2.3)$$

It has been generally observed [64, 121] that the vibrational (ΔS_{vib}) and electronic (ΔS_{el}) contributions to the total entropy change ΔS do not vary much significantly when the composition of the alloys is varied. So, the increase in ΔS is generally attributed to the increase in the magnetic contribution (ΔS_{mag}). Hence it can be inferred that, the magnetic anisotropy increases in this alloy series as the Co at% is increased.

3.3. MASS DENSITY MEASUREMENT

The results of mass density measurement made on $Co_xNi_{25}Ga_{70-x}$ ($43 \leq x \leq 45$) alloys are given in Table 3.3. Density was also theoretically calculated by considering the individual contributions of mass density to the formula unit using the following empirical relation:

$$\rho_c = \{ x * \rho(Co) + 25 * \rho(Ni) + (75 - x) * \rho(Ga) \} / 100 \qquad (3.3)$$

where, ρ(Co), ρ(Ni) and ρ(Ga) are mass density of Co, Ni and Ga respectively

The calculated values are presented in Table 3.3 for the sake of comparison. The results obtained from individual calculation of density using the empirical relation are slightly lower than the experimental result. However, the closeness of the theoretical values with the experimental values suggests that the empirical rule provides reasonably good estimates of the density of the alloys as a function of composition.

Table 3.3: Mass Density (ρ_A) of $Co_xNi_{25}Ga_{75-x}$ ($43 \leq x \leq 45$) alloys

Co at.% (x)	Measured density ρ_A (g/cm^3)	Calculated density ρ_c(g/cm^3)
43	8.062 ± 0.004	7.944
43.5	8.160 ± 0.004	7.959
44	8.386 ± 0.004	7.974
44.5	8.463 ± 0.004	7.989
45	8.616 ± 0.004	8.004

Here ρ_A was measured by using Archimedes principle and ρ_c was calculated from the individual contribution of the constituent elements of the alloys. It is seen that density

increases with the increase in Co at % and decease of Ga at%. This is due to the lower mass density of the Ga as compared to Co.

3.4. MAGNETIC PROPERTIES

3.4.1. Temperature dependent AC susceptibility (ACS):

ACS data of $Co_xNi_{25}Ga_{75-x}$ ($43 \leq x \leq 45$) alloys obtained as a function of temperature are depicted in Fig. 3.4.1. The abrupt drop in the value of the real part of the susceptibility observed in the case of all the plots is the signature of the ferromagnetic to paramagnetic phase transition. The ACS data was used to find the Curie temperature of the as prepared samples at the initial stage of the alloy processing. T_C values have been measured from the local minimum point of the derivative of ac susceptibility versus temperature graph and are listed in the table 3.4.1 It is seen that T_C values increase with the increase of Co at % (x). It is expected as Co has the highest magnetic moment among the constituent element of this alloy series. The T_C value obtained by this method has been verified with the results obtained from magnetization measurement using vibration sample magnetometer.

Table 3.4.1: Currie temperature of $Co_xNi_{25}Ga_{75-x}$ ($43 \leq x \leq 45$) alloys

x	43	43.5	44	44.5	45
T_C [^oC]	-2	39	77	107	119

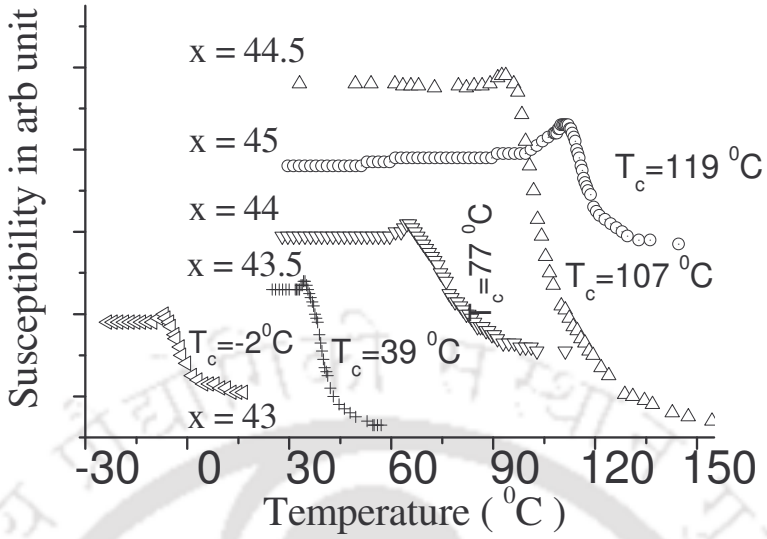

Fig.3.4.1: ac susceptibility of $Co_xNi_{25}Ga_{75-x}$ ($43 \leq x \leq 45$) alloys

3.4.2. Magnetization measurement as a function of temperature using VSM

Magnetization (M) of $Co_xNi_{25}Ga_{75-x}$ ($43.5 \leq x \leq 45$) alloys was measured at very low field (50 Oe) as a function of temperature using VSM. The M-T data are shown in Fig. 3.4.2. The alloy with the highest Co at % (x = 45) has the highest magnetization at 50 Oe field. The alloy with 43 at% Co exhibited very low magnetization typical of paramagnetic materials at room temperature. Referring to the ACS data presented in Table 3.4.1, it can confirmed that the T_C of this alloy is -2 ˚C. T_C value corresponding to each alloy composition was determined from the local minimum point of the derivative graph. T_C value obtained for various alloy compositions are listed in Table 3.4.2. It has been observed that magnetic moment and Curie temperature (T_C) of the magnetic materials linearly vary with the magnetic valence number *(Z_m)* [74]. A similar trend has been observed in this alloy system

also. The Z_m values calculated for $Co_xNi_{25}Ga_{75-x}$ $(43 \leq x \leq 45)$ alloys are listed in Table *3.4.2.* The details of the calculation of Z_m have been already discussed in section *1.2.5.*

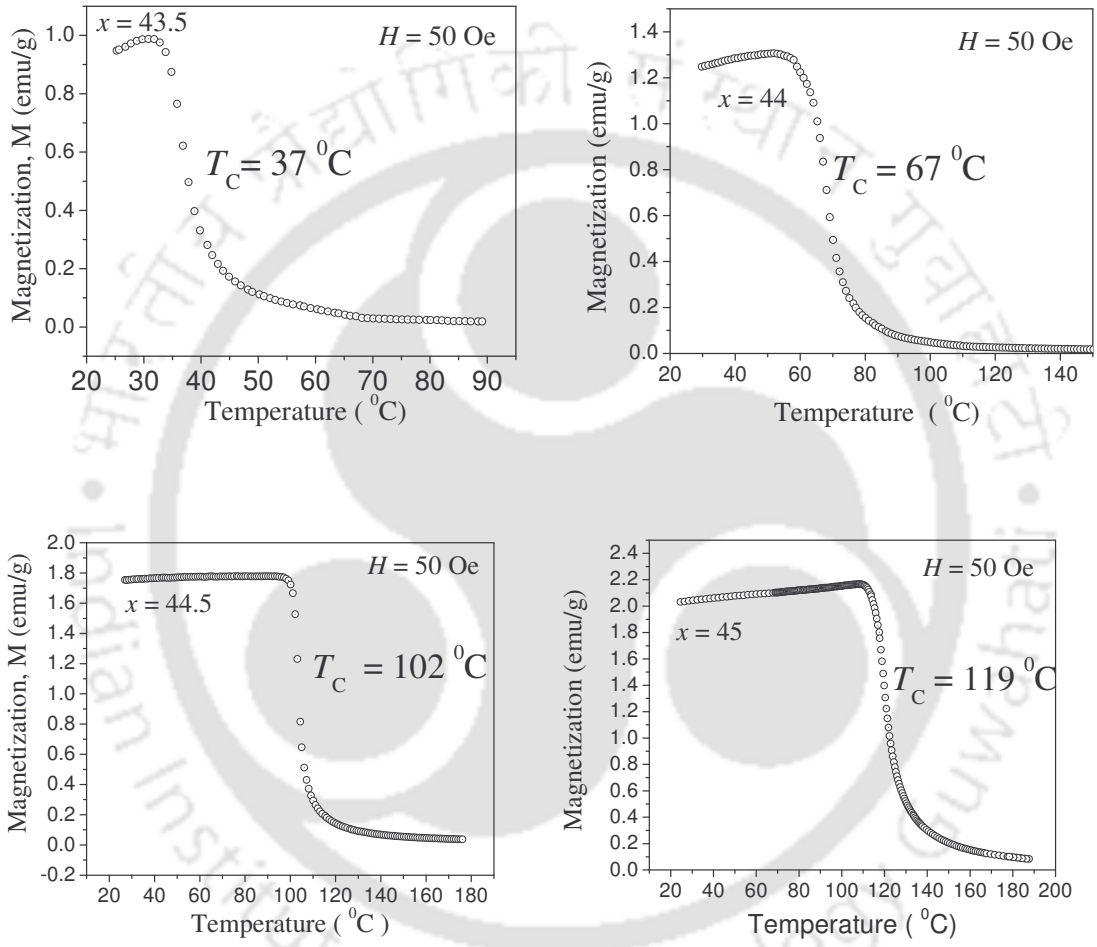

Fig. 3.4.2: Variation of magnetization of $Co_xNi_{25}Ga_{75-x}$ $(43 \leq x \leq 45)$ alloys with respect to temperature at constant field .

Table 3.4.2: Curie temperature (T_C) and magnetic valence number (Z_m) of $Co_xNi_{25}Ga_{75-x}$ ($43 \leq x \leq 45$) alloys

Composition of the alloy (x)	T_C (°C)	Z_m
$x = 43.5$	37	-0.51
$x = 44.0$	67	-0.49
$x = 44.5$	102	-0.47
$x = 45.0$	119	-0.45

The T_C values obtained from ACS measurement are close to the magnetization measurement by using VSM. The small differences in the T_C values obtained from the two measurements have been observed are due to the nature of the two measurements, and differences in the sensor type and temperature control employed in the two set-ups. While the ACS data was collected continuously using a small temperature ramp in the indigenous instrument, data was recorded at discrete temperature intervals and controlled by a PID temperature controller in the commercial VSM. So, the ACS measurements were rapid, whereas the VSM measurements were relatively slower. However, the latter yielded data with traceable accuracies when compared to the former. All the data presented in the table have been recorded during the heating cycle. Since the reverse martensitic transformation temperature (A_s) for all the alloys in this series are higher than its T_C value, no signature of the martensitic ttransofrmation has been observed in the data presented in Fig. 3.4.2.

3.4.3. Magnetization as a function of applied field at constant temperature using VSM

Magnetization measurement was carried out on $Co_xNi_{25}Ga_{75-x}$ ($43 \leq x \leq 45$) alloys at 25 °C at different applied field values. The M-H plots are depicted in Fig. 3.4.3a. The alloys with x =

44, 44.5 and 45 exhibit almost the same magnetic moment at an applied field of 20 kOe, but alloys with $x = 43.5$ and 43 exhibit lower magnetic moment at this field. It can also observed from the graphs that alloys x = 43, 43.5 and 44, attain saturation faster than the other two alloys. This gives the inference that the magneto crystalline anisotropy of the alloys increases with increasing Co at. %.

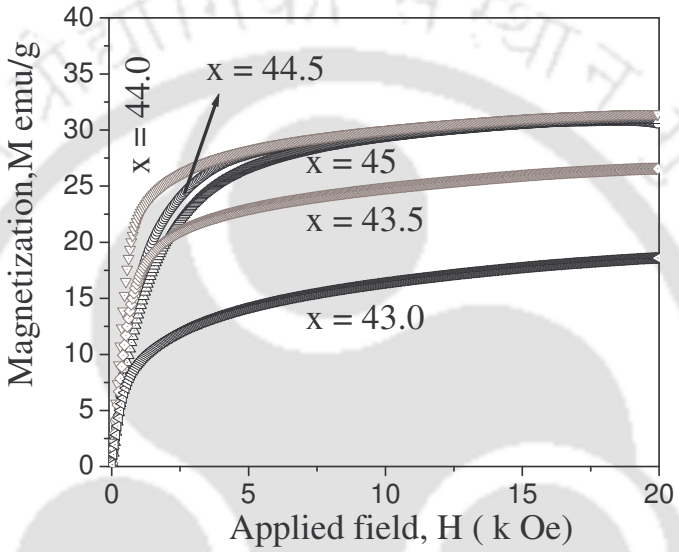

Fig. 3.4.3a: Variation of magnetization of $Co_xNi_{25}Ga_{75-x}$ ($43 \leq x \leq 45$) alloys with applied field.

The effective magnetic anisotropy constant K_{eff} of the alloys can be calculated by fitting the magnetization curves using the equation 3.4.3a

$$M = M_{sat}\left(1 - \frac{b}{H^2}\right) \qquad (3.4.3a)$$

The co-efficient b is related to the magnetocrystalline anisotropy by the equation.

$$K_{eff} = \sqrt{\frac{15b}{4}}\,\mu_0 M_{satt} \quad [Ref.109] \qquad (3.4.3b)$$

It can be observed from Fig. 3.4.3a that the applied field of 20 kOe is not sufficient to saturate the magnetic moment of the alloys with x = 44, 43.5 and 43. Careful observation of the data between 9 kOe and 18 kOe would reveal that apart from ferromagnetic contribution some paramagnetic contributions are also present in these alloys. The saturation magnetization was estimated from M-H curve after subtracting the paramagnetic component from the curve. This was done by fitting the following equations separately to the observed M-H data in the high field region.

$$M = M_{sat} + \chi_p H \qquad (3.4.3c)$$

$$M = M_{sat}\left(1 - \frac{a}{\sqrt{H}}\right) + \chi_p H \qquad (3.4.3d)$$

$$M = M_{sat}\left(1 - \frac{b}{H^2}\right) + \chi_p H \qquad (3.4.3e)$$

Each fit yielded very close values of the high field susceptibility, χ_p from which a good estimate of the same was obtained. Paramagnetic contributions were eliminated from the experimental M-H curve by the subtracting linear ($\chi_p H$) contribution from it. The subtracted data was then fitted to equation 3.4.3a. to obtain the best values of M_{sat}, a and b value. Fig. 3.4.3b shows the experimental (unsubtracted) M-H data (represented by darkened triangles), M-H data with the paramagnetic component subtracted (open circles) and the least squares fit of the high field data to eqn. 3.4.3d (solid line) corresponding to each alloy. The gradual decrease in the paramagnetic component in the M-H data as a function of Co at % is evident from Fig. 3.4.3(iii). The parameters obtained from the least squares fitting procedure are listed in Table 3.4.3.

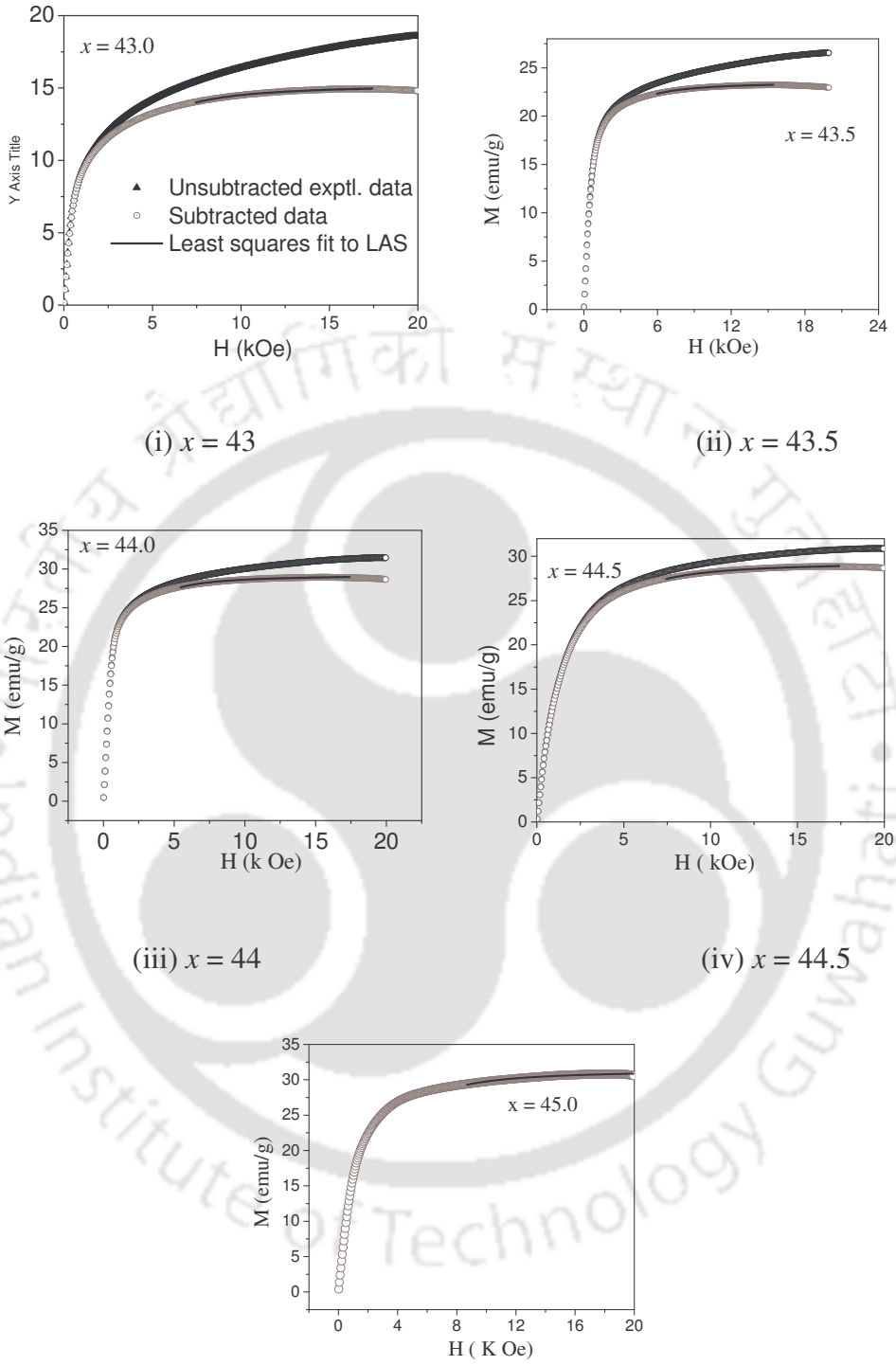

Fig. 3.4.3b:. M-H graph of $Co_xNi_{25}Ga_{75-x}$ alloys fitted to the equation of law of approach to saturation. The black dark lines are the fit line to the observed data

The value of b was converted from Oe to A/m to get K_{eff} value in terms of J/m^3. Likewise, M_{sat} value was also converted to volume magnetization (A/m) by multiplying corresponding mass density of the alloy. Taking $\mu_0 = 4\pi \times 10^{-7}$ N/A^2 (or $J/m\ A^2$) , he value of K_{eff} was obtained. The Estimated K_{eff} values corresponding to the different alloys are listed in Table 3.4.3. K_{eff} increases in these alloys as the Co at.% is increased. This indicates that the magneto crystalline anisotropy increases in this series of Co-Ni-Ga alloys as the Co at. % is increased.

Table: 3.4.3: M_{sat} and K_{eff} of $Co_xNi_{25}Ga_{75-x}$ ($43 \le x \le 45$).

Co at% in alloy (x)	Volume M_{sat} (Am^2/kg)	Density (kg/m^3)	$M_{sat} \times 10^5$ (A/m)	$b \times 10^6$ $(Oe)^2$	$\chi_p \times 10^{-6}$ (m^3/kg)	$K_{eff} \times 10^5$ (J/m^3)
43.0	15.52 ± 0.04	8062 ± 10	1.251	3.39 ± 0.10	2.38	0.45
43.5	23.84 ± 0.03	8160 ± 10	1.945	2.0 ± 0.07	2.01	0.53
44.0	29.69 ± 0.03	8386 ± 10	2.490	1.84 ± 0.07	1.51	0.65
44.5	29.37 ± 0.04	8463 ± 10	2.486	3.13 ± 0.07	1.23	0.85
45.0	30.96 ± 0.15	8616 ± 10	2.626	4.82 ± 0.07	0.25	1.24

Saturation magnetization (M_{sat}) obtained by J. Liu et.al [39] for almost similar composition of the alloys {$Co_x(Ni_{25}Ga_{30})$; x = 43.5, 44,44.5,45}are in reasonable agreement with the values obtained in this study. Chernenko et.al [42] observed a higher saturation magnetization (≅ 40 emu/g) at room temperature and comparatively smaller field of 10 kOe in single crystals of $Co_{49}Ni_{22}Ga_{29}$. The higher M_{sat} observed could be attributed to the single crystal nature of the sample and the higher at % of Co present at the alloy. A similar value (≅ 40 emu/g) has been reported by M. Zhang et.al [54] at room temperature at an applied field

of 50 kOe applied field in melt-spun ribbons of $Co_{50}Ni_{20}Ga_{30}$. Room temperature M_{sat} and K_{eff} of 52.1 A-m^2/kg and 1.01 $\times 10^5$ J/m^3, respectively has been reported [122] in polycrystalline $Ni_{50}Mn_{30}Ga_{20}$ ($\mu_0 H$ = 20 mT) at applied field of 20 kOe. Appreciable increase in M_{sat} and K_{eff} has been reported near the stoichiometric composition in [122]. Though M_{sat} of these alloys is much lower than that of Ni-Mn-Ga alloy, K_{eff} of these alloys is comparable to that of Ni-Mn-Ga alloys. The K_{eff} of polycrystalline $Ni_{49}Fe_{18}Ga_{27}Co_6$ alloy has been reported as 1.2×10^6 erg/cm^3 (M_{sat} = 40 emu/g) at 300 K [94]. For inducing magnetic field induced strain (MFIS), a large magnetocrystalline anisotropy energy is required to move the twin boundary [14,23]. Higher values of M_{sat} and K_{eff} value are expected with the increase of Co at % in Co-Ni-Ga alloys.

3.5. SUMMARY:

To realize the shape memory effect it is initially necessary to determine the correct alloy composition. The most promising means by which a substantial shape and dimensional change can be achieved in an FSMA is through the application of a magnetic field. In the case of FSMA in which martensitic and magnetic transformations occur closely, application of magnetic field can induce large MFIS. Thus, it is necessary to determine the main physical parameters of these alloys.

XRD and SEM studies revealed that single phase martensite phase exists in $Co_xNi_{25}Ga_{75-x}$ alloys when $x < 45$. The martensitic phase has been structurally identified as bct or $L1_0$ and the austenite phase as $A2$ by Rietveld analysis. It has been observed that in the case of $Co_xNi_{25}Ga_{75-x}$ alloys, the MT temperatures are higher than room temperature, but the Curie temperature (T_C) of all the alloys are below MT. All but one of the alloys have

ferromagnetic martensite structure at and above room temperature. It has been found that both *MT* and T_C decrease with the reduction of Co at%. Thus there is no chance to prepare alloy with close *MT* and T_C values by adjusting the alloy composition in this series. The magnetic anisotropy constant has been estimated for the alloys. The saturation magnetization (H = 20 kOe) observed at room temperature for these alloys are almost 1.5 times lower than the prototype Ni-Mn-Ga alloys [122] but K_{eff} of the alloy with x = 45 is comparable to the reported value of other alloys. It has been observed that magnetization increases with the increase of Co at %. Thus, by maintaining Ga at % constant, Co and Ni content can be adjusted to achieve higher saturation magnetization. Oikawa et al. observed [19] that T_C and *MT* temperature variation exhibit opposite trends when Ni at% is varied for constant Ga at%. Considering the Oikawa et al.'s results as a guideline, new series of alloys exhibiting higher saturation magnetization and magneto crystalline anisotropy can be prepared.

INVESTIGATION ON $Co_{70-x}Ni_xGa_{30}$ ($20 \leq x \leq 25$) ALLOYS

In this chapter, investigations performed on a series of Co-Ni-Ga alloys with compositions $Co_{70-x}Ni_xGa_{30}$ ($20 \leq x \leq 25$) are presented. In this series, Ga content is held constant and the concentration of the two transition metals in the alloys is varied.

4.1. PREPARATION AND PROCESSING OF THE ALLOYS

The alloy ingot of each composition was prepared by arc melting method, following the procedures already outlined in chapter 2. Quenching medium and annealing temperature are two crucial factors that influence the properties of the FSMAs. In order to comprehensively understand the influences of these factors on Co-Ni-Ga FSMAs, these alloys were processed in different ways. Alloys discussed here are mainly ingots annealed at 1150 °C and quenched in ice water. However, in order to investigate the effect of annealing temperature on the properties of $Co_{70-x}Ni_xGa_{30}$ alloys, ingots of one alloy composition were annealed individually at different temperatures such as 1230 °C, 1150 °C, 1000 °C and 900 °C and subsequently quenched in ice water. Moreover, for understanding the influence of quenching rate on this series of Co-Ni-Ga alloys, ingots of one alloy compositions were annealed at 1150 °C and individually quenched in liquid nitrogen, ice water or air. Alloys annealed at 1150 °C were brittle. In order to prepare alloys of large sizes suitable for mechanical property measurements, ingots of all the alloy compositions were cast in a cylindrical shape, annealed at 1000 °C and quenched in ice water.

The composition of the master alloys was determined by SEM-EDS analysis. A typical EDS spectrum is displayed in Fig. 4.1a. Table 4.1 lists the nominal starting and final (after annealing and quenching stages) alloy compositions. It can be seen that the measured composition values are very close to the starting composition. The martensitic microstructure observed in these alloys is also shown with the corresponding SEM micrograph in Fig.4.1b.

Table 4.1: Composition of $Co_{70-x}Ni_xGa_{30}$ obtained from EDS observations.

Starting alloy composition			Composition of the final processed alloys		
Co at%	Ni at%	Ga at%	Co at%	Ni at%	Ga at%
50	20	30	50.41	19.87	29.72
49	21	30	49.49	20.73	29.78
48	22	30	48.18	21.67	30.15
47	23	30	46.80	22.92	30.28
46	24	30	46.03	24.13	29.84
45	25	30	44.67	24.79	30.54

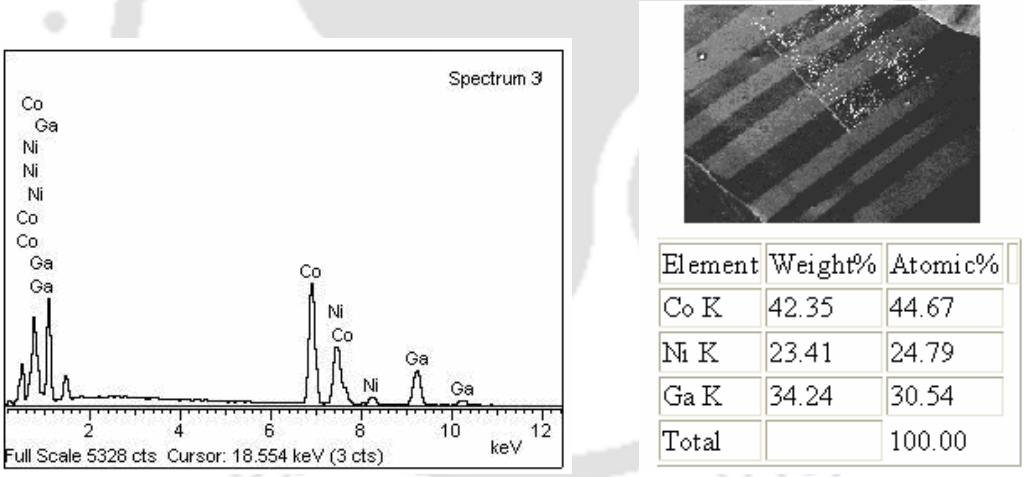

(a) (b)

Fig. 4.1. (a): EDS spectrum of $Co_{45}Ni_{25}Ga_{30}$ is shown as a typical example, (b): SEM micrograph of the martensite twins in the alloy and the corresponding SEM-EDS data.

4.2. CRYSTAL STRUCTURE AND MICROSTRUCTURE

4.2.1. Structure of alloys quenched from 1150 ˚C

X-ray diffraction (XRD) patterns of $Co_{70-x}Ni_xGa_{30}$ ($20 \leq x \leq 25$) alloys are shown in the Fig. 4.2.1a. The XRD patterns of alloys with $x = 20$ and the rest (with $x \geq 21$) exhibit different features. Alloys with $x \geq 21$ seem to exhibit a single phase structure. Microstructural analyses of these alloys support this observation. The twin microstructure observed in the optical micrograph is a typical signature of the martensite phase (Fig.4.2.1b). For alloys with $x < 21$, the intensity of the XRD peaks corresponding to the martensite phase was found to be weak and the presence of additional peaks was also observed. The optical micrograph of the alloy with x=20 reveal only weak features of the austenite phase, clearly showing that the major phase is austenite in this alloy. Unlike the alloys investigated in the previous chapter, γ-phase was observed only in the optical micrograph of the alloy with $x = 20$. The big black spots observed in some optical micrographs are porosities, which are common in cast alloys.

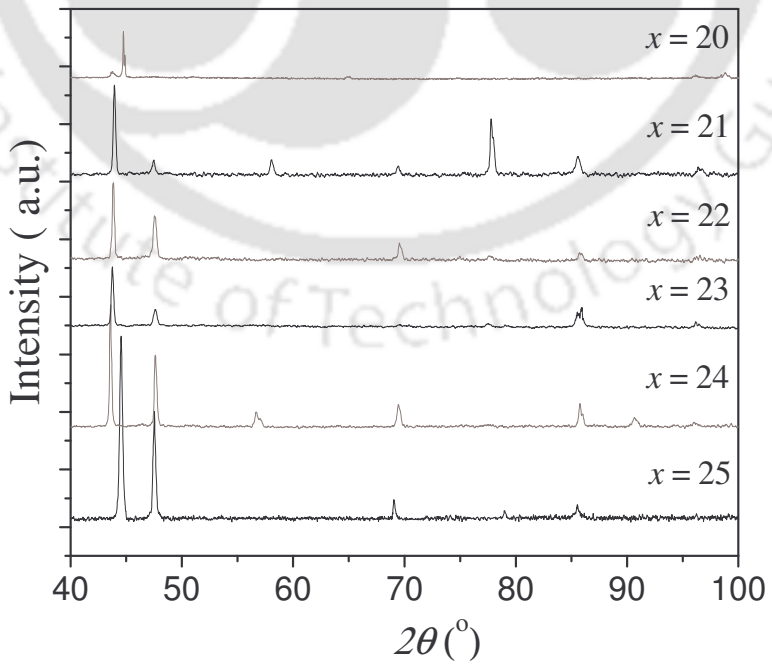

Fig. 4.2.1a: XRD patterns of $Co_{70-x}Ni_xGa_{30}$ ($20 \leq x \leq 25$) alloys.

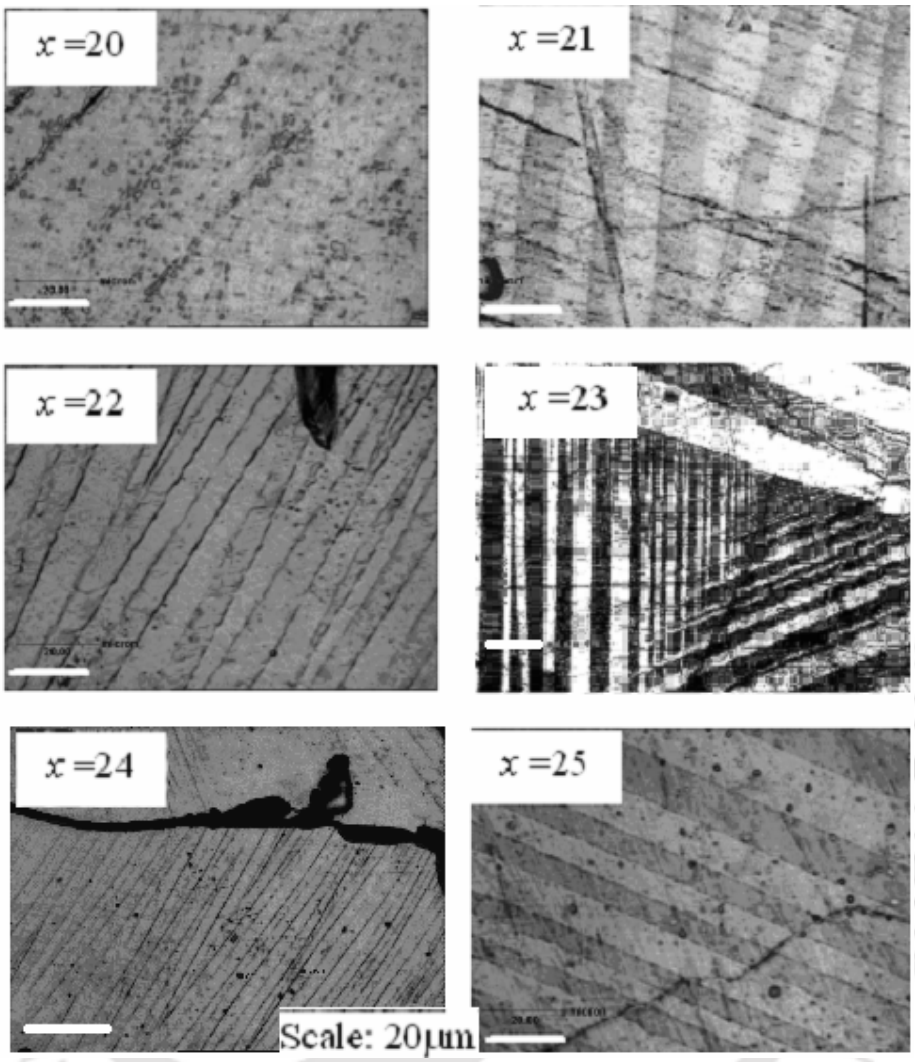

Fig. 4.2.1b: Optical micrograph of $Co_{70-x}Ni_xGa_{30}$ ($20 \leq x \leq 25$) alloys annealed at 1150 °C.

To determine the crystal structure of the alloys, the Rietveld refinement technique was employed. Both *I4/mmm* (bct) and *P4/mmm* (fct) models were used to refine the crystallographic parameters. Typical least squares fit to the data of alloy with x = 24 for both the model are shown as in the Fig.4.2.1c and Fig.4.2.1d, respectively. The XRD pattern of alloy with x = 20 exhibits a three phase structure (Fig.4.2.1e). The phases have been identified as bct martensite (β') phase, *A2* austenite (β)-phase and fcc γ-phase. The lattice parameters and atom positions in the unit cell for both the models are listed in Table 4.2.1.

Table 4.2.1: Crystallographic data of $Co_{70-x}Ni_xGa_{30}$ ($20 \le x \le 25$) alloys annealed at 1150 ˚C.

Space Group	*P4/mmm*							*I4/mmm*						
Wyckoff Position →	Ga: 1a (0.0, 0.0, 0.0) Ni: 1c (0.5, 0.5, 0.0) Co: 2e (0.0, 0.5, 0.5)							Ga: 2a (0, 0, 0) Ni: 2a (0, 0, 0) Co: 2a (0, 0, 0)						
Ni at. % (*x*) ↓	*a* (Å)	*c* (Å)	*c/a*	*V* (Å)^3	χ^2	R_{wp}	R_B	*a* (Å)	*c* (Å)	c/a	V (Å)^3	χ^2	R_{wp}	R_B
25	3.816	3.254	0.853	47.384	1.8	17	21	2.698	3.254	1.206	23.687	2.4	9	14
24	3.819	3.245	0.850	47.328	0.8	10	15	2.701	3.245	1.201	23.674	2.0	16	16
23	3.829	3.225	0.842	47.300	3.5	18	25	2.708	3.225	1.191	23.649	4.8	8	13
22	3.827	3.224	0.842	47.215	4.2	20	22	2.706	3.224	1.191	23.608	5.2	10	15
21	3.837	3.205	0.835	47.180	3.0	18	21	2.713	3.205	1.181	23.590	4.0	7	14

x = 20	*a* (Å)	*c* (Å)	*c/a*	*V* (Å)^3	χ^2	R_{wp}	R_{Bragg}
Martensite phase (β′) *Space group: I4/mmm*	2.713	3.213	1.184	23.649	1.92	20	23
Austenite phase (β) *Space group:* $Im\bar{3}m$	2.887	2.887	1.000	24.062		18	11
γ- phase *Space group:* $Fm\bar{3}m$	3.605	3.605	1.000	46.850		17	18

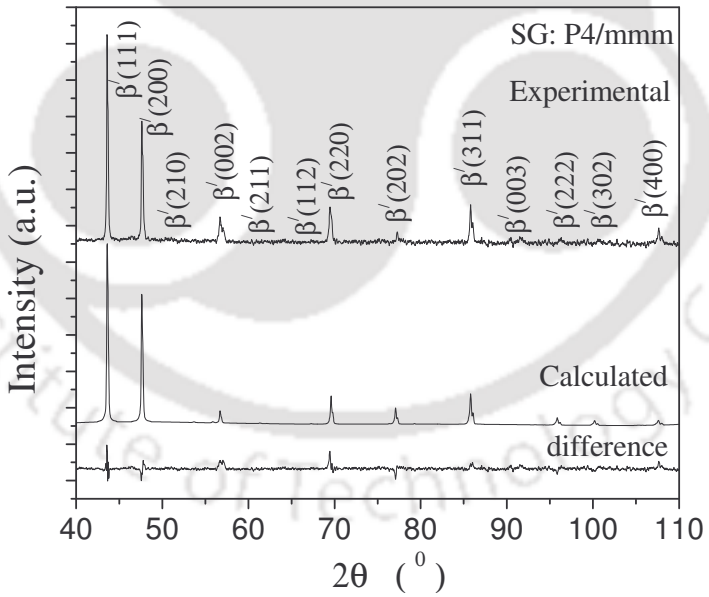

Fig. 4.2.1c: Rietveld fit to XRD pattern of $Co_{46}Ni_{24}Ga_{30}$ alloy annealed at 1150 °C showing the fit to *P4/mmm* space group.

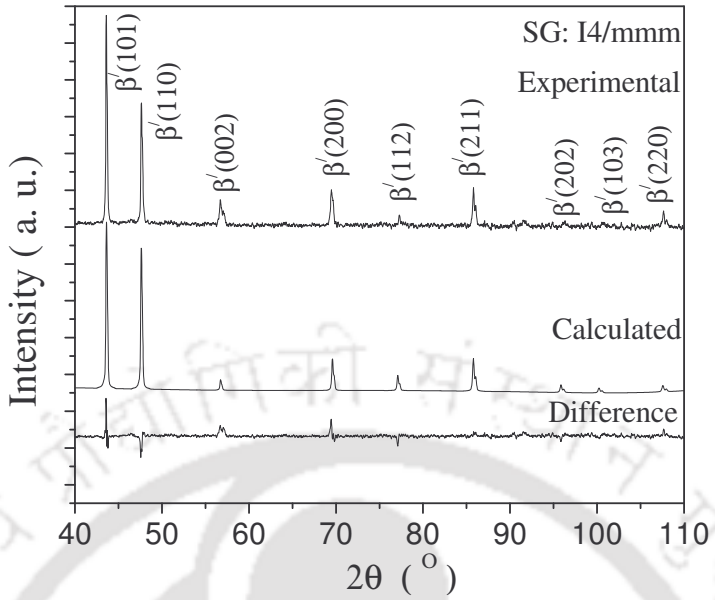

Fig. 4.2.1d: Rietveld fit to XRD patterns of $Co_{46}Ni_{24}Ga_{30}$ alloy annealed at 1150 °C showing the fit to *I4/mmm* space group.

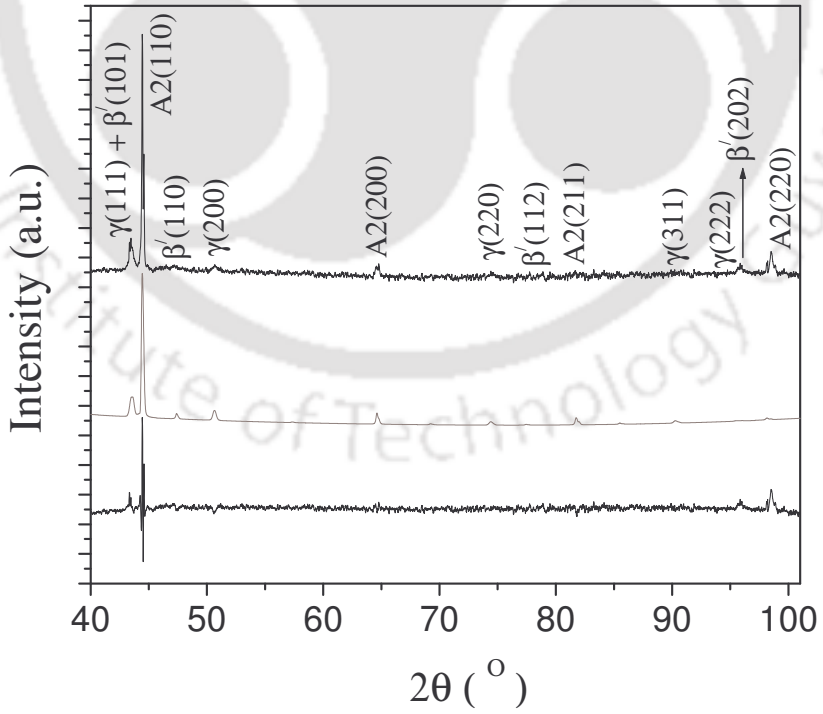

Fig.4.2.1e: Rietveld fits to XRD patterns of $Co_{50}Ni_{20}Ga_{30}$ alloy annealed at 1150 °C.

It can be seen from the data presented in Table 4.2.1 that the unit cell volume does not change appreciably with the change of Ni and Co at%. Since the atomic radius of Co and Ni are comparable, no appreciable change in unit cell volume is expected when these two atoms replace each other. A small change of *c/a* ratio has been observed with the decrease in *e/a* ratio. But the *e/a* ratio changes with the change of Ni and Co at %. The lattice parameters reported by Brown *et al*. from their neutron diffraction studies [32] and by Chernenko *et al.* from TEM observations [55] are in reasonable agreement with our results. The percentage of martensite, austenite and γ-phases in $Co_{50}Ni_{20}Ga_{30}$ at room temperature alloy was found from the Rietveld analysis to be 17.56%, 43.36% and 39.08%, respectively. M. Zhang et al. [54] reported the crystal structure of the austenite phase in $Co_{50}Ni_{20}Ga_{30}$ ribbons as B2 and that of the low temperature structure as tetragonal. However, no space group was assigned by them for the two crystal structures. Lattice parameter for austenite structure has been reported as a = 5.80 Å and that for martensite as a = 6.05 Å and c = 5.79 Å. It seems that a double unit cell has been considered for indexing the XRD pattern. We could not fit our XRD data using these lattice parameters.

4.2.2. Effect of annealing temperature on the crystal structure

Co-Ni-Ga and Co-Ni-Ga FSMAs have certain advantages over the prototype Ni-Mn-Ga FSMA [19] Compositions of Co-Ni-Ga(Al) alloys can be selected in such a way that they are located near the two-phase (β + γ) region [19], which facilitates the introduction of appropriate amounts of the cubic γ-phase in the β-matrix by proper choice of alloy composition and heat treatment conditions. The hot workability and room temperature ductility of these alloys are significantly improved by the introduction of the γ-phase, which is a great advantage for practical applications [38]. These alloys melt near 1200 ˚C. Alloy samples quenched in ice water from 1230 °C were ductile and hence could not be powdered well by grinding with a pestle and mortar. The alloys when quenched in liquid nitrogen were less ductile which facilitated grinding of the alloy pieces with minimal effort. Hence, pieces of alloys were sealed

under vacuum in a fused silica tube, annealed at 1230 °C and quenched at liquid nitrogen. As-quenched pieces were carefully crushed into a coarse powder. Certain amount of strain is expected to be present in the powders due to the rapid cooling as well as grinding done on the quenched sample pieces. No further heat treatment was given to the alloy powders prior to the X-Ray diffraction (XRD) measurements. The reason for this is the lack of complete information on the ageing behaviour of this alloy system [34,123], and there is a possibility of inducing γ-phase precipitation during heat treatment. The XRD patterns of $Co_{70-x}Ni_xGa_{30}$ ($20 \leq x \leq 25$) alloys quenched from 1230 °C are shown in Fig.4.2.2a.

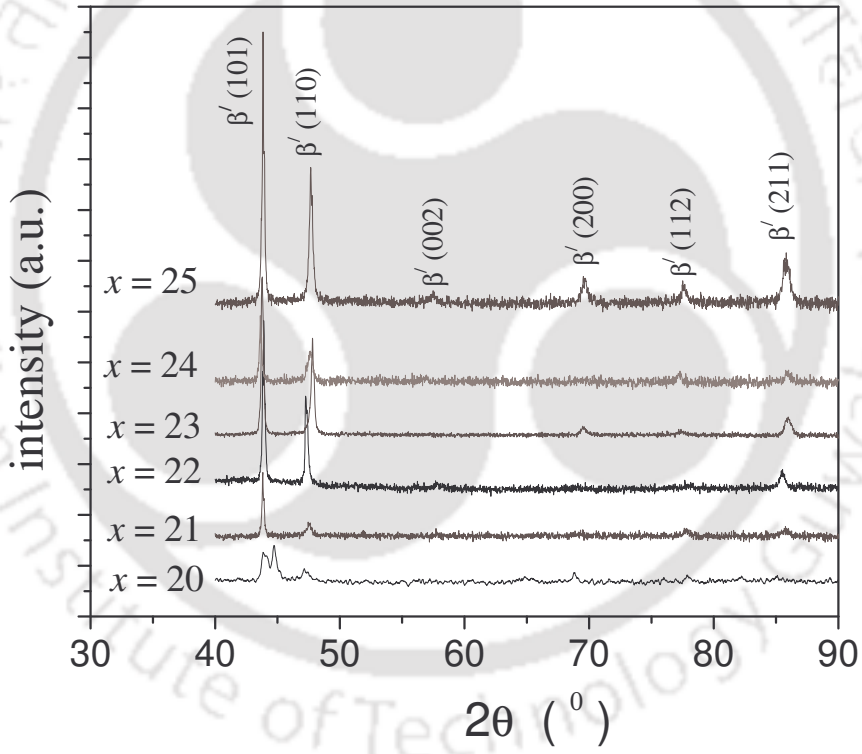

Fig.4.2.2a: XRD patterns of the $Co_{70-x}Ni_xGa_{30}$ alloys annealed at 1230 °C.

Table 4.2.2a: Structural data of bct unit cell and characteristic temperatures of $Co_{70-x}Ni_xGa_{30}$ alloys annealed at 1230°C.

x (Ni at.%) and lattice type	*a* (Å)	*c* (Å)	*V* (Å)^3	*c/a*
25 (tetragonal)	2.692	3.239	23.473	1.206
24 (tetragonal)	2.696	3.235	23.513	1.200
23 (tetragonal)	2.704	3.228	23.602	1.194
22 (tetragonal)	2.706	3.224	23.608	1.191
21 (tetragonal)	2.709	3.215	23.593	1.187
20 (cubic)	2.875	2.875	23.764	1.000
20 (tetragonal)	2.733	3.166	23.648	1.158

Lattice parameter corresponding to the fct unit cell ($L1_0$ –type structure) can be easily calculated by using the formula, $a_{L1_0} = \sqrt{2}a_{bct}$ and $c_{L1_0} = c_{bct}$ [46]. It is observed that the lattice parameters of the alloys quenched from 1150 °C and 1230 °C do not show appreciable differences. Only the FWHM (full width at half maximum) of the Bragg peaks of the alloys quenched from 1230 °C are more than those of the alloy quenched from 1150 °C. This is due to the smaller crystallite size of the alloy quenched from 1230 °C, the temperature at which the alloy is in molten state. However, alloys processed under both these quenching conditions were brittle. To make the alloys more ductile by introducing the γ-phase, the alloys were annealed at 1000 °C for six hours and quenched in ice water. XRD patterns of the alloys quenched from 1000 °C did not show any appreciable difference from the ones quenched from higher temperatures, except for the alloy with $x = 20$. Since the percentage of secondary (γ) phase developed during annealing at 1000 °C was very small, Bragg peaks due to the γ-phase were very weak. The intensity of the primary (martensite) phase peaks were also reduced due to the presence of the secondary phase. For the alloy with $x = 20$, a two phase structure ($A2 + \gamma$) was observed (Fig. 4.2.2a). It is to be noted that $\beta + A2$ phase structure was observed for this alloy ($x = 20$) when it was quenched from 1230 °C. A three-phase structure was observed for the same alloy when it was quenched from 1150 °C. Fig. 4.2.2b shows the XRD patterns of $Co_{50}Ni_{20}Ga_{30}$ alloy annealed from (i) 1230°C and (ii) 1000 °C.

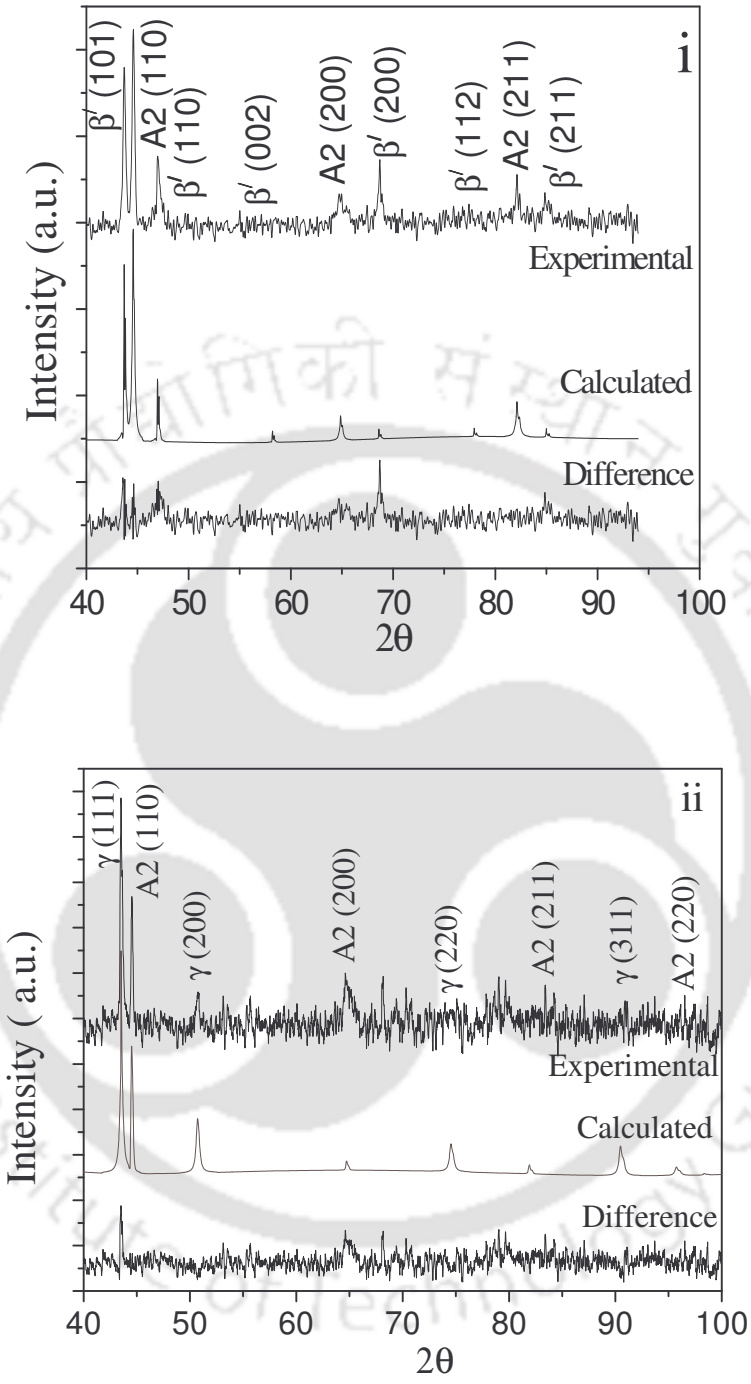

Fig.4.2.2b: XRD patterns of the $Co_{50}Ni_{20}Ga_{30}$ alloy annealed at (i) 1230°C and (ii) 1000 °C.

The evolution γ-phase due to the low temperature annealing has been observed clearly in the optical micrographs shown in (Fig.4.2.2c). The gray spots in the micrographs represent

the secondary phase developed due to the annealing at 1000 °C. The presence of secondary phase was verified with the help of compositional analysis using SEM-EDS measurement.

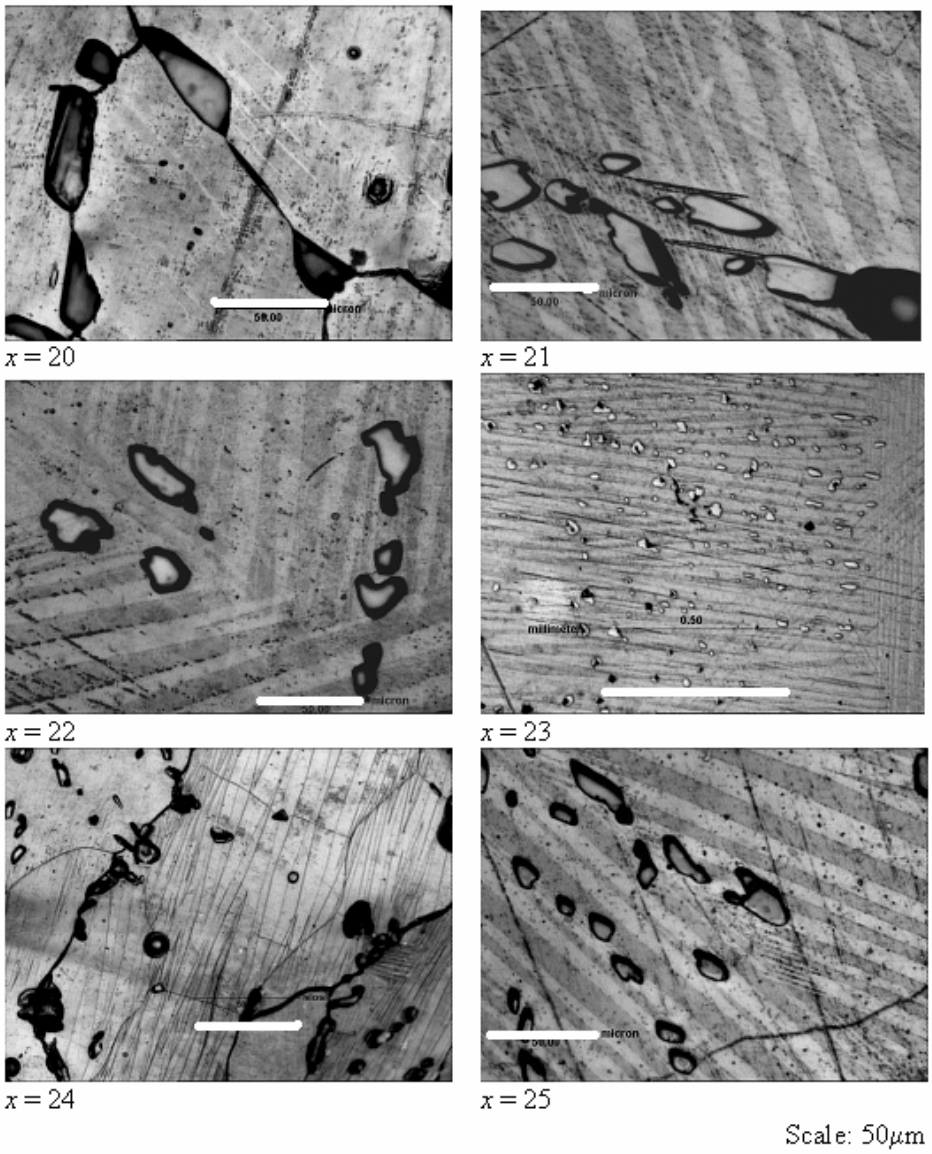

Fig. 4.2.2c: Optical micrographs of $Co_{70-x}Ni_xGa_{30}$ ($20 \leq x \leq 25$) alloys annealed at 1000 °C.

Batches of the pre-homogenized and ground powders of $Co_{47}Ni_{23}Ga_{30}$ alloy were separately annealed at 1230 °C, 1150 °C, 1000 °C and 900 °C for 6 hours each, and then quenched in ice water. No further heat treatment was performed on the quenched powders since the ageing characteristics of this alloy system are not well documented. The percentage

of γ phase present in the alloys annealed below 1150 ^{0}C was estimated from the optical micrographs using a commercial software package based on area scan method.

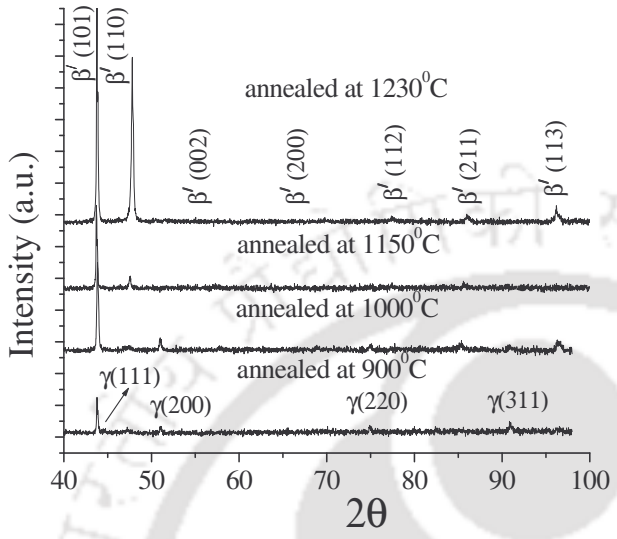

Fig. 4.2.2d: XRD patterns of $Co_{47}Ni_{23}Ga_{30}$ alloy annealed at different temperatures.

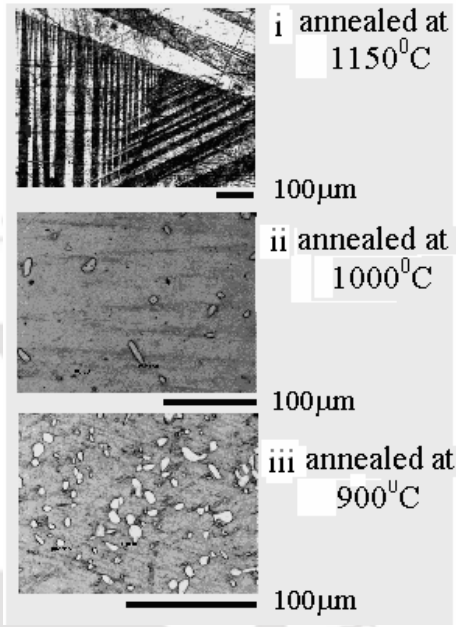

Fig.4.2.2e**:** Optical micrographs of the alloy annealed at various temperatures.

XRD patterns of the alloys annealed at 1150 °C and 1230 °C exhibited a single-phase martensite structure (bct β'-phase) at room temperature, whereas, presence of a face centered cubic γ-phase along with the martensite phase was observed in alloys annealed at 900 °C and 1000 °C (Fig.4.2.2d).

Rietveld refinement method was used to refine the lattice parameters of the two phases present in different samples. Lattice parameters of the martensite (β') phase were found to be $a = b = 2.71$ Å, $c = 3.23$ Å and the unit cell volume was 23.55 Å^3. Lattice parameters of the γ phase were found to be $a = 3.59$ Å and the unit cell volume was 46.27 Å^3. The unit cell parameters did not show much variation with change in annealing temperature as inferred from the unit cell volume change of 0.15 Å^3 between alloys annealed at 1230 °C and 900 °C. Liu *et al.* [40] claimed to have observed a change of 0.4 Å^3 in unit cell volume when the annealing temperature was changed from 1200 °C to 900 °C. Though the martensite structure

of Co-Ni-Ga alloys was reported by them [40] as tetragonal, it is evident that the lattice parameters, Miller indices of the peaks and the angular position of peaks in the reported XRD patterns did not fit in the indexing scheme of tetragonal crystal system. Hence, our observation on the unit cell volume change in alloys annealed at different temperatures is expected to be more reliable than the high value reported by Liu *et al*. The percentage of γ phase present in the alloy annealed at different temperatures was estimated from the least squares fit to the appropriate XRD data. The estimates obtained were 4.0% and 13.8% for the alloys annealed at 1000 °C and 900 °C, respectively.

Optical micrographs of polished $Co_{47}Ni_{23}Ga_{30}$ alloy samples annealed at 1150 °C, 1000 °C and 900 °C are shown in Fig. 4.2.2e(i - iii), respectively. The characteristic twinned structure of a single martensitic microstructure can be seen in the micrograph shown in Fig.4.2.2e.i. The white spots in Fig. 4.2.2e.ii and Fig. 4.2.2e.iii represent the γ phase precipitated during the annealing treatment at lower temperatures. The small black spots in the micrographs have been identified as porosities, which are usually present in cast alloys. It is clearly seen from Fig. 4.2.2e.ii and Fig. 4.2.2e.iii the amount of γ phase precipitated in the alloy increases as the annealing temperature is lowered. The percentage of γ phase estimated from optical microscopy was 4.4% and 16% for the alloys annealed at 1000 °C and 900 °C, respectively. This result is in close agreement with those obtained from the analysis of XRD data. The compositions of single martensite (β') phase and combined $\beta' + \gamma$ phases determined by EDS analysis are given in Table 4.3.2. It is evident from Table 4.3.2 that the composition of the β' phase varies slightly in samples annealed at lower temperatures. This variation in the composition of the β' phase is due to the precipitation of the γ phase. As a consequence of this change in the composition of the β' phase, the *e/a* ratio of the β' -matrix decreases when annealed below 1150 °C. Liu *et al.* [40] have also observed the precipitation of γ-phase in alloys annealed below 1120 °C. However, our results refute their claim that the amount of γ-

phase precipitates does not change with annealing temperature. In fact, a closer look at the XRD data presented by them [Fig. 5 in ref. 40] clearly shows the enhancement of the γ-phase reflections of the sample annealed at 900 °C when compared with that of the sample annealed at 1200 °C.

4.2.3. Effect of quenching rate on the crystal structure

The normal procedure for preparation of these alloys involves preparation of the master alloy ingots by arc melting (or induction melting) followed by homogenization at high temperature and quenching into cold temperature. This is done to retain a high temperature phase at room temperature and to avoid precipitation some intermediate phase normally present in the system. The effect of quenching rate on the crystal structure of one alloy composition was investigated. Ground powders of $Co_{45}Ni_{25}Ga_{30}$ alloy and three small discs cut out from the slowly cooled alloy were sealed in three different fused silica ampoules at a pressure ~10^{-5} mbar, annealed at 1150 °C for 4 hours and then quenched separately into liquid nitrogen, ice cold water and air, respectively. In this manner, three alloys were prepared under different cooling rates.

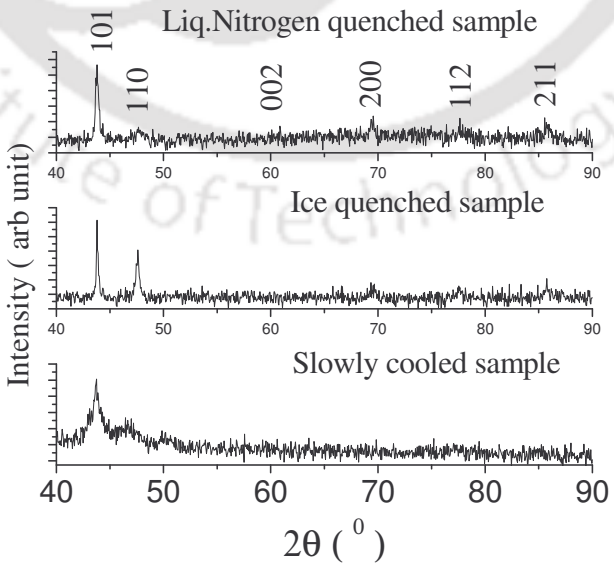

Fig. 4.2.3.a**:** XRD patterns of $Co_{45}Ni_{25}Ga_{30}$ alloys prepared with different quenching rate.

The XRD patterns of the alloy sample quenched under three different conditions are shown in Fig. 4.2.3a. The XRD pattern of the slowly cooled alloy showed a mixed phase structure. The extra peaks present in this XRD pattern is due to the presence of some other phase in the slowly cooled alloy. The surface relief due to martensitic transformation was observed in optical microscope for all the three quenched samples (Fig.4.2.3b). The thickness of the twin lines increased for samples cooled at higher rates. This is probably due to the larger displacement of lattice points required to accumulate higher elastic energy in samples quenched at higher rate. The twin lines are not distinct in the air cooled sample.

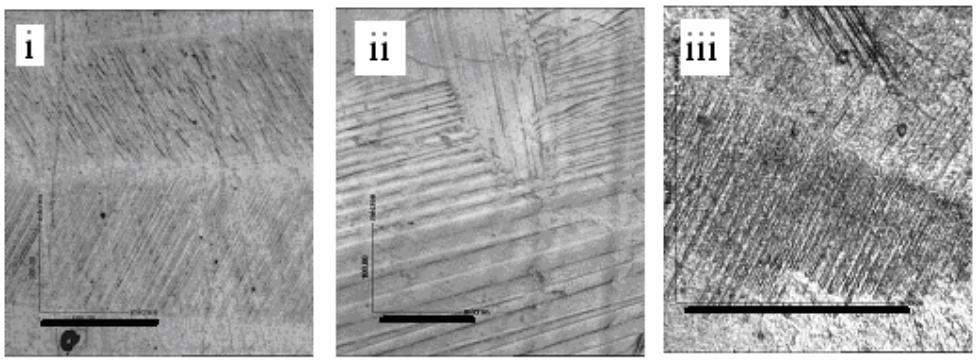

Liquid nitrogen quenched Ice quenched Air cooled

Fig. 4.2.3b: Optical microscope images of $Co_{45}Ni_{25}Ga_{30}$ alloy prepared under three different quenching rates.

4.3. THERMAL PROPERTIES

4.3.1. DSC studies of alloys quenched from 1150 ˚C

DSC thermograms depicting martensitic transformation temperatures corresponding to various compositions of $Co_{70-x}Ni_xGa_{30}$ alloys are shown in Fig.4.3.1a. Each DSC thermogram involving a heating and cooling cycle shows an endothermic and an exothermic peak corresponding to and $A \rightarrow M$ transformations, respectively. The $M \rightarrow A$ and $A \rightarrow M$ transformation temperatures for each alloy composition is different (cf. Table 4.3.1).

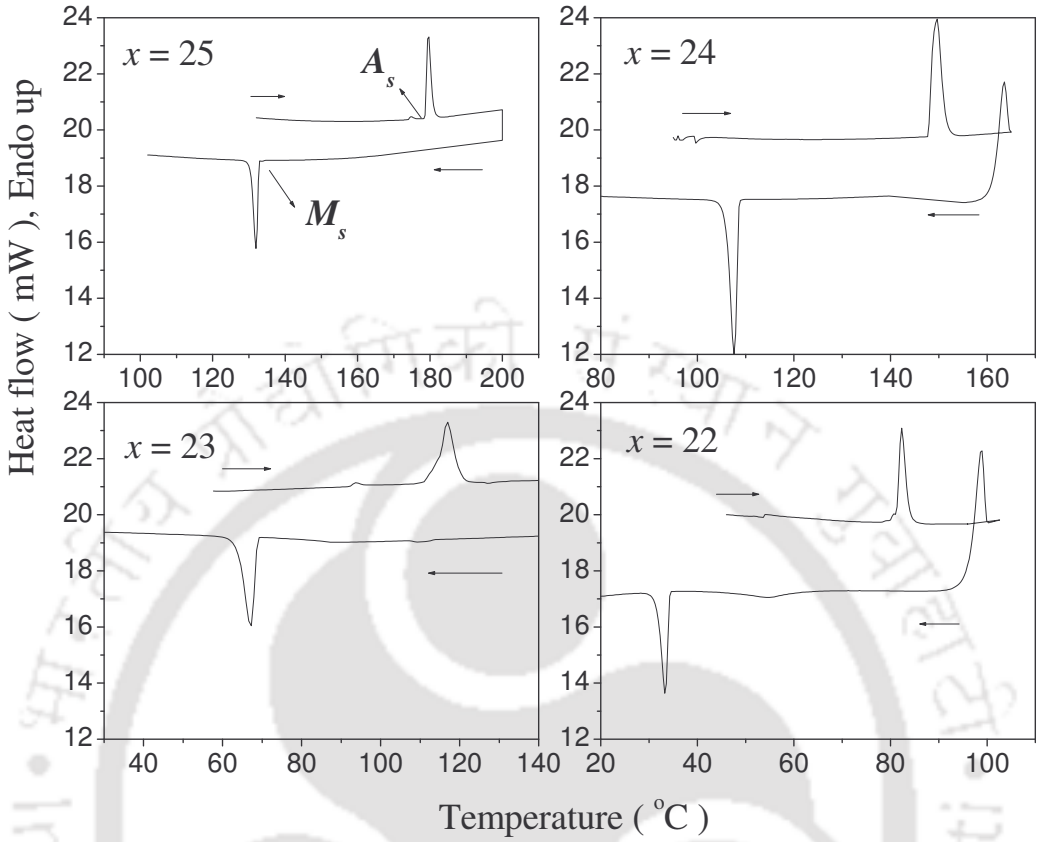

Fig. 4.3.1a: DSC thermograms of $Co_{70-x}Ni_xGa_{30}$ ($22 \leq x \leq 25$) alloys.

Table 4.3.1**:** Martensite transformation parameters (M_s, M_f, A_s, A_f and T_0) of $Co_{70-x}Ni_xGa_{30}$ ($22 \leq x \leq 25$) alloys.

Ni (at %)	M_s [°C]	M_f [°C]	A_s [°C]	A_f [°C]	T_0 [°C]	e/a
25	133	125	178	187	160.0	7.45
24	103	100	147	149	126.0	7.44
23	69	61	111	120	94.5	7.43
22	37	35	78	81	59.0	7.42
21*	15	18	44	49	32	7.41
20*	0	-38	6	15	7.5	7.40

* Martensitic transformation (MT) temperatures of alloys with x = 21 and 22 were near room temperature or below it. These data were obtained from low temperature AC susceptibility measurements.

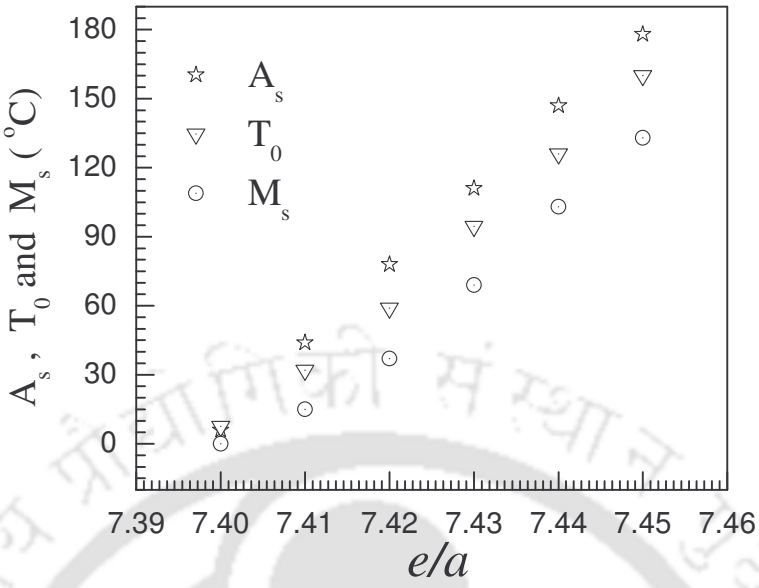

Fig. 4.3.1b**:** Variation of A_s , T_0 and M_s with e/a ratio of $Co_{70-x}Ni_xGa_{30}$ ($0 \leq x \leq 25$) alloys.

It can be seen from Fig. 4.3.1b that A_s, T_0 and M_s increase linearly with an increase in *e/a* value. The calculated value of *e/a* for all the Co-Ni-Ga alloys are listed in Table 4.3.1. Oikawa *et al.* [19] reported phase equilibrium between β and γ phases in this alloy system and pointed out similar variation of M_s, A_s and T_C of $Co_{70-x}Ni_xGa_{30}$ alloys in the $\beta + \gamma$ region. M_s and A_f were shown to decrease with increasing Co content. M_s and A_s values can be read from the data by them in graphical form for $Co_{45}Ni_{25}Ga_{30}$ alloy as $M_s \cong 130$ °C and $A_s \cong 160$ °C. Our observations are in close agreement with their results. Dadda *et al.* [124] reported the M_s and A_s temperature from AC susceptibility (ACS) measurements for $Co_{49}Ni_{21}Ga_{30}$ single crystal alloy as -5.3 °C and 6.3 °C, respectively. We observed higher A_s and M_s in our sample with x = 21. This may be due to the different processing condition under which single crystal and polycrystalline alloys are prepared. Zhang *et al.* [54] reported the MT temperature from ACS measurement for $Co_{50}Ni_{20}Ga_{30}$ ribbons as -3 °C (270 K) and 2 °C (275 K). But the graph shown in their paper reveals that A_s and M_s values are lower than the reported result. From ACS measurements, we observed A_s and M_s as 6 °C and 0 °C, respectively for this alloy. Dai *et al.*

[25] reported martensitic and reverse martensitic transformation temperatures of melt spun ribbons from ACS measurement as -18 °C and -8 °C, respectively. The low value obtained by them may be due to the smaller grain size of the melt spun alloys. Liu *et al.* [40] reported the A_s and M_s for alloy with *e/a* = 7.42 as 42 °C and 39 °C, respectively. Our M_s value is closer to their reported value but our A_s is higher than their reported value. This may be due to the fact that alloy prepared by them exhibited two phase ($\beta + \gamma$) structure after annealing at 700 °C and the presence of γ-phase has influenced the reverse martensitic transformation. For Co-Ni-Ga alloys, *MT* is so sensitive to composition that a decrease of 1 at% Ga leads to about 50 °C increases in M_s [125].

4.3.2. Effect of annealing temperature on martensitic transformation temperature

Properties of FSMAs have been found to be sensitive to alloy composition, homogenization (or annealing) temperature, cooling rate during preparation and post-preparation heat-treatment [40]. $Co_{47}Ni_{23}Ga_{30}$ alloy was taken up for study to investigate the influence of different annealing temperatures on the transformation temperature. Small pieces of the alloy was vacuum sealed in three fused silica tubes and separately annealed at 900 °C, 1000 °C and 1150 °C for 6 hours each and then quenched in ice water. DSC curves of $Co_{47}Ni_{23}Ga_{30}$ alloy annealed at 1230 ^{0}C, 1150 °C, 1000 °C and 900 °C are shown in Fig. 4.3.1a. The transformation parameters, namely, M_s and A_s, corresponding to the alloy annealed at different temperatures are listed in Table 4.3.1. The decrease in M_s and A_s observed in alloys annealed at lower temperatures can be understood on the basis of the change in the *e/a* ratio of the β'-matrix in the respective samples. It is now established [20, 40] that M_s and A_s of FSMAs vary linearly with *e/a* value. Hence, the decrease in M_s and A_s in alloys annealed at lower temperature is due to the decrease in the *e/a* ratio of the β'-matrix. The *e/a* ratio of the β'-matrix of the alloy annealed 900 °C is very close to 7.30 (cf. Table 4.3.1). This shows that annealing below 900 °C may not yield sufficient amount of martensite phase in $Co_{47}Ni_{23}Ga_{30}$ alloy.

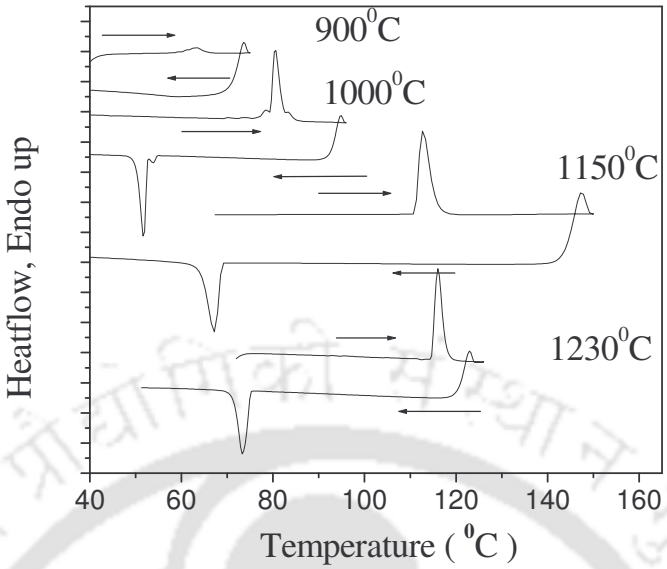

Fig. 4.3.2a: DSC curves of alloy samples annealed at different temperatures.

Table 4.3.2: Composition of constituent phases and characteristic temperatures of $Co_{47}Ni_{23}Ga_{30}$ alloy annealed at different temperatures.

Annealing temperature of alloy (ºC)	Composition of β´ matrix (at.%) from EDS measurements			*e/a* ratio	Composition of γ phase (at.%) from EDS measurements			A_s (°C)	M_s (°C)	T_C (°C)
	Co	Ni	Ga		Co	Ni	Ga			
1230	47.5	22.6	29.9	7.432	0	0	0	114	77	100
1150	46.9	23.1	30.0	7.431	0	0	0	111	69	105
1000	46.3	23.5	30.2	7.423	54.8	28.8	16.4	79	57	94
900	44.5	24.0	30.5	7.320	64.2	22.1	13.7	60	– 47	64

4.3.3. Effect of quenching rate on the martensitic transformation temperature

Three small discs of $Co_{45}Ni_{25}Ga_{30}$ alloy were sealed in three different fused silica ampoules at a pressure ~10^{-5} mbar, annealed at 1150 °C for 4 hours and then quenched separately into liquid nitrogen, ice cold water and air, respectively. The DSC curves of the three quenched samples are shown in Fig. 4.3.2a The transformation parameters, namely, M_s, M_f, A_s, A_f and the enthalpy involved in the transformations (ΔH_A and ΔH_M) are listed in Table 4.3.2. No evidence

of $M \rightarrow A$ and/or $A \rightarrow M$ transformations was observed in furnace-cooled sample. This indicates that the martensite phase could be formed in this alloy only by rapidly cooling the homogenized master alloy.

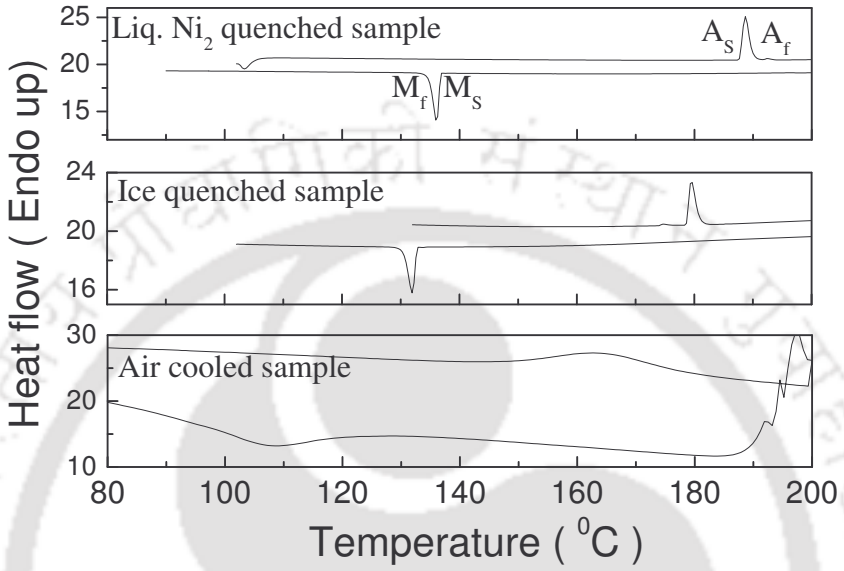

Fig. 4.3.3a: DSC curves of $Co_{45}Ni_{25}Ga_{30}$ alloy prepared under different quenching rates.

Table 4.3.3: DSC data of $Co_{45}Ni_{25}Ga_{30}$ alloy prepared under different quenching rate.

Quenching medium	Transformation parameter						
	A_s (°C)	ΔH_A ($=A_s \sim A_f$) (°C)	ΔH_A (J/g)	M_s (°C)	ΔM ($=M_s \sim M_f$) (°C)	ΔH_M (J/g)	Hysteresis ($=A_f \sim M_s$) (°C)
Liq. N_2	187	4	4.203	137	4	4.917	44
Ice water	178	4	4.588	133	5	4.306	33
Air	148	31	2.318	124	32	3.45	55

Analysis of the DSC data of the air cooled, ice quenched and liquid nitrogen quenched alloys showed higher A_s and A_f temperatures for the liquid nitrogen quenched sample. When samples were quenched from a high temperature to a very low temperature suddenly, the

elastic energy of the system can not be dissipated. Thus, the system accumulates (self accumulation of martensite) the elastic energy by displacive transformation of the lattice points. Thus, higher quenching rate introduces more elastic energy (or density of dislocation) in the system. To change from martensite state to austenite state, the SMA has to overcome more elastic energy and hence the transformation temperatures are higher for samples quenched at higher rates. Thus, it can be said that higher transformation temperatures can occur due to the presence of a higher concentration of defects in the martensite phase [126]. The same phenomenon causes larger thermal hysteresis, (A_f~M_s) in a sample quenched at higher rates. The elastic energy around the martensite resists the growth of the martensite unless a further driving force (i.e. cooling) is given [10]. The endothermic and exothermic peak of air cooled sample is very weak and wide. Thus, the $M \leftrightarrow A$ transformation in air cooled sample is not sharp and hence the cooling rate is not sufficient for the formation of shape memory alloys. The $M \leftrightarrow A$ transformation of ice quenched and liquid nitrogen quenched samples are very sharp. However, very high rates of quenching introduce more thermal strain into the system and cracks develop in the bulk sample. Taking account of these, one can say that the ice quenching method is more suitable for the preparation of Co-Ni-Ga alloys.

4.4. MASS DENSITY MEASUREMENT

The results of mass density measurement from Archimedes principle are given in Table 4.4. Here ρ_A was measured on the alloy samples. ρ_c (= 8.003 g/cm^3) was calculated from the individual contribution of the constituent elements of the alloys. It is seen that density does not vary with the change of Co at % and Ni at %. It is due to the fact that density of Co and Ni are almost same.

Table 4.4: Mass Density of $Co_{70-x}Ni_xGa_{30}$ ($20 \leq x \leq 25$) alloys.

Ni at% (x) in the alloy	Measured density ρ_A (g/cm^3)
20	8.583 ± 0.004
21	8.608 ± 0.004
22	8.587 ± 0.004
23	8.606 ± 0.004
24	8.620 ± 0.004
25	8.616 ± 0.004

4.5. MAGNETIC PROPERTIES

4.5.1. AC susceptibility as a function of temperature:

Temperature dependence of the AC susceptibility data of all the samples are shown in Fig. 4.5.1a. All samples show a characteristic decrease in the real component of ACS near the ferromagnetic to paramagnetic phase transition. The ferromagnetic to paramagnetic transition temperature (T_C) of $Co_{70-x}Ni_xGa_{30}$ alloys was determined from the magnetic susceptibility versus temperature data recorded while heating the sample (Fig. 4.5.1a) and the corresponding values are given in Table 4.5.1.

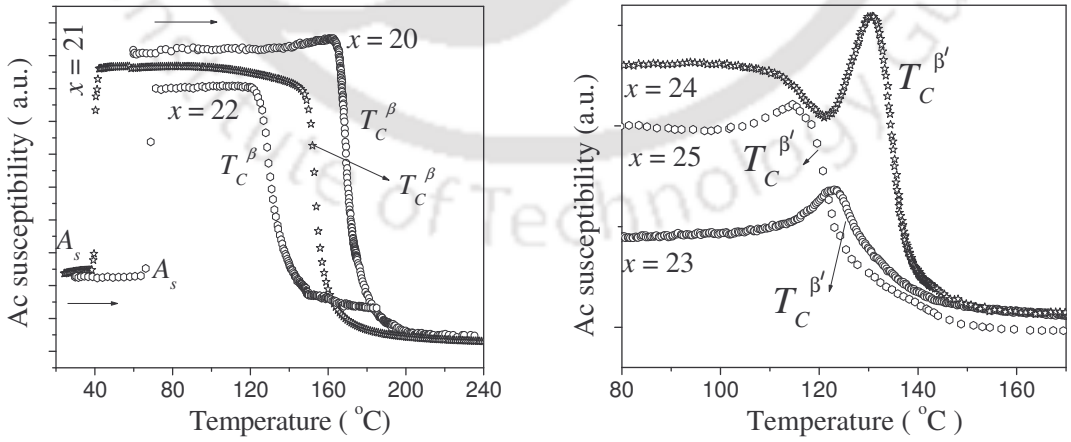

Fig. 4.5.1a: AC susceptibility of $Co_{70-x}Ni_xGa_{30}$ ($20 \leq x \leq 25$) alloys.

Table 4.5.1: Curie temperature of $Co_{70-x}Ni_xGa_{30}$ ($20 \leq x \leq 25$) alloys.

x	20	21	22	23	24	25
T_C [^oC]	169	151	129	125	133	119

T_C values have been measured from the local minimum point of the derivative AC susceptibility vs temperature graph and are listed in the Table 4.5.1 Curie temperature for the austenite state is conventionally written as T_C^{β} and that of the martensite state as $T_C^{\beta'}$. It is seen that T_C^{β} value is highest for x = 20 (50 at % Co), which decreases with an increase of x. A discontinuity is observed at x = 23, where T_C^{β} changes to $T_C^{\beta'}$. A similar trend has been reported in Ni-Mn-Ga [59], Fe-Ni-Ga [22], Co-Ni-Ga and Co-Ni Al [19] alloys (Ref. Chep1. page 27). The discontinuity has been observed for the alloys having close MT and T_C values. As the sample is heated, a sudden increase in magnetic susceptibility is observed at A_s followed by a sharp decrease in susceptibility at T_C. In the case of the alloy with x = 23, A_s (111 °C) and T_C (125 °C) are very close. At A_s, the susceptibility tries to rise sharply, whereas at T_C it tries to drop down. Due to the proximity of A_s and T_C values, precise measurement of T_C is difficult for this alloy. This could have been the cause for the difficulty faced by Oikawa *et al*. [19] in precisely determining the T_C of the $Co_{47}Ni_{23}Ga_{30}$ alloy quenched from 1150 °C on the heating cycle. A detailed investigation has been carried out on this sample to find T_C and the influence of different annealing and conditions on T_C.

4.5.2 Effect of annealing temperature on the Curie temperature

Some small pieces of alloys was vacuum sealed in three fused silica tubes and separately annealed at 900 °C, 1000 °C and 1150 °C for 6 hours each and then quenched in ice water. No further heat treatment was performed on the quenched powders. T_C was determined from the ACS data.

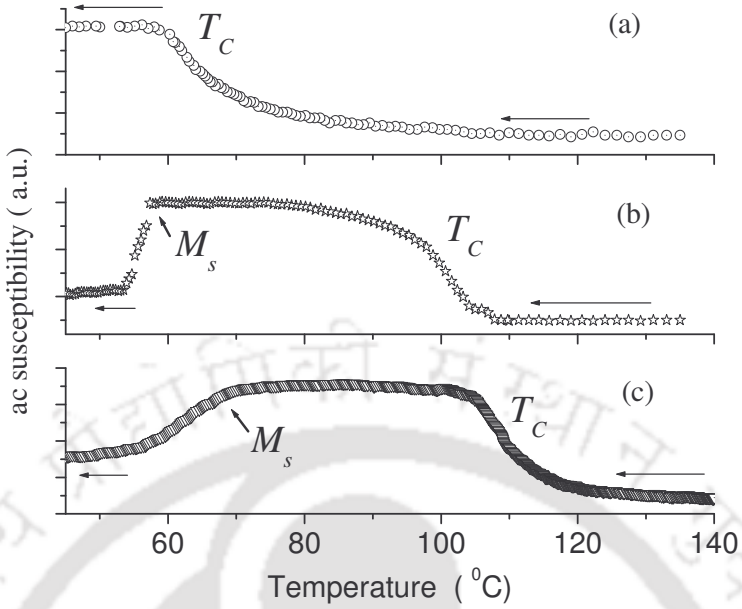

Fig. 4.5.2a: ACS data of $Co_{47}Ni_{23}Ga_{30}$ alloy annealed at (a) 900 °C (b) 1000 °C & (c) 1150 °C.

The ACS data of $Co_{47}Ni_{23}Ga_{30}$ alloy annealed at 1150 °C, 1000 °C and 900 °C are shown in Fig. 4.5.2a. The plots correspond to data collected on the cooling cycle. A small difference of ≤ 5°C was observed in T_C of the investigated alloys obtained during heating and cooling cycle. This difference was minimized by slowly heating or cooling the samples. As the sample is cooled, a sudden increase in magnetic susceptibility is observed at T_C followed by a decrease in susceptibility at M_s. Since M_s (69 °C) and T_C were far away there was no influence of the MT on T_C of this alloy. For this reason, we have presented the susceptibility data obtained on the cooling cycle.

T_C of the alloy decreases as the annealing temperature is decreased, except for the case of the sample annealed at 1230 °C. When the sample is quenched below 1120 °C, a secondary (γ) phase develops with the primary β-phase. The presence of γ phase introduces some crystallographic disorder in the alloys. Increased crystallographic disorder tends to shift T_C to lower temperatures. The lower T_C exhibited by the alloy quenched from 1230 °C can be understood as follows. Lowering of T_C has been observed in ribbons quenched at higher

cooling rates [127]. The alloy melts near 1220 °C. When the alloy is quenched from 1230 °C in molten condition, the grain size of the resultant alloy is considerably reduced than those quenched from the solid state. This smaller grain size and higher cooling rate results in shifting the T_C towards low temperature side with respect to the alloy quenched from 1150 °C.

4.5.3. Effect of quenching rate on the Curie temperature

The ferromagnetic to paramagnetic transition (Curie) temperature (T_C) was measured by ACS for $Co_{45}Ni_{25}Ga_{30}$ prepared under different cooling rate and the T_C values are given in Table 4.5.3. T_C was lower for samples prepared with higher cooling rate (i.e. samples quenched in liquid nitrogen). T_C is sensitive to local crystallographic environment. When the sample is quenched from high temperatures, the solidification is not under equilibrium conditions and this introduces some crystallographic defects in the sample. These defects create a local disorder in their vicinity. Faster cooling rates introduce more defects in the sample. Thus, the degree of disorder in the sample prepared by quenching in liquid nitrogen is more than in the other two samples. The increased crystallographic disorder is manifested in decreased grain size. T_C value shifts to lower temperature side with the reduction of grain size. Hence, lower T_C value of alloys quenched at higher rate is an expected result. Similar results have been reported in rapidly solidified Nd -Fe-B samples [127].

Table 4.5.3: Curie temperature of $Co_{45}Ni_{25}Ga_{30}$ alloy prepared under different cooling rate.

Quenching medium	Liq. N_2	Ice water	Air cooled
T_C (°C)	98	119	131

4.5.4. Magnetization as a function of temperature using VSM:

Magnetization vs temperature (*M-T*) graphs corresponding to the alloys annealed at 1150 °C and 1000 °C are shown as in Fig. 4.5.4a and Fig. 4.5.4b, respectively T_C was measured from the local minimum point of the derivative curve of *M-T* (*H* = 50 Oe) data.

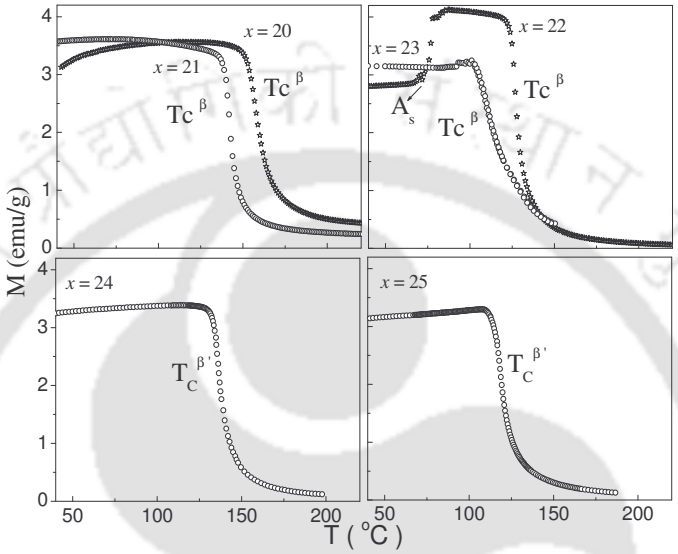

Fig.4.5.4a: Variation of magnetization of with respect to temperature at constant field. $Co_{70-x}Ni_xGa_{30}$ ($20 \le x \le 25$) alloys annealed at 1150 °C.

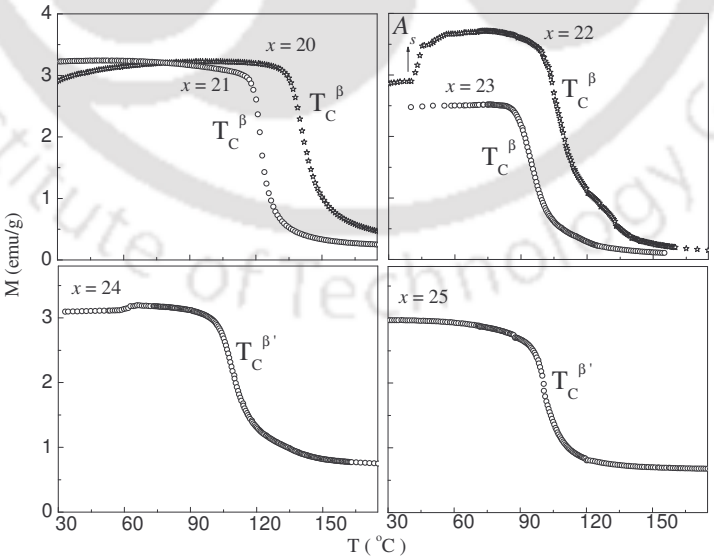

Fig.4.5.4b: Variation of magnetization of with respect to temperature at constant field. $Co_{70-x}Ni_xGa_{30}$ ($20 \le x \le 25$) alloys annealed at 1000 °C. The term 'β' and 'β/' are used for cubic phase and martensite phase respectively.

Table 4.5.4: Curie temperature (T_C) of $Co_{70-x}Ni_xGa_{30}$ ($20 \leq x \leq 25$) alloys obtained by quenching from different temperatures along with magnetic valence number (Z_m).

Composition of the alloy (x)	T_C (alloy annealed at 1150 °C)	T_C (alloy annealed at 1000°C)	Z_m
20	156 °C	139 °C	-0.40
21	141 °C	121 °C	-0.41
22	126 °C	105 °C	-0.42
23	109 °C	92 °C	-0.43
24	135 °C	107 °C	-0.44
25	117 °C	100 °C	-0.45

T_C values obtained from AC susceptibility measurements are close to the values obtained from magnetization measurements. All the data presented have been recorded on the heating cycle. A higher value of T_C was observed for the alloy annealed at higher temperature (1150 °C) than the alloy annealed at 1000 °C. The lower T_C exhibited by the alloy annealed at 1000 °C may be due to the presence of the γ-phase precipitates in the β - matrix. The magnetic ordering is likely to be disturbed due to the presence of the cubic secondary phase. A linear dependence of T_C and T_0 with annealing temperature has been reported [38] in $Co_{38}Ni_{34}Al_{28}$ alloy with two (β+ γ) phase structure. In the present studies, T_C of the alloys annealed at 1150 °C and 1000 °C decreases with the decrease in magnetic valence number Z_m as shown in Fig. 4.5.4c. The slope and y-intercept of the T_C vs Z_m graph changes at $x = 23$. This is because the Curie temperature of martensite phase ($T_C^{\beta'}$) is higher than that of the austenite phase (T_C^{β}) [17, 22]. For the alloys with $x = 24$ and 25, the reverse martensitic transformation temperature (A_s) is higher than the T_C. Thus, the ferromagnetic to paramagnetic transition of these two alloys occurs in the martensite phase during the heating cycle, whereas, the other alloys (i,e., $20 \leq x \leq 23$) undergo the magnetic transition in the austenite phase.

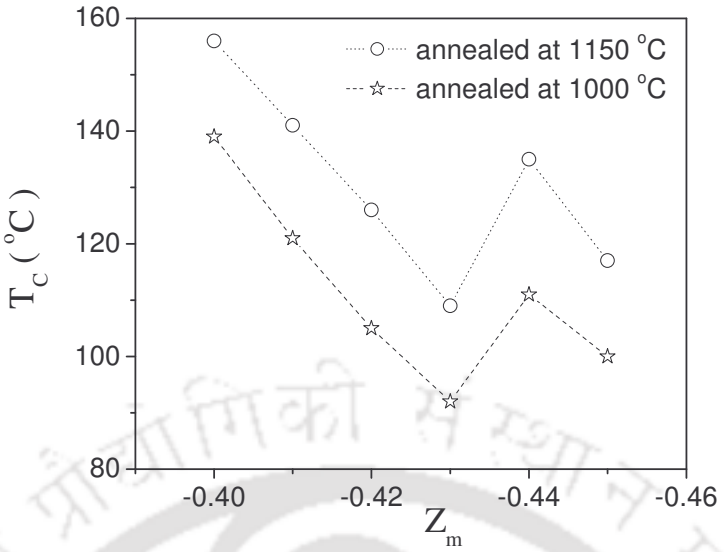

Fig.4.5.4c: Variation of T_C of $Co_{70-x}Ni_xGa_{30}$ ($20 \leq x \leq 25$) alloys with Z_m.

4.5.5. *M-H* measurements at constant temperature:

The magnetization (*M-H*) loops of $Co_{70-x}Ni_xGa_{30}$ ($20 \leq x \leq 25$) alloys show very small coercively (<100 Oe) at room temperature. This shows that the sample is soft magnetic both in austenite and martensite phases. The variation of magnetization with applied field for all the alloys annealed at 1150 °C and 1000 °C are shown as in Fig. 4.5.5a and Fig. 4.5.5b, respectively. Magnetization was measured at room temperature (25 °C). It can be observed from the insets in the two figures that the alloy with composition $x = 20$, annealed from 1150 °C saturates much faster than the other alloy compositions. A similar behavior has been observed for the alloys with composition $x = 20$ and 21, annealed at 1000 °C. This behaviour is due to the lower magneto crystalline anisotropy of these alloys as they are in the austenite state (cubic phase). The martensite phase has higher magneto crystalline anisotropy energy.

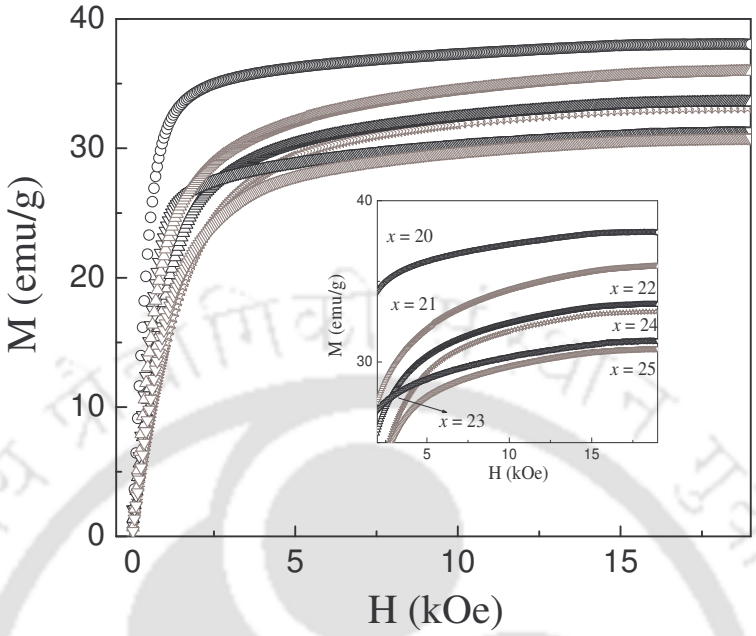

Fig. 4.5.5a: *M-H* curves of $Co_{70-x}Ni_xGa_{30}$ ($20 \leq x \leq 25$) alloys annealed at 1150 °C.

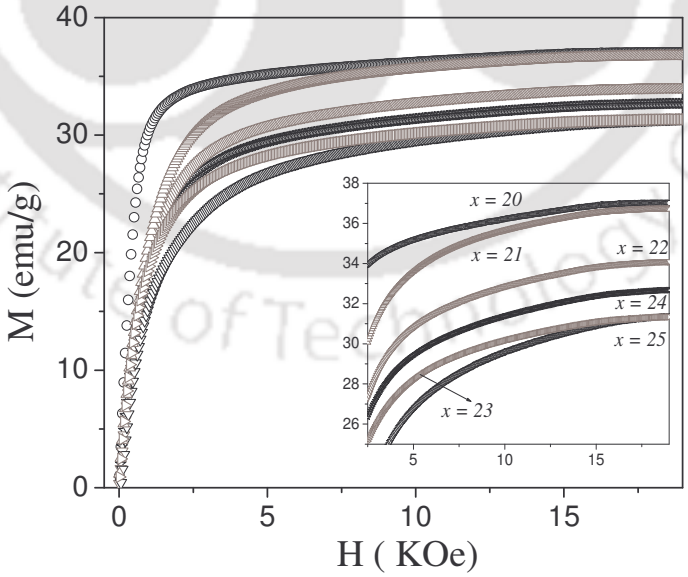

Fig. 4.5.5b: *M-H* curves of $Co_{70-x}Ni_xGa_{30}$ ($20 \leq x \leq 25$) alloys annealed at 1000 °C.

A higher magneto crystalline energy is required for a good FSMA. The anisotropy constants at room temperature have been estimated for these alloys from their *M-H* curve using law of approach to saturation (LAS).The equation used for non linear curve fit is

$$M(H) = M_{sat}[1 - \frac{b}{H^2}] \qquad (4.5.5a)$$

The saturation magnetization, co-efficient b and the K_{eff} estimated from it are listed in the Table 4.5.5a.

Table: 4.5.5.a: Magnetization and magneto crystalline anisotropy constants for $Co_{70-x}Ni_xGa_{30}$ ($20 \le x \le 25$) alloys obtained by quenching from 1150 °C.

Composition of Alloy (x)	$*M_{sat}$ (A-m^2/kg)	$*M_{sat}$ (A/m)	$** b \times 10^6$ (Oe)^2	$*** K_{eff} \times 10^5$ (J/m^3)
20	38.66 ± 0.01	332476	0.42 ± 0.03	0.4
21	37.14 ± 0.04	319404	5.04 ± 0.02	1.39
22	34.26 ± 0.01	294636	5.95 ± 0.03	1.39
23	31.94 ± 0.01	274684	5.84 ± 0.05	1.29
24	33.86 ± 0.01	291196	5.72 ± 0.03	1.34
25	30.96 ± 0.01	266256	4.82 ± 0.03	1.25

** emu/g ≅A-m^2/kg; M_{sat} is multiplied by corresponding density to obtain it in A/m.*

***Coefficient 'b' was estimated in Oe^2 and converted to A/m (1 Oe = $10^3/4\pi$ A/m)*

*** $K_{eff} = \sqrt{\frac{15b}{4}}\,\mu_0 M_{sat}$ [109] *for tetragonal structure.*

In order to minimize the demagnetization field, samples of very small cross sectional area (cylindrical sample with very small diameter) were placed perpendicular to the applied field during the experiment. Demagnetization field was also estimated for few samples from

the initial susceptibility (χ_{in}) of the initial magnetization curves. Demagnetizing factor (N_d) is expressed [128, 129] as,

$$N_d = 1/\chi_{in} = dH/dM \mid_{H=0} \qquad (4.5.5b)$$

The actual field (H_{ac}) inside the material can be obtained from the applied field from the relation,

$$H_{ac} = H_a - N_d M \qquad (4.5.5c)$$

These estimates showed that the difference in M_{sat} and K_{eff} values with and without demagnetization correction was very small.

Table 4.5.5b: Magnetization and magneto crystalline anisotropy constant of $Co_{70-x}Ni_xGa_{30}$ ($20 \leq x \leq 25$) alloys obtained by quenching from 1000 °C.

Composition of Alloy (x)	M_{sat} (A-m^2/kg)	M_{sat} (A/m)	$b \times 10^6$ (Oe)^2	$K_{eff} \times 10^5$ (J/m^3)
20	35.52 ± 0.01	305472	0.80 ± 0.03	0.52
21	35.72 ± 0.01	307192	2.33 ± 0.02	0.90
22	34.80 ± 0.01	299280	6.21 ± 0.03	1.44
23	32.32 ± 0.01	277780	6.56 ± 0.03	1.38
24	33.33 ± 0.01	286638	6.53 ± 0.02	1.42
25	31.95 ± 0.01	274684	6.18 ± 0.03	1.32

It was observed that M_{sat} was highest for the alloy with x = 20 (38.66 emu/g which corresponds to 1.72 μ_B / formula unit). Figure 4.5.5c shows the variation of M_{sat} with magnetic valence number (Z_m). M_{sat} of the alloy with x = 20 and 21 decreases with decrease in quenching temperature. When quenched from 1150°C, alloy with x = 20 exhibits austenite (cubic) structure, whereas, the alloy with x= 21 exhibits martensite structure. When quenched from 1000 °C, a secondary fcc (γ) phase developed along with the austenite (bcc,β) phase which causes some crystallographic disorder in the system. The decrease of saturation magnetization

may be due to the presence of γ-phase in β-matrix, which lowers the magnetic interaction between the atoms.

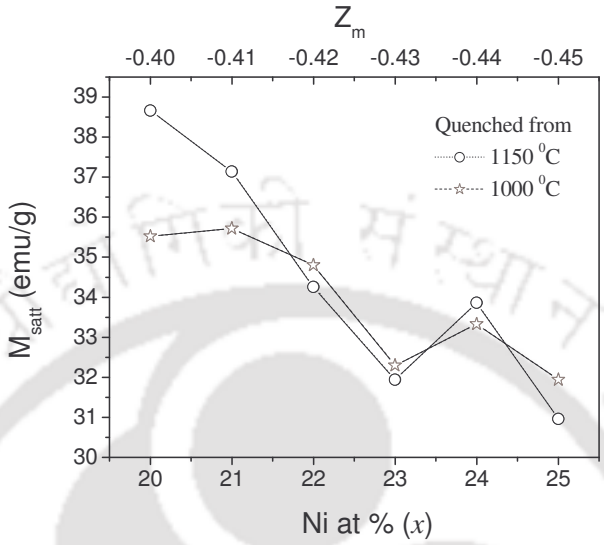

Fig. 4.5.5c: Variation of M_{sat} with Z_m for $Co_{70-x}Ni_xGa_{30}$ ($20 \leq x \leq 25$) alloys obtained by quenching from 1150 °C and 1000 °C.

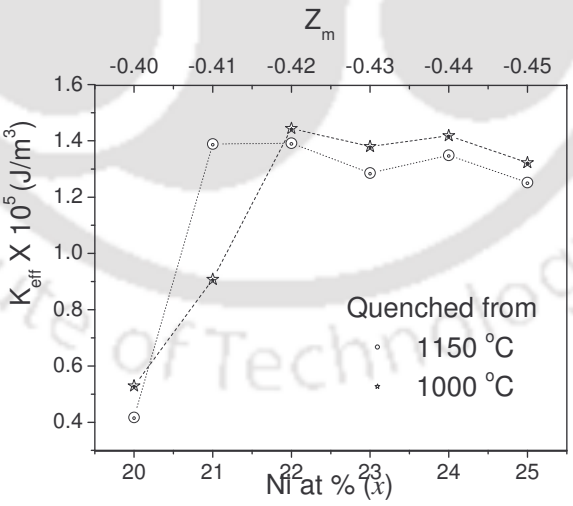

Fig. 4.5.5d: Variation of K_{eff} with Z_m for $Co_{70-x}Ni_xGa_{30}$ ($20 \leq x \leq 25$) alloys obtained by quenching from 1150 °C and 1000 °C.

K_{eff} is higher for the ferromagnetic martensite phase than the ferromagnetic austenite phase. The alloy with $x = 20$ quenched from 1150 °C and alloys with $x = 20, 21$ quenched from

1000 °C have the austenite phase at room temperature. Thus, K_{eff} for these alloys are much lower than that of the other alloys as shown in Fig. 4.5.5c. K_{eff} of polycrystalline $Ni_{49}Fe_{18}Ga_{27}Co_6$ alloy has been reported as 1.2×10^6 erg/cm^3 (M_{sat} = 40 emu/g) at 300 K [94]. K_{eff} estimated in the present studies are close to this value. The variation of M_{sat} and K_{eff} with different quenching temperatures for the alloy with x = 23 is presented in Fig. 4.5.5.d. Due to the increase in the amount of γ-phase (fcc) precipitates in the β matrix in samples quenched from lower temperatures, K_{eff} increases with decrease in quenching temperature. Since alloy melts near 1230 °C, homogenization at this molten state and subsequent quenching from this temperature into ice water results in smaller grains in the sample. Magnetic interaction enhances with smaller grain size and decreases with an increase in the amount of secondary phase.

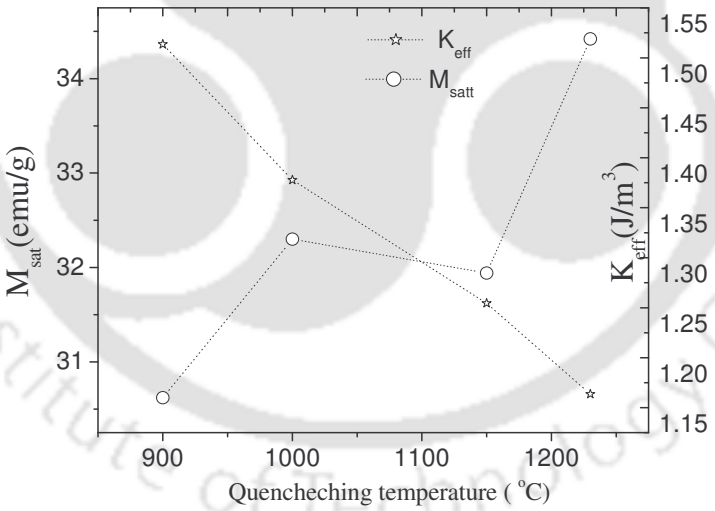

Fig. 4.5.5.e: Variation of K_{eff} and M_{sat} for $Co_{47}Ni_{23}Ga_{30}$ alloy quenched from different temperatures.

For the accurate determination of the Curie temperature from *M-T* curves curves, the applied field needs to be as low as possible. The task becomes tough especially when high magnetocaloric materials are involved. The Arrott plot is the most appropriate method for

determining the projected Curie temperature since this method is not susceptible to external factors such as influence of the applied magnetic field and thermal effects. Moreover, the critical constants corresponding to the ferromagnetic to paramagnetic transition can be determined from the modified Arrott plot. In order to obtain these plots, *M-H* data were recorded near T_C (= 100 °C in this case). The *M-H* isotherm for $Co_{45}Ni_{25}Ga_{30}$ alloy (annealed at 1000 °C) from 95 °C to 107 °C at an interval of 1 °C is shown in the Fig. 4.5.5f. Saturation of magnetization is not fully attained at this applied field. Such behavior also found in other compounds [116,117], is characteristic of the samples without true long-range order ferromagnetism. These data were used to determine the critical exponents β and γ corresponding to the exponents for the temperature dependence of the spontaneous magnetization (M_{sat}) and inverse initial susceptibility (χ_0^{-1}), respectively.

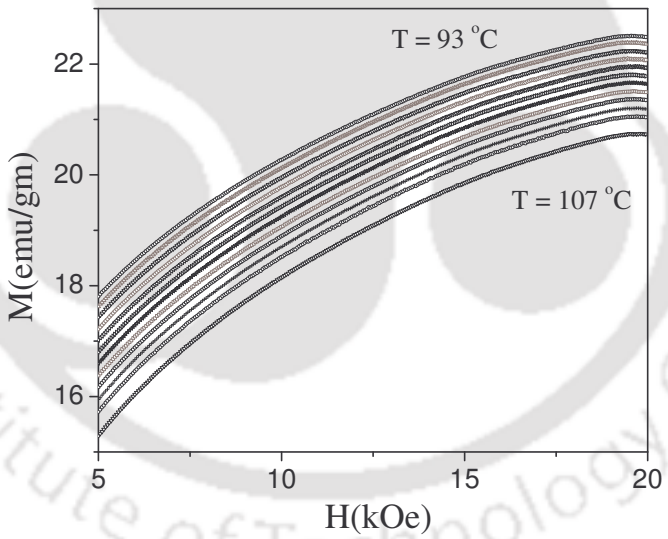

Fig.4.5.5f: *M-H* curves of $Co_{45}Ni_{25}Ga_{30}$ alloy (annealed at 1000 °C) taken near T_C. Only a truncated part of the graph is shown for the sake of clarity.

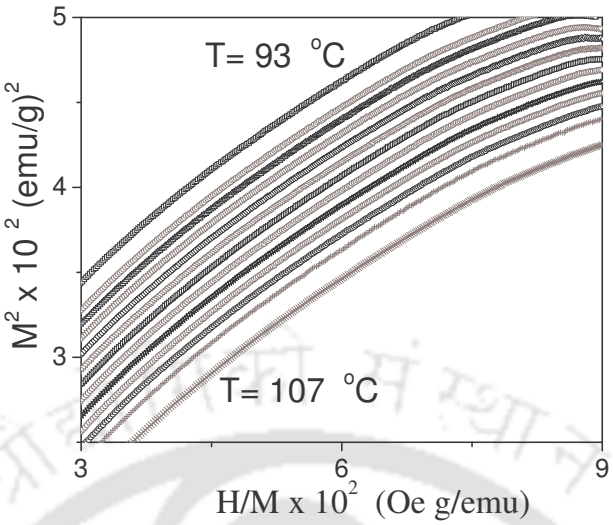

Fig. 4.5.5g: Arrott plot of $Co_{45}Ni_{25}Ga_{30}$ alloy near T_C.

As the first step in the process of obtaining accurate T_C, M^2 versus H/M plots were created from the data (Fig. 4.5.5g). The nonlinear curves obtained for the data close to the magnetic phase transition indicate that the mean field theory is not applicable to this data [113]. It is to be noted that a standard Arrott plot uses mean field theory exponents, $\gamma = 1$, $\beta = 0.5$ and $\delta = 3$, which are the characteristics of a system with long range interaction. Therefore, modified Arrott plots, i.e. $M^{1/\beta}$ versus $(H/M)^{1/\gamma}$ plots, which are based on Arrott-Noakes equation of state were obtained from the data. This modified Arrot [i.e., $M^{1/\beta}$ versus $(H / M)^{1/\gamma}$] plot with correct values of the exponents yields isotherms near the Curie temperature that are linear and parallel over a wide range of H/M values. Fig. 4.5.5h shows the $M^{1/\beta}$ versus $(H / M)^{1/\gamma}$ plots obtained for $Co_{45}Ni_{25}Ga_{30}$ alloy with optimized β and γ values. M_{sat} (0) was obtained from the positive y-intercept and χ_0^{-1} was obtained from the positive x-intercept of the above graph and the same are shown in Fig. 4.5.5i. The fitting equations used to obtain the plot are:

$$M_{sat}(0) = M_0(T_C - T)^{\beta} \; ; \quad T < T_C \tag{4.5.5d}$$

$$\chi_0^{-1} = (h/M_0)(T-T_C)^{\gamma} \quad ; \quad T > T_C \tag{4.5.5e}$$

where M_0 and h/M_0 are proportionality constants.

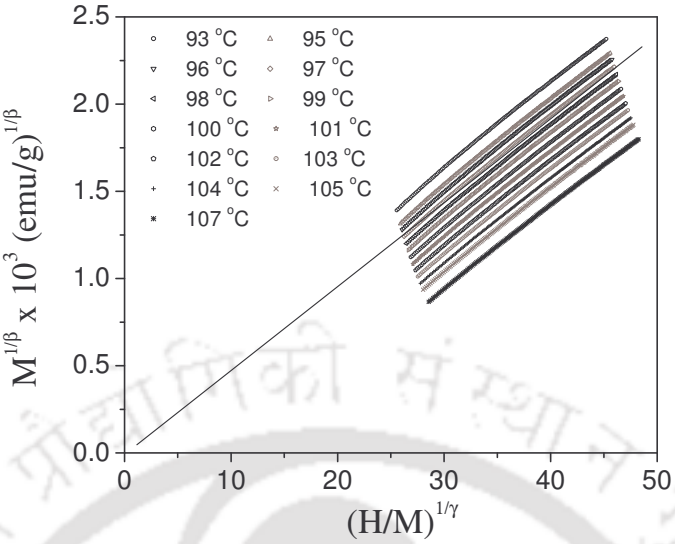

Fig. 4.5.5h: Modified Arrott [$M^{1/\beta}$ vs. $(H / M)^{1/\gamma}$] plot for $Co_{45}Ni_{25}Ga_{30}$ alloy. Data in the applied field range of 4 kOe ≤ H ≤ 15 kOe have been considered.

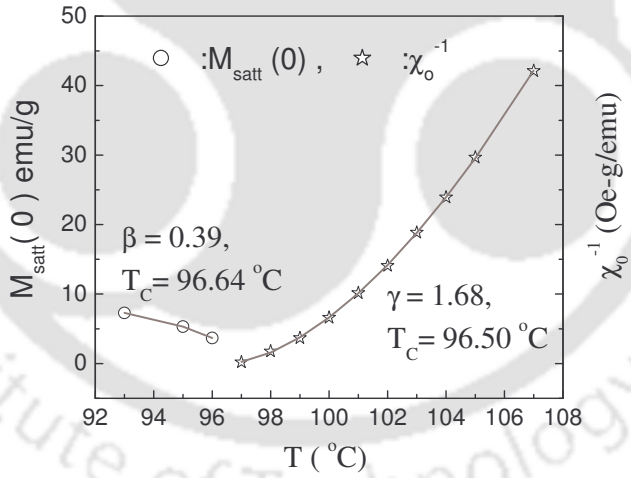

Fig. 4.5.5i: Variation of spontaneous magnetization and zero field inverse susceptibility with temperature close to T_C. Solid lines are least squares fit to eqn. (4.5.5d) and (4.5.5e), respectively.

T_C values obtained from nonlinear curve fitting are 96.50 °C and 96.64 °C, respectively. It can be seen that T_C obtained from both the fitting equations are reasonably close. The best (fitted) values of β and γ are 0.39 and 1.68, respectively. The critical constant δ was

determined from the scaling law, $\beta + \gamma = \beta\delta$, as 5.31. *M-H* data taken at 97 °C was plotted and fitted to the equation $M = C_1 H^{1/\delta}$ (where C_1 is proportionality constant) in order to extract the value of δ. This procedure yielded a value of 5.34 for δ, which is close to 5.31 obtained from the earlier method. The difference in δ is most likely due to the difference in the T_C used in the two procedures; the earlier was 96.57 °C (average of 96.50 °C and 96.64°C) and the latter was 97 °C. The critical exponents predicted by the 3-*d* Heisenberg model are $\beta = 0.367$, $\gamma = 1.388$ and $\delta = 4.78$ [130]. The values of the critical exponents depend on the range of exchange interaction *J(r)*. Fisher et.al [131] has performed a renormalization group analysis of systems with an exchange interaction of the form $J(r) = 1/r^{d+\sigma}$ (where *d* is the dimension of the system and σ is the range of interaction). If $\sigma > 2$, then Heisenberg exponents ($\beta = 0.365$, $\delta = 4.8$ and $\gamma = 1.386$) are valid. The mean field exponents ($\beta = 0.5$, $\delta = 3$ and $\gamma = 1$) are valid for $\sigma < ½$. There are no reports on the critical constants of FSMAs reported in the literature for comparison with our results. The critical constants estimated for $Fe_{29}Ni_{49}P_{14}B_6Si_2$ magnetic alloys ($\beta = 0.44$, $\delta = 5.25$ and $\gamma = 1.7$) [132] are very close to our estimated value for $Co_{45}Ni_{25}Ga_{30}$ alloy. For Ni, it has been found to be $\beta = 0.42$ $\gamma = 1.35$ and $\delta = 4.22$ [133]. Critical exponents estimated [116] for $La_{0.9}P_{0.1}MnO_3$ sample are $\beta = 0.498$, $\gamma = 1.456$ and $\delta = 3.92$ and it was concluded that at temperature below T_C the ferromagnetic (*FM*) order orientation of spin results in the β exponent being close to the value of the mean field theory. However, tenacious existence of the *FM* phase even above T_C has given rise to the γ-exponent value close to the 3-*d* short range isotropic Heisenberg model value. This conjecture is reasonable for unconventional ferromagnets where FM-PM transition is not sharp. The *FM-PM* transition of this present alloy is also not sharp (Fig.4.5.4b). The γ-exponent value estimated for the Co-Ni-Ga alloy is found to be higher than the value predicted by the Heisenberg 3-*d* model. Hence, it is proposed that the presence of *FM* phase above T_C might have caused the

shift of γ value toward the value which is higher than the one predicted by the Heisenberg 3-*d* model.

4.6. MECHANICAL PROPERTIES

It has been observed that the alloys under investigation annealed at 1150 °C have single phase structure and are brittle for machining. When they are annealed at 1000 °C, small amounts of the secondary (γ) phase precipitates in the martensite phase (β), thereby enhancing the ductility of the alloys. In order to obtain ductile $Co_{70-x}Ni_xGa_{30}$ ($20 \leq x \leq 25$) alloys, the respective homogenized alloys were molded in a copper cylinder to obtain cylindrical sample of diameter 7 mm and length ~ 11 to 15 mm. These samples were then annealed at 1000 °C for six hours and quenched in ice water so that sufficient amount of γ-phase precipitates in the β matrix. The martensitic transformation temperatures (A_s and M_s) and Curie temperature (T_C) of the alloys processed at 1000 °C are listed in the Table 4.6 in order to facilitate comparison. It may be noted that low temperature ACS and VSM were used for the determination of A_s and M_s for the alloy with composition x = 20 and 21, due to the limited low temperature range of the DSC. Suitable sizes of these samples obtained in the form of cylinders were used for mechanical testing.

Table 4.6: A_s, M_s and T_C of $Co_{70-x}Ni_xGa_{30}$ ($20 \leq x \leq 25$) alloys

Alloy composition (x)	25	24	23	22	21	20
A_s (°C)	145	119	79	40	-13*	- 43*
M_s (°C)	107	87	57	-6*	-38 *	-60*
T_C (°C)	100	107	92	105	121	139

* Data obtained using low temperature ACS

4.6.1 Microhardness (VHN)

Small discs of 7 mm diameter and 1mm thick were cut from the cylindrical samples, mounted on resin and polished for microhardness measurement. The results obtained from the Vickers microhardness measurement are listed in Table 4.6.1a. A typical indentation is shown in Fig. 4.6.1a as viewed under an optical microscope.

Table 4.6.1a: Microhardness of $Co_{70-x}Ni_xGa_{30}$ ($20 \leq x \leq 25$) alloys. Load applied for the indentation is 100gf

x	20	21	22	23	24	25	Steel ball*	Al bar *
VHN (GPa)	386	347	313	287	275	300	1770	167

*VHN of stainless steel ball bearing used in the rear wheel of Maruti 800^{TM} car and commercial aluminum bar are also listed in the table for the sake of comparison.

It has been observed that the VHN of the alloys are low as compared to stainless steel automobile ball bearing. But the alloys were almost twice harder than commercial aluminum. Thus, cutting, drilling or polishing can be done on these alloys with relative ease as compared to the same alloys processed at higher temperatures. It can be seen from the data presented in the table that the alloy with x = 20 exhibited the highest VHN and the alloy with x = 23 displayed the lowest VHN. Hardness for the alloy with x = 20 was measured for different indenter loads and the results obtained are listed in the Table 4.6.1b.

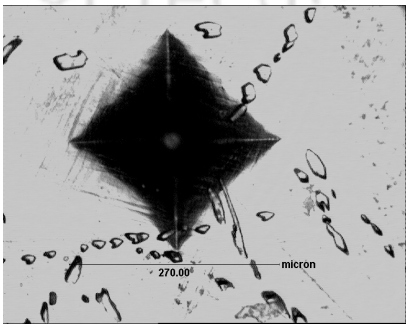

Fig. 4.6.1a: A typical pyramidal indentation obtained on Co-Ni-Ga alloy surface. The small spots seen in the optical micrographs are the γ-phase precipitates.

Table 4.6.1b: Microhardness of $Co_{50}Ni_{20}Ga_{30}$ alloy at different indentation load.

Indentation load (gf)	100	200	300	500	2000
VHN (GPa)	386	340	397	349	343

Yan *et al.* employed the dimensional analysis and the finite element approach to study the spherical indentation hardness of SMAs [77]. It has been observed by them that the indentation hardness increases with the maximum indentation depth. Therefore, they concluded that the measured indentation hardness cannot be treated as a material property of SMAs. It can be found from Table 4.6.1b that VHN of Co-Ni-Ga alloys does not depend on the applied load or indentation depth. Hence, systematic variation of the property can be expected in a series of FSMA which are subjected to identical loads. The highest VHN obtained for the alloy with x = 20 is due to the austenite (*bcc*) structure of this alloy. It can be observed from Table 4.6.1.b that the VHN decreases from its highest value for the alloy with x = 20 to the lowest value for the alloy with x = 24. An increase in VHN is observed for the alloy with x = 25. Although the VHN has a complicated dependence on the elastic moduli [119] of the material, it also provides a clue to the amount of γ-phase introduced into the β matrix. A careful comparison of the VHN of the alloys processed at different temperatures could provide a simple and indirect means of estimating the amount of γ-phase introduced into the β matrix during the processing stage.

4.6.2. Stress-strain behavior

To determine the mechanical strength of the alloys under investigation, samples of 7 mm diameter and 10.5 mm length were used for compression test in a servo hydraulic universal testing machine. Load was applied on the sample along its length till its mechanical failure point. Stress-strain (*S-S*) curves obtained from the compression test are shown as in Fig.4.6.2a.

It can be observed that alloys with x = 20 and 21, which are in the austenite phase (highest symmetry in crystal structure) have more ultimate compression strength than the alloys in martensite phase (lower symmetry crystal structure). J. Liu *et al.* [98] reported a very high compressive strength (2000 MPa) of $Co_{50}Ni_{22}Ga_{28}$ polycrystalline alloy as compared to our result for $Co_{50}Ni_{20}Ga_{30}$ alloy. The high compressive strength obtained by them may be due to the lower annealing temperature (900 °C) used and higher Ga content in their alloy. It is possible that the percentage of γ-phase is very high in their sample processed at 900 °C. Similar higher ultimate compressive strength (~1600MPa) has been reported [134] for samples near the stoichiometric composition and annealed at 800 and 900 °C. Since the MT peaks observed in DSC curves were very weak for the alloys annealed at lower temperature, SME is also expected to be low for these alloys. So, we did not investigate *S-S* behavior of alloys annealed lower than 1000 °C.

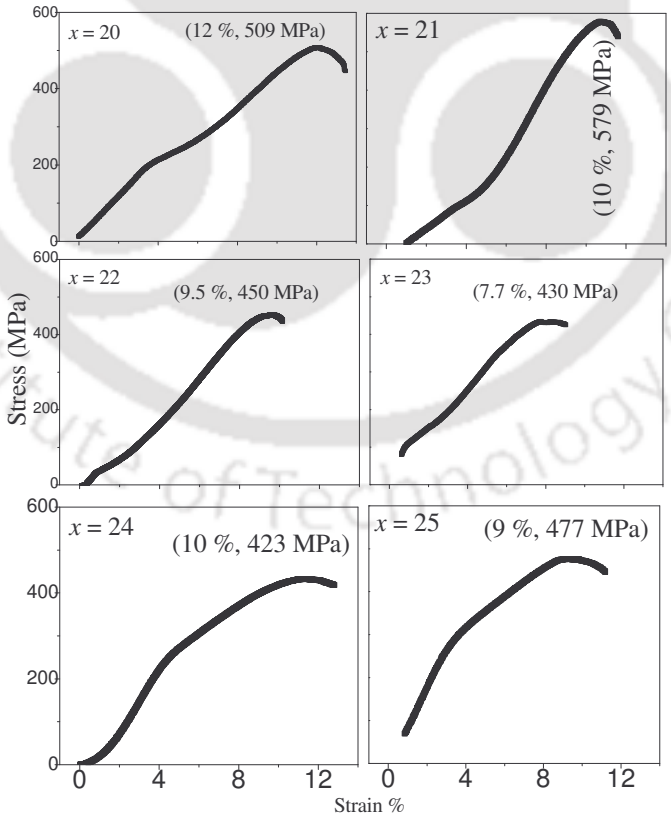

Fig. 4.6.2.a: Stress-Strain curve of $Co_{70-x}Ni_xGa_{30}$ ($20 \leq x \leq 25$) alloys obtained from compression test.

SME of the alloys was estimated by measuring the length of the sample before and after compression and then after the recovery of the residual strain after heating the load cycled alloy above the austenite finish temperature. The stress-strain data was recorded during compression loading and during the release of the load. The corresponding data are shown in Fig. 4.6.2b. The pre-strain (ε_p) value for ~ 200 MPa compressive load, residual strain (ε_r), strain recovery percentage (ε_{SME}) and the recovery ratio and strain permanently left with the samples (ε_{per}) are listed in Table 4.6.2

Table 4.6.2: Shape memory effect in $Co_{70-x}Ni_xGa_{30}$ ($20 \leq x \leq 25$).

x	ε_p %	Pressure(MPa)	ε_r %	ε_{SME} %	Recovery ratio	ε_{per} %
20	4.19	220	0	0	Super elastic	0
21	5.4	201	3	3.3	86.7	0.5
22	4.4	215	3	2	67.3	1
23	2.65	209	2	1	48.1	1
24	4.2	209	3	2	65.4	1
25	2.29	200	0.5	0	0	0.5

The alloy with x = 20 shows the pseudo elastic behavior i.e., after releasing the compressive load, it reverts back to the original length. This behavior is expected from this sample since the austenite finish temperature of this alloy is lower than room temperature. All the other alloys exhibited some residual strain after releasing the applied load (compression) and recovery of the length (ε_{SME} %) was observed for these alloys after heating them to temperatures above A_f. The alloy with x = 25 exhibited very small residual strain on application of 200 MPa pressure and the recovery of the length of the sample was also very small. This may be due to the higher A_s temperature of this alloy, requiring a higher applied pressure to induce SME in it.

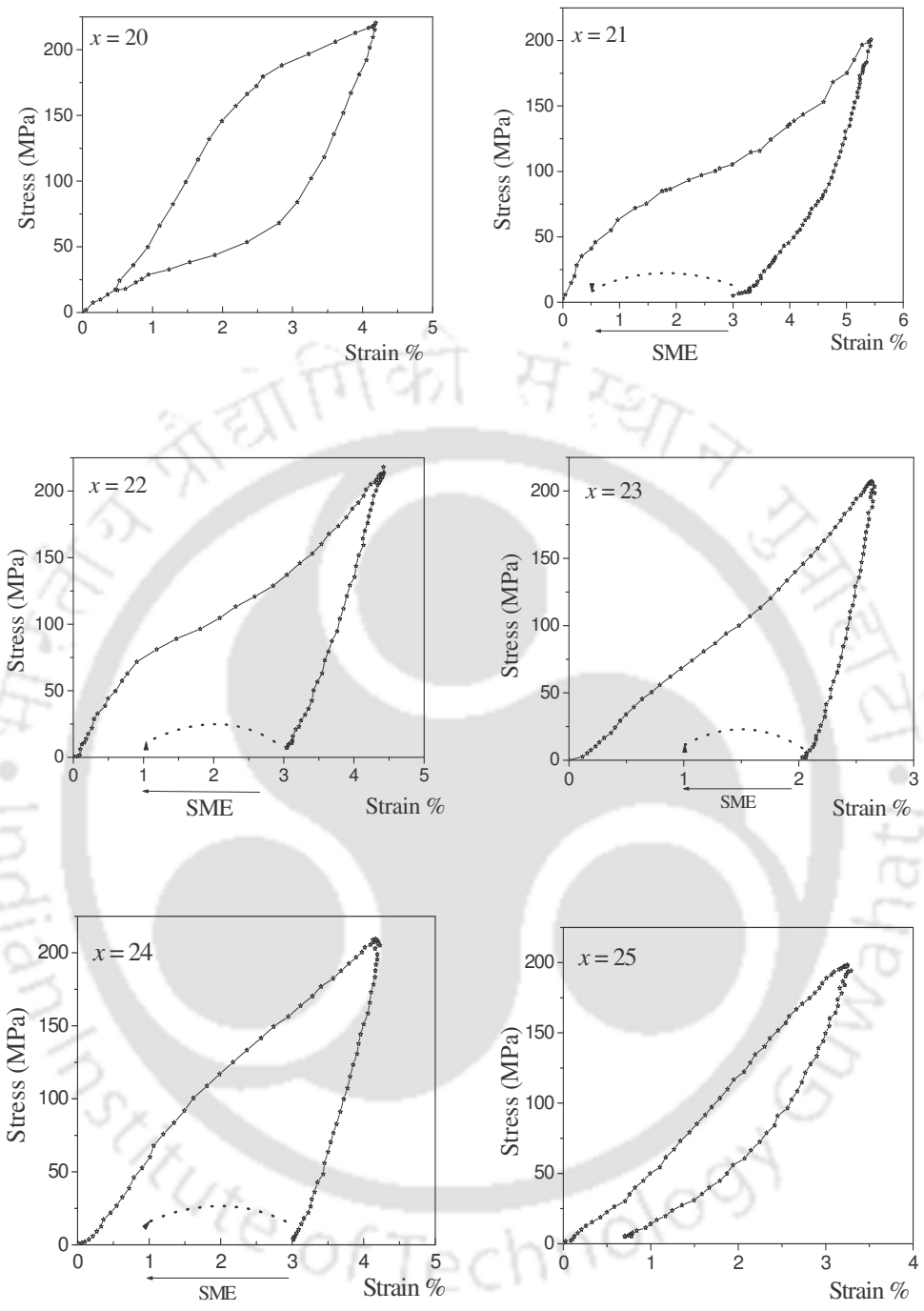

Fig. 4.6.2b: Shape memory effect of $Co_{70-x}Ni_xGa_{30}$ ($20 \leq x \leq 25$) alloys.

The pseudo elastic behavior of $Co_{49}Ni_{21}Ga_{30}$ single crystal has been observed by Dadda *et al.* [124] under compression with maximum recoverable pseudo-elastic strain of 4%. Chernwenko *et al.* [42] compressed $Co_{49}Ni_{22}Ga_{29}$ single crystal alloy to 200 MPa and after releasing the load, 3.7% residual strain was observed. A complete recovery of the residual

strain was observed after heating the sample above the austenite finish temperature (~ 360K). Y. Chumlyakov et al [134] observed 4.5 % shape memory effect at room temperature for $Co_{49}Ni_{21}Ga_{30}$ single crystal alloy. We observed 3.3 % shape memory effect with $Co_{49}Ni_{21}Ga_{30}$ polycrystalline alloy at room temperature after releasing the load (stressed to 200 MPa , ε_p = 5.4%). The smaller SME observed with our sample may be due to the polycrystalline nature of the alloy. A recovery of 86.7% residual strain on heating to a temperature above A_f has been observed for this sample.

4.7. SUMMARY

$Co_{70-x}Ni_xGa_{30}$ ($20 \leq x \leq 25$) alloys were processed under different conditions in order to understand the variation in the structure and properties of the alloys. Different processing conditions such as annealing temperature, quenching temperature and quenching rate were adopted. The alloys were structurally, thermally, magnetically and mechanically characterized. The highlights of the results obtained from these studies are listed below:

- All alloys, except the one with x =20, when quenched above 1150 °C, show single phase martensite (tetragonal) structure at room temperature.
- A secondary phase develops along with the primary martensite/austenite phase, when quenched below 1150 °C.
- The percentage of γ-phase precipitation increased with the decrease of quenching temperatures.
- All the alloys except the alloys with x = 20 and 21, exhibit MT above room temperature.
- M_s and A_s vary linearly with *e/a* ratio.
- M_s and A_s shift to lower temperatures with a decrease in quenching temperature.
- All the alloys are ferromagnetic at room temperature.
- T_C decreased with a decrease in quenching temperature.
- T_C was lower for samples prepared with higher cooling rate.

- The highest M_{sat} was observed in the alloy with x = 20 at 20 kOe. M_{sat} of this series of alloys was higher than that of $Co_xNi_{25}Ga_{75-x}$ alloys.
- K_{eff} estimated for these alloys in martensite phase are comparable to Ni-Mn-Ga alloy and $Ni_{49}Fe_{18}Ga_{27}Co_6$ alloys.
- K_{eff} increases with a decease in quenching temperature whereas, M_{sat} shows the opposite trend.
- Critical exponent β estimated near the magnetic phase transition in $Co_{45}Ni_{25}Ga_{30}$ alloy yielded a value close to the one predicted by the 3-*d* Heisenberg model. The γ-exponent's value was slightly higher than the value predicted by the model.
- The ultimate compressive strength of these alloys ranged from 423 to 579 MPa.
- The alloy with x = 20 exhibited perfect super-elastic behavior.
- Alloys with $x > 21$ showed shape memory effect. Residual strain of 3% was observed in the alloy with x = 21 after applying a strain of 5.4% (200 MPa) at room temperature. Recovery of strain due to SME has been observed for this sample is 4.2%; shape recovery percentage of this alloy has been observed as 86.7%.

INVESTIGATION ON $Co_{48-x}Ni_{22}Ga_{30-y}T_{x+y}$ (T = Fe, Mn and $x + y = 1$, 3 and 6) ALLOYS

It has been reported [135] that partial substitution of Mn by Fe in Ni-Mn-Ga alloy enhances the magnetic properties of the alloys. Fe substitution increases the Ni magnetic moment from the value of 0.33 μ_B [86] for the Heusler composition to 0.41 μ_B. The local magnetic moment of Mn in Ni-Mn-Ga alloy is very high compared to the other constituent elements. In this work, small amount of Fe or Mn has been substituted for Co and Ga in $Co_{48}Ni_{22}Ga_{30}$ alloy in order to change the magnetic and mechanical properties of the alloy. The e/a ratio decrease rapidly with the addition of Fe/Mn atom. From the results obtained in the last two chapters of this thesis, it is evident that the *e/a* has to be greater than 7.42 for ensuring that the *MT* occur above room temperature in Co-Ni-Ga alloys. This was kept in mind and substitution was done in such a way that e/a value was between 7.42 and 7.46 in the $Co_{48-x}Ni_{22}Ga_{30-y}T_{x+y}$ (T = Fe, Mn and $x + y = 1$, 3 and 6) alloys.

5.1. PREPARATION AND PROCESSING OF THE ALLOYS

The alloy ingot of each composition was prepared by arc melting method, as per procedures already outlined in chapter 2. Subsequently, the alloy ingots were cast in a cylindrical shape, annealed at 1150 °C and quenched in ice water. Alloys annealed at 1150 °C were found to be suitable for machining. Cylindrical shaped samples of ~10 mm diameter and ~ 7.5 mm length were cut out for compression testing. Samples of the same

diameter but smaller length were used for microhardness measurement. The composition of the master alloys was determined by SEM-EDS analysis as per procedure described in chapter 2. The EDS data presented are the mean of at least three independent observations. Table 5.1 shows the compositions of the starting and finally processed alloy samples.

Table 5.1: Compositions of various quaternary alloys obtained from EDS observations

Starting alloy compositions (at. %)					Composition.of the processed alloys (at.%)				
Co	Ni	Ga	Fe	Mn	Co	Ni	Ga	Fe	Mn
48	22	29	1	0	47.69	21.63	29.35	1.33	0
46	22	29	3	0	45.68	21.99	28.90	3.43	0
43	22	29	6	0	42.47	21.83	29.32	6.38	0
48	22	29	0	1	47.27	22.71	28.73	0	1.29
46	22	29	0	3	46.06	21.87	29.41	0	2.66
44	22	28	0	6	43.72	21.60	28.47	0	6.21

It can be seen from that data presented in Table 5.1 that the mean composition values of the processed alloys are very close to the starting compositions. These studies show that with the addition of the fourth element, Ni concentration reduces slightly, whereas, Ga concentration varied slightly. As a result, the *e/a* value decreases with respect to that of the starting composition. Here after, alloys substituted with 1 at.%, 3

at.% and 6 at.% Fe will be designated as Fe1, Fe3 and Fe6, respectively. Similarly, the Mn substituted alloys will be designated as Mn1, Mn3 and Mn6, respectively.

5.2. CRYSTAL STRUCTURE AND MICROSTRUCTURE

5.2.1. Crystal Structure

It was difficult of make fine powders of the processed alloys for XRD measurement due to their highly ductile nature. Thus, coarse powders of Fe1 and Mn1 samples, and polished plates of bulk Mn6 and Fe6 samples were used for recording the XRD patterns. XRD patterns of Fe1 and Mn6 alloys are shown in the Fig. 5.2.1.a and Fig. 5.2.1.b, respectively. It can be seen from the typical XRD patterns shown in the two figures that the quality of the data obtained is not suitable for Rietveld refinement. Hence, these XRD patterns were merely used to identify the phases present in various samples and no least squares refinement was attempted with the data. The XRD pattern of Fe1 alloy is similar to the unsubstituted parent $Co_{48}Ni_{22}Ga_{30}$ alloy (*cf.* Fig.5.2.1a) and could be indexed to *bct* structure (martensite phase). The peak near $2\theta = 51°$ indicates that some amount of γ- phase is present in both Fe1 and Mn1 alloys. In the case of Mn6 sample (Fig. 5.2.1b), one broad peak at $2\theta = 44°$ and one weak peak at $2\theta = 65°$ have been observed. XRD patterns recorded under slow scan near the Bragg peak at $2\theta = 44°$ is shown as inset in Fig. 5.2.1.b. The inset reveals the presence of two overlapping peaks at this 2θ value. These two peaks have been identified as $\gamma(111)$ and *A2* (110) when compared with the XRD data on $Co_{50}Ni_{20}Ga_{30}$ alloy (*cf.* Fig.4.2.1e). Similarly, the peak at $2\theta = 65°$ has been assigned to *A2* (200) plane.

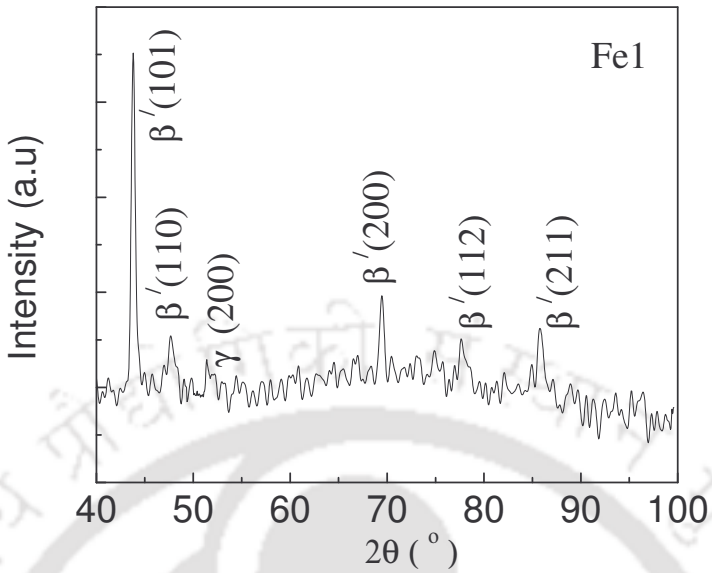

Fig. 5.2.1.a: XRD pattern of Fe1 alloy

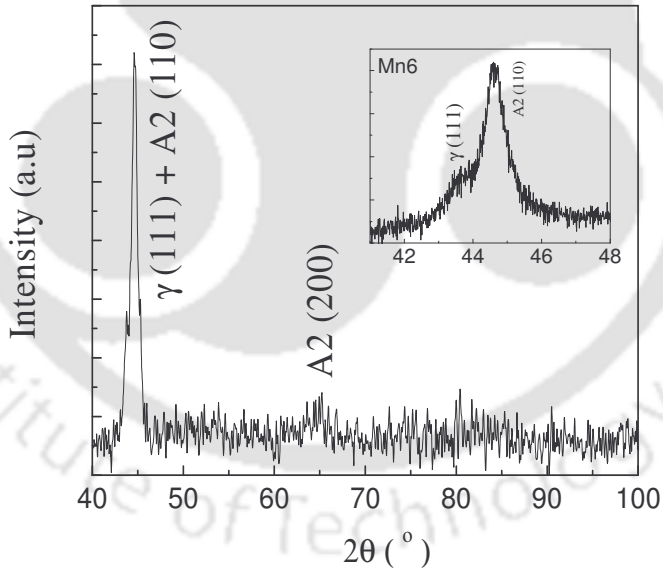

Fig. 5.2.1.b: XRD pattern of Mn6 alloy

Thus, the XRD studies on the quaternary alloy samples established that Fe1 and Mn1 alloys have martensite structure at room temperature, whereas, the rest, *viz*., Fe3,

Mn3, Fe6 and Mn6 alloys have austenite structure at room temperature. All the alloys contained small amount of γ-phase precipitates. The presence of the γ-phase has resulted in the high ductility of the samples. The presence of the γ-phase precipitates in all the alloys clearly shows that the alloys have to be processed at temperatures higher than 1150 °C for preventing the precipitation of the additional phase.

5.2.2. Microstructure

Optical micrographs of the quaternary alloys are shown in Fig.5.2.2.a-f. Micrographs of Fe1 and Mn1 alloys contained all the features of parent alloy of (Fig. 4.2.1.a) with one difference, *viz*., the additional presence of the white (γ-phase). It is interesting to note that addition of just 1 at.% of Fe/Mn to Co-Ni-Ga can induce γ-phase precipitat ion in this series of alloys. This merely confirms that the structure and properties of Co-Ni-Ga FSMAs are strongly influenced even by a small compositional and constituent variation. The twins present in the micrographs (Fig. 5.2.2.a & d) are the characteristics of the martensite phase. In the micrographs of Fe3 and Mn3 alloys, the secondary γ- phase is present along with the primary phase. But no twins are visible in these micrograph which means that the martensitic transformation temperatures of Fe3 and Mn3 are lower than room temperature. Thus, the optical micrographs of Fe3, Fe6, Mn3 and Mn6 alloys provide visual confirmation of the austenite structure revealed by XRD studies.

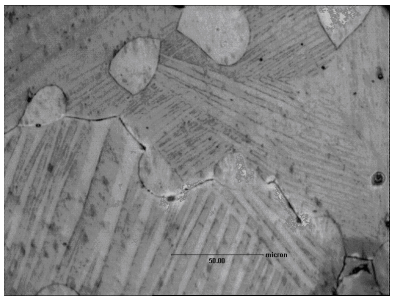

(a) Fe1; Full Scale bar represents 50µm

(d) Mn1; Full Scale bar represents 50µm

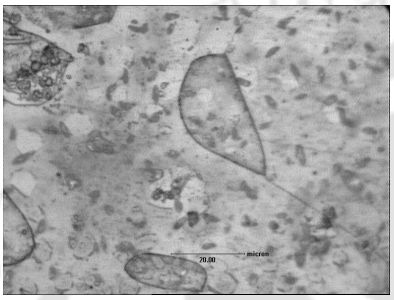

(b) Fe3; Full Scale bar represents 20 µm.

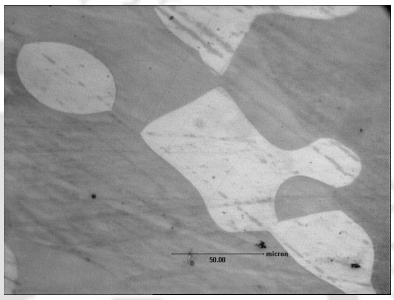

(e) Mn3; Full Scale bar represents 50 µm.

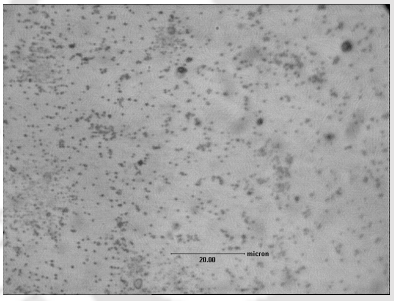

(c) Fe6 Full Scale bar represents 20µm.

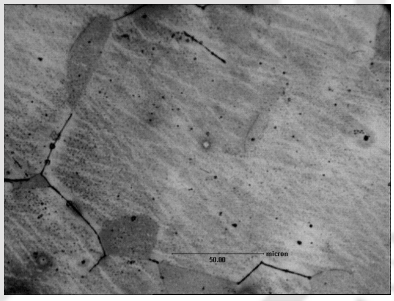

(f)Mn6; Full Scale bar represents 50 µm.

Fig. 5.2.2: Optical micrographs of (a) Fe1, (b) Fe3, (c) Fe6, (d) Mn1 (e) Mn3, and (d) Mn6 alloys. Thick dark lines and dark spots in (d) represent minor cracks and porosities present in the sample.

5.3. THERMAL CHARCTERIZATION

DSC curves obtained for Fe1 and Mn1 alloys are shown in Fig.5.3. The DSC curve of the parent alloy is also shown in the figure for comparison. Fig. 5.3 shows that Fe1 and Mn1

alloys have martensitic transformation (MT) temperatures above room temperature. DSC curves of Fe3, Fe6, Mn3 and Mn6 alloys recorded above room temperature did not show any endothermic peak on the heating cycle, which confirmed that the MT of Fe3, Fe6, Mn3 and Mn6 alloys is below room temperature. The same was confirmed by low temperature magnetization measurements (since the working range of the available DSC was from room temperature to 660 ˚C). It is evident from the DSC results that addition of Fe / Mn shifts the MT temperatures to higher temperature. However the shift caused by Mn addition is less than Fe addition. The DSC peaks of Fe1 and Mn1 alloys are wide and spread over a wide temperature range. This is the signature of existence of other phase(s) along with the martensite phase. XRD and optical microscopy studies have already confirmed the presence of γ-phase along with the martensite phase in these alloys. The MT temperatures of Fe1 and Mn1 determined from the DSC curves are listed in Table 5.3.

Table 5.3: Martensitic transformation temperature of Fe1 and Mn1 alloys

Composition of alloy	e/a	A_s (°C)	A_f (°C)	M_s (°C)	M_f (°C)
Parent alloy ($Co_{48}Ni_{22}Ga_{30}$)	7.42	78	81	37	35
Fe1	7.44*	91	120	57	40
Mn1	7.44*	86	111	78	50

* *e/a* ratio is calculated from the composition obtained from EDS measurements.

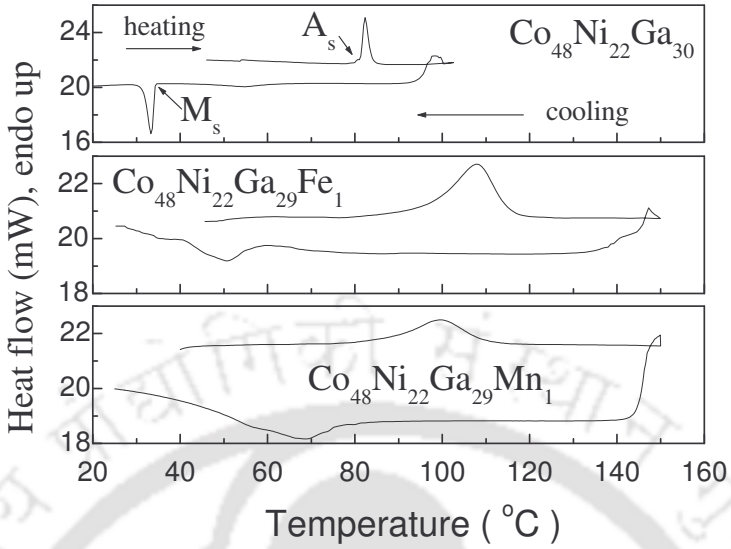

Fig. 5.3. DSC curves of Mn1, Fe1 and the parent alloy.

The *e/a* ratio of Fe3, Fe6, Mn3 and Mn6 calculated from the compositions determined from EDS measurement are 7.43, 7.39, 7.40 and 7.38, respectively. Hence, MT temperatures of these alloys must be lower than Fe1 and Mn1 alloys. Substitution of Ga (instead of Co) with Mn/Fe would yield alloys with higher e/a ratio which would have MT higher than room temperature. In the previous chapter, it was seen that the alloy with e/a = 7.43, yields A_s = 111 °C and M_s = 69 °C. In the case of Fe3, e/a = 7.43, A_s has been found as 12 °C (from low temperature magnetization measurement as shown in Fig.5.5.1.a below). This shows that though the MT temperatures vary linearly with e/a for SMAs, the slope of the *e/a* versus M_s or *e/a* versus A_s plots are different for different sets of SMAs. Similar observations have been made by Krenke et al [63] with respect to different Ni-Mn based Heusler alloys.

5.4. MASS DENSITY

Density of the quaternary alloys is listed in Table 5.4. Density decreases with an increase in Fe/Mn at%. This composition dependence of density is due to the relatively smaller mass density of the substituting atoms Fe (7.87 g/cm^3) and Mn (7.4 g/cm^3) as compared to that of Co.

Table 5.4: Mass Density of Fe1, Mn1, Fe3, Mn3, Fe6 and Mn6 alloys

Alloy sample	Measured density ρ_A (g/cm^3)	Alloy sample	Measured density ρ_A (g/cm^3)
Fe1	8.603 ± 0.004	Mn1	8.596 ± 0.004
Fe3	8.378 ± 0.004	Mn3	8.298 ± 0.004
Fe6	8.108 ± 0.004	Mn6	8.142 ± 0.004

5.5. MAGNETIC PROPERTIES

5.5.1 Variation of magnetization with temperature (M-T) at low temperatures

DSC curves of Fe3, Mn3, Fe6 and Mn6 recorded from room temperature onwards did not show any signature of the martensitic transformation (*MT*) in these alloys. In order to locate the *MT* in these alloys, magnetization measurements were performed on these samples from 100 K to 300 K (on the heating cycle) at a constant applied field of 50 Oe. The *M-T* curves for the Fe and Mn alloys are shown in Fig. 5.5.1.a and Fig. 5.5.1.b, respectively. Austenite phase has higher magnetocrystalline anisotropy than the martensite phase. Thus, an increase in magnetization is observed during reverse martensitic transformation as depicted in Fig. 5.5.1.a and Fig. 5.5.1.b.

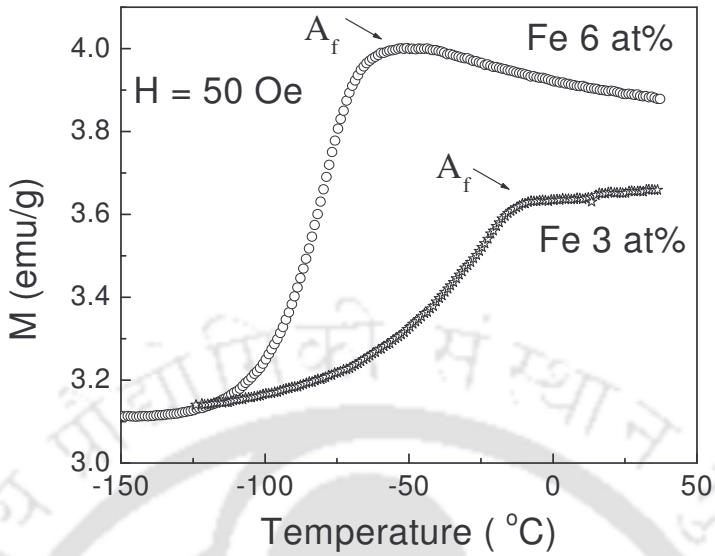

Fig. 5.5.1.a:. M-T graph of Fe3 and Fe6 alloy

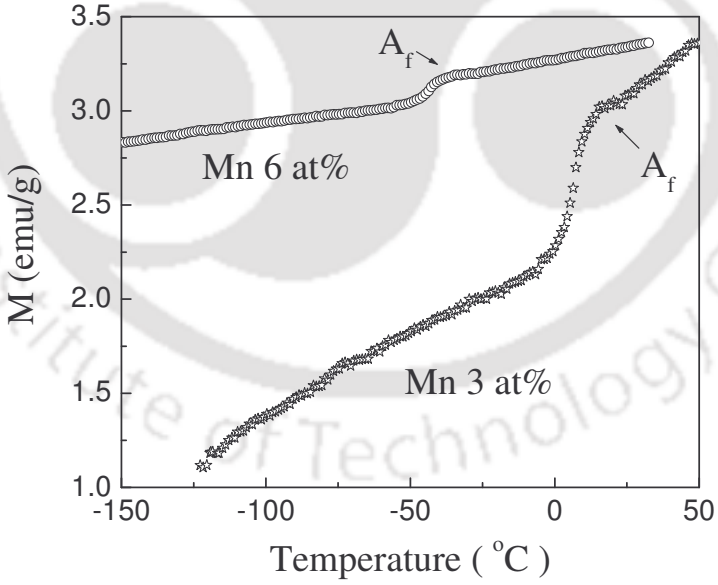

Fig. 5.5.1.b: M -T graph of Mn3 and Mn6 alloys.

The increase in magnetization at the structural transitions is not very sharp for all the samples. This gentle increase in magnetization conveys the same information as the broad peaks observed in the DSC curves of Fe1 and Mn1 samples (Fig. 5.3), namely, the presence of the additional phase along with the primary phase in these alloys. Due this broad nature of the reverse maternsitic transformation, we have estimated only the austenite finish temperature A_f from this data. A_f for Mn3, Fe3, Mn6 and Fe6 measured from the *M-T* graphs are 15 °C, -10 °C, -40 °C and -59 °C, respectively.

5.5.2 Variation of magnetization with temperature (M-T) at high temperatures

All the alloys were ferromagnetic at room temperature. In order to determine the Curie temperature of the alloys, *M-T* measurements were carried out from room temperature onwards under a constant applied field of 50 Oe. *M-T* plots of Fe1, Fe3, Fe6 and Mn1, Mn3, Mn6 alloys are shown in Fig. 5.5.2.a and Fig. 5.5.2.b, respectively. T_C estimated from the local minimum point in the *dM/dT vs. T* plots and listed in Table 5.5.2.

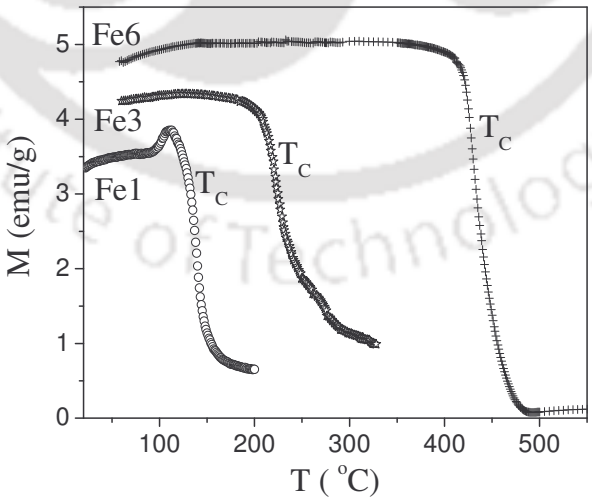

Fig. 5.5.2a: Variation of magnetization with temperature of Fe1, Fe3 and Fe6 alloys

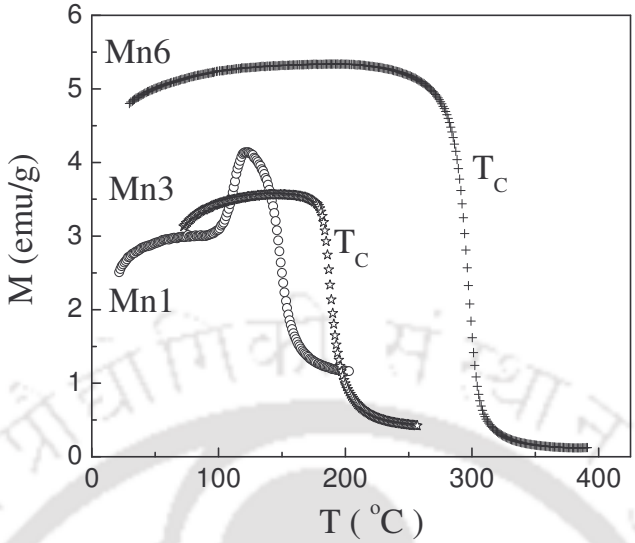

Fig. 5.5.2b: Variation of magnetization with temperature of Mn1, Mn3 and Mn6 alloys.

Table 5.5.2: Curie temperature (T_C) of Fe1, Mn1, Fe3, Mn3, Fe6 and Mn6 alloys

Alloy	T_C (°C)	Z_m	Alloy	T_C (°C)	Z_m
Fe1	139	-0.37	Mn1	141	-0.36
Fe3	219	-0.35	Mn3	185	-0.32
Fe6	428	-0.32	Mn6	288	-0.22

It has been observed that T_C of the quateranry samples are higher than the T_C of $Co_{48}Ni_{22}Ga_{30}$ (T_C = 126 °C). This increase in T_C may be attributed to the high magnetic moments of Fe and Mn [135]. Wu *et.al* [86] have reported that $Ni_{52}Mn_{16}Fe_8Ga_{24}$ has a higher T_C (381 K) than $Ni_{52}Mn_{24}Ga_{24}$ (348K). Substitution of Fe for Mn strengthens the magnetic exchange interactions, thereby increasing the Curie temperature to 381 K. It can be seen from Table 5.5.2 that T_C increases with the increase of Fe/Mn concentration. This

is expected as the magnetic valence number increases with the increase in Fe/Mn concentration. However, Z_m for Mn3 and Mn6 are higher than Fe3 and Fe6, respectively. Thus T_C of Mn3 should be higher than Fe3, and that of Mn6 should higher than Fe6. The opposite behavior observed in this study may be due to the antiferromagnetic alignment of the moments of neigbouring Mn atoms. It has also been pointed out [74] that magnetization of Mn alloys obeys the Slater-Pauling curve only for very dilute concentrations of Mn, which helps us in re-concluding the above results.

5.5.3. Variation of magnetization with field (M-H) at room temperature

The *M-H* data recorded at room temperature for the alloys under investigation are shown as in Fig. 5.5.3.a and Fig. 5.5.3.b. Magnetization increases with an increase of Fe/Mn concentration due to the higher magnetic moments of the Fe or Mn atoms as compared to that of Co and Ga atoms. The saturation magnetization (M_{sat}) of Fe1 was found to be 48 emu/g, corresponding to the magnetic moment 2.12 μ_B per formula unit and that of Mn1 has been observed to be 39 emu/g, corresponding to 1.73 μ_B per formula unit (*cf.* Table 5.5.3). However, Fe6 and Mn6 samples were found to have the same magnetic moment of 2.44 μ_B per formula unit. Room temperature M_{sat} of polycrystalline $Ni_{50}Mn_{30}Ga_{20}$ at an applied field of 20 kOe has been reported as 52.1 emu/g [122]. A comparison will show that Co-Ni-Ga with Fe/Mn substitution can yield alloys with M_{sat} values comparable with the prototype Ni-Mn-Ga alloy. K_{eff} was estimated for each alloy using law of approach to saturation. M_{sat} and K_{eff} estimated for the quaternary alloys are listed in Table 5.5.3. K_{eff} of polycrystalline $Ni_{50}Mn_{30}Ga_{20}$ at room temperature has been reported [122] to be 1.01×10^5 J/m^3. .

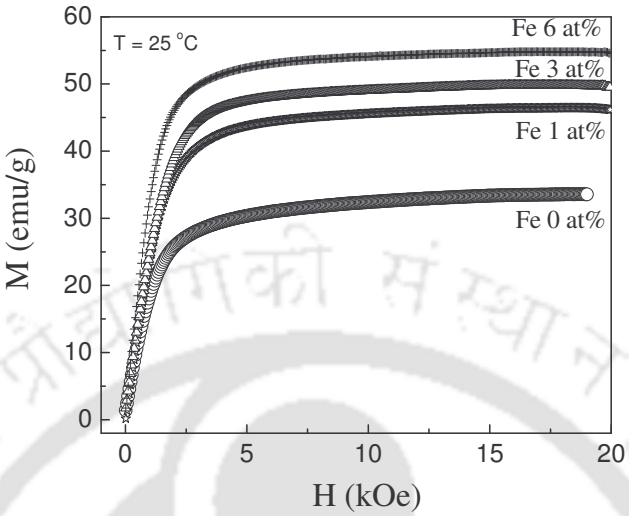

Fig. 5.5.3a: Room temperature *M-H* plots of $Co_{48}Ni_{22}Ga_{30}$ (Fe0), Fe1, Fe3 and Fe6 alloys.

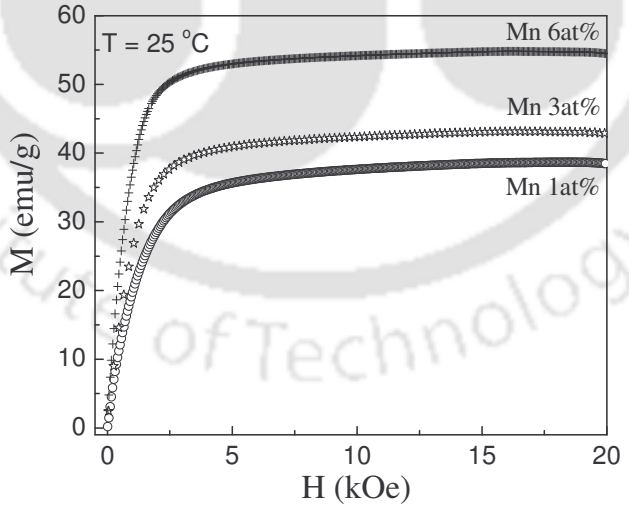

Fig. 5.5.3b: Variation of magnetization with applied field of Mn1, Mn3 and Mn6 alloys.

Table 5.5.3: M_{sat} and K_{eff} of Fe1, Mn1, Fe3, Mn3, Fe6 and Mn6 alloys

alloy	M_{sat} (Am^2/kg)	K_{eff} x 10^5 (J/m^3)	alloy	M_{sat} (Am^2/kg)	K_{eff} x 10^5 (J/m^3)
Fe1	47.82	1.28	Mn1	39.10	1.25
Fe3	50.14	1.20	Mn3	43.63	1.04
Fe6	55.10	1.16	Mn6	55.12	1.13

** emu/g ≅A-m^2/kg; M_{satt} is multiplied by corresponding density to obtain it in A/m.*

Density values of the alloys are listed in Table5.4

*** the coefficient 'b' was estimated in $(Oe)^2$ and converted to A/m (1 Oe = $10^3/4\pi$ A/m)*

*** $K_{eff} = \sqrt{\frac{15b}{4}}\,\mu_0 M_{sat}$ [109] *for tetragonal structure.*

5.6 MECHANICAL PROPERTIES

5.6.1 Microhardness (VHN)

The results obtained from microhardness measurement on the quaternary alloys are listed in Table 5.6.1. It is seen that microhardness (VHN) increases with an increase in the concentration of Fe/Mn. The soft martensite primary phase in Fe1 and Mn1 alloy is expected to exhibit lower hardness as compared to the cubic austenite phase alloys. The increased hardness of the alloys with higher Fe/Mn also shows that the amount of γ-phase decreases as the Fe/Mn concentration is increased. Liu et.al [98] has reported a gradual disappearance of γ-phase with an increase in Fe concentration in $Co_{50}Ni_{22-x}Ga_{28}Fe_x$ alloys.

It has to be pointed out that high VHN is a not desirable attribute for a good shape memory alloy.

Table 5.6.1: Microhardness of Fe1, Fe3, Fe6, Mn1, Mn3 and Mn6 alloys. Load applied for the indentation is 100 gf in all the cases.

x ⟶	Fe1	Fe3	Fe6	Mn1	Mn3	Mn6
VHN (GPa)	312	384	439	308	360	409

5.6.2 Compressive strength

Alloys of cylindrical shape (~10 mm diameter and 7.5mm length) with flat ends were used for the tests. Compressive stress was applied vertically in a UTM till failure. The stress-strain curves of Fe1, Mn1, Fe3, Mn3, Fe6 and Mn6 alloys are shown in Fig.5.6.2. It can be seen from Fig. 5.6.2 that Mn addition yields higher compressive strength than Fe addition. The mechanical strength of Mn6 alloy was so high that even for 1200 MPa load (~80 kN force), it could not be cracked. Mn3 alloy has been found to have the highest strain before failure. A very high compressive strength (~2000 MPa) and corresponding strain (~20 %) has been reported for $Co_{50}Ni_{21}Ga_{28}Fe_1$ alloy [98]. We observed a similar strain at very low compressive stress in Mn1 and Mn3 samples. The high compressive strength reported in $Co_{50}Ni_{21}Ga_{28}Fe_1$ alloy may be due to the low annealing and quenching temperature (900 °C) used to prepare the alloy. The strain exhibited by Fe1, Mn1, Fe3 and Mn3 for 400 MPa stress are 7.8%, 6.7%,, 8.8% and 6.9%, respectively. But strain exhibited by Fe6 and Mn6 alloys is very low (4% and 3.5%, respectively). Thus, addition of Fe or Mn beyong 3 at% will not help to enhancing the SME of these alloys.

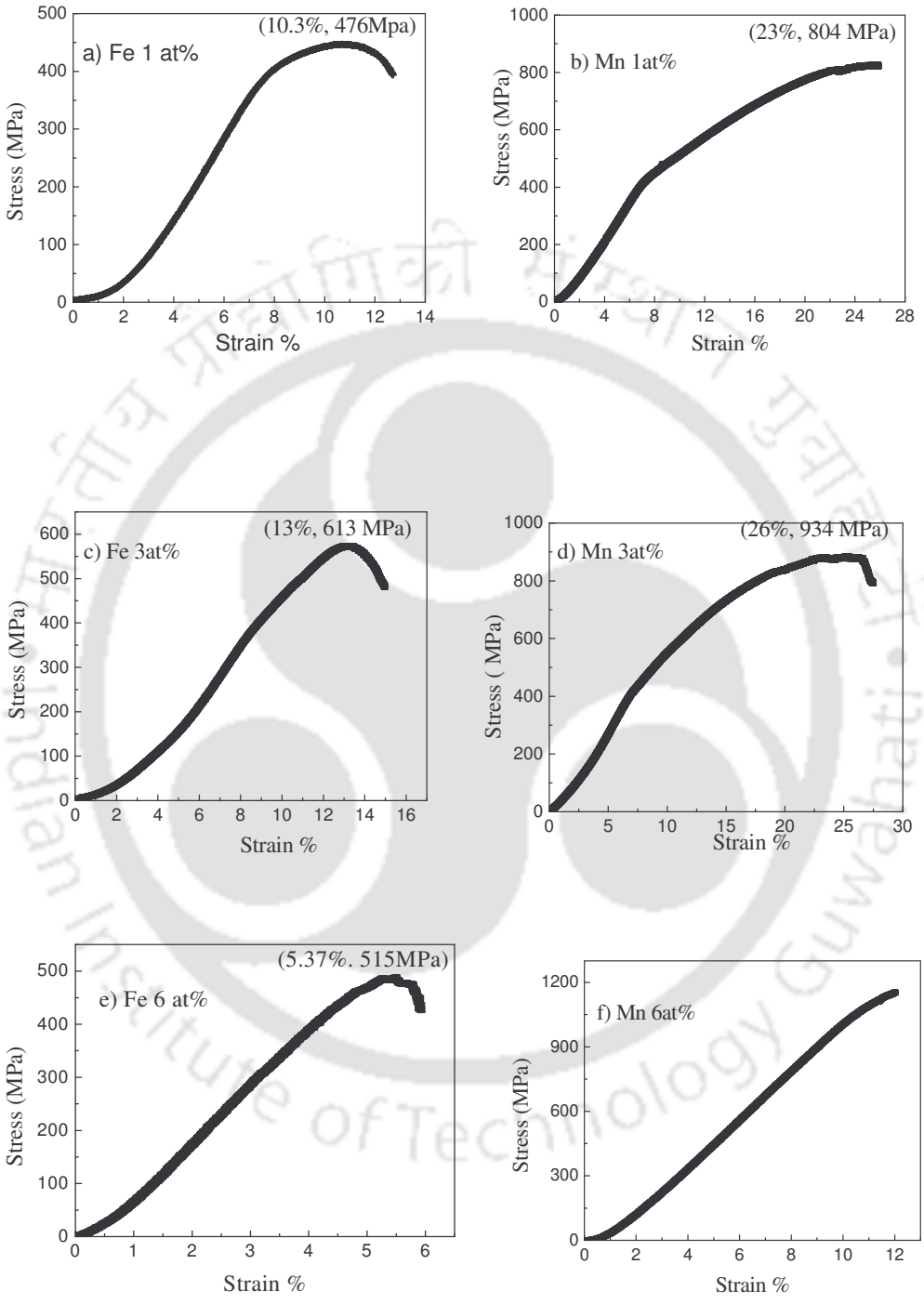

Fig.5.6.2: Compressive strength of (a) Fe1, (b) Mn1, (c) Fe3, (d) Mn3, (e) Fe6, and (f) Mn6 alloys

5.6.3. Shape memory effect and pseudo-elasticity

Stress-strain data of the alloys recorded during loading (to ~ 400 MPa) and unloading cycles are shown in Fig. 5.6.3.a-f. SME was estimated from the recovery of the residual strain by heating the sample above A_f after one cycle of loading and unloading. The pre-strain (ε_p %) due to loading, residual strain (ε_r %), shape memory effect (ε_{SME} %), recovery ratio due to heating and permanent strain (ε_{per} %) left on the sample determined from experiments are listed in Table 5.6.3. Residual strain and ε_{SME} % for the parent (*i.e.* $Co_{48}Ni_{22}Ga_{30}$) alloy is also listed again to facilitate comparison. The alloys Fe1 and Mn1 show SME% of 1.9% with recovery ratio of almost 60. The Fe3 and Mn3 alloys exhibit comparatively smaller SME% but recovery ratio is 100. Thus, it can be inferred that Fe3 and Mn3 behave more like psudo-elastic materials. No residual strain was observed for Fe6 and Mn6 alloys and hence they have pseudo–elastic behavior.

Table 5.6.3: Shape memory effect in Fe1, Fe3, Mn1 and Mn3 alloys.

alloy	ε_p %	Stress (MPa)	ε_r %	ε_{SME} %	Recovery ratio	ε_{per} %
Parent	4.4	215	3.0	2.0	67.3	1
Fe1	8.8	445	3.0	1.9	60	1.2
Mn1	7.39	417	3 .6	2.2	59.2	1.5
Fe3	7.1	354	1.6	1.6	100	0
Mn3	8.9	423	1.9	1.9	100	0

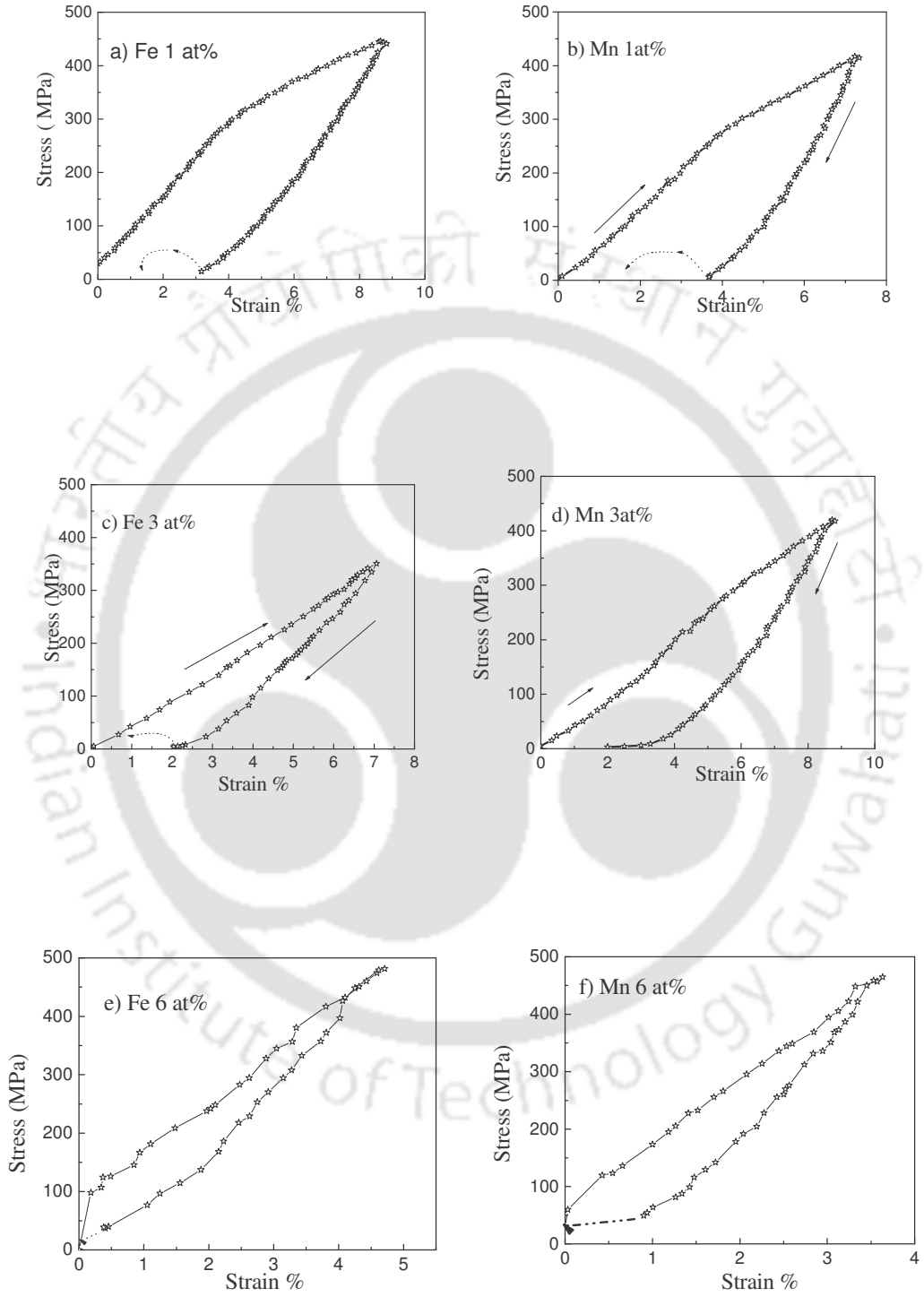

Fig. 5.6.3: Shape memory and pseudo-elastic of Fe_x and Mn_x (x = 1, 3, and 6) alloys.

The ε_{SME} % reported for $Co_{49}Ni_{21}Ga_{30}$ single crystal was 4.9% to 6.7% [134], for Ni-Mn-Ga was 2.8% to 6.1% [57] and for Ni-Fe-Ga was 5.1% to 8.1% [57]. The ε_{SME} % values obtained in the present samples are much lower than the reported values on other FSMAs. The low ε_{SME} % obtained in the current investigations may be attributed to the polycrystalline nature of the alloys.

5.6.4 Magnetic Field Induced Strain (MFIS)

Magnetic field induced strain (MFIS) measurement at room temperature was carried out without the application of any mechanical load. Samples of disc shape with diameter ~ 10 mm and length ~ 3 mm were used for the measurement. MFIS measurements were performed on four samples, out of which two are in the martesite phase (Fe1 and Mn1) and the two are in austenite phase (Fe3 and Mn 3). MFIS was measured for the samples as a function of magnetic field using the MFIS set-up described in chapter 2. In each measurement, magnetic field was raised up to 5000 G and then lowered back to zero. The results are shown as in Fig. 5.6.4. The graphs show that the strain% increases as a function of magnetic field and attains the maximum value near 5 kG. For the unsubstituted sample MFIS was found to be very small (~ 0.0035% at B = 5 kG). With the addition of Fe/Mn, the maximum MFIS increased to 0.012 % (for Fe3), and 0.011% (for Mn3).

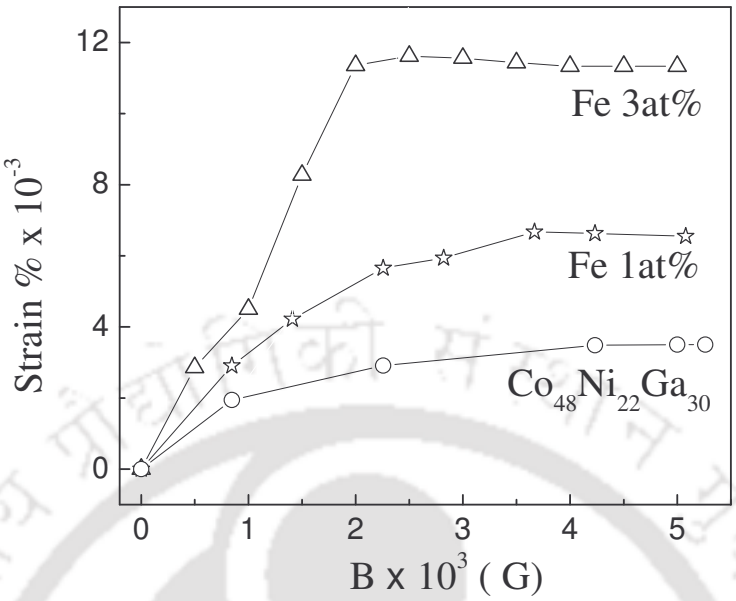

Fig. 5.6.4a: MFIS of $Co_{48}Ni_{22}Ga_{30}$, Fe1 and Fe3

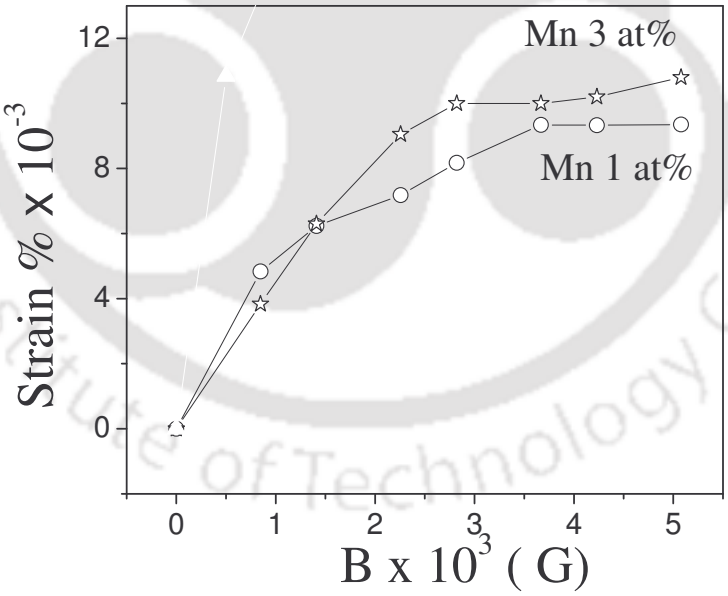

Fig. 5.6.4b: MFIS of Mn1, Mn3 and Mn6 alloys

MFIS of ~ 0.19% has been reported in unstressed single crystals of Ni_2MnGa with magnetic fields of 8 kG applied at 265 K [23], whereas in Fe_3Pt FSMA, MFIS of 0.6%

has been reported at 4.2K [43]. MFIS in polycrystalline samples was much smaller than that observed in single crystal samples. Soonjong Jeong *et. al*. [80] observed MFIS in $Ni_{19.5}Mn_{27}Ga$ polycrystalline alloys at different temperatures. They obtained maximum MFIS of 0.01% at ~ 37˚C under 1 kG applied magnetic field in the martensite phase. Our results (0.009 % at 5 kG for Mn1) are comparable to their reported value. The higher MFIS observed for austenite Fe3 and Mn3 alloys may be due to the magneto-super-elastic effect [80, 137]. This effect is the magnetic analogue of the mechanical super-elastic effect. When magnetic field is applied well above the A_f, all martensitic transition temperatures, e.g. M_s, M_f, A_s and A_f shift to higher temperature side. With this feature, it is possible to induce a structural phase transformation which can be reversed by withdrawing the magnetic field. In the case of $Ni_{54}Mn_{21}Ga_{25}$, the rate of shift of the transformation temperatures on application of a magnetic field is reported to be only about ~1 K/T [137-138]. But for $Ni_{50.3}Mn_{33.8}In_{15.9}$, it has been reported to be as high as ~10 K/T [137]. Thus, field induced structural transformation may be possible in Fe3 (A_f = -10 °C) and Mn3 (A_f = 15 °C) alloys. In magnetic field induced super-elasticity, the maximum field induced strain relies on the difference of crystallographic dimensions in the martensite and austenite state. When a field of sufficient strength is applied at a temperature corresponding initially to the austenitic state, the shift in all characteristic temperature can be large enough to stabilize the martensitic state is stabilized.

To observe FSME, one has to deform the alloy in martensite state by applying external mechanical stress before measuring the strain in magnetic field. The highest MFIS of 10% has been reported [78] for mechanically stressed Ni-Mn-Ga alloy. It may be possible to achieve higher MFIS in the quaternary alloys by a applying a mechanical

stress. Directionally solidified or single crystal Co-Ni-Ga samples would also help in achieving higher uniaxial strains.

5.7. SUMMARY

A series of $Co_{48-x}Ni_{22}Ga_{30-y}T_{x+y}$ (T = Fe, Mn and $x + y = 1$, 3 and 6) alloys have been prepared and their properties have been investigated in this chapter. The basic interest of substitution of Ga and Co by Fe or Mn is to enhance the saturation magnetization and magneto-crystalline anisotropy of these alloys, so that better FSMAs could be obtained.

1. XRD and optical micrograph show that Fe1 and Mn1 alloys exhibit tetragonal martensite structure with precipitation of some amount of γ - phase. Fe6 and Mn6 exhibit a mix structure of bcc austenite and fcc γ - phase.

2. Martensitic transformation temperature was observed for Fe1 and Mn1 alloys above room temperature whereas it was observed lower than room temperature for Fe3, Fe6, Mn3 and and Mn6 alloys

3. T_C of the alloys increased with an increase in Fe/Mn concentration. M_{sat} also increased substantially (almost twice) with the increase of Fe/Mn concentration.

4. Microhardness increased with the increase of Fe/Mn concentration.

5. Compressive strength of the alloy increases with an increase in Mn concentration. A very high compressive strength was observed for the Mn6 alloy.

6 Shape memory effect has been observed in Fe1, Fe3, Mn1 and Mn3 alloys. The other two alloys exhibited pseudo-elastic properties.

7. MFIS of polycrystalline Co-Ni-Ga alloys has been measured for the first time. Our results reveal that MFIS of Fe1 and Mn1 alloys are comparable to the reported value of the unstressed polycrystalline Ni-Mn-Ga alloys.

8. Since MFIS was measured without applying mechanical load on the samples, the strain observed in Fe1 and Mn1 alloys are very low. A high MFIS is expected from these alloys on application of external stress before exposing them to magnetic field.

Three key parameters controlling the magnetic SME are (i) magnetic anisotropy of the martensite, (ii) twinning stress (macroscopic parameter reflecting resistance of martesitic microstructure to rearrangement) and (iii) distortion of lattice. In non-modulated tetragonal martensite, higher compressive stress is required as compared to the modulated structure for radical re-arrangement of martensite microstrucrure by the motion of twin boundaries. Thus, comparatively lower FSME effect is expected in the non-modulated structure alloys. Still from ductility point of view, these quaternary alloys have some potential for actuator application.

CONCLUSION AND SCOPE FOR FUTURE WORK

6.1. Conclusion

A systematic investigation on Co-Ni-Ga ferromagnetic shape memory alloys has been presented in this thesis. Four series of alloys have been prepared and their structural, magnetic and mechanical properties have been discussed. In the first series, Co and Ga contents were varied, maintaining the Ni content constant. In the second series, Ni and Co contents were varied keeping Ga content constant. $Co_{48-x}Ni_{22}Ga_{30-y}Fe_{x+y}$ (where $x+y$ = 1, 3, 6) and $Co_{48-x}Ni_{22}Ga_{30-y}T_{x+y}$ (where $x+y$ = 1, 3, 6) are the last two series of alloys.

In the first series studied, *viz.*, $Co_xNi_{25}Ga_{75-x}$ ($43 \leq x \leq 50$) alloys, single phase martensite phase were exhibited at room temperature by alloys with $x \leq 45$. Alloys with $x \geq 45.5$ exhibited a two phase ($\beta+\gamma$) structure at room temperature. T_C of all the alloys in this series was found to be lower than M_s and A_s. M_{sat} and K_{eff} of these alloys increased with increase in Co at %.

In the second series, viz., $Co_{70-x}Ni_xGa_{30}$ ($20 \leq x \leq 25$), all alloys with $x \geq 21$ exhibited martensitic phase at room temperature. The alloy with $x = 20$ showed austenite structure at room temperature. An increase in M_s and A_s, and a decrease in T_C have been

observed as Co is gradually substituted by Ni in this series of alloys. $Co_{47}Ni_{23}Ga_{30}$ alloy has A_s and T_C very close to each. Such alloys are expected to show giant magneto caloric effect.

M_{sat} was found to be smaller for Co-Ni-Ga than Ni-Mn-Ga alloys. However, K_{eff} estimated for the Co-Ni-Ga alloys was comparable to Ni-Mn-Ga and Fe-Ni-Ga alloys. A considerable increase in M_{sat} and T_C has been observed when small amounts of Fe or Mn are added to Co-Ni-Ga alloys.

Apart from investigating the influence of changes in the constituent elements of Co-Ni-Ga alloys, the studies performed in this thesis have also showed that the structure of the alloys is sensitive to the preparative conditions. Presence of a secondary (γ) phase has been observed when the alloy is quenched from temperatures below 1150 °C. This γ-phase is responsible for the enhancement of ductility of the samples. However, large amounts of γ-phase adversely affects the SME. Thus, an optimum annealing and quenching conditions is required to obtain alloys with good ductility and SME.

The ultimate compressive strength of these alloys ranged from 423 to 579 MPa. Very high compressive strength has been observed in Mn substituted alloys. Highest recovery of strain (3.3 %) was observed in $Co_{49}Ni_{21}Ga_{30}$ alloy. Pseudo-elastic effect was in $Co_{50}Ni_{20}Ga_{30}$ which was pre-strained to 4.2%. MFIS in Co-Ni-Ga has been reported for the first time in this thesis. MFIS values of the investigated alloys are comparable to reported values of polycrystalline Ni-Mn-Ga alloys. Higher MFIS has been observed in Fe/Mn substituted Co-Ni-Ga alloys. However, with the substitution of Fe/Mn, MT

temperatures shifted to lower temperatures. Pseudo–elastic behavior has been observed at room temperature in alloys with higher Fe/Mn substitution.

6.2. Scope for future work

Giant magneto-caloric effect has been reported in various magnetic materials including Ni-Mn-Ga alloys in which magnetic and structural transformations co-occur. The magneto-caloric effect is gaining at lot of attention due to its potential in magnetic refrigeration. We observed very close magnetic and reverse martensitic structural transitions (tetragonal to cubic) in $Co_{47}Ni_{23}Ga_{30}$ alloy prepared by quenching ingots annealed at 1150 °C.

We have observed that the Co-Ni-Ga alloys are very sensitive to ageing. Stabilization of the martensite and precipitation of s secondary phase have been observed in some Co-Ni-Ga samples upon ageing in the martensite or austenite phase. Due to time constraint this work could not be completed and hence did not form part of this thesis. Since the ageing behaviour of these alloys has not well documented, the same is worthy of study.

MFIS observed in this work is comparable to that of polycrystalline Ni-Mn-Ga. Higher MFIS can be achieved in the present alloys by applying mechanical stress on them before exposing them to magnetic field. Recovery of shape can also be observed by deforming the alloys in the martensite phase and then exposing them to magnetic field. Samples in ribbon form may be more suitable for such measurements. Ribbons of these alloys can be prepared by melt spinning technique. Enhancement of magnetic properties

has been observed in Co-Ni-Ga alloys substituted with small amounts of Fe and Mn. It would be interesting to verify whether the properties of Co-Ni-Ga alloys can be further enhanced by the substitution of other elements.

REFERENCES

[1] A. Lendlein and S. Kelch: *Angew. Chem. Int. Ed.* **41** (2002) 2034.

[2] T. Okano and A. Kikuchi: *Proceedings of Third International Conference on Intelligent Materials*, *Third European Conference on Smart Structures and Materials*, Lyon, France, 3–5 June 1996, Edited by P. F. Gobin and J. Tatibouët, 34–41.

[3] B. Culshaw: *Smart Structures and Materials*, San Diego, CA, Artech House Publisher, 1996, 1–16.

[4] J. Hu: *Shape memory polymers and textiles*, Woodhead Publishing Limited, Cambridge, 2007.

[5] L. N. Christophorov: *Proceedings of the Third International Conference on Intelligent Materials*, *Third European Conference on Smart Structures and Materials*, Lyon, France, 3–5 June 1996, Edited by P.F. Gobin and J. Tatibouët, 58–65.

[6] V. V. Varadan, L. C. Chin, and V. K. Varadan: *Proceedings First European Conference on Smart Structures and Materials*, Glasgow, 12–14 May 1992, Edited by B. Culshaw, P. T. Gardiner and A. McDonach, 1–6.

[7] http://en.wikipedia.org/wiki/Shape_memory_alloy

[8] G. B. Kauffman and I. Mayo: *Invention Tech. Magazine* **9** (1993) (available at www.americanheritage.com/articles/magazine/it/1993/2/1993_2_18.shtml).

[9] http://www.scielo.br/scielo.php

[10] K. Otsuka and C. M. Wayman (editor): *Shape Memory Materials*, Cambridge University Press, UK (1998).

[11] K. Otsuka and X. Ren: *Intermetallics* **7** (1999) 511.

[12] L.G. Machado and M.A. Savi: *Braz. J. Med. Biol. Res.* **36** (2003) 683.

[13] P. J. Webster, K. R. A. Ziebeck, S. L. Town and M. S. Peak: *Philos. Mag.B* **49** (1984) 295.

[14] R.D. James and M. Wutting: *Philos. Mag. A* **77** (1998) 1273.

[15] T. Kakeshita, T. Takeuchi, T. Fukuda, T. Saburi, R. Oshima, S. Muto and K. Kishio: *Mater. Trans. JIM* **41** (2000) 882.

[16] F. Gejima, Y. Sutou, R. Kainuma and K. Ishida: *Matell. Mater. Trans.* **30** (1999) 2721.

[17] K. Oikawa, L. Wulff, T. Iijima, F. Gejima, T. Ohmori, A. Fujita, K. Fukamichi, R. Kainuma and K. Ishida: *Appl. Phys. Lett.* **79** (2001) 3290.

[18] R. Kainuma, M. Ise, C. -C. Jia, H. Ohtani and K. Ishida: *Intermetallics* **4** (1996) S151.

[19] K. Oikawa, T. Ota, F. Gejima, T. Ohmori, R. Kainuma and K. Ishida: *Mater. Trans.* **42** (2001) 2472.

[20] M. Wuttig, J. Li and C. Craciunescu: *Scripta Mater.* **44** (2001) 2393.

[21] K. Oikawa, T. Ota, Y. Sutou, T. Ohmori, R. Kainuma and K. Ishida: *Mater. Trans.* **43** (2002) 2360.

[22] K. Oikawa, T. Ota, T. Ohmori, Y. Tanaka, H. Morito, A. Fujita, R. Kainuma, K. Fukamichi and K. Ishida: *Appl. Phys. Lett.* **81** (2002) 5201.

[23] K. Ullakko, J.K. Huang, C. Kantner, R.C. O'Handley and V.V. Kokorin: *Appl. Phys. Lett.* **69** (1996) 1966.

[24] V.V. Khovalio, T. Takagi, A.N. Vasilev, H. Miki, M. Matsumoto and R. Kainuma: *Phys. Stat. Sol.(a)* **183** (2001) R1-R3.

[25] S. Banik, R. Ranjan, A. Chakraborti, S. Bhardwaj, N.P Lalla, A.M. Awasthi, V. Sathe, D.M. Phase, P.K. Mukhopadhyay, D. Pandey and S.R. Barman: *Phys. Rev. B* **75** (2007) 104107.

[26] X. F. Dai, H. Y. Wang, G. D. Liu, Y. G. Wang, X.F. Duan, J.L. Chen and G. Wu: *J. Phys.D: Appl. Phys.* **39** (2006) 2886.

[27] D.Canadinc, J. Dadda, H. J. Maier, I. Karaman, H. E Karaca and Y. I-Chumlyakov: *Smart Mater. Struct.* **16** (2007)1006.

[28] V. A. Chernenko, E. Cesari, V. V. Kokorin and I. N. Vitenko: *Scripta Metall. Mater.* **33** (1995) 1239**.**

[29] Y. Li, Y. Xin, C. Jiang and H. Xu: *Scripta Mater.* **51** (2004) 849.

[30] W. H. Wang, F. X. Hu, J. L. Chen, Y. X. Li, Z.Wang, Z. Y. Gao,Y. F. Zheng, L. C. Zhao, G.H.Wu and W. S. Zan: *IEEE Trans. Magn.* **37** (2001) 2715.

[31] P. J. Brown, J. Crangle, T. Kanomata, M. Matsumoto, K-U Neumann, B. Ouladdiaf and K. R. A. Ziebeck: *J. Phys: Condens. Matter* **14** (2002) 10159.

[32] P. J. Brown, K. Ishida, R. Kainuma, T. Kanomata, K-U Neumann, K Oikawa, B. Ouladdiaf and K. R. A. Ziebeck: *J. Phys: Condens. Matter* **17** (2005) 1301.

[33] *A*. Planes, L. Mañosa, X. Moya, T. Krenke, M. Acet and E.F. Wassermann: *J. Magn. Magn. Mater.* **310** (2007) 2767.

[34] R. Santamarta, J. Font, J. Muntasell, F. Masdeu, J. Pons, E. Cesari and J. Dutkiewicz: *Scripta Mater.* **54** (2006) 1105.

[35] K. R. Priolkar, P. A. Bhobe, S. D. Sapeco and R. Paudel: *Phys. Rev. B* **70** (2004) 132.

[36] S. Majumdar, V. K. Sharma, M. Manekar, R. Kaul, K. J. S. Sokhey, S. B. Roy and P. Chaddah: *Sol. Stat. Com.* **136** (2005) 85.

[37] S. Kustov, M. Corró and E. Cesari: *Appl. Phys. Lett.* **91** (2007) 141907.

[38]Y. Tanaka, K. Oikawa, Y. Sutou, T. Omori, R. Kainuma and K. Ishida: *Mater. Sci. Engg. A* **438** (2006) 1054.

[39] J. Liu, H. X. Zheng, M. X. Xia, Y. L. Huang and J. G. Li: *Scripta Mater.* **52** (2005) 935.

[40] J. Liu, M. Xia, Y. Huang, H. Zheng and J. Li: *J. Alloys Compd.* **417** (2006) 96.

[41] P. Müllner,V. A. Chernenko, M. Wollgarten and G. Kostorz: *J. Appl. Phys.* **92** (2002) 6708.

[42] V. A. Chernenko, J. Pons, E. Cesari and A. E. Perekos: *Mater. Sci. Engg. A* **378** (2004) 357.

[43] T. Sakamoto, T. Fukuda, T. Kakeshita, T. Takeuchi and K. Kishio: *Sc. Tech. Adv. Mater.* **5** (2004) 39.

[44] V. V. Martynov: *J. Phys. IV* **5** (1995) C8-91.

[45] B. Wedel, M. Suzuki, Y. Murakami, C. Wedel, T. Suzuki, D. Shindo and K. Itagaki: *J. Alloys and Compd.* **290** (1999)137.

[46] J. Pons, V. A. Chernenko, R. Santamarta and E. Cesari: *Acta Mater.* **48** (2000) 3027.

[47] R. Ranjan, S. Banik, S. R. Barman, U. Kumar, P. K. Mukhopadhyay and D. Pandey: *Phys. Rev. B* **74** (2006) 224443.

[48] H. X. Zheng, M. **X**. Xia, J. Liu and J. G. Li: *J. Alloys Compd.* **385** (2004) 144.

[49] G. D. Liu, Z. H. Liu, X. F. Dai, S. Y. Yu, J. L. Chen and G. H. Wu: *Sc. Techn. Advan. Mater.* **6** (2005) 772.

[50] Y. Sutou, N. Kamiya, T. Omori, R. Kainuma, K. Ishida and K. Oikawa: *Appl. Phys. Lett.* **84** (2004) 1275.

[51] Y. Murakami, D. Shindo, K. Oikawa, R. Kainuma and K. Ishida: *Acta Mater.* **50** (2002) 2173.

[52] Z. H. Liu, X. F. Dai, Z. Y. Zhu, H. N. Hu, J. L. Chen, G. D. Liu and G. H. Wu: *J. Phys. D: Appl. Phys.* **37** (2004) 2643.

[53] J. Liu, H. Xie, Y. Huo, H. Zheng and J. Li: *J. Alloy Compd.* **420** (2006) 145.

[54] M. Zhang, E. Brück, F. R. de Boer and G. Wu: *J. Phys. D: Appl. Phys.* **38** (2005) 1361.

[55] V. A. Chernenko, J. Pons, E. Cesari and I. K. Zasimchuk: *Scripta Meter.* **50** (2004) 225.

[56] P. Müllner, V. A. Chernenko and G. Kostorz: *J. Magn. Magn. Mater.* **267** (2003) 325.

[57] Y. Ma, C. Jiang, Y. Li, H. Xu, C. Wang and X. Liu: *Acta Mater.* **55** (2007) 1533.

[58] M. Matsumoto, M. Ebisuya, T. Kanomata, R. Note, H. Yoshida and T. Kaneko: *J. Magn. Magn. Mater.* **239** (2002) 521.

[59] S. Banik, A. Chakrabarti, U. Kumar, P. K. Mukhopadhyay, A. M. Awasthi, R. Ranjan, J. Schneider, B. L. Ahuja and S. R. Barman: *Phys. Rev. B* **74** (2006) 085110.

[60] M. Wuttig, L. Liu, K. Tsuchiya and R. D. James: *J. Appl. Phys.* **87** (2000) 4707.

[61] S. K. Wu and S.T. Yang: *Mater. Lett.* **57** (2003) 4291.

[62] V. A. Chernenko: *Scripta. Mater.* **40** (1999) 523.

[63] T. Krenke, X. Moya, S. Aksoy, M. Acet, P. Entel, L. Mañosa, A. Planes, Y. Elerman, A. Yücel and E.F. Wassermann: *J. Magn. Magn. Mater.* **310** (2007) 2788.

[64] V.V. Khovalio, K. Oikawa, T. Abe, T. Tagaki, arXiv.cond-mat:0302352 v1 (2003)1.

[65] S. Miura, S. Maeda and N. Nakanushi: *Philos. Mag.* **30** (1974) 56.

[66] Y. Nakajima, S. Aoki, K. Otuka and T. Ohba: *Mater. Lett.* **21** (1994) 271.

[67] H. Sakamoto, K. Otsuka and K. Shimizu: *Scripta Mater.* **11** (1977) 607.

[68] L. Dai, M. Wuttig and E. Pagounis: *Scripta Mater.* **55** (2006) 807.

[69] C. Seguí, E. Cesari, J. Font, J. Muntasell and V.A. Chernenko: *Scripta Mater.* **53** (2005) 315.

[70] V. A. Chernenko, V. A. L'vov and E. Cesari: *J. Magn. Magn. Mater.* **196** (1999) 859.

[71] V. A. L'vov, E. V. Gomonaj and V. A. Chernenko: *J. Phys: Condens. Matter* **10** (1998) 4587.

[72] S. V. Andreev, M. I. Bartashevich, V. I. Pushkarsky, V. N. Maltsev, A. Pamyatnykh, E. N. Tarasov, N. V. Kudravatykh and T. Goto: *J. Alloys and Compd.* **260** (1997) 196.

[73] A. Arrott and J. Noakes: *Phys. Rev. Lett.* **19** (1967) 786.

[74] A. R. Williams, V. L. Moruzzi, A. P. Malozemoff and T. Terakura: *IEEE Trans. Magn.* **19** (1983) 1983.

[75] G. Li, Y. Liu and B. K. A. Ngoi: *J. Magn. Magn. Mater.* **303** (2006) 261.

[76] C. Biswas, R. Rawat and S. R. Barman: *Appl. Phys. Lett.,* **86** (2005) 202508.

[77] W. Yan, Q. Sun and H.Y. Liu: *Mater. Sci. Engg. A* **425** (2006) 278.

[78] A. Sozinov, A. A. Likhachev, N. Lanska and K. Ullakko: *Appl. Phys. Lett.* **80** (2002) 1746.

[79] S. J. Murray, M. Marioni, R. C. O'Handley and T. A. Lograsso: *Appl. Phys. Lett.* **77** (2000) 886.

[80] S. Jeong, K. Inoue, K. Koterazawa, M. Taya, K. Inoue: *Mater. Sci. Engg. A* **359** (2003) 253.

[81] T. Kakeshita, J.-H. Kim and T. Fukuda: *Mater. Sci. Engg. A* **481** (2007) 40.

[82] Z. Q. Zhao, W. Xiong, S. X. Wu and X. L. Wang: *J. Iron Steel Res.* **111** (2004) 55.

[83] Z. Q. Zhao, S. X. Wu, F. S. Wang, Q. Wang, L. P. Jiang and X. L. Wang: *Rare Met.* **23** (2004) 241.

[84] L. Gao, W. Cai, A. L. Liu and L. C. Zhao: *J. Alloys Compd.* **425** (2006) 314.

[85] L. Gao, J. H. Sui and W. Cai: *J. Magn. Magn. Mater.* **320** (2008) 63.

[86] G. H. Wu, W. H. Wang, J. L. Chen, L. Ao, Z. H. Liu, W. S. Zhan, T. Liang and H. B. Xu: *Appl. Phys. Lett.* **80** (2002) 634.

[87] D. Kikuchi, T. Kanomata, Y. Yamaguchi, H. Nishihara, K. Koyama, K. Watanabe: *J. Alloys Compd.* **383** (2004) 184.

[88] H. Zheng, M. Xia, J. Liu, Y. Huang and J. Li: *Acta Mater.* **53** (2005) 5125.

[89] K. Oikawa, Y. Imano, V.A. Chernenko, F. Luo, T. Omori and Y. Sutou: *Mater. Trans.* **46** (2005) 734.

[90] Imano, T. Omori, K. Oikawa, Y. Sutou, R. Kainuma and K. Ishida: *Mater. Sci. Engg.* A **438** (2006) 970.

[91] H. Zheng, J. Liu, M. Xia and J. Li: *Mater. Sci. Engg.* A **438** (2006) 1011.

[92] H. X. Zheng, J. Liu, M. X. Xia and J. G. Li: *J. Alloys Compd.* **387** (2005) 265.

[93] H. Morito, K. Oikawa, A. Fujita, K. Fukamichi, R. Kainuma and K. Ishida: *Scripta Mater.* **53** (2005)1237.

[94] H. Morito, K. Oikawa, A. Fujita, K. Fukamichi, R. Kainuma and K. Ishida*: J. Magn. Magn. Mater.* **290** (2005) 850.

[95] Z. H. Liu, H. Liu, X. X. Zhang, X. K. Zhang, J. Q. Xiao and Z. Y. Zhu: *Appl. Phys. Lett*. **86** (2005) 182507.

[96] H. Morito, A. Fujita, K. Oikawa, K. Ishida, K. Fukamichi and R. Kainuma: *Appl. Phys. Lett.* **90** (2007) 062505.

[97] C. Picornell, J. Pons, E. Cesari and J. Dutkiewicz: *Intermetallics* **16 (** 2008) 751.

[98] J. Liu and J. G. Li: *Scripta Mater.* **56** (2007) 109.

[99] B. D. Cullity and S. R. Stock: *Elements of X-ray Diffractions*, 3rd ed., Prentice Hall, Upper Saddle River, N J (2001).

[100] H.M Rietveld: *Acta Cryst.* **22** (1967) 151.

[101] H. M Rietveld: *Acta Cryst.* **2** (1969) 65.

[102] D. Louer: *Acta Cryst*. **A 54** (1998) 922.

[103] T. Hatakeyama and Z. Liu (editor): *Hand Book of Thermal Analysis*, John Wiley & Sons , Chichister (1998).

[104] H. Sehitoglu, C. Efstathiou, H. J. Maier and Y. Chumlyakov: *Mech. Mater.* **38** (2006) 538.

[105] W. R. Abel, A. C. Anderson and J. C. Wheatley: *Rev. Sci. Instrum.* **35** (1964) 444.

[106] S. Sarma, M. P. C. Kalita, A. Perumal and A. Srinivasan: *Proc. National Workshop Adv. Tech. Material Characterization*, M. S. University of Baroda, Vadodara (2006) 19.

[107] D. J. Griffith: *Introduction to Electrodynamics*, 2nd ed., Prentice hall, NewDelhi (1995).

[108] M. Fähnle and H. Kronmüller: *J. Magn. Magn. Mater.* **8** (1978) 149.

[109] Z. -Q. Jin, W. Tang, J. -R Zhang, H. -X. Qin and Y. -W. Du: *Eur. Phys J.B* **3** (1998) 41.

[110] J. P. Wang, D. -H. Han, H. -L. Luo, Q. -X. Lu and Y.-W. Sun: *Appl. Phys. A* **61** (1995) 407.

[111] C. D. Graham and M. R. J. Gibbs: *IEEE Trans. Magnet.* **29** (1993) 3457.

[112] A. Arrott and J. Noakes: *Phys. Rev. Lett.* **19** (1967) 786.

[113] J. S. Kovel and M. E. Fisher: *Phys. Rev. B* **136** (1964) A1626.

[114] S. N. Kaul: *Phys. Rev. B* **22** (1980) 278.

[115] S. N. Kaul: *J. Magn. Magn. Mater.* **53** (1985) 5.

[116] T. L. Phan, S. G. Min, S. C. Yu and S. K. Oh: *J. Magn. Magn. Mater.* **304** (2006) e-778.

[117] K. Ghosh, C.J. Lobb, R. L. Greene, S.G. Karabashev, D.A. Shulyatev, A. A. Arsenov and Y. Mukovskii: *Phys. Rev. Lett.* **81** (1998) 4740.

[118] A. S. Khan and X Wang: *Stress measurement and Strain anlysis*, Prentice Hall, Upper Saddle River (2001).

[119] M. Yamane and J. D. Mackenzie: *J. Non-Cryst. Solids* **15** (1974) 153.

[120] A. D. Helfrick and W. D. Cooper: *Modern Electronic Instrumentation and Measurement Techniques*, Prentice Hall, New Delhi (1996).

[121] A. Planes, L. Manosa, D. Rios-Jara and J. Ortin: *Phys. Rev. B* **45** (1992) 7633.

[122] C. Jiang, Y. Muhammad, L. Deng, W. Wu and H. Xu: *Acta Mater.* **52** (2004) 2779. [123] J. Pons, C. Segui, V. A. Chernenko, E. Cesari, P. Ochin and R. Portier: *Mater. Sci. and Engg. A* **273** (1999) 315.

[124] J. Dadda, H. J. Maier, I. Karaman, H. E. Karaca, Y. I. Chumlyakov: *Scripta Mater.* **55** (2006) 663.

[125] C. Craciunescu, Y. Kishi, T. A. Lograsso and M. Wuttig: *Scripta Mater.* **47** (2002) 285.

[126] J. S. Koehler, F. Seitz and J. E. Bauerle: *Phys. Rev. B* **107** (1957) 1499.

[127] L. H. Lewis, M. J. Kramer, R.W. McCallum and D. J. Branagan: *Proc. III Intel. Workshop Mater. Sci.*, Hanoi (1999) BNL-66785.

[128] H. Grimm and K. Kronmoller: *Phys. Stat. Solid b* **117** (1983) 663.

[129] O. Heczko and P. Ruuskanen: *IEEE Trans. Magnet.* **30** (1994) 513l.

[130] S. Blundell: *Magnetism in Condensed Matter* (Oxford Univ. Press, Oxford, 2001) 119.

[131] M. E. Fisher, S-K. Ma and B. G. Nickel: *Phys. Rev. Lett.* **29** (1972) 917.

[132] R. Malmhall, G. Backstrom, K. V. Rao, S. M. Bhagat, M. Meichle and M. B. Salamon : *J. Appl. Phys.* **49**(1978) 1727.

[133] H. E. Stanley: *Intr. Phase Transitions and Critical Phenomena* (Oxford Univ. Press, Newyork (1987) 47.

[134] Y. Chumlyakov, E. Panchenko, I. Kireeva, I. Karaman, H. Sehitoglu, H. J. Maier, A. Tverdokhlebova and A. Ovsyannikov: *Mater. Sci. Engg. A* **481** (2008) 95.

[135] T. Krenke, X. Moya, S. Aksoy, M. Acet, P. Entel, Ll. Mañosa, A. Planes, Y. Elerman, A. Yücel and E. F. Wassermann: *J. Magn. Magn. Mater.* **383** (2004) 184.

[136] T. Sakamotoa,T. Fukudaa,T. Kakeshitaa,T. Takeuchib and K. Kishioc*: Sci. Tech. Adv. Mater.* **5** (2004) 39.

[137] T. Krenke, E. Duman, M. Acet, E. F. Wassermann, X. Moya, L. Mañosa, A. Planes, E. Suard and B.Ouladdiaf: *Phys. Rev. B* **75** (2007) 104414.

[138] I. E. Dikshtein, D. I. Ermakov, V. V. Koledov, L.V. Koledov, T.Tagaki, A. A. Tulaikova, A. A. Cherechukin and V. G. Shavrov: *JETP Lett.* **72** (2000) 373.

PUBLICATIONS

Paper published/communicated in Journals:

1. **Sidananda Sarma** and A. Srinivasan, Development of Co-Ni-Ga ferromagnetic shape memory alloys with enhanced properties, Mater. Sci. Forum **587** (2008) 650.
2. **Sidananda Sarma** and A. Srinivasan, Influence of annealing temperature on the properties of Co-Ni-Ga ferromagnetic shape memory alloy, Advance Mater. Res. **52** (2008) 63.
3. **Sidananda Sarma** and A. Srinivasan, Structural characterization of $Co_{70-x}Ni_xGa_{30}$ ferromagnetic shape memory alloys, Advance Mater. Res. **52** (2008) 103.
4. A. Srinivasan and **Sidananda Sarma**, Co-Ni-Ga alloys with room temperature ferromagnetic martensite phase, Advance Mater. Res. **52** (2008) 95.
5. **Sidananda Sarma** and A. Srinivasan, Influence of cooling rate on the properties of ferromagnetic shape memory alloy, Indian J. Phys. **82** (2008) 701.
6. **Sidananda Sarma**, Study of structural and magnetic phase transformations in Co-Ni-Ga alloys. Research Journal of Contemporary Concern, Cotton College Research Council, Research Journal of Cotton College (accepted for publication).

Paper published in Conference Proceedings:

1. **Sidananda Sarma**, A Perumal and A. Srinivasan, The nature of ferromagnetic phase transition in Co-Ni-Ga alloys, Proc. of International Workshop and Conference on Statistical Physics Approaches to Multi-disciplinary Problems, 2007, I.I.T. Guwahati, India.
2. **Sidananda Sarma** and A. Srinivasan, Magnetic and thermal characterization of Co-Ni-Ga ferromagnetic shape memory alloys, Proc. of National Conference on Sensors and Actuators: Emerging Technological challenges (NCSA-06), 2007, CGCRI, Kolkata, India.
3. **Sidananda Sarma** and A. Srinivasan, Investigation of shape memory effect in Co-Ni-Ga alloy using differential scanning calorimeter, Proc. of National Workshop on Advance Techniques for Material characterization, 2006, M.S. University, Baroda, India.
4. **Sidananda Sarma**, Manos P.C. Kalita, A. Perumal and A. Srinivasan, Development of a high temperature and low-field ac susceptometer, Proc. of National Workshop on Advance Techniques for Material characterization, 2006, M.S. University, Baroda, India.
5. **Sidananda Sarma** and A. Srinivasan, Preparation and characterization of Co-Ni-Ga ferromagnetic shape memory alloys, Proc. of National Conference of Material Science, 2006, Periyar University, Salem, India.

-----^-----